Reconstruction of a palaeolake system at the UNESCO World Heritage Site Tsodilo Hills, Kalahari, Botswana: LGM climate, weather and environmental variation

DISSERTATION

submitted to the

Department of Earth Sciences of the

FREIE UNIVERSITÄT BERLIN

in fulfilment of the requirements for the

academic degree

Doctor rerum naturalium

(Dr. rer. nat.)

by

M.Sc.

Marielle Geppert

Berlin, May 2022

Abstract

One of the most pressing problems of the 21st century is the current human-induced climate change. In order to assess the expected impacts of climate change, the understanding of past climatic conditions and the reconstruction of the respective paleo-environments is of great importance, as this provides information about possible environmental responses to corresponding climate changes. Especially, the late Quaternary climate of southern Africa is still controversially discussed because palaeoclimate modelling and reconstruction from various proxies of different systems are contradictory. Some contradictions can be related to dating uncertainties, others to the complexity of the systems. The large Quaternary lacustrine systems in the Kalahari, for example, are influenced by tectonics and have inter-regional catchments and, therefore, complicate the identification of climatic and non-climatic signals in sedimentary proxy records.

The first part of this dissertation focusses on the reconstruction of a small palaeolake basin west of the Tsodilo Hills. With its regional catchment that lies solely in the Kalahari, the Palaeolake Tsodilo has high potential as a palaeoclimate archive. The palaeolake has already been shown to have been active at least during Last Glacial Maximum (LGM) and mid Marine Isotope Stage (MIS) 3 and archaeological studies have explored signs of human occupation of the hills for the last 100 ka. The latter is especially interesting, as the region of the Okavango Delta, where the hills are located, was recently considered the geographic origin of evolutionary modern humans and it was proposed that subsequent out-of-homeland migration was induced by climate shifts. Therefore, the first objective of the present dissertation is to gain more reliable information about the hydrological dynamics of the fluvio-lacustrine system using a multi-method approach, with focus on the evolution of the lake during ca. 43–19 ka BP. Thus, also a better understanding of the Late Pleistocene environment of the ancient Tsodilo people can be obtained, concerning the palaeo-hydrological conditions. The multidisciplinary approach included different remote sensing and geophysical methods, comprehensive application of differential GPS, and sedimentological analyses concentrating on the lake beds. A high-resolution digital elevation model from the TanDEM-X mission and multiple Landsat images were analysed to identify geomorphological features, such as shorelines or channels, and related processes. Furthermore, differential GPS measurements as well as ground-penetrating radar and seismic refraction surveys enabled a deeper investigation of these structures. Using this approach, four palaeo-shorelines could be identified. Three of these indicate highstands during which the Tamacha palaeo-river drained the Palaeolake Tsodilo towards the Okavango Panhandle. Furthermore, the two highstands during mid

MIS 3 and LGM are related to periods of largely increased fish consumption by humans as has been documented by archaeologists. The palaeolake probably had its greatest extent about 100 ka ago or earlier, when it was about ca. 70 km^2 in size and 16 m deep. A single (neo-)tectonic fault could be detected, so geologically, the Tsodilo Hills were comparatively calm. The findings suggest that there have been major hydrological changes during the Late Pleistocene from MIS 3 to the LGM, which yet need to be further investigated. The identified spatial and stratigraphical interrelations of geomorphological processes are relevant for the palaeo-hydrological interpretation of sediment records of Palaeolake Tsodilo regarding the role of the sediment cascade and can enable to separate climatic and non-climatic signals.

In the second part of this dissertation, the focus lies on the investigation of stable isotope patterns in modern precipitation. To asses the palaeoclimate and to answer the question of where the moisture that fed the Quaternary lacustrine systems in the Kalahari came from and when, different proxies within the lake sediments can be used. The δ^{18}O and δ^{13}C values in fossil gastropod shells, for example, are often used to reconstruct palaeoclimate and its variability. By analysing these C and O stable isotopes, it is possible to draw conclusions about the hydro-climatic conditions at the location of precipitation, but also at the moisture source region and along the moisture trajectory. However, in order to interpret such information from palaeo-archives, a sound understanding of the present climate and stable water isotope patterns of the region is needed as a reference. The second objective of the dissertation is therefore, to investigate spatial differences in the isotopic composition of water in southern Africa, and moreover to examine relationships between the stable isotopic composition of water and the corresponding moisture source regions and transport patterns. In a first step, end-member modelling allowed to analyse the precipitation distributions over the year in southern Africa. Collected water samples from the different identified rainfall zones (RFZs) were then measured for their isotopic composition and a comparison of the compositions made among the RFZs. Backward trajectories were calculated to determine the main moisture uptake regions for the different RFZs. Finally, the relationship between the isotopic composition and transport characteristics were investigated. Five RFZs were identified for southern Africa of which some are significantly differing in their isotopic compositions. Furthermore, the isotopes are generally lighter during rainfall season compared to off-season. Differing moisture source regions could be identified for the RFZs and characteristic driving atmospheric forces assigned for the zones. The results furthermore show the importance of the amount effect for the general isotopic composition over whole southern Africa as well as a great importance of the travelled distance of the moisture. The diagnosed patterns

and relationships enhance our understanding of the atmospheric water cycle of southern Africa and the connected stable water isotopes. Future work should focus on more detailed relationships between the stable isotopic composition of water and the corresponding moisture source regions and transport patterns within the single RFZs. However, the presented findings already have potential to be used for further applications, for example, the interpretation of palaeoclimate proxies from other lake records across southern Africa.

These two studies allowed to reconstruct active stages of the fluvio-lacustrine system at the Tsodilo Hills during late Quaternary and to analyse the relationship of the modern climate and stable isotopes of water as an interpretation basis for proxiies to reconstruct moisture sources and precipitation patterns. These results are a prerequisite for follow-up steps to better understand the southern African palaeoclimate of the Late Pleistocene, such as to analyse the isotopic characteristics of fossil mollusc shells at Palaeolake Tsodilo and additional locations around southern Africa. Drawing conclusions about the palaeoclimate regarding moisture sources and precipitation seasonality, based on the knowledge gained within this thesis about modern moisture trajectories and related isotope compositions of water, might then allow to answer the question where and when the moisture feeding the large Quaternary lacustrine systems in the Kalahari came from and to resolve some of the contradictions about the late Quaternary climate.

Kurzfassung

Eines der drängendsten Probleme des 21. Jahrhunderts ist der gegenwärtige, vom Menschen verursachte Klimawandel. Um die zu erwartenden Auswirkungen des Klimawandels abschätzen zu können, ist das Verständnis vergangener klimatischer Bedingungen und die Rekonstruktion der jeweiligen Paläolandschaften von großer Bedeutung, da dies Aufschluss über mögliche Reaktionen der Umwelt auf entsprechende Klimaänderungen gibt. Besonders das spätquartäre Klima des südlichen Afrikas wird nach wie vor kontrovers diskutiert, da die Modellierung des Paläoklimas und die Rekonstruktion anhand verschiedener Proxies aus unterschiedlichen Systemen widersprüchlich sind. Einige Widersprüche lassen sich auf Datierungsunsicherheiten zurückführen, andere auf die Komplexität der Systeme. Die großen quartären lakustrinen Systeme in der Kalahari beispielsweise werden tektonisch beeinflusst und haben überregionale Einzugsgebiete, was die Identifizierung von klimatischen und nichtklimatischen Signalen in sedimentären Proxy-Datensätzen erschwert.

Der erste Teil dieser Dissertation konzentriert sich auf die Rekonstruktion eines kleinen Paläoseebeckens westlich der Tsodilo Hills. Mit seinem regionalen Einzugsgebiet, das ausschließlich in der Kalahari liegt, hat der Paläosee Tsodilo großes Potenzial als Paläoklimaarchiv. Es wurde bereits nachgewiesen, dass der Paläosee zumindest während des letzten glazialen Maximums (Last Glacial Maximum, LGM) und des mittleren marinen Isotopenstadiums (MIS) 3 aktiv war, und bei archäologischen Untersuchungen wurden Anzeichen für eine menschliche Besiedlung der Hügel während der letzten 100 ka gefunden. Letzteres ist besonders interessant, da die Region des Okavango-Deltas, in der sich die Hügel befinden, vor kurzem als geografischer Ursprung des evolutionären modernen Menschen in Erwägung gezogen wurde und angenommen wird, dass die anschließende Migration aus der Heimat durch Klimaveränderungen veranlasst wurde. Daher besteht das erste Ziel der vorliegenden Dissertation darin, die Phasen des fluvio-lakustrinen Systems mit Hilfe eines multimethodischen Ansatzes zu rekonstruieren, wobei der Schwerpunkt auf der Entwicklung des Sees während ca. 43–19 ka BP liegt. Auf diese Weise lässt sich auch ein besseres Verständnis der spätpleistozänen Umwelt der früheren Tsodilo-Bevölkerung erlangen, insbesondere hinsichtlich der paläohydrologischen Bedingungen. Der multidisziplinäre Ansatz umfasste verschiedene Fernerkundungs- und geophysikalische Methoden, eine eingehende Anwendung von Differential-GPS und sedimentologische Analysen, die sich auf den Seeboden konzentrierten. Ein hochauflösendes digitales Höhenmodell aus der TanDEM-X-Mission und mehrere Landsat-Bilder wurden analysiert, um geomorphologische Strukturen, wie Uferlinien oder Flussläufe, und damit verbundene Prozesse zu identifizieren.

Darüber hinaus ermöglichten differentielle GPS-Messungen sowie Bodenradar- und seismische Refraktionsmessungen eine genauere Untersuchung dieser Strukturen. Mit diesem Ansatz konnten vier Paläo-Uferlinien identifiziert werden. Drei davon deuten auf Hochphasen hin, in denen der Paläofluss Tamacha den Paläosee Tsodilo in Richtung Okavango-Panhandle entwässerte. Darüber hinaus stehen die beiden Hochphasen während des mittleren MIS 3 und des LGM im Zusammenhang mit Perioden, in denen der Fischkonsum der Menschen stark zunahm, wie von Archäologen dokumentiert wurde. Der Paläosee hatte seine größte Ausdehnung wahrscheinlich vor etwa 100 ka oder früher, als er ca. 70 km^2 groß und 16 m tief war. Es konnte eine einzige (neo-)tektonische Verwerfung festgestellt werden, so dass die Tsodilo Hills geologisch gesehen vergleichsweise ruhig waren. Die Ergebnisse deuten darauf hin, dass es während des Spätpleistozäns vom MIS 3 bis zum LGM große hydrologische Veränderungen gegeben hat, die jedoch noch genauer untersucht werden müssen. Die ermittelten räumlichen und stratigraphischen Zusammenhänge geomorphologischer Prozesse sind für die paläohydrologische Interpretation der Sedimentaufzeichnungen des Paläosees Tsodilo im Hinblick auf die Rolle der Sedimentkaskade von Bedeutung und können die Trennung klimatischer und nicht-klimatischer Signale ermöglichen.

Im zweiten Teil dieser Dissertation liegt der Schwerpunkt auf der Untersuchung von Mustern der stabilen Isotope in den Niederschlägen der heutigen Zeit. Zur Beurteilung des Paläoklimas und zur Beantwortung der Frage, woher und wann die Feuchtigkeit kam, die die quartären lakustrinen Systeme in der Kalahari speiste, können verschiedene Proxies in den Seesedimenten als Paläoarchive verwendet werden. Die δ^{18}O- und δ^{13}C-Konzentrationen in fossilen Schneckenschalen werden zum Beispiel häufig zur Rekonstruktion des Paläoklimas und seiner Variabilität verwendet. Durch die Analyse diese stabilen Isotope lassen sich Rückschlüsse auf die klimatischen und physikalischen Bedingungen am Ort des Niederschlags, aber auch im Bereich der Feuchtigkeitsquelle und entlang des Feuchtigkeitsverlaufs ziehen. Um solche Informationen aus Paläoarchiven zu interpretieren, ist jedoch ein fundiertes Verständnis des gegenwärtigen Klimas und der Muster stabiler Wasserisotope in der Region als Referenz erforderlich. Das zweite Ziel der Dissertation besteht daher darin, die räumlichen Unterschiede in der Isotopenzusammensetzung des Wassers im südlichen Afrika zu untersuchen und darüber hinaus die Beziehungen zwischen der stabilen Isotopenzusammensetzung des Wassers und den entsprechenden Feuchtigkeitsherkunftsgebieten und Transportmustern zu untersuchen. In einem ersten Schritt ermöglichte die Modellierung der End-member eine Analyse der Niederschlagsverteilung über das Jahr im südlichen Afrika. Gesammelte Wasserproben aus den verschiedenen identifizierten Regenfallzonen (RFZ) wurden dann auf

ihre Isotopenzusammensetzung hin gemessen und ein Vergleich der Zusammensetzungen zwischen den RFZ vorgenommen. Es wurden Rückwärts-Trajektorien berechnet, um die wichtigsten Regionen für die Feuchtigkeitsaufnahme in den verschiedenen RFZ zu bestimmen. Schließlich wurde die Beziehung zwischen der Isotopenzusammensetzung und den Transporteigenschaften untersucht. Für das südliche Afrika wurden fünf RFZ ermittelt, von denen sich einige in ihrer Isotopenzusammensetzung signifikant unterscheiden. Außerdem sind die Isotope während der Regenzeit im Allgemeinen leichter als außerhalb der Regenzeit. Für die Niederschlagszonen konnten unterschiedliche Feuchtigkeitsquellen identifiziert und den Zonen charakteristische treibende atmosphärische Kräfte zugeordnet werden. Die Ergebnisse zeigen darüber hinaus die Bedeutung des Mengeneffekts für die allgemeine Isotopenzusammensetzung über dem gesamten südlichen Afrika sowie eine große Bedeutung der zurückgelegten Entfernung der Feuchtigkeit. Die festgestellten Muster und Beziehungen verbessern unser Verständnis des atmosphärischen Wasserkreislaufs im südlichen Afrika und der damit verbundenen stabilen Wasserisotope. Zukünftige Arbeiten sollten noch detaillierter die Beziehungen innerhalb der einzelnen RFZ zwischen der stabilen Isotopenzusammensetzung des Wassers und den entsprechenden Feuchtigkeitsquellgebieten und Transportmustern untersuchen. Die vorgestellten Ergebnisse haben jedoch bereits jetzt das Potenzial, für weitere Anwendungen genutzt zu werden, zum Beispiel für die Interpretation von Paläoklima-Proxies.

Die beiden Studien ermöglichten die Rekonstruktion aktiver Phasen des fluvio-lakustrinen Systems in den Tsodilo Hills während des späten Quartärs und die Analyse der Beziehung zwischen dem modernen Klima und stabilen Wasserisotopen als Interpretationsgrundlage für die Rekonstruktion von Feuchtigkeitsquellen und Niederschlagsmustern. Diese Ergebnisse sind eine Voraussetzung für weitere Schritte zum besseren Verständnis des Paläoklimas im südlichen Afrika während des Spätpleistozäns, wie z.B. der Analyse der Isotopeneigenschaften fossiler Molluskenschalen am Paläosee Tsodilo und an weiteren Standorten im südlichen Afrika. Rückschlüsse auf das Paläoklima hinsichtlich der Feuchtigkeitsquellen und der Saisonalität der Niederschläge, die auf den im Rahmen dieser Arbeit gewonnenen Erkenntnissen über die modernen Feuchtigkeitsverläufe und die damit verbundenen Isotopenzusammensetzungen des Wassers beruhen, könnten es dann ermöglichen, die Frage zu beantworten, woher und wann die Feuchtigkeit kam, die die großen quartären lakustrinen Systeme in der Kalahari speiste, und einige der Widersprüche über das Klima des späten Quartärs aufzulösen.

Table of contents

List of figures

List of tables

List of acronyms

AD	anno domini
AMWL	African meteoric water line
ANOVA	Analysis of Variance
BLH	boundary layer height
BP	before present
CAB	Congo Air Boundary
clr	centred logratio
DEM	digital elevation model
DFG	Deutsche Forschungsgemeinschaft
DGPS	differential global positioning system
DLR	Deutsches Zentrum für Luft- und Raumfahrt
DWT	discrete wavelet transformation
ECMWF	European Centre for Medium-Range Weather Forecasts
EM	end-member
ENSO	El Niño-Southern Oscillation
GISP	Greenland Ice Sheet Precipitation
GMWL	global meteoric water line
GNIP	Global Network for Isotopes in Precipitation
GNSS	Global Navigation Satellite Systems
GPR	ground penetration radar
IAEA	International Atomic Energy Agency
ICP-OES	inductively coupled plasma optical emission spectrometry
IDWT	inverse discrete wavelet transformation
ITCZ	Intertropical Convergence Zone
LGM	Last Glacial Maximum
LMWL	local meteoric water line
MIS	Marine Isotope Stage
MWL	meteoric water line
OSL	optically stimulated luminescence
PCA	principal component analysis
PD	precipitation distribution

RFZ	rainfall zone
RF	Random Forest
RTK	real-time kinematic
SAR	synthetic aperture radar
SHW	Southern Hemisphere westerlies
SIOCZ	Southern Indian Ocean Convergence Zone
SLAP	Standard Light Antarctic Precipitation
SRZ	summer rainfall zone
SRZe	eastern summer rainfall zone
SRZm	mixed summer rainfall zone
SRZw	western summer rainfall zone
TanDEM-X	TerraSAR-X add-on for Digital Elevation Measurement
TIC	total inorganic carbon
TOC	total organic carbon
TTT	tropical temperate troughs
VSMOW	Vienna Standard Mean Ocean Water
WMO	World Meteorological Organization
WPS	White Paintings Rock Shelter
WRZ	winter rainfall zone
XRF	X-ray fluorescence
YRZ	year-round rainfall zone

Introduction

1.1 Motivation

The current man-made climate change is globally affecting societies and has become one of the most pressing issues of the 21st century. It is of concern on many levels: scientific, economic, political and morally.

For assessing the expected impact of climate change, methods to investigate the past, present and future climate are applied and combined. The history of Earth's climate shows how climate changed in the past and reconstruction of palaeo-environments allows insights into possible environmental responses to respective climate changes. Observations of modern climate and its recent changes provide necessary understanding of our climate system and highlight the rapidly increasing human impact and changing natural climate forcing. Projections of future climate conditions for alternative climate scenarios are made possible by climate models, which, in turn, also facilitate the interpretation of observations and measurements on all time scales. Thus, it is very important to understand past climate conditions in order to properly predict future development. Information about the palaeoclimate is furthermore important to calibrate models for future climate changes, whereby much less data exists for the southern hemisphere than for the northern hemisphere, particularly for Africa.

The palaeoclimate evolution of Africa however is of particular interest, as climate change is one of the most discussed forces for the "Out of Africa" theory. This theory describes the model of the geographic origin of anatomically modern humans in Africa and their early migration off the continent. However, while the African origin of our species is largely undisputed, it is still open to debate where precisely in Africa *Homo sapiens* originated (e.g. Gunz et al., 2009; Tishkoff et al., 2009; Batini and Jobling, 2011; Henn et al., 2011; Soares et al., 2016; Rito et al., 2019). For a long time, eastern Africa was considered by most scientists as the place of origin of our species, since two of the oldest known fossils of *H. sapiens* have been found in Ethiopia (McDougall et al., 2005), but recently southern Africa has again been proposed as the possible origin of modern humans based on mitochondrial DNA (Chan et al., 2019).

Nowadays, southern Africa is shaped by huge drylands, such as the Kalahari, the Karoo and the Namib desert. In these arid regions, present-day climate conditions inhibit the existence of perennial lakes and therefore, permanent water bodies are rare in southern Africa. However, a multitude of old basins and nowadays (seasonally) dry riverbeds show that in the past, large persistent lakes and drainage systems existed in southern Africa (Figure 1.1). Especially in Botswana and Namibia, large (almost completely) dry basins exist, such as the Makgadikgadi Pans, Lake Ngami, the Mababe depression, Palaeolake Tsodilo, or the Etosha Pan. Further south, numerous intermittent or completely dry river channels can be found, like for example the Okwa River, the Molopo River, the Auob and the lower Nossob. Previous research revealed that these palaeolakes and -rivers were active in the Late Pleistocene and Holocene (Brook et al., 2007; Hürkamp et al., 2011; Riedel et al., 2014; Ramisch et al., 2017; Wiese et al., 2020), especially during the Last Glacial Maximum (LGM), defined as the period of the most recent maximum global ice volume (21±2 ka BP; Mix, 2001). Yet, regional studies on the prevailing palaeoclimate of this time period have led to different interpretations (Stone, 2014; past 50 ka reviewed in Riedel et al., 2014). It is still a controversial issue, whether the LGM has generally been wetter, similar or drier than present (Partridge et al., 1999; Thomas
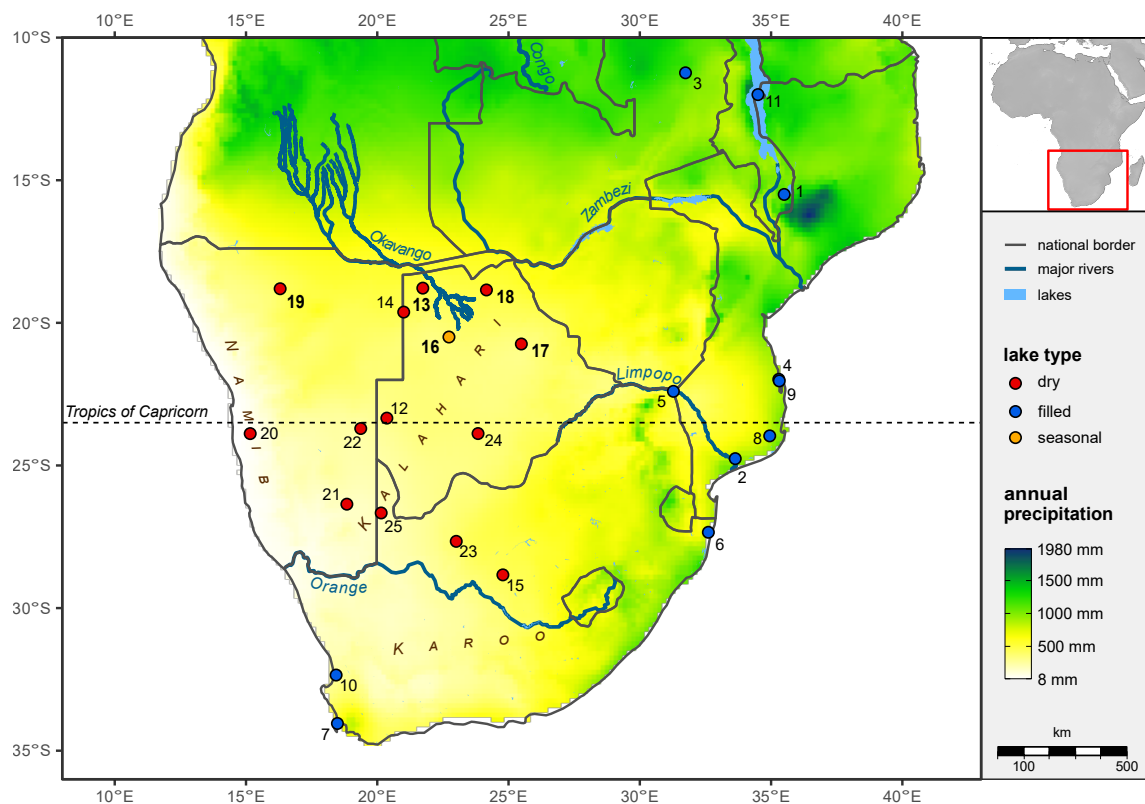
Figure 1.1: Map of southern Africa plotting the locations of late-Quaternary lakes (database from de Cort et al., 2021) against the present annual precipitation. Points are colour-coded by the current hydrology of the sites, differentiating between dry, seasonally dry/filled and filled basins. Sites referenced in the text are the Makgadikgadi Pans (17), Lake Ngami (16), Mababe depression (18), Palaeolake Tsodilo (13) and the Etosha Pan (19). Site numbers refer to Table A.1.

and Shaw, 2002; Chase and Meadows, 2007; Gasse et al., 2008; Kim et al., 2008; Brook et al., 2010; Schüller et al., 2018; Wiese et al., 2020; Hahn et al., 2021). Additionally, which climate features controlled the moisture transport, yet needs to be resolved (Gasse et al., 2008; Hahn et al., 2021).

Various hypotheses have been put forward to explain how sufficient moisture input could be provided for lakes to exist. They include changes in the amount and/or seasonality of rainfall and discuss the role of controlling climate features. Central to this discussion has been the hypothesis that due to large ice masses at both poles, a southward shift of the Intertropical Convergence Zone (ITCZ) and a northward shift of the Southern Hemisphere westerlies (SHW) were induced and caused a reorganization of the global climate system (e.g. Hahn et al., 2021).

The controversial discussions about palaeoclimate conditions during the LGM have several reasons, including the complex climatic system as such but also the choice of appropriate climate archives and reconstruction methods. Some contradictions among palaeoclimate records might be explained by differing small-scale climatic zones (Hahn et al., 2021), others by dating uncertainties due to different dating methods and materials in regional studies. Other contradictions could be the result of the complexity of the lake systems that are characterized, for instance, by different sources of moisture or tectonic activity in the catchment area. Tectonic activity, for example, can reshape the landscape, initiate drainage reorganizations and also permanently alter sedimentation rates or overprint sediments after deposition. Thus, if tectonic activity in the catchment is not considered or excluded, climate impact on lake level changes can be over- or underestimated leading to strong misinterpretation (Hartmann et al., 2011; Moore et al., 2012). Such circumstances further complicate the interpretation of climate proxy data, so reconstruction of environmental change is not always straightforward.

Lake sediments represent unique environmental archives and contain multiple palaeo-environmental proxies that can be used for various climatological reconstructions, even on different time scales. In general, the proxies are of different categories, such as the sediments (terrigenous, chemical, and biogenic), cosmogenic and volcanogenic particles, fossils that originated outside of the lake (like pollen), or in the lake (like fish, molluscs) and aerosol and waterborne pollutants. An overview of the many different types of proxy data provided by lake sediments is given, e.g., by Cohen (2003). The proxies are indicators of environmental conditions and can be used as substitutes for direct measurement of the original forcing variable controlling them. However, the various forcing variables, such as climate, tectonic

and human activity or aquatic biota are highly interactive. Thus, it is essential to distinguish climatic and non-climatic factors for interpretation of environmental changes recorded in the sediment.

Therefore, interpretation of possible climate proxies in the sediment of (palaeo-)lakes requires a good understanding of the lake basin and its catchment. Important features are, for example, the geomorphology of a lake basin, in particular its shoreline and shape characteristics, and its catchment configuration, like size, drainage system and geology.

A very interesting palaeolake system in southern Africa, especially because of its size, is the fluvio-lacustrine system of the mega-palaeolake Makgadikgadi. However, its complex environment comprises a supra-regional catchment (e.g. Schmidt et al., 2017) and structural sub-basins that are all related to the East African Rift System (e.g. Scholz et al., 1976), and thus complicate reconstruction and interpretation.

Therefore, to minimize the problem of system complexity, the Palaeolake Tsodilo was chosen due to its rather small and local catchment (Wiese et al., 2020) that lies solely within the northern Kalahari. The Palaeolake Tsodilo is located at the Tsodilo Hills about 40 km west of the Okavango panhandle within the Kalahari drainage system (No. 13 in Figure 1.1). Despite the nearby Gumare fault, there is no indication so far for tectonic influences of the drainage system according to previous research. Accordingly, the phases of the lake's existence were mainly dependent on the local climate over the northern Kalahari.

Furthermore, the region of the Tsodilo Hills is very interesting regarding human history. Archaeological investigations of over 4500 rock paintings revealed that humans have lived in this area for at least 100 ka (UNESCO, 2001). For this reason, the hills were declared a UNESCO World Heritage Site in 2001. Moreover, they are located in the region where the cradle of human kind was recently proposed to be (Chan et al., 2019).

The local studies, however, have not been very conclusive and are even controversial regarding the local palaeoclimate of the Tsodilo area. While some research finds evidence for the existence of a lake during the proclaimed LGM (Brook et al., 1992; Robbins et al., 1994; Wiese et al., 2020), other studies indicate a desiccation of the basin and regional aridity during that time (Robbins et al., 2000; Thomas et al., 2003). This controversy might be explained by different approaches of dating concerning the used material (e.g. sediment, fossils) or methods (^{14}C, OSL). Yet, the problem of dating uncertainty for the LGM period could possibly be avoided here by dating fossil mollusc shells. Riedel et al. (2014) radiocarbon-dated recent mollusc shells from four regional rivers that all showed modern ages. Thus, no hard water reservoir effect is assumed in the region.

Fossil molluscs are furthermore a particularly suitable proxy to investigate the climate of the Late Pleistocene and Holocene at the Tsodilos, because sclerochronological analysis on the shells, due to their potential high resolution, offer the possibility to investigate the established hypotheses about the seasonality of precipitation during the LGM (Leng and Marshall, 2004; Taft et al., 2012, 2013). It has been shown that the oxygen and carbon stable isotope values of shell carbonate reflect the isotopic composition of the lake water (Fritz and Poplawski, 1974; Leng et al., 1999). With a detailed understanding of the lake system, fossil shells can thus act as proxies for the local precipitation even on a sub-seasonal scale.

Yet, as the application of a climate proxy is generally based on the relationship between the parameter and its signal in an archive, for solid interpretation of a climate proxy, knowledge of the current climate and its influence on the investigated proxy is a prerequisite. In case of mollusc shells, the relationship between the prevailing climate and the isotope signal recorded within the shells needs to be thoroughly investigated. This includes the influence of moisture sources, transport pathways, and precipitation patterns on the isotopic composition of precipitation. Using mollusc shells from the Palaeolake Tsodilo sediments as a proxy, also those factors are important, which influence the living animal and as a consequence alter the isotopic composition of the shell. Those are, for example the life cycle, habitat, growth period, shell material, potential vital effects, radius of movement, food supplies, etc. (Leng et al., 1999; Leng and Marshall, 2004; Taft et al., 2012).

In summary, the potential value of a climate proxy depends heavily on how well we understand and quantify the processes that link the corresponding climate parameter and its signal in the proxy archive. In this thesis, therefore, the focus is on the hydro-climatic processes influencing the sediment archives at Palaeolake Tsodilo and the processes influencing the isotope record in the regional precipitation.

1.2 Background

1.2.1 Palaeolake Tsodilo

The basin of Palaeolake Tsodilo, located about 40 km west of the Okavango panhandle (Figure 1.1), is situated at the western flanks of the Tsodilo Hills, a 15 km long hill chain consisting of four quartzite-schist inselbergs (Key and Ayres, 2000; Wendorff, 2005). It is embedded within a large linear dune system and thus the location yields evidence of both, wetter and drier conditions (Thomas et al., 2003). The adjacent linear dunes are up to

20–30 m high, oriented from east to west and are located 1–2.5 km apart (Brook et al., 1992; Brook, 2010).

Sand drift during dune formation probably originated from the east, which can be reconstructed from the sand piled on the east side of the Tsodilo Hills and a sand shadow depression in the west that extends for up to 40 km (Brook et al., 1992). Dune activity and formation processes of these linear dune fields in the Kalahari are still under investigation and often debated (Thomas et al., 2000; McFarlane and Eckardt, 2007; Ringrose et al., 2008).

Nowadays, the basin of Palaeolake Tsodilo lies at an altitude of 1010 m a.s.l.. It is a dry plain with low relief, comprising sandy sediments and carbonates that contain gastropod shells (Grove, 1969). In this flat landscape, hardly any palaeo-shorelines are visible on-site and in aerial photographs or elevation data, except for the southern part of the basin, where the lake transgressed into the linear dunes during its greatest extent. At this extension, the lake was probably at least 40 km^2 wide and 5–7 m deep (Brook et al., 1992; Brook, 2010).

To date, only few studies have investigated the Palaeolake Tsodilo itself (Brook et al., 1992; Thomas et al., 2003; Wiese et al., 2020) and other studies mention the palaeolake briefly (Passarge, 1904; Grove, 1969; Robbins et al., 1994, 2000; Linol et al., 2015). The Palaeolake Tsodilo was first indicated in Passarge's map "Übersichtskarte der Mittleren Kalahari" (1904) and later mentioned by Grove (1969) as a 5 km^2 wide and flat area of calcretes containing gastropods. In a first study of the lake, Brook et al. (1992) inferred a stagnant water body at 17.5 thousand years before present (kyr BP; uncalibrated radiocarbon age) and a lake at 15 kyr BP that may have dried out seasonally. These assumptions derived from differences in sedimentology and diatom assemblages of two lacustrine carbonate surface samples. Based on aerial photographs they also estimated a possible maximum extent of the lake of 40 km^2. In a following study from Robbins et al. (1994) additional radiocarbon dates on lake carbonates indicate standing water in three phases from 22.5 to 19.2 kyr BP, 17.5 to 11.7 kyr BP and around 7.5 kyr BP. Later Robbins et al. (2000) mentioned lacustrine carbonates from three different lake phases, different from those previous ones, at 36–32 thousand calendar years BP (cal kyr BP, calibrated radiocarbon age), 26.5–22.5 cal kyr BP and 19–11 cal kyr BP (Brook, unpublished data; no uncalibrated ages given – probably calibrated after Bard et al., 1990). The carbonates contained freshwater mollusc shells and diatoms, indicating permanent shallow lakes that varied in size seasonally.

From morphological and sedimentological characteristics and fossil assemblages (diatoms and molluscs) of radiocarbon-dated lacustrine carbonate surface samples, Thomas et al. (2003) identified three lake stands indicating wetter regional conditions than present. The oldest lake

stand between 40 and 32 cal kyr BP (no uncalibrated ages published – calibrated using Calib v4.0 after Stuiver et al. (1999) for radiocarbon ages < 18 kyr BP, older ages formulaically) was a shallow oligotrophic lake with more seasonal and eutrophic conditions starting around 36 cal kyr BP; then there was a deeper lake from 27 to 22 cal kyr BP and a possible phase of desiccation during LGM was followed by an extensive shallow and oligotrophic lake from 19 to 12 cal kyr BP.

In the most recent study, Wiese et al. (2020) investigated a sediment pit within the lake basin. Here, radiocarbon ages of fossil shells suggested two periods of lake existence: one during 17–15.5 kyr BP and another between 39.5 kyr BP and 35.5 kyr BP. The fossil assemblages indicated a relatively deep (> 5 m) freshwater to oligohaline lake with an open basin-situation during LGM that was assumed to be more stable and deeper than the lake phase during mid Marine Isotope Stage (MIS) 3 (about 40 kyr ago) with a possible open or semi-open lake basin. The temperature regime was assumed to be similar to modern times, while sclerochronological stable isotope patterns indicate a humid climate with two intra-annual rainfall maxima during LGM and one rainy season during mid MIS 3.

These previously reconstructed lake phases are shown in Figure 1.2, which includes ages calibrated using the most current method (i.e. Calib 8.1, Stuiver and Reimer, 2020; where possible). As illustrated, it is apparent that the reconstructions of lake phases from the various studies during the LGM are contradictory. A possible reason for these inconsistencies might be the influence of a reservoir effect. For example, Brook et al. (1992), assumed an upper limit of 15 % old carbon content in the sediment, so that the measured ages would actually be younger. However, studies by Riedel et al. (2014) have found no significant amounts of old carbon in the nearby fluvio-lacustrine Makgadikgadi-System. Thomas et al. (2003) determined the ages of the sediment matrix of some of their samples and of its containing shells, and revealed that the matrix was 18–51 % younger (Figure 1.2) than the shells. They concluded that the matrix developed after deposition of the shells and represents several phases of matrix development. Hence, it seems that a more appropriate method to date this lake system is the usage of fossil shell-dates for age chronologies.

So far, all previous studies on the Palaeolake Tsodilo (Brook et al., 1992; Thomas et al., 2003; Wiese et al., 2020) focused on the southern sub-basin. However, by analysing a differential global positioning system (DGPS) transect in N–S orientation across the entire depression west of the hills, Wiese et al. (2020) identified another basin in the north, and a ridge separating the two sub-basins. New high resolution digital elevation models also indicate a much larger lake basin.
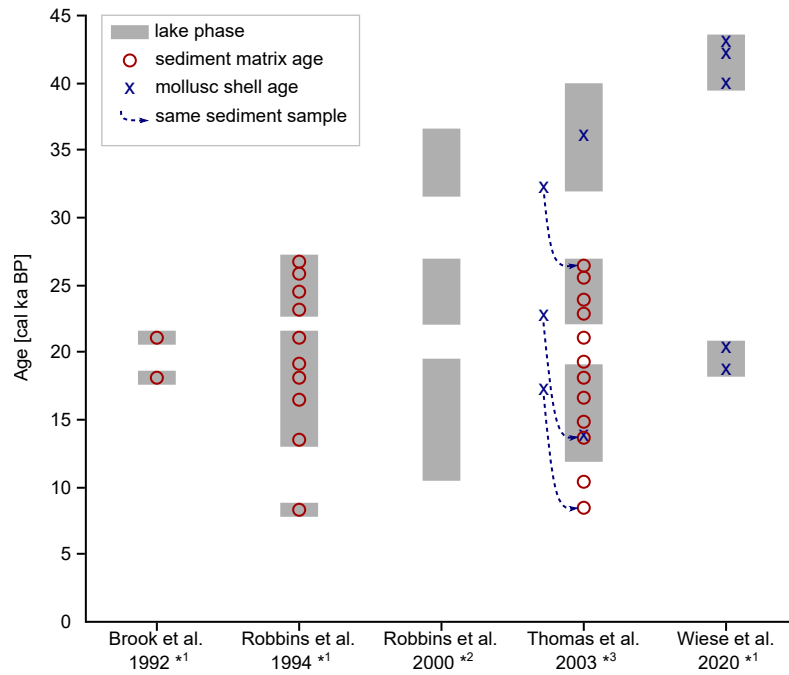
Figure 1.2: Overview of the reconstructed lake phases of Palaeolake Tsodilo from previous studies. Single measurements of calibrated ^{14}C ages are given, where available. The ^{14}C ages were recalibrated using Calib 8.1 (Stuiver and Pearson, 1993; Stuiver and Reimer, 2020) with the southern hemisphere calibration curve SHCAL20 (Hogg et al., 2020), if original radiocarbon ages had been published (*1) or else taken calibrated as published (*2: calibrated using relationships in Bard et al. (1990) and Kitagawa and van der Plicht (1998); *3: with Stuiver et al. (1999) for original ages under 18 kyr BP, older ages formulaically)

1.2.2 Climate hypotheses for the Late Glacial Maximum

Nowadays, southern Africa is influenced by both tropical and mid-latitude circulation systems due to its location in the subtropics (Tyson and Preston-Whyte, 2000). Thus, numerous forcing factors interact with each other, causing a rather complex climate regime over southern Africa (Tyson and Preston-Whyte, 2000; Reason et al., 2006). However, main forcings influencing the regional climate are the two convergence zones, ITCZ and CAB (Congo Air Boundary), as well as the Southern Oscillation and the SHW, but also the development and position of continental and oceanic anticyclones (Tyson and Preston-Whyte, 2000).

The African rain belt, associated with the ITCZ and CAB, is at its southernmost position in austral summer. During this time, a low-pressure cell dominates southern Africa, allowing tropical temperate troughs (TTT), which are formed at the Southern Indian Ocean Convergence Zone (SIOCZ), to bring precipitation from the Indian Ocean into the region. During the austral winter, this precipitation is suppressed by a subtropical high-pressure cell over southern Africa (Figure 1.3a).

Precipitation in winter originates off extratropical cloud bands and thunderstorms linked to the frontal systems which develop in the main SHW flow. These frontal systems can be
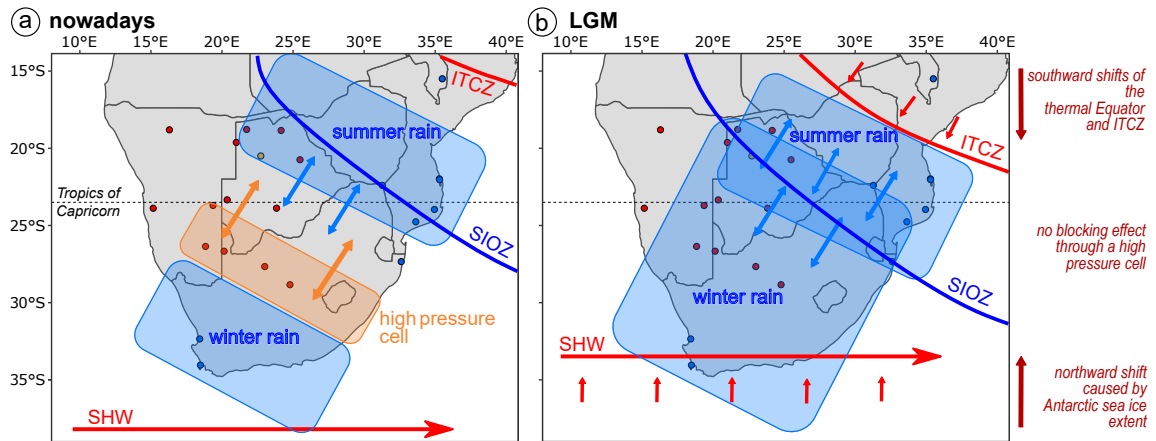
Figure 1.3: Conceptual model of precipitation shifts during **a)** interglacial (present conditions) vs. **b)** glacial (LGM) intervals. Points indicate locations of late-Quaternary lakes as in Figure 1.1.

truncated and displaced equator-ward when the SHW shifts the northward in winter, bringing precipitation as far north as 25°S (Mason and Jury, 1997; Tyson and Preston-Whyte, 2000; Baray et al., 2003).

Thus, most parts of southern Africa receive rainfall in the austral summer (DJF), except for the Western Cape area, in the south-west, and the southern coast where rain falls in the austral winter (JJA) and year-round (Tyson and Preston-Whyte, 2000; Chase and Meadows, 2007). Therefore, a distinction can be made between a summer rainfall zone (SRZ), with a decreasing rainfall gradient from east to west (Jury, 2012), a winter rainfall zone (WRZ) and year-round rainfall zone (YRZ). Due to this strong seasonality that characterizes the southern African rainfall distribution, the climate regime can be categorized as dry/wet seasons (IPCC, 2021).

Over the last glacial–interglacial cycle, hydrological variability over southern Africa, concerning the amount and seasonality of precipitation, has been linked to the relative dominance of the climate features described above. One of the most prevalent hypotheses is the northward shift of the WRZ (van Zinderen Bakker, 1976; Heine, 1981; Chase and Meadows, 2007; Hürkamp et al., 2011; Riedel et al., 2014; Miller et al., 2019; Hahn et al., 2021), which is nowadays situated above the southern Cape region. But also, the southward shift of the ITCZ has often been discussed (Nicholson and Flohn, 1980; Chiang et al., 2003; Broccoli et al., 2006; Hürkamp et al., 2011; Hahn et al., 2021). The northward shift of the WRZ is assumed to be related to the northward shift of the SHW caused by the increased Antarctic sea ice extent during the LGM. In addition, in the studies by Hahn et al. (2021), there was no indication that the South African high-pressure cell suppressed precipitation, as is observed nowadays during austral winter. Therefore, after their study, the SHW-related winter rain could have reached much further north directly influencing the Kalahari region

(Figure 1.3b). The southward shift of the ITCZ on the other hand, is generally assumed to be induced by the southward displacement of the thermal Equator as a result of the large ice masses of the Northern Hemisphere. Hence, the Kalahari region may have been under the direct influence of the ITCZ during the LGM. However, it is also possible that the southward shift of the ITCZ resulted in a southward shift of the SIOCZ and thus an increase in precipitation via the TTT (Hahn et al., 2021). Either way, the southward shift of the ITCZ would have resulted in an increased rainfall over the Kalahari region.

Thus, during LGM, those palaeolake-systems in the Kalahari could possibly have received precipitation not only from the African rainbelt and SIOCZ-related TTTs but also from SHW-related disturbances. Recent findings of Wiese et al. (2020) on two intra-annual precipitation maxima during the LGM at Palaeolake Tsodilo support this assumption.

1.2.3 Isotopic composition of precipitation

Studying the stable isotopic composition of water allows to obtain information about the physical processes leading to the formation and transport of water (Dansgaard, 1964; Gat, 1996). Such insight is made possible because isotopes change their composition during phase transitions, a phenomenon known as isotope fractionation. Two types of isotopic fractionation exist, thermodynamic and kinetic fractionation (Hoefs, 2004; Tiwari et al., 2015). The thermodynamic or equilibrium fractionation is an exchange reaction where the isotope distribution changes between different phases and which is temperature dependent (Gat, 1996). The kinetic or non-equilibrium fractionations are unidirectional reactions taking place during phase changes, for example when the evaporated water vapour above the water surface is continuously transported away. The two main processes for the formation of precipitation are the evaporation of surface (ocean) water, and the progressive rain-out of the vapour during transport based on the Rayleigh fractionation model (Figure 1.4). These fractionation processes result in temporal and spatial variation in the stable isotopic composition, which are expressed in ratios in the conventional delta notation (δ^{18}O, δ^{2}H) in per mil (‰) relative to the Vienna Standard Mean Ocean Water (VSMOW) as defined by Craig (1961b) and Gonfiantini (1978).

The global long-term mean annual averages of δ^{18}O and δ^{2}H in precipitation typically show a strong linear correlation, described by the formula δ^{2}H $= 8\,\delta^{18}$O $+ 10$, which was first documented by Craig (1961a), later refined to δ^{2}H $= (8.17\,\pm 0.06)\,\delta^{18}$O $+ (10.35\,\pm 0.65)$ with $r^{2} = 0.99$ by Rozanski et al. (1993) and is known as the global meteoric water line (GMWL).
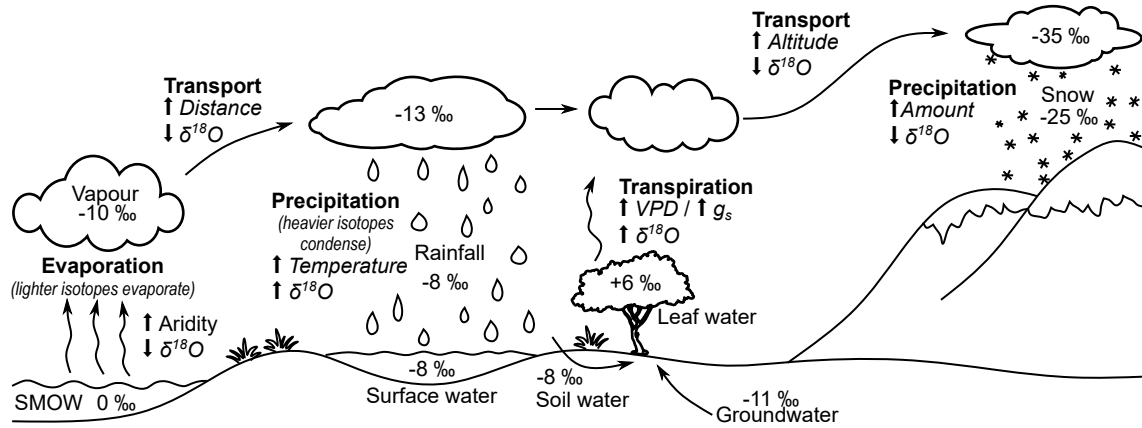
Figure 1.4: Conceptual model of main isotope fractionation steps in meteoric precipitation and typical oxygen isotope values (δ^{18}O versus SMOW) in temperate climates (recreated and modified after Ferrio et al., 2005). SMOW: standard mean δ^{18}O in ocean water; VPD: vapour pressure deficit; gs: stomatal conductance. ↑: increase; ↓: decrease. The same fractionation processes apply to hydrogen isotopes.

The values of δ^{18}O and δ^2H in precipitation are affected by different characteristics of prevailing local climate conditions (e.g. temperature, humidity, rainfall amount) and physical characteristics of the target location (e.g. elevation, distance from ocean, moisture sources) and thus the local meteoric water line (LMWL) show variations in slope and intercept from the GMWL. Dansgaard (1964), described the following relationships to the isotope composition: a latitude effect, an altitude effect, a continental effect, an amount effect, and a seasonal effect (Figure 1.5).

There is furthermore the second-order isotope parameter deuterium excess (d-excess), defined by d = δ^2H − 8 δ^{18}O (Dansgaard, 1964). D-excess is correlated with the temperature of the air and sea surface and with the humidity at the oceanic source of precipitation (Merlivat
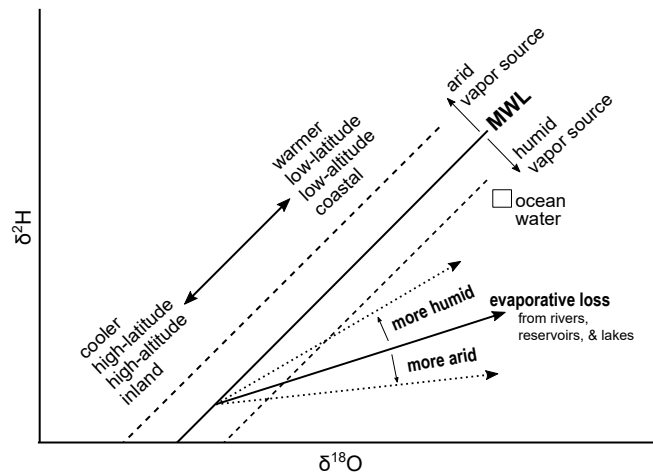
Figure 1.5: Meteoric water line (MWL) and factors leading to variations in slope and intercept of local MWLs. This figure is adapted from Sahra (2005).

and Jouzel, 1979; Pfahl and Wernli, 2008). Furthermore, additional uptake of moisture from continental sources along the moisture trajectory increases the d-excess (Guan et al., 2013).

To improve our understanding of the hydrological processes, stable isotopes of water (oxygen and hydrogen) are widely used as environmental tracers by investigating the origin, transport, storage and mixing of water, for example through investigation of precipitation patterns (Feng et al., 2009; Baker et al., 2015; Kaseke et al., 2016; Wanke et al., 2018), the analysis of water movement into and within water bodies and wetlands (Dincer et al., 1979; Mekiso and Ochieng, 2014; Bowen et al., 2018) or groundwater recharge (e.g. Burgman et al., 1979; Harris et al., 2010; Leketa et al., 2018; Parlov et al., 2019; Yang et al., 2019). Thus, by analysing stable isotopes, it is possible to draw conclusions about climatic and physical conditions at the moisture source region, along the moisture trajectory and at the location of precipitation.

Additionally, stable isotopes of oxygen are often used to reconstruct palaeoclimate and its variability by analysing their concentration in palaeo-archives such as ice cores, speleothems, tree rings, or mollusc shells (Dansgaard et al., 1993; Holmgren et al., 1999; Taft et al., 2014; Schmidt et al., 2017; Wiese et al., 2020). Yet, it is crucial to understand today's pattern of local oxygen isotope variability as a precondition for the interpretation of past patterns.

For a global monitoring of stable isotopes in precipitation, the Global Network for Isotopes in Precipitation (GNIP) has been initiated by the International Atomic Energy Agency (IAEA) and the World Meteorological Organization (WMO) in 1960. However, for many regions, the spatial density of stations and their temporal resolution are not sufficient to analyse spatial and temporal changes. Only 8 GNIP stations are located in southern Africa (here defined as south of 15°S), none of them in Botswana and only 4 of them have good temporal coverage, two of which, are in Cape Town (IAEA/WMO, 2021).

Additionally, most studies on stable water isotopes over southern Africa have been of regional scope (Dincer et al., 1979; West et al., 2014; Kaseke et al., 2016; Wanke et al., 2018; Leketa and Abiye, 2020; de Wet et al., 2020) and thus there is relatively little data on the variability of stable water isotopes across whole southern Africa. Yet, understanding the spatio-temporal variation in rainfall and isotopic patterns across whole southern Africa could provide important information on hydrological processes at both global and local scales. Gained knowledge could be used for hydrological, archaeological and ecological, but also for forensic studies in southern Africa, as well as enabling a better planning and preparation for climate change (West et al., 2014).

1.3 Thesis objectives

This thesis is integrated in a DFG (Deutsche Forschungsgemeinschaft) project aiming to reconstruct the Palaeolake Tsodilo ecosystem dynamics and variations in climate, weather and environment, with focus on the last Glacial, i.e. MIS 3 and MIS 2. The intention of this thesis is to advance the reconstruction of the Palaeolake Tsodilo and to provide a framework to improve the accuracy of future interpretations of climate proxies based on stable water isotopes, e.g., mollusc shells, at the Tsodilo Hills but also other systems in the Kalahari region. Thus, a basis will be established to investigate the common hypotheses about regional and southern African climate in the LGM.

From the state of the research described above, the following two objectives arise for this dissertation:

The **1st objective** is to gain more reliable information about hydrological dynamics of the catchment and basin and to complement information on the entire basin of Palaeolake Tsodilo, which are a prerequisite to interpret climate proxies in the sediment. Of special interest are therefore following questions:

(1) How is the catchment characterised, regarding the drainage system and possible outflows?

(2) What was the maximum extent of the lake and is it possible to identify different lake phases?

(3) What were the characteristics of the identified lake phases?

(4) Is there evidence of tectonic activity?

The **2nd objective** is to investigate influences of the recent climate on the isotope signal in precipitation over southern Africa to provide a basis for the interpretation of stable water isotope-based proxies. The focus here is the on following questions:

(1) Are there spatial differences in the isotopic pattern?

(2) What are the source region(s) of moisture?

(3) Are the moisture source region(s) and transport characteristics affecting the stable isotope composition?

1.4 Methodological approaches

The two main objectives of this thesis aim to address the parts I, II and IV of the encompassing DFG project, as visualized in Figure 1.6.
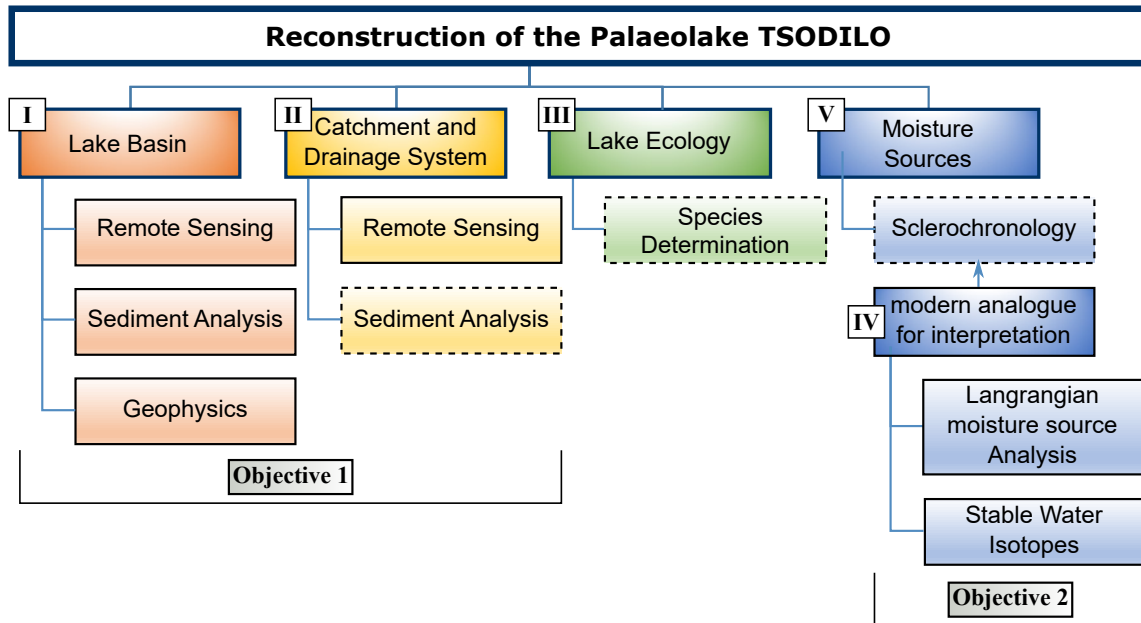
Figure 1.6: Overview of different research parts and respective methods of the encompassing DFG project and assignment to the two main objectives of this thesis. Methods with a dashed line are not covered by this thesis.

The catchment area and basin of Palaeolake Tsodilo are investigated with a multidisciplinary approach including different remote sensing and geophysical methods, comprehensive application of DGPS, and sedimentological analyses. The size of the catchment and its drainage system were calculated based on a high-resolution digital elevation model (DEM) from the TanDEM-X mission (TerraSAR-X add-on for Digital Elevation Measurement; Schulze et al., 2008; Rizzoli et al., 2017). Geomorphological remote-sensing data analyses, using the TanDEM-X DEM, Landsat multispectral and multi-temporal imagery and aerial images, are applied for the detection of surface structures to obtain a geomorphological map of the lake area. The focus hereby is on the determination of the maximum extent of the lake and the identification of different lake phases. Verification of the accuracy of the used DEM, as well as the acquisition of precise elevation data for detected geomorphological features and selected sampling locations, are accomplished through elevation measurements using the DGPS. The geophysical measurements, including ground penetration radar (GPR) and seismic refraction, allowed subsurface explorations such as the analysis of spatial variations in the stratigraphy of the lake basin and detection of evidence for tectonic activity. Finally, sediment analysis of several pits in the lake basin, including radiocarbon dating for age chronology, were done to investigate characteristics of the recorded lake phases, including depositional processes and lake ecology. A total of four field trips (Table 1.1) to the Tsodilo Hills were completed to collect data for the numerous analyses.

Table 1.1: Overview of sampling and survey periods of: sediment sampling, differential GPS (DGPS) survey of six transects (T0–T5), geophysical survey using seismic refraction (SR) and ground penetrating radar (GPR), and an additional remote sensing survey based on a drone survey (UAV = unmanned aerial vehicles).

	Sediment sampling	DGPS	Geophysical Survey	Remote sensing
August 2015	pit S-15	transect T0	SR (northern 3 km) + GPR (12-km N-S transect)	
August 2017	surface samples			
July 2018	pits S1-18, S2-18 & N18 + surface samples	transects T1-T5	SR (N-S transect completed)	
July 2019	pit S-15 resampling			UAV survey

Table 1.2: Overview of the timing of water sampling with corresponding number of samples in each month during the sampling period 2016–2021.. Sampling locations are shown in Figure 3.4.

	Jan	Feb	Mar	Apr	May	Jun	Jul	Aug	Sep	Oct	Nov	Dec
2016								8	31			
2017	2											17
2018	11						3	6	4	6		1
2019		19	23		31	5	3	1	6		8	
2020		7	12									
2021	39											

To investigate the influences of recent climate on isotope signals in precipitation over southern Africa, Lagrangian moisture source diagnostic is coupled with water isotope measurements. Precipitation distribution patterns over southern Africa are analysed by end-member modelling to infer respective rainfall zones. To achieve better spatial coverage, in additional to the available data from selected GNIP stations, water samples were collected from precipitation and surface waters during several field trips from 2016 to 2021 (Table 1.2) and their stable isotope composition has been determined. This combined dataset is then analysed for spatial differences in the isotopic pattern based on the previously determined rainfall zones. Backward trajectories are calculated to determine the source regions of moisture. The effects of the moisture source regions and transport patterns on the isotopic composition of precipitation are analysed by tracking various meteorological variables along these trajectories and combining them with the isotopic signals.

In the material and methods sections of Chapters 2 and 3, the used materials and methodological procedures are described in more detail.

1.5 Outline and scientific contribution

This thesis is designed as a cumulative dissertation and therefore includes two individual manuscripts (Chapters 2 and 3) that have been prepared for publication in peer-reviewed scientific journals and constitute the main content of this thesis. An overview for each manuscript with title, authorship and the selected scientific journal with the current publication status is given in Table 1.3. The main research findings of this thesis are summarized in Chapter 4, along with a short discussion of implications, additional results and future perspectives. Most of the data supporting this research is either available in the supplements or archived in the Open Access library PANGAEA.

As first author, I was predominantly responsible for the conceptualization and performing of the research as well as collecting, analysing and interpreting the data and illustrating the results. Prof. Dr. Frank Riedel and Dr. Kai Hartmann, who are the PIs of the DFG-founded project where this thesis is integrated, built the general scientific frame for the project. Further, I was mainly responsible for the preparation of the manuscripts and the revision process. My co-authors Prof. Dr. Frank Riedel and Dr. Kai Hartmann supervised my scientific activities and contributed to the development and major revisions of the manuscripts. An overview of my scientific contribution to the different parts of the research is listed in Table 1.4.

Data collected in the field for the first manuscript was acquired during trips in 2015, 2018 and 2019 (see Table 1.1) with the support of other expedition participants. The TanDEM-X data was obtained by Dr. Kai Hartmann. Analyses and interpretation of sediment samples were performed to a large extent by Venise Gummersbach, and the geophysical analysis and

Table 1.3: Overview of the manuscripts presented in this thesis and their current publication status

Chapter	Manuscript title *Authorship*	Journal *Status (May 2022)*
2	**Late Pleistocene hydrological settings at world heritage Tsodilo Hills (NW Kalahari, Botswana), a site of ancient human occupation**	**Quaternary Science Advances, Volume 3**
	Marielle Geppert, Frank Riedel, Venise Gummersbach, Stine Gutjahr, Philipp Hoelzmann, Maria Reyes Garzón, Elisha Shemang, Kai Hartmann	*published: April 2021*
3	**Differences in the Isotopic Composition of Precipitation over Southern Africa depending on the Rainfall Zone and its Moisture Source Regions**	**Journal of Geophysical Research: Atmospheres**
	Marielle Geppert, Kai Hartmann, Stephan Pfahl, Ingo Kirchner, Ulrich Struck, Frank Riedel	*submitted: April 2022*

interpretation was predominantly done by Maria Reyes Garzón. The collection of water samples for the second manuscript was carried out by Prof. Dr. Frank Riedel from 2016 to 2021 and the isotope measurements were performed by Prof. Dr. Ulrich Struck.

Table 1.4: Overview of my scientific contribution to the research presented in the included manuscripts of this thesis

Manuscript	Concept and study design	Data acquisition	Data analyses and interpretation	Manuscript writing
1	45 %	40 %	50 %	75 %
2	55 %	45 %	100 %	85 %

Late Pleistocene hydrological settings at world heritage Tsodilo Hills (NW Kalahari, Botswana), a site of ancient human occupation

Abstract

Based on genetic studies, a Pleistocene Kalahari "palaeo-wetland", which spanned the region of the Okavango Delta and the Makgadikgadi Basin, was recently considered the geographic origin of evolutionary modern humans. It was proposed that subsequent out-of-homeland migration was induced by climate shifts. The Tsodilo Hills, which are in relative proximity to the Okavango Delta, represent a site of ancient human occupation since at least 100 ka. Local hydrological dynamics were predominately controlled by climate variability and are archived in the sediments of Palaeolake Tsodilo. This study seeks to better understand the Late Pleistocene environments of the ancient Tsodilo people with a focus on palaeo-hydrological settings, which played a major role for their livelihoods.

Our multidisciplinary approach included different remote sensing and geophysical methods, comprehensive application of differential GPS, and sedimentological analyses concentrating on the lake beds. Four palaeo-shorelines could be identified, three of which indicate highstands during which the Tamacha palaeo-river drained Palaeolake Tsodilo towards the Okavango Panhandle. Two highstands during MIS 3b and LGM are related to periods of largely increased fish consumption by humans as has been documented by archaeologists. The palaeolake was likely most extended about 100 ka ago or earlier, when it covered ca. 70 km^2 and was 16 m deep. A single (neo-)tectonic fault could be detected.

We assume that the Tamacha palaeo-river was a gateway for ancient humans to reach the Tsodilo Hills from these palaeo-wetlands. The people took advantage of the Tsodilo Hills as shelter from weather hazards and as a natural fortress against predators and elephants. Geologically, the Tsodilo Hills were comparatively calm. They represented a relatively safe haven where the social behaviour of early modern humans could evolve to a higher complexity, which relates to the fundamental question when and where modern human behaviour began.

2.1 Introduction

The southern African Kalahari was recently considered the cradle of humankind (Chan et al., 2019), which was based on genetic studies and triggered controversial discussion (Gibbons, 2019) in respect of methodology but also against the background that specific palaeontological and archaeological evidence for the suggested interval from ca. 240–165 ka (Chan et al., 2019) is lacking (Robbins et al., 2016). Homo sapiens fossils from Morocco and South Africa dated to about 350–260 ka are rather considered a "pre-modern" evolutionary phase (Stringer and Galway-Witham, 2017) and thus estimation of split-time of African human genetic lineages is currently the most promising approach to frame the temporal origin of modern humans (e.g. Tishkoff et al., 2009). "Living human mitochondrial DNA haplotypes coalesce ∼200,000 years ago" (Weaver, 2012). Although the African origin of our species is largely undisputed, it has never been established from which region we came. Eastern, southern and central Africa have all been proposed (e.g. Henn et al., 2011; Rito et al., 2019). A challenging idea is that modern *Homo sapiens* actually emerged within the interactions of many different populations across Africa (Scerri et al., 2018).

Tishkoff et al. (2009) suggested a potential shared ancestry of central African Pygmies and Khoisan-speaking people and considered the origin of modern humans' migration in southwestern Africa, near the coastal border of Namibia and Angola (Figure 2.1 circle 1). Interestingly, this area is in relative proximity to the Kalahari comprising the "Makgadikgadi-Okavango palaeo-wetland" pinpointed by Chan et al. (2019); Figure 2.1 circle 2). This area is nowadays semi-arid and has a pronounced seasonality with dry winters and wet summers (Peel et al., 2007; Gasse et al., 2008; Chevalier and Chase, 2016),

Permanent natural and freely accessible sources of potable water are found further in the north, with the Kunene, Cubango-Okavango, Cuando-Linyanti-Chobe and Zambezi river systems (Figure 2.2), encompassing both of the suggested origin areas (Tishkoff et al., 2009; Chan et al., 2019). The active head waters of these rivers are in the (semi-)humid tropics
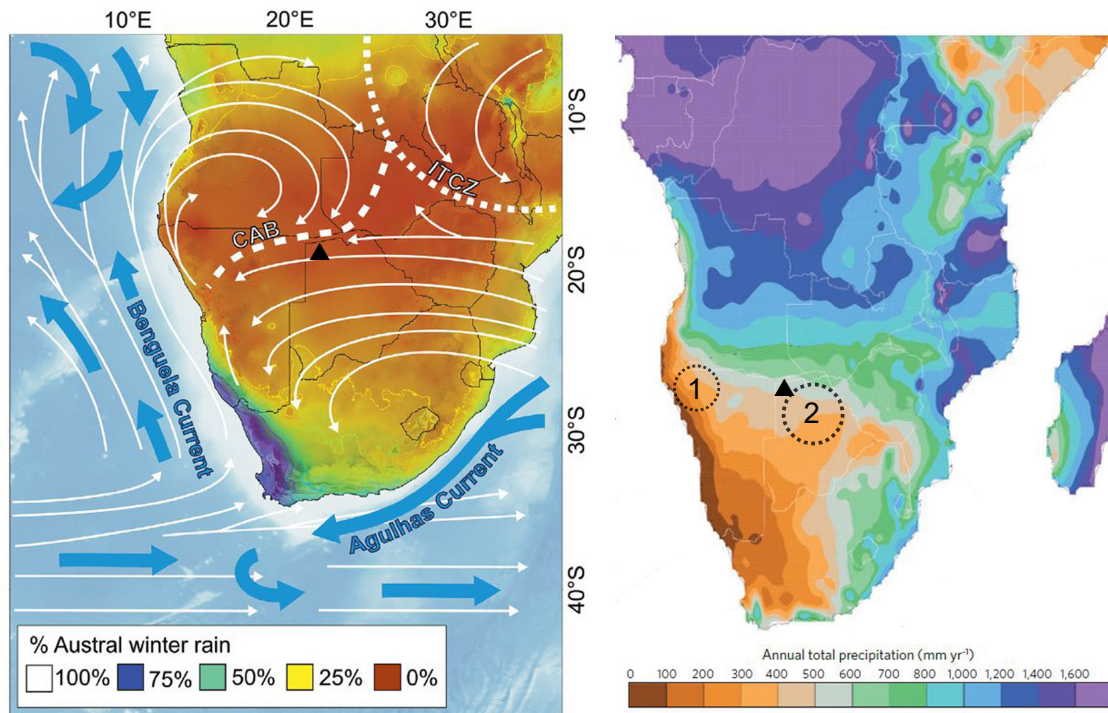
Figure 2.1: Position of Tsodilo Hills (black triangle) in the modern southern African climate setting. **Left:** Major atmospheric (white arrows) and oceanic (blue arrows) circulation systems are shown as well as austral summer positions of ITCZ and Congo Air Boundary (CAB). Predominant ($\geq 50\,\%$) austral winter rainfall is confined to violet to green coloured areas (permission for the use of artwork granted from Chevalier and Chase, 2016). **Right:** Zonation of mean annual precipitation (after Conway et al., 2015). Circles outline areas from where earliest modern humans may have originated (1=Tishkoff et al., 2009; 2=Chan et al., 2019).

(Burrough et al., 2009b; Riedel et al., 2014) Figure 2.2), and taking long-term periodical migration of the ITCZ into consideration (McGee et al., 2014; Schneider et al., 2014), still perennial conditions should have prevailed during the rise of modern humans, and beyond. Ancient human dispersal is commonly related to climate change (Blome et al., 2012; Timmermann and Friedrich, 2016; Heine, 2019). Rito et al. (2019) concluded that during the last ca. 200 ka only soon after 70 ka, the climate was humid enough for human migrations between southern and eastern Africa and subsequent out-of-Africa expansions. Outside the humid tropics, stable environments were rather the exception, however, and landscape evolution was dynamic (Burrough, 2016). Huge lakes repeatedly existed in the structural basins of the northern and central Kalahari (Figure 2.2) during the last 200 ka and before, which is that lakes developed, vanished and reappeared under changing climates (e.g. Grove, 1969; Heine, 1982; Burrough et al., 2009b; Riedel et al., 2014; Schmidt et al., 2017; Heine, 2019). The structural basins of the Kalahari evolved with the southwestern spread of the East African Rift System (Modisi et al., 2000; Kinabo et al., 2007; Shemang and Molwalefhe, 2011). Water availability in this area therefore does not solely depend on climate but also on tectonic processes, vividly exemplified by the structural redirection of

the Cuando-Linyanti-Chobe river system (Riedel et al., 2014), Figure 2.2). On the one hand, absence or presence of lakes in the extended depressions of the Makgadikgadi-Okavango-Zambezi Basin (Ringrose et al., 2008), Figure 2.2) do not necessarily reflect climate dynamics, and on the other hand the regional climate must not be in phase with evolution of lakes primarily controlled by remote active catchments.

It can tentatively be summarized that aridity prevailed in the Kalahari during the last ca. 200 ka, and more humid periods were rather exceptional (e.g. Brook et al., 1996; Burrough et al., 2009b; Blome et al., 2012). A predominately arid climate concurs with special adaptations of Khoisan-speaking people, including traits which are absent in other human groups such as the ability to store water and lipid metabolites in body tissues (Schuster et al., 2010). These evolutionary adaptations indicate, however, that the small populations of Khoisan-speaking people living in the Kalahari (Bushmen or San) do not represent relics
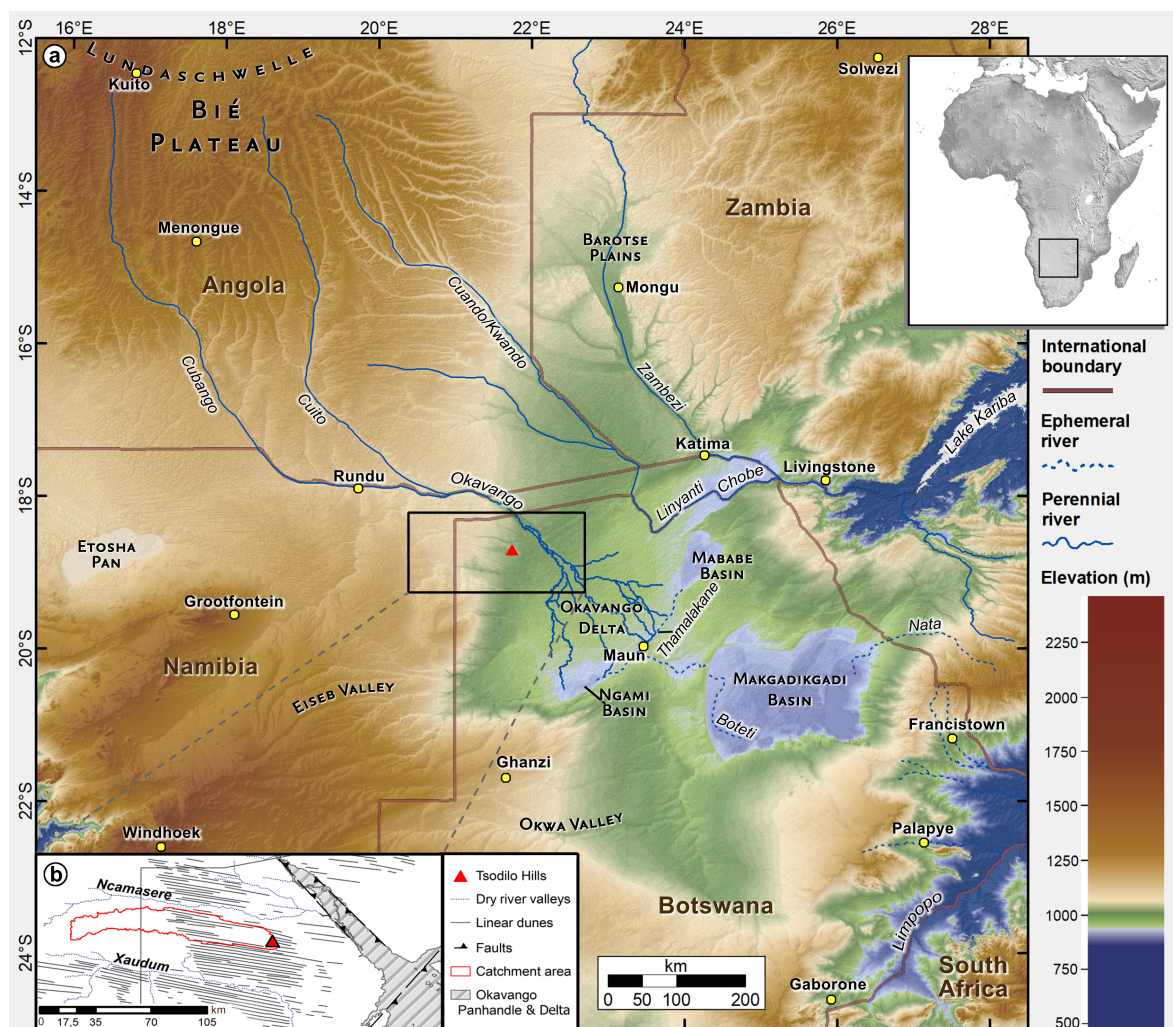
Figure 2.2: a) DEM of the Kalahari drainage system with position of Tsodilo Hills (after Riedel et al., 2014). Mean annual precipitation and temperature for indicated settlements are compiled in Table B.1; **b)** Extension of the drainage basin west of Tsodilo Hills, which is in the focus of this study (after Wiese et al., 2020).

of earliest modern humans but are descendants as well. Oldest (ca. 100 ka) direct evidence for modern human behaviour in southern Africa comes from Blombos Cave, located on the South African coast (Henshilwood et al., 2011) in the year-round rainfall zone (Chase and Meadows, 2007). The cave does not archive a permanent cultural record from the Middle into the Late Stone Age, though (Henshilwood et al., 2011). A site of permanent human occupation during the last ca. 100 ka does exist in the northern Kalahari (Robbins et al., 1994, 2000, 2010, 2016). These people inhabited rock shelters of the Tsodilo Hills (Figure 2.3), inselbergs in proximity to the Okavango wetlands (Figure 2.2) and which became UNESCO World Heritage Site in 2001 due to its outstanding rock art and its exceptionally long human occupation (Segadika, 2006). The Tsodilo Hills are more or less in the area where Chan et al. (2019) suspected the cradle of modern humans. Chan et al. (2019) proposed that out-of-homeland migration was induced by regional shifts in climate, shaping the genetic diversity of humans.

The Late Pleistocene climate variability is directly reflected by the dynamics of a fluvio-lacustrine system with lake formation along the western cliffs of the Tsodilo Hills. The drainage basin does not extend more than 200 km to the west (Figure 2.2b), is therefore primarily controlled by local to regional climate, and lithospheric fracturing and seismicity are much lower compared to the Okavango Rift Zone (Hutchins et al., 1976; Nthaba et al., 2018; Ntibinyane et al., 2019). The lake basin is dry nowadays and the dynamics of the palaeolake have been discussed controversially (Brook et al., 1992; Thomas et al., 2003; Brook et al., 2010; Wiese et al., 2020). Sediments from this "Palaeolake Tsodilo" were dated from ca. 43 ka (Wiese et al., 2020; this study) to approximately the Early Holocene (Thomas et al., 2003; Brook, 2010; Robbins and Murphy, 2011). The sedimentary archive thus comprises the transition from the Middle to the Late Stone Age (McCall and Thomas, 2009; Robbins and Murphy, 2011; Villa et al., 2012).

Robbins et al. (2010) emphasized the importance of fishing for the ancient people of Tsodilo, at equal rank with hunting game. The bones of cichlid freshwater fishes were found abundantly in cultural layers of the White Paintings Shelter located at the base of the Male Hill (Robbins et al., 2016), Figure 2.3) and therefore at least periodically close to the shore of the palaeolake (Figure B.8). Cichlids are tropical freshwater fish with low salinity tolerance (e.g. Salzburger and Meyer, 2004; Sparks and Smith, 2005). This implies that ancient people from Tsodilo either caught them from rivers such as the Ncamasere (Figure 2.2b), which flowed north of the Tsodilo Hills into the Okavango still in historical times (Robbins et al., 1994; Brook, 2010) or from Palaeolake Tsodilo if it was not saline but contained freshwater. Gastropod and diatom assemblages from lake sediments rather point at periodically low salinities (Thomas et al., 2003; Wiese et al., 2020). This corresponds with a palaeo-outflow at the southern flank of the
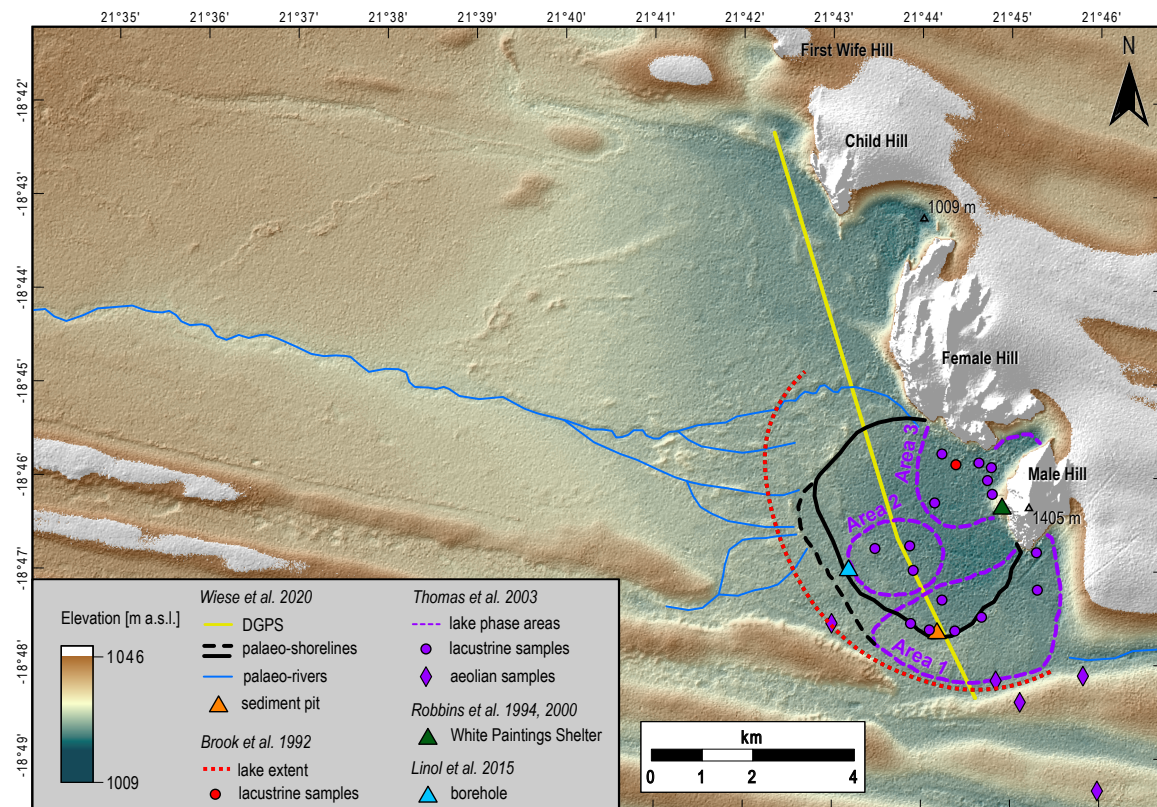
Figure 2.3: TanDEM-X DEM of the study area showing the palaeolake depressions west of the Tsodilo Hills and sampling locations of previous studies with corresponding assumed palaeolake extensions (Brook et al., 1992; Robbins et al., 1994, 2000; Thomas et al., 2003; Linol et al., 2015; Wiese et al., 2020).

Male Hill (Figure 2.3), which was active at least during lake highstands (Wiese et al., 2020; this study). On the other hand, neither hippopotamuses nor crocodiles seem to have ever reached Palaeolake Tsodilo, which is e.g. in contrast to other regional rather unstable lakes such as Ngami (Spinage, 2012), Figure 2.2). The question, which role Palaeolake Tsodilo may have played for ancient people's livelihoods remains unanswered. A closer look at palaeo-hydrological settings probably helps to better understand whether the lake itself may have promoted human occupation of the Tsodilo Hills since the Middle Stone Age or whether the hydroclimate under which the lake could develop was more important. The small number of 70–80 extant Khoisan-speaking people, which could sustain on potable water from wells hidden in the Tsodilo Hills until they were removed from their sacred place two decades ago (after declaration of Tsodilo Hills as UNESCO World Heritage site in 2001, personal communication), may provide a rough idea about past population sizes under a dry climate. It further suggests that ancient migration to the north (e.g. Rito et al., 2019), towards the tropical rain belt, was rather triggered by increasing aridity and not by increasing humidity when likely larger populations could occupy the Tsodilo Hills.

The aim of our study is to reconstruct stages of the fluvio-lacustrine system at the Tsodilo Hills with a multi-methodological approach focusing on lake evolution during ca. 43–19 ka. We test whether our results correspond with local archaeological evidence and human-environment interaction respectively, and attempt to promote the discussion about subsistence strategies, that is e.g. local versus regional fishing. Our hydrological interpretations will be briefly compared with contemporary hydroclimate signals inferred from other archives across the northern and central Kalahari and beyond.

2.2 Study area

The Tsodilo Hills are a group of five Neoproterozoic, ca. 12 km NW to SE trending inselbergs composed of metasedimentary, kyanite-grade quartz-muscovite schists and ferruginous quartzites (Key and Ayres, 2000; Singletary et al., 2003; Wendorff, 2005). The individual hills have traditional names (Campbell and Robbins, 2010) with the "Female" most wide-ranging and the "Male" with the highest peak (1405 m a.s.l.; Figure 2.3). The northern tip of the hill chain is located little more than 6 km south of the Ncamasere river valley (Figure 2.2b). The landscape to the west of Child, Female and Male Hills (Figure 2.3) shows little relief and comprises features of a former fluvio-lacustrine system, which levels at ca. 1010 m a.s.l. near the inselbergs (Grove, 1969; Brook, 2010; Wiese et al., 2020), Figure 2.3). We refer to the lacustrine sub-system as Palaeolake Tsodilo.

Beyond the flat area, linear dunes, which are spaced ca. 1.5–2 km apart, trend from WNW to ESE (Figure 2.3). In proximity to the Tsodilo Hills, the somewhat rounded dune crests rise about 20–30 m above the interdune areas (Grove, 1969; this study). Sand has piled up at the eastern flanks of the Tsodilo Hills indicating the major wind direction during dune formation and the wind-shadow position of the Palaeolake Tsodilo depressions (Brook, 2010; this study). Thomas et al. (2003) provided OSL-dated samples from two longitudinal dunes in a range from 107 to 23 ka. The so far oldest reconstructed lake highstand during ca. 43–41 cal ka BP, however, eroded the dunes (Wiese et al., 2020) indicating that OSL-dates younger than that reflect reworking of dune crests. The age of the extended Northern Kalahari fields of linear dunes has been discussed in a wide range, from "Late Tertiary" (Cooke, 1980) to "Late Quaternary" (e.g. Chase, 2009; Thomas and Burrough, 2016, cf. Discussion). Brook et al. (1992), Thomas et al. (2003) and Wiese et al. (2020) all focused on the southern area of the palaeolake (Figure 2.3). Their chronologies of lake phases are not in line. Thomas et al. (2003) presented surface sample (see Figure 2.3) dates from ca. 41 to 8 cal ka BP indicating site-specific differences in lake bed erosion. The surface or near-surface sediments of the

palaeolake depressions are characterised by carbonatic duricrusts (Brook et al., 1992; Thomas et al., 2003; Wiese et al., 2020). Wiese et al. (2020) assigned a potential palaeo-outflow to the east, ca. 2 km south of Male Hill (Figure 2.3). The vegetation is generally considered the sandveld type (de Wit and Bekker, 1990; Bekker and de Wit, 1991), that is open grass- and shrubland with clusters of trees such as *Acacia* and *Terminalia* (cluster-leaf) (e.g. Cole and Brown, 1976; cf. van Wyk and van Wyk, 1997). A preliminary survey along a transect from the deep sand-areas west of the lake beds, across the lake beds and up to Female Hill exhibited different vegetation zones (Figure 2.4). A true sandveld community (e.g. Sianga and Fynn, 2017) is rather confined to the deep sand-area while vegetation is more diverse on the lake beds, where also the tallest trees flourish, including *Combretum* (bushwillow) and *Adansonia* (baobab) (see Discussion). The vegetation grows under a semi-arid climate, with annual evapotranspiration almost three times higher than precipitation (Figure 2.5). A yearly mean of ca. 700 mm rain falls during austral summer while there is little to no precipitation in winter (Figure 2.5). The lake depressions can be flooded to shallow depths during heavy rains (Brook, 2010); Figure B.1). Perennial water is scarce at Tsodilo nowadays and only one site ("Python Spring") is commonly known (Campbell and Robbins, 2010) while other sources do exist but are secret (personal communication with Xontae Xhao, headman of local San).
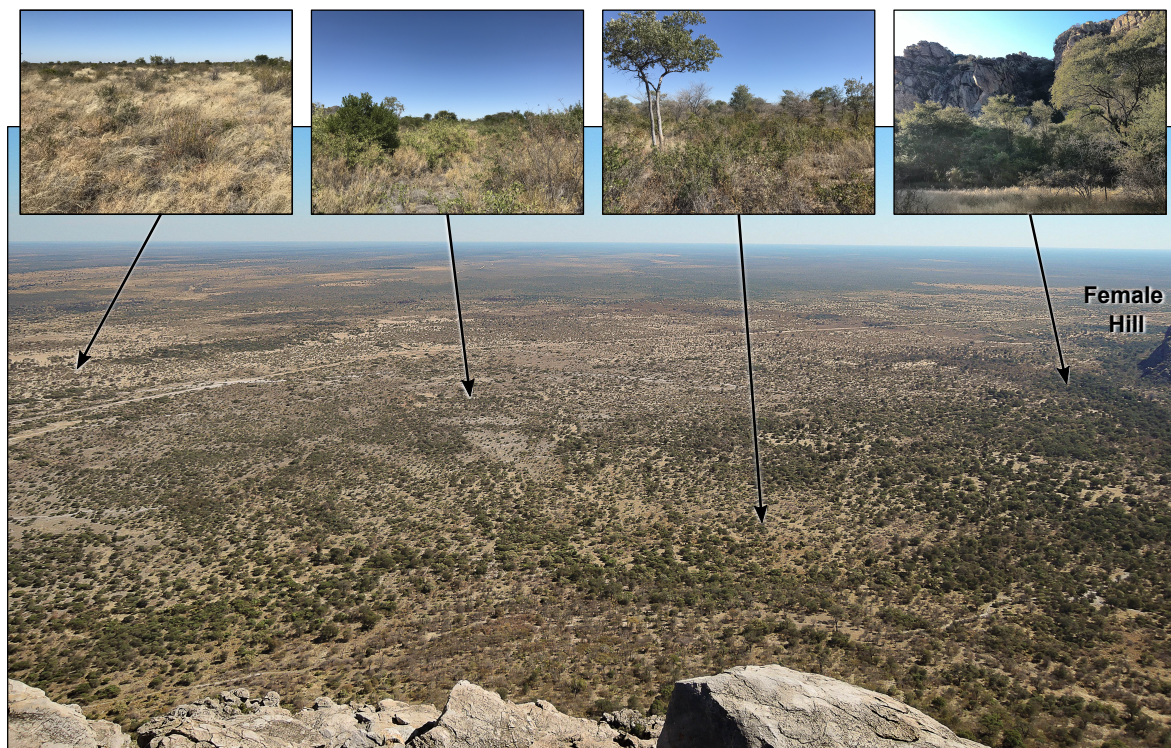
Figure 2.4: View from Male Hill to the northwest, across the palaeolake beds. Vegetation types are exemplified.
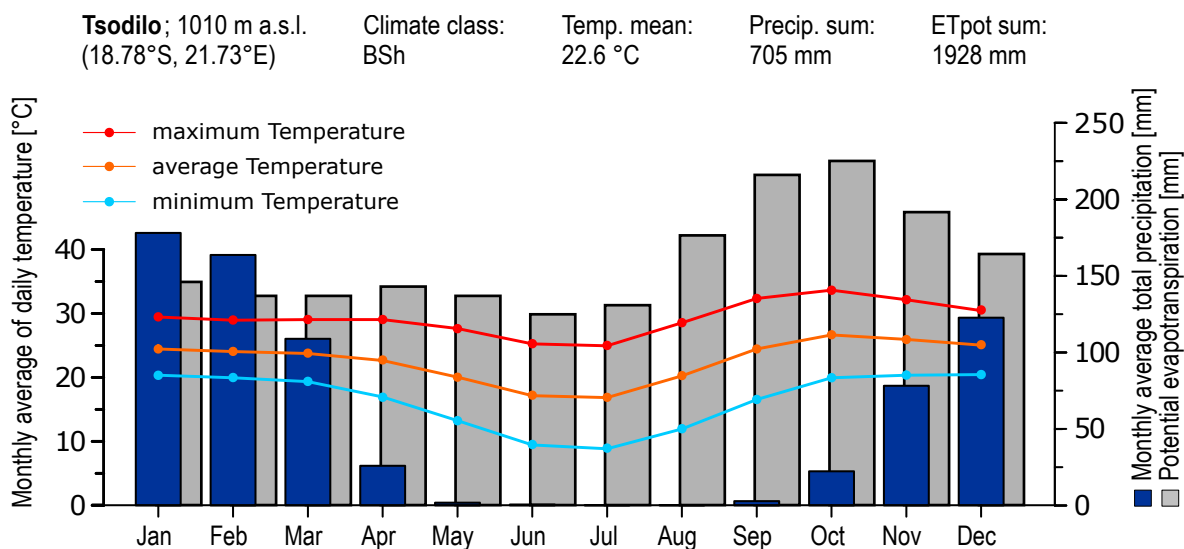
Figure 2.5: Climate chart (AD 1981–2010) for Tsodilo. Precipitation and temperature values derived from the ERA5 reanalysis dataset (Copernicus Climate Change Service, 2019). Evapotranspiration values calculated with ETo calculator (FAO, 2012).

2.3 Material and methods

2.3.1 Morphometric satellite data analysis

TanDEM-X and Landsat data

The satellite data used for the geomorphological mapping was of two types: (1) a high-resolution digital elevation model (DEM) and (2) Landsat multispectral and multitemporal imagery. The high-resolution elevation data from the TanDEM-X mission (TerraSAR-X add-on for Digital Elevation Measurement; Schulze et al., 2008; Rizzoli et al., 2017) was supplied in 2017 by the DLR (Deutsches Zentrum für Luft- und Raumfahrt; German Aerospace Centre). The elevation data for the studied basin area spans three overlapping source scenes of the TanDEM-X DEM, recorded on 2011-May-26 and 2012-Aug-08, and thus resulting in 2–3 coverages with a spatial resolution of $12{\times}12$ m. The height error for the DEM is annotated in the respective TanDEM-X HEM (height error map) with a maximum of about 1 m.

Landsat data from missions 5, 7 and 8 were downloaded from the USGS EarthExplorer website (Table B.3). Only datasets with no cloud cover and no bush fire influence (checked with MODIS data — MOD14A2 from EarthExplorer) were chosen, primarily covering the same period as TanDEM-X data (May 2011, August 2012). Due to a failure of Landsat 7's Scan Line Corrector, the raster data include black stripes with missing data, and thus datasets from other years (2008–2018) but for the same months were added. Additionally, data covering the periods of field campaigns (August 2015, August 2017, June 2018) were acquired, particularly for direct comparison with ground observations of the vegetation.

Datasets with best coverage for one whole year (2016) were chosen to retrace seasonal changes of the landscape.

TanDEM-X DEM noise reduction

The elevations in the TanDEM-X DEM are defined in terms of the reflective surface of X-Band interferometric SAR (Synthetic Aperture Radar) returns. As for short wavelengths (X-band: $\sim 3\,\text{cm}$; DLR, 2009) the penetration of vegetation cover is limited, the backscattered signals originate from within the vegetation cover. Therefore, shrubs and trees are included in the elevation model. The measured vegetation height is affected by SAR inherent effects, as the elevation of the scattering centre depends on the vegetation density, shape and wetness (Figure B.2; Izzawati et al., 2006; Schumann and Moller, 2015; Tanase et al., 2015). Drier and sparser vegetation cover allows deeper penetration than a dense and moist, placing the scattering centre closer to the ground (Weydahl et al., 2007; Perko et al., 2011; Rizzoli et al., 2017). Vegetation cover may produce a pronounced zigzag-pattern along a TanDEM-X elevation transect, which can clearly be demonstrated in comparison with DGPS data (Figure B.4). In order to reduce such noise in the TanDEM-X DEM, six different filters were tested: (i) inverse discrete wavelet transformation (IDWT; Kalbermatten et al., 2012), (ii) the geomorphological filters erode (min) and (iii) dilate (max) (Pipaud et al., 2015) as well as (iv) a mean filter, (v) a filter using the Fill Tool (Spatial Analyst Tools) in ArcGIS (ESRI, 2018) on the inverted TanDEM-X DEM and (vi) the low pass filter using the Filter Tool (Spatial Analyst Tools) in ArcGIS. IDWT filters were applied using the Wavelet toolbox from MATLAB (The MathWorks, 2015a,b) whereas the min, max and mean filters were applied with R (R Core Team, 2019).

Filters that improved correlation with the DGPS profiles were the following: mean filter with a rectangle of 3×3 or 5×5 pixels, lowpass filter and fill filter with $1\,\text{m}$ (Table B.5). In areas with dense shrub and tree cover, the filtered data still deviate significantly from DGPS elevations e.g. along the northernmost part of T1 (Figure B.4). Apart from the fill filter, the application of filters resulted in a decreased spatial resolution. As most of the study area is shrubby grassland, which produces relatively low elevation errors (Figure B.4; Wessel et al., 2018), we decided to use the original TanDEM-X elevations, locally cross-correlated with DGPS data.

Geomorphological mapping

Three different approaches were combined for the geomorphological mapping: (1) Edge enhancement by a discrete wavelet transform (DWT) filtering procedure (Kalbermatten et al., 2012) for outlining topographic discontinuity that may be related to geomorphological features. The DWT is used to extract these discontinuities of the elevation data, which are then quantified and highlighted in terms of detail coefficients, i.e. scaling coefficients of the DWT (Doglioni and Simeone, 2014). The detail coefficients are mapped and analysed, whereby sudden variations of the coefficients are related to slope variations and discontinuities of the DEM and thus enable the delineation and identification of characteristic landforms (Doglioni and Simeone, 2014). Iteratively applying DWT, a multilevel decomposition of a topographic profile, was helpful for separating large-scale features from local features. This transformation was applied on the TanDEM-X DEM using the Wavelet toolbox in MATLAB (The MathWorks, 2015a,b). In a first step, all wavelet functions available in the toolbox were grouped after similarity of shape. To cover all sorts of shape, at least one wavelet of each group was chosen for the analysis, resulting in 19 different wavelets. After the filtering procedure, linear structures visible in the detail coefficients of different levels from each wavelet transformation (Figure B.5a) were mapped in ArcGIS (ESRI, 2018). Only the details of levels 1–4 were analysed because higher levels gave no additional information.

(2) The application of the TopHat-Transform function allowed the extraction of ridges and valleys (Rodriguez et al., 2002). The whiteTopHat function hereby returns the difference between the original image, here the TanDEM-X DEM, and its opening (erosion followed by a dilation) and thus extracts only the peaks with a specified radius, while the blackTopHat function subtracts the original image from its closing (dilation followed by an erosion) and thus retains the valleys with the specific radius (Rodriguez et al., 2002). These morphological operations were performed on the TanDEM-X DEM using the functions whiteTopHat and blackTopHat from the R-package EBImage (Pau et al., 2010; Oleś et al., 2018) with the kernel shape set as 'disc' of different radii (5, 9, 11, 15, 19, 23 and 27 px). Again, the linear structures in the resulting images (Figure B.5b) were mapped in ArcGIS (ESRI, 2018).

(3) Enhancement of the multispectral Landsat images (Figure B.5c) enabled us to identify hydrologically related geomorphologic entities (see Imbroane et al., 2007). This approach uses various band combinations, band ratios and principal components analysis (PCA) of the bands from each scene. In arid and semi-arid environments, three band colour composites such as RGB images can provide excellent lithologic discrimination (Imbroane et al., 2007). False colour composite imagery e.g. has been proved useful to provide further information on palaeohydrology as it indicates compositional differences of sediments (e.g. Schuster et al.,

2005; Drake et al., 2008; Breeze et al., 2015). Image processing, such as band ratios, can reveal information about the chemical composition of rocks and minerals on the Earth's surface if not completely covered by dense vegetation (Harding and Forrest, 1989; Okada et al., 1993; Imbroane et al., 2007). As the reflectance properties of rock-forming minerals are a function of chemical composition and crystal structure, many minerals have distinctive spectral absorption properties (Hunt, 1980; Goetz et al., 1985; Figure B.5c). Ferric oxides, for example, have characteristic absorption features in the visible (380–800 nm) and near-infrared region (800–1100 nm), while various phyllosilicates, carbonates and sulphates show their spectral features in the short-wave infrared region 1100–2500 nm) (Okada et al., 1993; Sabins, 1999; Percival et al., 2014). Thus, e.g. for Landsat 5, the ratio of bands 5/7 is expected to be high for clay minerals, because their reflectance is high in band 5 and relatively low in band 7 (Yazdi et al., 2013). A ratio of bands 5/4 enhances areas containing rocks which are rich in ferrous iron (Imbroane et al., 2007) and ratios of bands 3/1 and bands 3/4 are high for iron oxide minerals (Yazdi et al., 2013). Combining the band ratio images to colour composites (colour-ratio-composite images) allows the distinguishing of similar depositional environments. PCA reduces dimensionality while highlighting the information in the whole band spectrum. For Landsat 5 and 7, only the six reflective bands 1–5 and 7 were evaluated together. For Landsat 8, bands 1–7 were used as input for the PCA accordingly. The analyses were done in R (R Core Team, 2019) and ArcGIS (ESRI, 2018). Detected zones and structures in the resulting images were mapped in ArcGIS. Finally, only those zones and structures that were found in the majority of the analysed TanDEM-X and Landsat images were accepted. A classification of the detected zones and structures to different landforms was done based on conventional photo-interpretation keys (Loelkes, 1983) such as size, pattern, shape, context and relative positioning of the structures and was complemented with a visual interpretation of aerial imagery from the World Imagery layer of ESRI (Figure B.5d).

Identified former shorelines with a consistency in altitudes were assembled and connected based on TanDEM-X elevations to obtain continuous structures. Lake level heights were derived by filling the basin in ArcGIS (ESRI, 2018) until the respective shorelines were reached. Further lake morphometry metrics were calculated in R (R Core Team, 2019) using the package lakemorpho (Hollister and Stachelek, 2017; Hollister, 2018), under the simplifying assumption that the former basin morphology was similar to today. The metrics are thus approximated.

2.3.2 Geophysical measurements

A geophysical survey was carried out in August 2015 along the northern part of the DGPS transect T0, in NNW-SSE orientation through the lake depression (Figure 2.6). A total of 2.85 km of seismic refraction data and 12 km of ground penetrating radar (GPR) were acquired along the same profile line. However, for this study only the northern GPR radargram (2.6 km) that coincides with the seismic refraction profile has been processed. Both methods use the principle of wave propagation for subsurface imaging. GPR measures traveltimes of electromagnetic waves that are reflected at contrasts of dielectric permittivity. During refraction seismic surveys the measured traveltimes of direct and critically refracted waves depend on the elastic properties of the subsurface materials. Both data sets are combined aiming to enhance the reliability of data interpretation.

The GPR data were acquired using a MALA GPR system set up. Electric pulses were generated with a 30 MHz rough terrain antenna. These relatively low frequency signals can reach larger depths but at the expense of resolution. Electromagnetic pulses were generated every 10 cm along the 2596 m long profile and recorded with a second antenna at constant distance to the source antenna. The data processing was performed using the processing software ReflexW (Sandmeier, 2017). In a first step, the data were pre-processed.
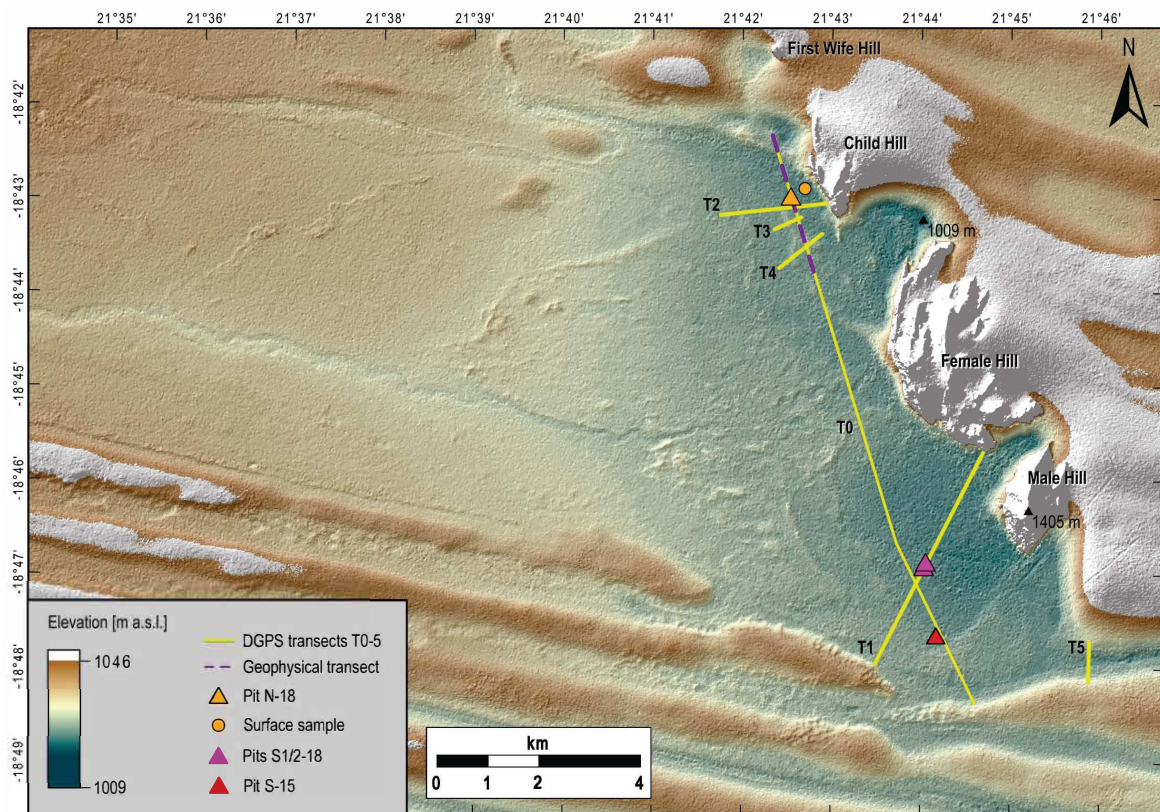
Figure 2.6: TanDEM-X DEM showing DGPS and geophysical transects and sediment pits

This included high-pass filtering to eliminate low-frequency noise produced by the recording system, static corrections to account for time delays of first arrivals, manual gain in order to compensate for amplitude decay with time and depth, and a background removal filter. Traces were stacked at intervals of three traces in order to amplify the signal. To convert the radargram from time to depth domain, the velocity of the average subsurface electromagnetic waves was estimated using the method of hyperbolic fitting (Cassidy, 2009). Afterwards, Kirchhoff migration (Schneider, 1978) was performed to convert the reflection signals from time domain to its spatial position in the subsurface (Cassidy, 2009).

The seismic refraction soundings were performed using a DMT$^©$ Summit II Plus seismic system. A total of 41 geophones (10 Hz, vertical type) were arranged in a split-spread geometry with a geophone spacing of 7.5 m (= 300 m spread). The source was initially located at the northern edge of the spread and moved 30 m after each of the first 6 shots until it was located at the middle of the profile, then the whole spread was moved 30 m after each shot. Seismic signals were produced as a series of pulses, according to a specific pre-programmed sequence by a Bosch Vibrometric VIBSIST-50 as surface seismic source. A total of 91 shots was performed to cover the profile of 2850 m length. Analyses of the resulting 91 single-shot sections were done with ReflexW (Sandmeier, 2017). For the model (Figure 2.9), the southernmost 150 m were not included, resulting in 2.7 km distance. The processing sequence included (1) bandpass Butterworth filter (Butterworth, 1930; Acharya et al., 2014), (2) automatic gain control, (2) first-arrival picking, (3) traveltime analysis, (4) wavefront inversion, and (5) seismic tomography. For filtering, a bandpass Butterworth filter (Butterworth, 1930; Acharya et al., 2014) was selected between 25 Hz and 80 Hz. An automatic gain control with a time window of 400 ms was applied to enhance weak signals. The picking of first arrivals was done manually. Each pick was accounted to the arrivals of direct and critically refracted waves. Based on the arrival times of each wave type, wavefront inversion gives a model of layer thicknesses and layer velocities. The tomography uses this model as starting model to invert for further lateral velocity changes.

2.3.3 Differential global positioning system (DGPS) elevation measurements

The DGPS-survey was used to obtain accurate elevation data of selected transects including sample sites and as ground control for remote sensing data. In total, 6 transects (T0–T5 in Figures 2.6 and 2.10) were measured during field campaigns in August 2015 and June 2018. The data were acquired with a measuring device setup from Leica Geosystems AG, consisting

of a Leica Viva CS15 field controller, two Leica Viva GS14 GNSS (Global Navigation Satellite Systems) Receivers (3.75G & UHF Single Frequency Smart Antenna) as base and rover, and an external Real-Time Kinematic (RTK) Antenna. The measurement distance between two points was approximately 25 or 50 m, depending on changes in the landscape, with a measurement time of 60–90 s and RTK processing. For quality control, the limit for maximum acceptable coordinate quality (CQ) for position and elevation was set to CQ3D(max)= 25 mm. Other measurement information such as the different values for positional measurement precision can be found in the supplements (Table B.4). These GNSS-RTK measurements were done without a known elevation (e.g. trigonometric point) as reference for the DGPS base station. Furthermore, the locations of the base station for the different transects were chosen to be on areas with a low density and low height of vegetation, to ensure an undisturbed satellite signal. For the 2018-transects, if possible, the base station was additionally located on points of the 2015-transect to allow cross-validation. We did not have the option to calibrate the position of the base station with a trigonometric point, thus absolute DGPS-heights have an uncertainty of 2–3 m(Leica Support, pers. communication April 2020); the uncertainty within a single transect, however, is only a few centimetres. For comparison between the transects as well as between transect and TanDEM-X data, all measured DGPS-heights needed to be corrected. Correction was done based on the TanDEM-X heights by subtracting or adding the height difference between each transect's DGPS base station and the respective TanDEM-X height at this location, or in case of T0 and T3, by applying the height difference between a DGPS point in an area with very low and sparse vegetation and the respective TanDEM-X value for the site (values for corrections in Table B.4). Generally, the locations for the DGPS base station were chosen correspondingly. For such sites with low and sparse vegetation, the absolute TanDEM-X elevation values should not exceed the maximum error of 1 m (Wessel et al., 2018; see paragraph on TanDEM-X and Landsat data).

2.3.4 Sediment analysis

Sampling and lithological description

Sediment Pit S-15 was dug and sampled in August 2015 and resampled in July 2019. The other three pits were dug and studied in July 2018. The pit locations (Figure 2.6; Table B.2) were chosen based on preliminary analysis of the TanDEM-X DEM and the geophysical transects. The pits N-18 and S1-18 were both located on sandy plains sparsely covered by shrubby grassland. S2-18 was dug at the edge of a 2 m deep depression (former water hole) surrounded by trees. Some details for Pit S-15 are published in Wiese et al. (2020).

The thoroughly cleaned sections of 0.9–3 m thickness were macroscopically described in terms of sedimentological properties as well as fossil content, sketched (Figure 2.11) and photographed. Afterwards, the sections were cleaned again and continuously sampled in 5-cm-steps (deviations in respect to lithological changes) using an angle grinder, except for the top metre of Pit S2-18 and the top 50 cm of Pit N-18, which were sampled in 10-cm-steps. Additionally, a surface sample (TD18-50; Figure 2.6) was taken that exhibited gastropod shells in abundance. The individual sample volume was about 1.5–2 l. The classification of sediments is based on observations in the field and refined by carbonate content estimated from LOI (see next paragraph). Limestone is characterised by $\geq 37\%$ $CaCO_3$ and marl by <37–20% $CaCO_3$. Below 20% $CaCO_3$ the material was classified as quartz sand.

Geochemical and mineral analysis

Measurements were performed at the Laboratory of Physical Geography, Department of Earth Sciences, Freie Universität Berlin. Homogenization of the measured aliquots of the bulk sediment samples was achieved in a continuous vibration disk mill. Organic matter and carbonate content were estimated by loss on ignition (LOI) of 1 g homogenized dried (105 °C) sample material at 550 °C (5 h) and 900 °C (5 h) respectively, following the procedures described by Heiri et al. (2001). LOI residuals (Si-remains) were corrected by CaO subtraction based on LOI_{900} CO_2 estimation, assuming that LOI_{900} is 100% related to calcite. To gain information on the variability of the elemental sediment composition, 2 g of the homogenized dried (105 °C) sample materials were semi-quantitatively measured in sample cups using a portable X-ray fluorescence (XRF) analyser (Thermo Scientific™ Niton™ XL3t XRF Analyser). Measurements were done in the manufacturer's 'mining mode' for (in-device) fundamental parameter calibration, and four filters were selected with an overall measurement duration of 120 s. Only elements with mean values at least four times larger than the 2σ error of the measurements were used for the analyses. Elements were excluded from further analysis if the proportion of samples with values below the detection limit exceeded 15%. Seven elements (Al, Ca, Fe, K, Si, Sr, Ti) were selected for further analyses. For comparison to measurements by inductively coupled plasma optical emission spectrometry (ICP-OES), the measurement unit was converted from the initial parts per million (ppm) to milligrams per gram (mg/g).

ICP-OES was conducted with a PerkinElmer Optima 2100 DV instrument after HCl (37%) digestion of 1 g homogenized and dried (105 °C) aliquots to determine the content of selected carbonate and/or sulphate related elements (Ca, Fe, K, Mg, Mn, Na, P, S, Sr).

The mineral composition was analysed by X-ray diffraction performed on homogenized dried (40 °C) samples using a Rigaku Miniflex 600. The 2θ range (3–80°) was analysed in 0.02° steps with a copper Kα X-Ray tube at 15 mA/40 kV. Identification of the minerals was based on Philipps X'Pert Highscore 1.0b software. Identified reflex intensities (counts per second: cps) from each mineral main peak were converted into a relative percentage (% cps) of each mineral with respect to the sum of all identified main reflexes of the bulk sediment (Wünnemann et al., 2010). However, estimations of the mineral compositions must be regarded as semi-quantitative.

Multivariate statistics

As the datasets of LOI, elemental and mineral analyses are considered to be compositional, the problem of spurious correlations and non-normality needed to be treated by log-ratio transformations of the intensities and concentrations (Aitchison, 1982, 1986). Therefore, the values were centred logratio (clr) transformed prior to the statistical analyses using the R-package compositions (van den Boogaart et al., 2020) in R (R Core Team, 2019). To overcome the problem of zero count values in the transformation results (Martín-Fernández et al., 2000), these values were set to the respective smallest value of possible detection, e.g. the minimal detection limit. Subsequently, the datasets were made comparable by standardization using a z-transformation. For exploration of the relative correlations and interdependencies between individual elements, PCA was used on the geochemical data. The PCA enables to generate proxies related to hydrological changes and to identify system variables (e.g. Hartmann and Wünnemann, 2009). As ratios of element intensities are considered to be useful for correlation and advantageous compared to the intensities of single elements (e.g. Vlag et al., 2004; Croudace et al., 2006; Richter et al., 2006; Weltje and Tjallingii, 2008), the PCA was also used to extract descriptive ratios of the geochemical data according to the identified system variables. The element ratios were solely built of elements measured with the same method for having a conclusive statement. As ratios are insensitive to dilution effects from the unit-sum constraint (Weltje and Tjallingii, 2008), the geochemical ratios were calculated from the non-transformed values converted in mg/g molar weights and the mineral ratios from the % cps values.

2.3.5 Radiocarbon dating

Fossil shells of aquatic gastropods were carefully extracted with a pneumatic engraving pen from selected samples of each pit. Shell fragments that could be clearly assigned to the genera *Bulinus* or *Radix* were first cleaned using needle and brush and then in an ultrasonic bath. Four shell samples were ^{14}C-AMS-dated at Beta Analytic Radiocarbon Dating Laboratory in Miami (Beta), USA, and three samples at Leibniz-Laboratory for Radiometric Dating and Stable Isotope Research in Kiel (KIA), Germany (Table 2.2). As pre-treatment method, (shell) acid etch was used for the four Beta-samples, while for the three KIA-samples no pretreatment was done due to the small amount of available sample material. The radiocarbon ages [^{14}C yr BP] were converted into calendar ages [cal yr BP] by calibration with Calib 8.1 (Stuiver and Pearson, 1993; Stuiver and Reimer, 2020), using the southern hemisphere calibration curve SHCAL20 (Hogg et al., 2020). Additionally, given point estimates were calculated using the mode, i.e. the maximum of the probability distribution of a calibrated ^{14}C-date as proposed by Michczyński (2007); in case of more than one age range, a weighted mode was calculated. No reservoir offset was applied, following Riedel et al. (2014).

2.4 Results

2.4.1 TanDEM-X and Landsat based geomorphology

The drainage basin (Figure 2.2b) extends to about 120 km west of the Tsodilo Hills, has a maximum N–S-extension of 19 km and spans ca. 1750 km^2. The major palaeolake-related results are compiled in Figure 2.7. A northern lake depression between Child and Female Hills and a southern depression south of Female Hill can be differentiated. A linear SW-trending structure roughly paralleling the northern heritage site fence (Figure 2.7B) represents the only potential fault we could identify (see Discussion). In relation to the lake depressions, four shoreline systems could be identified (see Material and methods section) and are termed as palaeolake phases P1–P4. P1 levelled at an elevation of ca. 1025 m a.s.l. and covered about 70 km^2. The P2-shoreline is about 5–6 m lower than the P1-shoreline and formed at about 1019.5 m a.s.l., while P3 levelled at 1018 m a.s.l. and P4 at 1017 m a.s.l., subdivided into P4 south and P4 north. Calculation of lake areas, water depths and volumes are listed in Table 2.1. P1 and P2 eroded linear dunes framing the lake basin in the south and dunes in the north, which had formed west of the corridor between Child and First Wife Hills. The western shoreline of P1 cannot unambiguously be identified but follows tentatively the landforms between the terminal southern and northern erosional features.

Table 2.1: Hydrological characteristics of the four identified lake phases. Lake levels were derived by filling the modern shape of the lake depressions in ArcGIS until the respective shorelines were reached. Other metrics were calculated using the R package lakemorpho (Hollister and Stachelek, 2017; Hollister, 2018).

Palaeolake phase	Lake level	Max. depth	Surface area	Water volume
	[m a.s.l.]	[m]	[km^2]	[10^6 m^3]
P1	1025.0	16.0	70.6	25.1
P2	1019.5	10.5	40.3	13.2
P3	1018.0	9.0	27.6	8.6
P4n (northern sub-basin)	1017.0	8.0	4.9	1.5
P4s (southern sub-basin)	1017.0	6.0	10.6	3.9
drainage area			1756.0	

Table 2.2: Radiocarbon ages of *Bulinus* and *Radix* shell fragments from the studied palaeolake sediments. *= Wiese et al. (2020). Conventional radiocarbon years [^{14}C yr BP] were converted into calendar years [ca yr BP] by calibration with CALIB 8.1 (Stuiver and Reimer, 1993, 2020), using the southern hemisphere calibration curve SHCAL20 (Hogg et al., 2020). The calibrated dates are given as a range or ranges with the associated probability. Point estimates for the calibrated ages were calculated using the probability distribution mode as proposed by Michczyński (2007).

Lab-ID	Sample-ID	Depth	Radiocarbon age $\pm 1\sigma$	Calibrated age (2σ range)
		[cm]	[^{14}C yr BP]	[cal. ka BP]
Beta-511707	TD18-50	0–10	23300 ± 80	27.4 (27.3 – 27.7)
Beta-511706	Pit N-18	0–10	38990 ± 380	42.6 (42.3–42.9)
Beta-511705	Pit N-18	140–145	> 43500	> 46.6
KIA-53512	Pit S2-18	125–130	38100 ± 1300	42.3 (40.5–44.1)
KIA-53510	Pit S1-18	15–20	33300 ± 800	37.7 (36.2–39.8)
Beta-511704	Pit S1-18	35–40	> 43500	> 46.6
KIA-53511	Pit S1-18	85–90	35200 ± 950	37.8 (37.8–38.0) (1 %)
				40.3 (38.0–41.9) (99 %)
Beta-421941	Pit S-15*	40–45	15540 ± 60	18.8 (18.7–18.9)
Beta-421942	Pit S-15*	90–95	16930 ± 60	20.4 (20.3–20.6)
Beta-421944	Pit S-15*	95–100	35380 ± 360	40.6 (39.7–41.1)
Beta-421940	Pit S-15*	95–100	37830 ± 500	42.2 (41.6–42.6)
Beta - 421943	Pit S-15*	125–130	39350 ± 470	42.8 (42.3–43.4)

Five major, partly interconnected palaeo-channels were identified, which are aligned from west to east in direction to the lake basin (Figure 2.7). The interconnecting SW–NE channels are less pronounced than the WSW–ESE channels and partly appear as positive relief. The central channel terminates between the northern and southern lake depressions where the P3-shoreline is concave for about 3 km (Figure 2.7). A channel, about 2 km south of Male Hill, is tracked to the Okavango Panhandle (Figure 2.8). The channel is approximately 56 km long and slumps from ca. 1015 m a.s.l. (Figure 2.8) at its western terminus to ca. 986 m a.s.l. at its eastern terminus. An asymmetric delta, which is about 10 km wide, corresponds to this palaeo-channel (Figure 2.8).
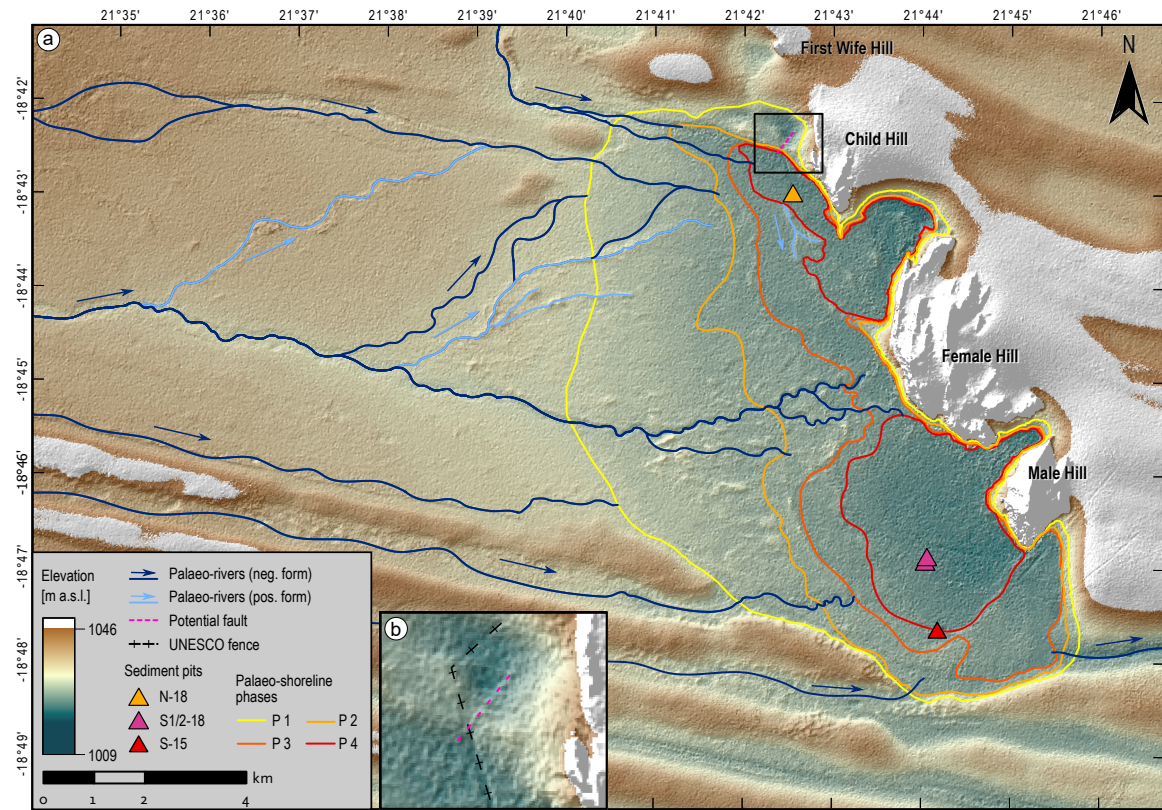
Figure 2.7: a) TanDEM-X DEM exhibiting major palaeo-shorelines and -rivers. **b)** Magnification of the area with a supposed tectonic fault.
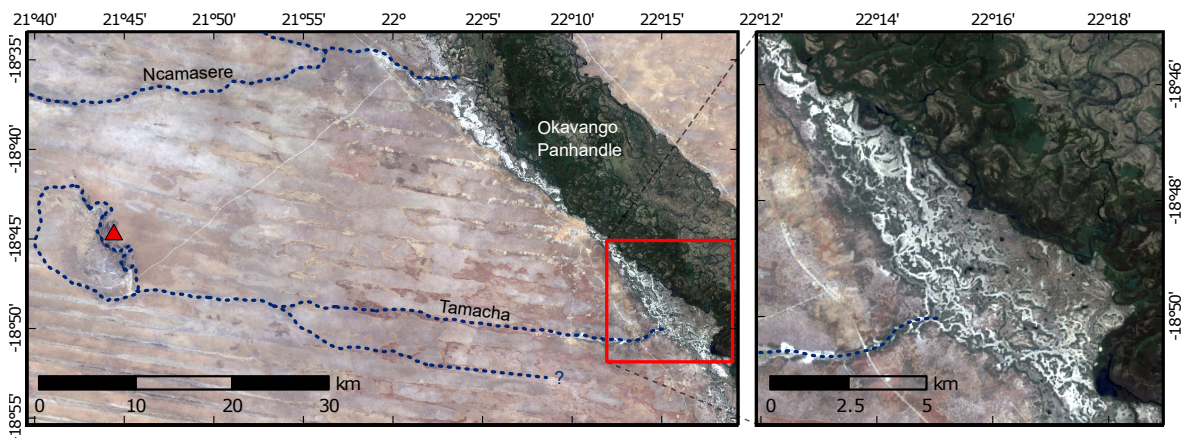
Figure 2.8: Landsat image with the course of the former Palaeolake Tsodilo outflow sketched. The outflow created the Tamacha River, which formed a pronounced delta in the Okavango Panhandle. The red triangle indicates the position of the Female Hill and the dashed line passing it follows the highest palaeo-shoreline we could infer.

2.4.2 Geophysically constrained subsurface structures

Seismic refraction

The generated tomographic velocity–depth model reaches a maximum depth of ca. 38 m, locally only around 20 m. P wave velocities range from ca. 200 to 2100 m/s (Figure 2.9). We are aware that the behaviour of the P wave velocity does not only depend on the rock type (e.g. Kearey et al., 2002) but on many lithological properties such as porosity, cracks, density or water saturation (e.g. Kearey et al., 2002; Kahraman and Yeken, 2008; Bailly et al., 2019). Velocities measured along the transect roughly provide a spectrum from dry sand to lithified sedimentary rocks (Kearey et al., 2002). A detailed analysis of the data is not in the scope of this paper but certain cross-correlations with surface structures and lithological data from our pits and from the literature (see Discussion). Generally, P wave velocity increases with depth, and tentatively, three main velocity layers can be derived (see Material and methods; Figure 2.9): The basic layer (violet to red) terminates at ca. 25 m (32–20 m) depth. The thickness of this layer remains unknown. The velocity values of 2100–1200 m/s possibly indicate compact sedimentary rocks (Kearey et al., 2002; see Discussion). The basic layer is relatively homogeneous but horizontal velocity differences are notable, e.g. between the 400–900 m and the 2000–2300 m section of the profile. The middle layer (pink to green) comprises velocities of 1200–500 m/s and ranges from 8 to 28 m in thickness. The interface between the basic and the middle layer produced strong refraction signals that are clearly visible in nearly each of the seismic sections. This strong velocity contrast indicates a prominent change to less compact or less water-saturated lithologies (Kearey et al., 2002).

The middle layer expires around 10 m depth, with significant differences between profile sections. In the northernmost ca. 300 m, e.g., the middle layer reaches 4 m depth, in the middle section (around 1300–1500 m distance) it is close to the surface, while it terminates in around 15 m depth in the southern section. The horizontal velocity variations, particularly in the southern section (from 1400 m distance), exhibit compositional differences. These are likely related to a higher degree of weathering and fracturing (Barton, 2006), or to uncertainties in traveltime picking as the headwave from this layer boundary is hardly visible in the data. A dipping refractor at the interface of the middle and top layer at around 400 m distance (Figure 2.9) is noteworthy.

The velocities of the top layer (blue-green to dark blue) range from 500 to 200 m/s which is commonly considered to indicate dry sand (e.g. Kearey et al., 2002). The thickness varies between ca. 1 and 15 m. The top layer exhibits contrasting velocities with ca. 400 m/s velocity (bright blue) on the one hand and ca. 200–300 m/s (dark blue) on the other hand. From

distance 1500 m on, a hinge-like pattern between ca. 12 m deep dark-blue areas and the bright blue zones is noticeable.

Ground penetration radar

The GPR data was interpreted by visually identifying sequence boundaries and hyperbolas along the profile, as well as calculating electric parameters to obtain further information from the subsurface (Figure 2.9). The velocity for the migration was calculated using the hyperbolas located between 3 and 18 m depth. Hyperbola fitting has given an average velocity of 0.13 m/ns. However, using hyperbola fitting, the velocity estimation was only possible to a depth of 20 m. The dielectric constant was determined to be 5.32, which is in the range
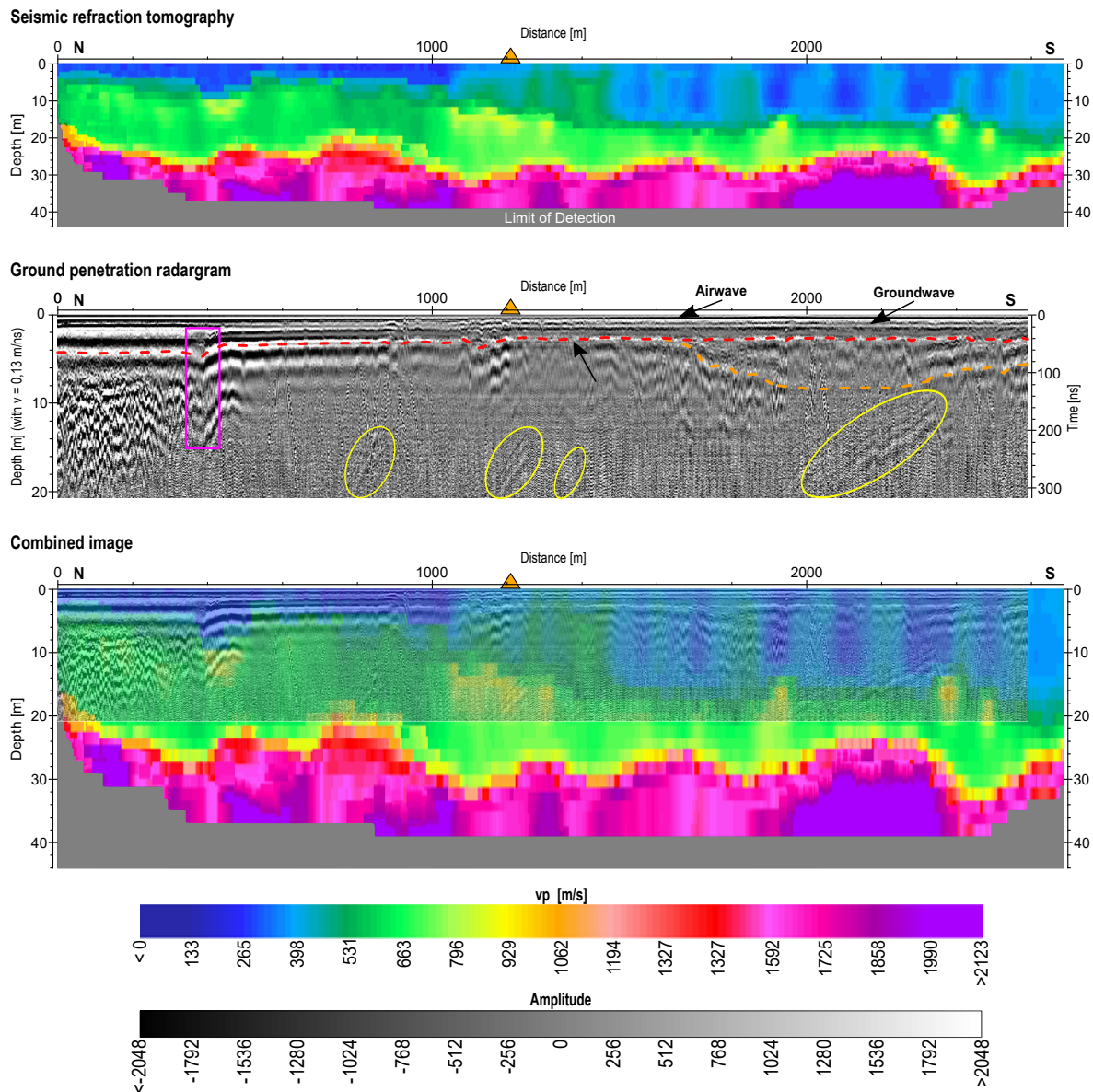
Figure 2.9: Seismic refraction tomography (**top**), ground penetration radargram (**middle**) and combined image (**base**). Orange triangle indicating the location of Pit N-18 (see Figure 2.6). Further information in the text.

of, e.g., dry soil, sand, limestone or sandstone (Cassidy, 2009). At the top of the radargram, the continuous black and white 2 m deep banding (Figure 2.9) is the result of the air- and groundwave travelling directly above and along the surface interface. These do not represent reflections and negate the ability to distinguish objects in the very shallow subsurface. The yellow ellipses (Figure 2.9) likely frame reflections from the surface because an unshielded antenna was used and therefore the electromagnetic field spread in all directions. A high concentration of hyperbolas, creating chaotic reflections, was found at the northern 400–500 m of the transect down to 18 m (Figure 2.9). The strong amplitudes in this section might indicate materials with high resistivity that could for example be related to cavities. However, these diffraction hyperbolas could also indicate solid objects in the subsurface. The size of the respective structures would be of around 1 m. A reflection band which is in ca. 4 m depth at 0–400 m distance is continuous along the whole profile but shows a vertical offset of ca. 1.5 m around 400 m distance and is thinning out southwards (Figure 2.9, red dashed line). The vertical offset area including greater depths is marked by a rectangle. At ca. 920 m and ca. 1100 m small bow-shaped excursions of the reflection layer can be observed. A larger bow-shaped structure down to 9 m depth is visible from ca. 1600 m to >2600 m (orange dashed line in Figure 2.9).

DGPS ground control

Six DGPS transects (T0–T5) were measured (Figure 2.10; Table B.4). **T0**: Ca. 12 km in NNW–SSE direction across the whole lake basin with an elevation amplitude of 10.2 m; T0 generally shows that a northern and a southern lake depression are separated by an incised ridge at ca. 4.5–7 km; the northern lake depression is more heterogeneous (compare Wiese et al., 2020). **T1**: Ca. 4.7 km in SSW–NNE direction across the southern lake depression with an elevation amplitude of 7.6 m; T1 shows a relatively regular altitudinal decline with the lowest position close to the Female Hill. **T2**: Ca. 2.1 km in W–E direction through the eastern part of the northern lake depression with an elevation amplitude of 5.5 m; T2 generally dips towards the Child Hill and exhibits two ridges at ca. 0.4 km and 1.2 km. **T3**: Ca. 0.6 km in WSW–ENE direction within the northern lake depression and with an elevation amplitude of 4 m; the main feature exhibited is a ridge from ca. 0.2 km to 0.4 km. **T4**: Ca. 1.1 km in SW–NE direction within the northern lake depression and with an elevation amplitude of 5 m; two ridges spaced ca. 0.4 km apart and a lower elevation in the east than in the west are exhibited. **T5**: Ca. 0.8 km in N–S direction across the potential palaeolake outflow area with

an elevation amplitude of 10 m; the profile is roughly U-shaped; the southern slope shows a terrace-like structure at the base.
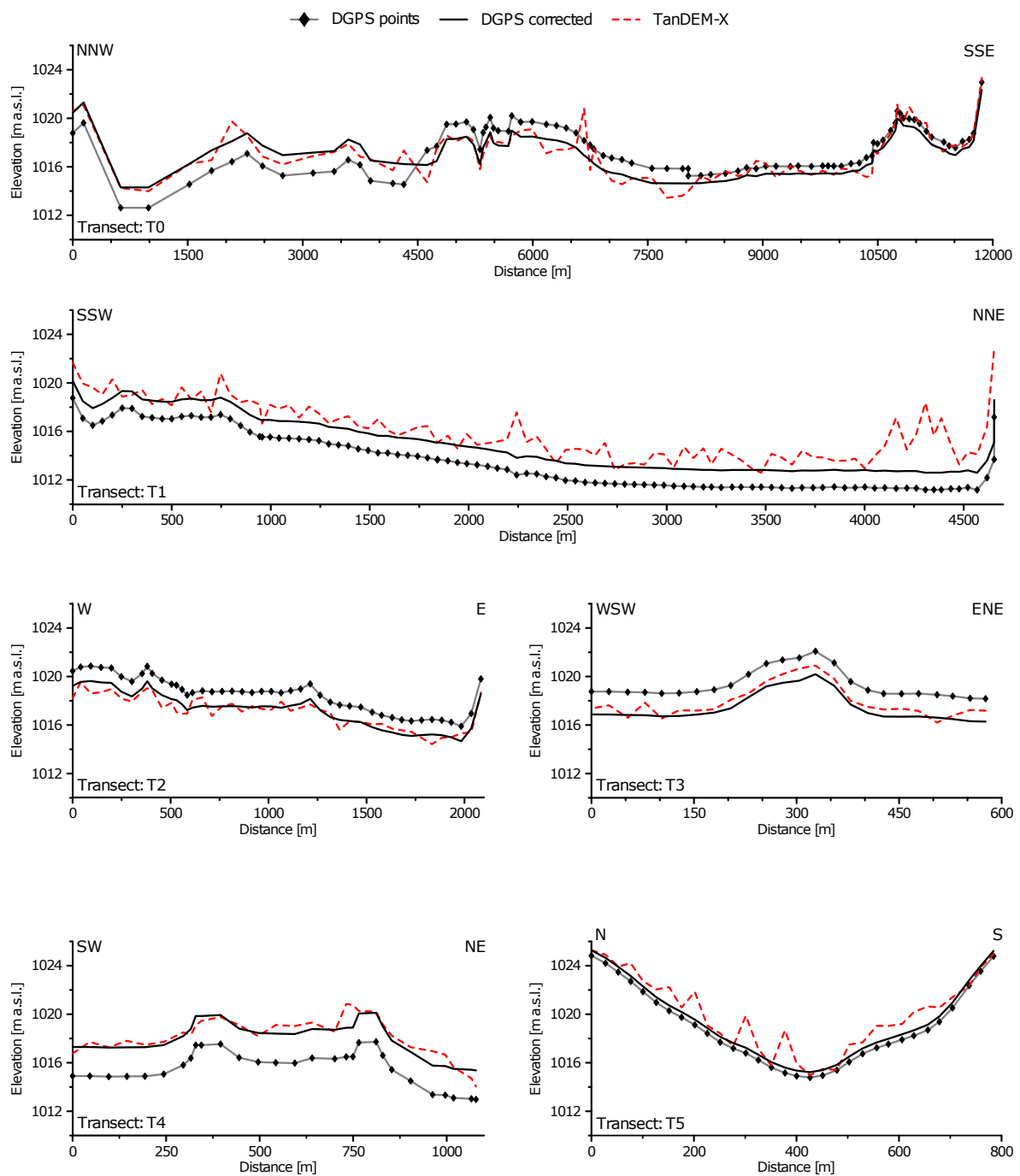
Figure 2.10: DGPS-elevation-profiles T0 to T5 (Figure 2.6) with corrected and uncorrected values in comparison with TanDEM-X data.

2.4.3 Sediment records

Lithology

In Pit N-18 (Figure 2.6), a geological profile (Figure 2.11a) from the surface to 190 cm depth exhibits predominantly cemented sand from 190 to 110 cm. From 145 to 140 cm gastropod shells were retrieved. Above this fossil bearing layer calcareous crusts and silcretes are intercalated. From 110 to 45 cm interbedding of marl and cemented sand is marked by silcrete layers. A 30 cm-sequence of light limestone follows. The sequence terminates with carbonate pebbles in a soil matrix in which gastropod shells were found.

The profile of Pit S2-18 (Figure 2.6) reached a depth of 220 cm (Figure 2.11a). The basic 30 cm are characterised by limestone containing gastropod shells, a soil sequence and marl. This marl and the 35 cm thick limestone sequence above exhibit pockets of soil. Subsequently, a few
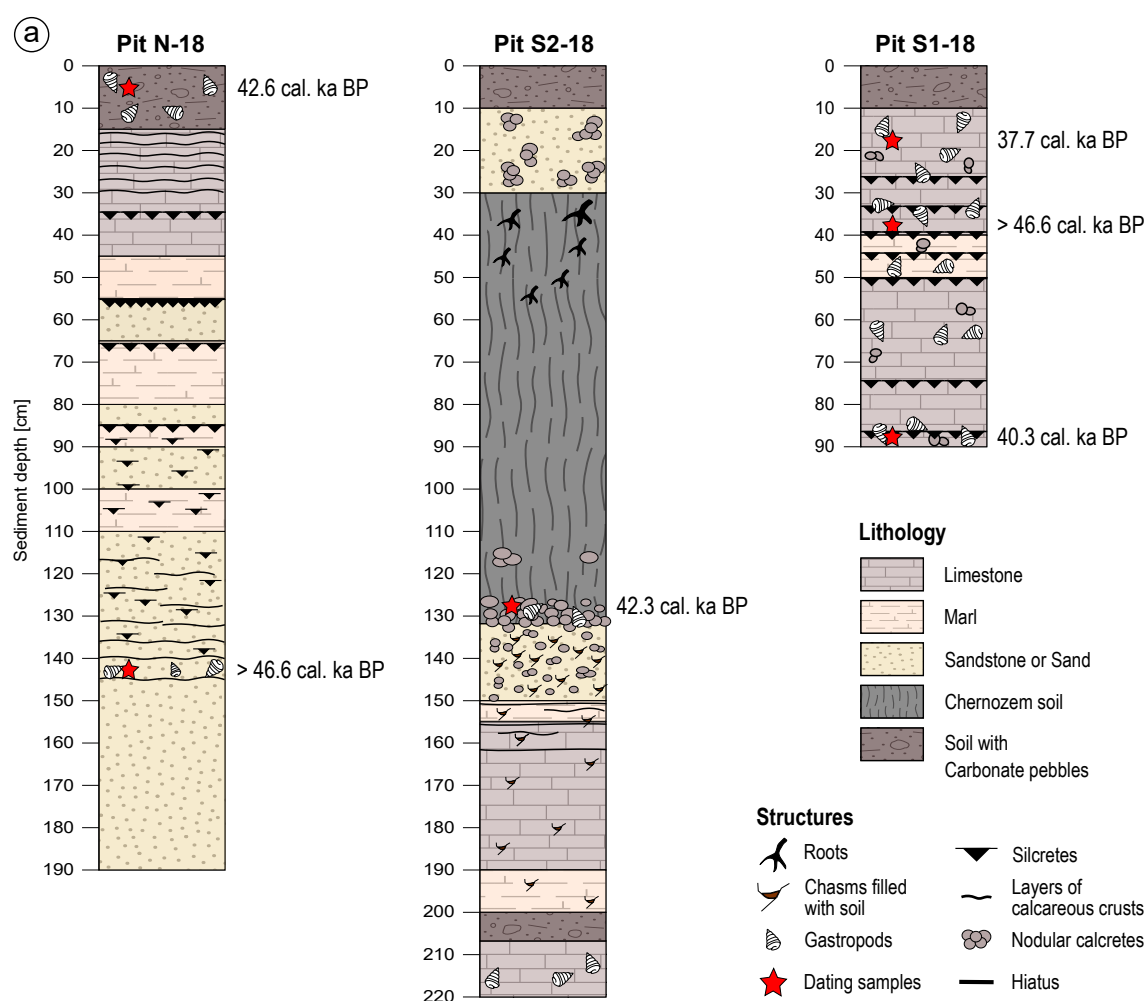
Figure 2.11: a) Lithologies and radiocarbon ages of pits N-18, S2-18 and S1-18. **b)** Lithology and selected geochemical and mineralogical properties for Pit S-15. Radiocarbon ages from Wiese et al. (2020) are marked with red asterisks.
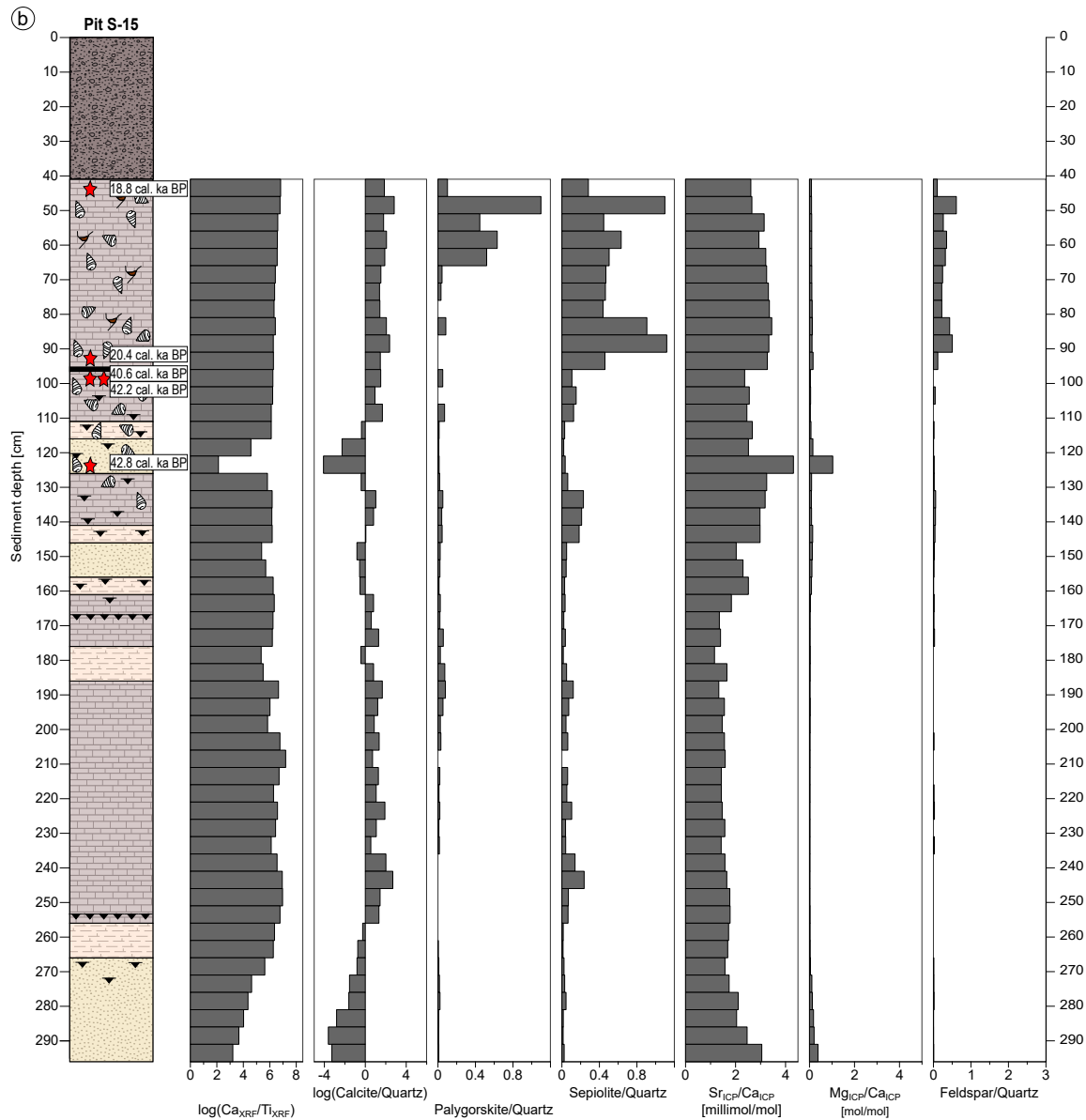
Figure 2.11: *(continued).*

centimetres of marl underlie a sandy sequence containing nodular calcretes. At the transition from that sandy facies to a ca. 1 m thick chernozem-like soil sequence, an accumulation of calcretes and carbonatic pebbles was found, with gastropod shells contained. The profile terminates with calcrete-rich sand and contemporary soil. The 90 cm-sediment profile of Pit S1-18 (Figures 2.6 and 2.11b) is characterised by 80 cm of carbonatic facies with a couple of silcrete layers intercalated and gastropod shells relatively abundant. The terminal 10 cm represents soil. The Pit S-15-record (Figure 2.6) covers 295 cm (Figure 2.11b). The basic 30 cm are composed of cemented sand, followed by 110 cm-interbedding of marl and light limestone, with two prominent silcrete layers found in the limestone. Subsequently, the facies changes from sand to marl and limestone. This pattern is repeated, with the difference that

the second limestone section is much thicker (from ca. 110 to 40 cm) and exhibits a prominent silcretic crust (at ca. 95 cm). Gastropod shells (details in Wiese et al., 2020) were found in abundance from ca. 140 to 40 cm, independent from a sandy, marly or carbonatic facies but in the latter, the abundance was particularly high. The terminal 40 cm are classified as a soil sequence.

Geochemical and mineralogical composition

In all four pits, eight minerals and mineral groups were identified from X-ray diffraction patterns: quartz, calcite, sepiolite, palygorskite, illite, albite, gypsum and leucite/potassic feldspar. The PCA of the geochemical data was reduced to PC1 and PC2, which account for 70 % of the total variance (PC1: 56 %; PC2: 14 %; Figure B.6). The variables of Al_{XRF}, Mn_{ICP}, Ca_{XRF}, TIC, Ca_{ICP}, Sr_{XRF}, Sr_{ICP} are highly correlated to each other (group 1) and negatively correlated to the variable group (2) of K_{XRF}, Fe_{ICP}, Ti_{XRF}, Fe_{XRF}, Si_{XRF}, Si_R, K_{ICP} (Figure B.6). Another group (3) of highly correlated variables is formed by $PO_{4\text{-}ICP}$, Mg_{ICP}, Na_{ICP} and TOC, which are uncorrelated to groups 1 and 2 but negatively correlated to S_{ICP}. Based on these observations, the ratios Ca/Ti, calcite/quartz, palygorskite/quartz, sepiolite/quartz, Sr/Ca, Mg/Ca and feldspar(sum)/quartz were chosen to infer sedimentological processes and are presented in Figures 2.11b and 2.12 and Figure B.7. The complete data set is compiled in Table B.6.

Chronology

The radiocarbon ages are compiled in Table 2.2. The Pit S-15-dates are from Wiese et al. (2020; red asterisks in Figure 2.11b). Three dates were obtained from Pit S1-18, one from Pit S2-18 and two from Pit N-18 (red asterisks in Figure 2.11b). One surface sample (TD18-50) from the northern sub-basin was dated as well. The ages range from 43.4 to 18.7 cal ka BP.

2.5 Discussion

2.5.1 Landscape evolution with focus on hydrological settings

The highest of the remote sensing analyses inferred palaeo-shoreline systems (Figure 2.7) implies that the maximum extension of Palaeolake Tsodilo was almost twice as large as suggested earlier (Brook, 2010). Based on the modern surface morphology, the lake reached a depth of ca. 16 m in proximity to the Tsodilo Hills and thus was much deeper than previously

assumed (e.g. see Thomas et al., 2003). Large areas further to the west, however, are considered shallow and the lacustrine environment was likely interlinked with wetlands. This assumption is extrapolated solely from the surface morphology as the sediment pits were dug in the deeper areas of the lake depressions. The satellite data suggest that during three of the four lake periods an outflow was active which terminated in the Okavango Panhandle (Figure 2.8). The bed of this palaeo-river passes the village of Tamacha (Tamatshaa in Brook, 2010) after which we name it Tamacha River (see also Tamacha Valley in Nash et al., 2006). The delta of the Tamacha River has a size similar to that of the Ncamasere River (Figure 2.8), which was reported active in historical times (Robbins et al., 1994) but in more recent times has mainly received inflow from Okavango floods (Nash et al., 1997). The Tamacha River is considered the most likely gateway of ancient people to the Tsodilo Hills. Migrating along rivers makes particularly sense in arid landscapes, and such human behaviour was e.g. suggested in respect of crossing the Sahara during 130–100 ka (Coulthard et al., 2013).

Wiese et al. (2020) identified two Palaeolake Tsodilo highstands which occurred during MIS 3b and LGM, respectively. Based on fossil gastropod communities which indicate littoral habitats under freshwater to oligohaline conditions, an active outflow was concluded (Wiese et al., 2020). Our data substantiate these conclusions. The MIS 3b-lake-highstand lasted from ca. 42.8 to ca. 37.7 cal ka BP. The older age originates from Pit S-15, which is situated in a 1–2 m higher position than the other pits (Table B.2), and thus clearly exhibits the onset of the highstand, while the termination of the lake period is only tentative. As the palaeo-lacustrine record is capped by erosion in the Pit S-15-record, the date of 37.7 cal ka BP comes from a ca. 1 m lower position indicating that the palaeolake was already regressing. Thomas et al. (2003) reconstructed lacustrine conditions during 40–32 ka using surface samples across the southern lake depression (Figure 2.3) and suggested a "rather deep" (5 7m) and permanent lake during ca. 40 ka which is in line with our results, except that we calculate the water depth a few meters deeper (Table 2.1). Shells from Pit N-18 and Pit S2-18 (Figure 2.6) were dated to ca. 43–42 cal ka BP confirming that a continuous freshwater lake spanned from off Child Hill to south of Male Hill. The different lithologies of the pits (Figure 2.11a) on the one hand reflect contrasts in erosion and soil formation and on the other hand the specific positions regarding fluvial inputs. A PCA of selected elements and chemical compounds indicates strongest differences between Pit N-18 and Pit S-15 (Figure B.6). Fluvio-lacustrine sedimentation at ca. 43–42 cal ka BP is in phase in pits S-15 and S2-18. In Pit S2-18, the subsequent lacustrine sediments must have been eroded and substituted by a chernozem-like soil, while in Pit S-15 the establishment of full lake conditions is archived and reflected by i) a higher Ca/Ti-ratio, ii) an overturn from allogenic quartz deposition to authigenic calcite precipitation, iii) increased

strontium values, which we relate with a stable lacustrine environment, iv) slightly amplified siallitic weathering of the Tsodilo rocks, indicating higher humidity, and v) significantly increased palygorskite and sepiolite precipitation (Figure 2.12). Precipitation of palygorskite and sepiolite, e.g., occurs preferably under shallow water conditions and pH values from 7.7 to 8.5 (palygorskite) and 8 to 9.5 (sepiolite), respectively (Birsoy, 2002; Galán and Pozo, 2011; Pozo and Calvo, 2018). Our data (Figures 2.12 and B.7a-c) therefore suggest that the pH varied around 8.5 throughout the lake during MIS 3b. Invading aquatic organisms from the Okavango River, which migrated via the Tamacha River to eventually reach Palaeolake Tsodilo, must have been able to cope with these slightly higher alkaline conditions. The pH of the Okavango Panhandle and Delta ranges from ca. 6.5 to 9.0 (Mmualefe and Torto, 2011).
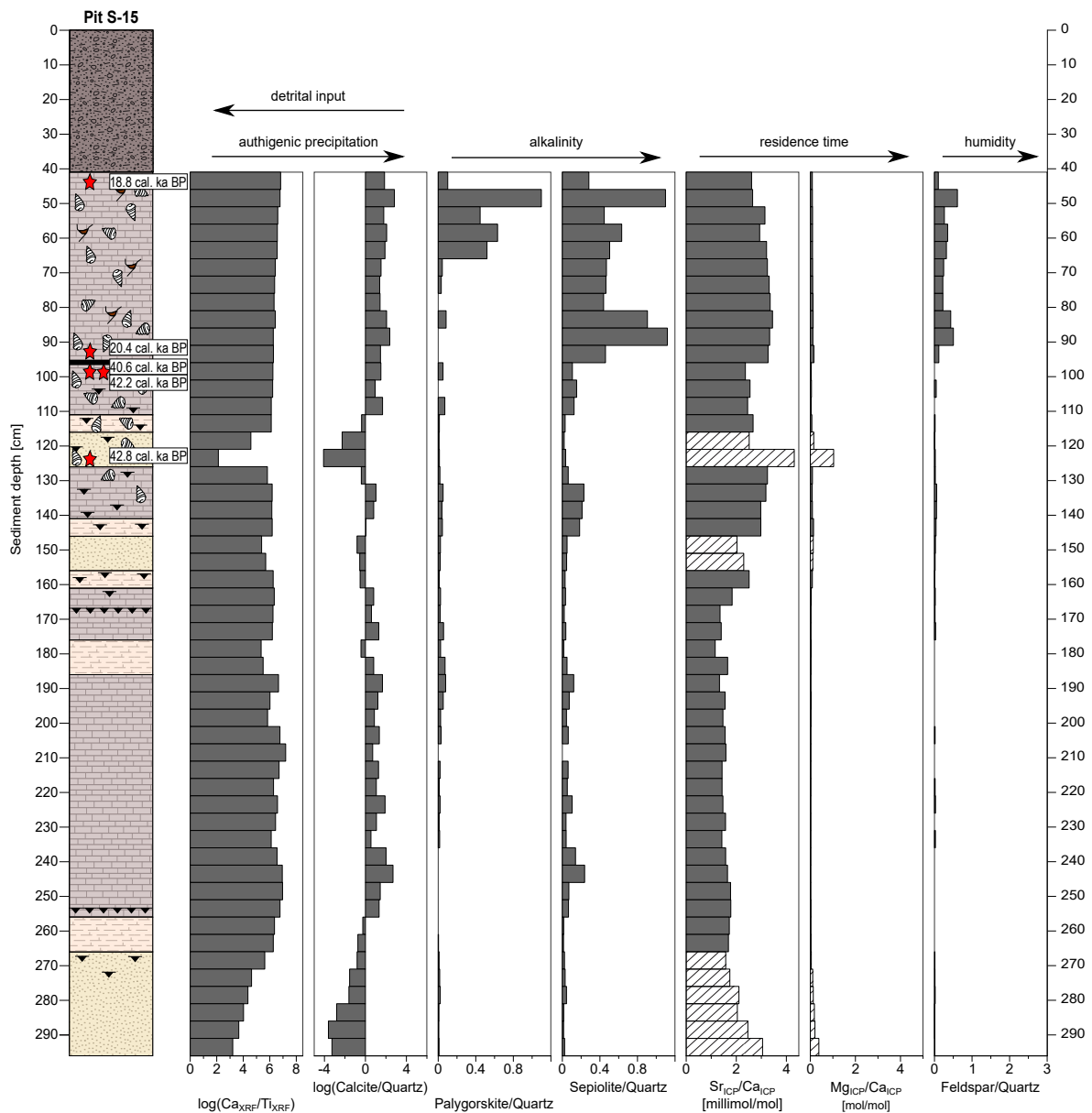
Figure 2.12: Interpretation of selected geochemical and mineralogical properties of Pit S-15-sediments. Cross-striped bars indicate values not considered for interpretation due to allogenic deposition. Corresponding graphs for other pits are provided in the supplements (Figure B.7a–c).

The LGM-highstand of Palaeolake Tsodilo is archived in Pit S-15 only (Figure 2.12). A major difference to the MIS 3b-lake is that the level was 1–2 m higher. This is mainly inferred from the fossil gastropod community (Wiese et al., 2020). Higher humidity favouring the development of an LGM-lake larger than the MIS 3b-lake is indicated by comparatively stronger siallitic weathering, which on the other hand favours precipitation of palygorskite (Singer, 1979) and thus could explain the relatively high quantities in our LGM-record. Precipitation of palygorskite became high only during the second half of the lake period while sepiolite precipitation increased strongly with the onset of the LGM-lake. The other geochemical proxies are in line (Figure 2.12). The age of ca. 27.4 cal ka BP (Table 2.2) of the surface sample from a lower position of the northern basin demonstrates that a less extended lake existed prior to the LGM-highstand. This corresponds to findings of Thomas et al. (2003).

The LGM-highstand can be related to Phase 2 of the palaeo-shoreline systems (Figure 2.7). A simulation of the palaeolake and corresponding fluvial systems is shown in Figure 2.14b. The MIS 3b-highstand relates to Phase 3 (Figure 2.7a) as outlined in Figure 2.14c. Phases 1 and 4 could not directly be identified in the records of the sediment pits. The limestone-like, solid carbonatic facies, a meter below the MIS 3b-lake-period in Pit S-15 (Figure 2.12), e.g., did not contain any fossil remains of aquatic taxa such as gastropod or ostracod shells or gyrogonites of characean algae. On the other hand, gastropod shells from Pit S1-18 and Pit N-18 were dated to >46.6 cal ka BP. Due to the stratigraphic position in Pit S1-18 (reverse age) and the sandy facies in Pit N-18, we consider both assemblages allochthon. We propose that the shells may originate from the palaeo-littoral of Phase 1 (Figure 2.7) from the higher position of which they were eroded and transported to lower areas. The western shoreline of Phase 1 is difficult to pinpoint because it is largely covered by sand. However, during Phase 1, the linear dunes framing the lake basin in the south and in the north were eroded by the lake and thus the age of the dunes may indicate the maximum age of the highstand. Thomas et al. (2003) luminescence-dated two dunes south of the palaeolake depressions (Figure 2.3) to ca. 23–107 ka. Ages increased with sample depth indicating that the upper few metres of the dunes were active until ca. LGM, but the major dune formation is older than 107 ka. Cooke (1980) assumed that the huge E–W-trending linear dune system, extending over hundreds of kilometres (see e.g. Lancaster, 1981; Chase, 2009), developed during the "late Tertiary" (see also McFarlane and Eckardt, 2007). Jahn et al. (2003) studied a sediment core from Walvis Basin and concluded strong easterlies during 1.5–0.58 Ma while afterwards the amplitude of aeolian input was much lower. We thus tentatively suggest that the formation of the linear dune pattern terminated ca. 600 ka ago. This provides a window of half a million years

during which Palaeolake Tsodilo Phase 1 had persisted for an unknown time. Following Robbins et al. (2016) that the Tsodilo Hills were inhabited by humans since at least 100 ka, an active Tamacha River may have served as a gateway during Phase 1. Schmidt et al. (2017) reconstructed a mega-lake period at ca. 100 ka in the Makgadikgadi Basin and suspected the Okwa River as the major tributary. The catchment of the Okwa River is only 400 km south of the Tsodilo Hills and thus it seems possible that climate settings of the two areas were similar.

The geophysical surveys of the sediments in the northern lake depression allows tentative identification of lake carbonates as well as geological and geomorphological structures (Figure 2.9). From observed thick sand layers on the surface and from the excavated sediments of Pit N-18, we interpret the dark blue colour in the seismic refraction tomography to indicate unsolidified sand and the bright blue colour solidified low-density carbonates or alternating deposition of unsolidified sand and solidified low-density carbonates. Down to the limit of detection, the greenish to violet colours indicate increasing solidity and density of sandy to carbonatic sediments. This corresponds roughly with the lithology of a sediment core from the southern lake basin (Linol et al., 2015; location in Figure 2.3). Weathering and erosional processes are supposedly indicated by the rugged course of the sediment layers (Figure 2.9 top). High concentration of diffraction hyperbolas in the ground penetration radargram (Figure 2.9 middle) may hint at karst formation, the local occurrence of which was directly observed in Pit S2-18. The ground penetration radargram exhibits a whitish layer just below the groundwave which levels close to the MIS 3b-carbonates. An exact assignment is not possible, however. The whitish layer in 4 m depth at distance 0 m shows a vertical offset of 1.5 m at 400 m distance, a position which corresponds well with the lineament observed on the surface (Figure 2.7). We thus consider a tectonic fault, which, however, had little or no influence on the MIS 3b- and LGM-lake-periods, but possibly on the 100 ka-highstand. This tectonic fault trends in the same direction as the major faults of the northern and central Kalahari (Shemang and Molwalefhe, 2011).

The large bow-shaped structure in the radargram, from ca. 1600 m distance (dashed orange line in Figure 2.9), corresponds to a Y-shaped positive structure (Figure 2.13). The bow-shaped structure represents a former river bed and the Y-structure is considered an inverted part of the fossil river with a bifurcation at the transition to a former alluvial fan delta. The relief inversion was triggered by accumulation of sand, likely under groundwater influence (Figure 2.13c). Such positive Y-structures have been described from certain ancient fluvial systems (e.g. Day et al., 2019). Relief inversion also occurred in channels west of the Y-structure (Figure 2.13a).
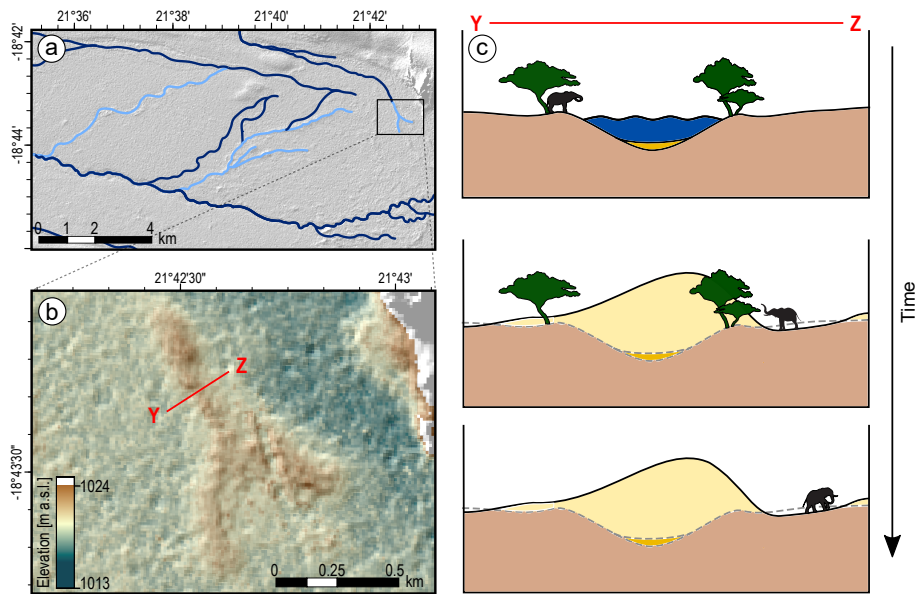
Figure 2.13: a) Inverted sections (light blue) of palaeo-river beds with focus on a Y-shaped structure. **b)** TanDEM-X image of Y-shaped positive form. Red line refers to the position of **c)** River bed inversion by accumulation.
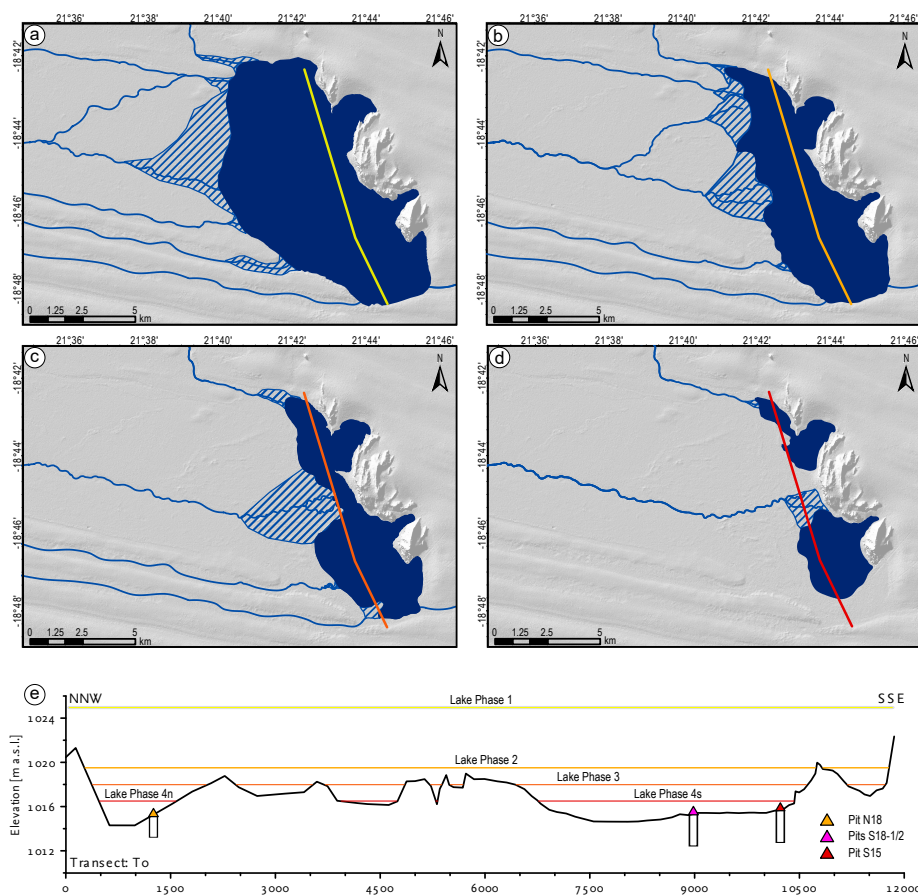
Figure 2.14: Simulation of reconstructed fluvio-lacustrine systems. Hatched areas indicate alluvial fan deltas. DGPS transect T0 indicated; different colours referring to Figure 2.14e. **a)** Hydrological setting during 100 ka. **b)** Hydrological setting during LGM. **c)** Hydrological setting during MIS 3b. **d)** Hydrological setting during an undetermined period. **e)** DGPS transect T0 in relation to settings a–d.

During Phase 4 (Figure 2.7), Palaeolake Tsodilo was separated by the progressing central alluvial fan delta into two sub-systems (Figure 2.14d). The outflow was most likely not active, leading to a higher salinity under which the gastropod communities, characteristic of the MIS 3b- and LGM-highstands, could not sustain for long. The water was not potable for ancient humans. Three of our sediment pits are within the area which Phase 4 spanned, a clear assignment of the lake stand is not possible, however. Possibly the sediments which were deposited during Phase 4 are not archived because of erosion. Alternatively, it can be assumed that Phase 4 is archived in Pit N-18 within the 45–15 cm sediments and in Pit S2-18 within the 190–155 cm sediments, both sequences older than ca. 43 ka. Interestingly, not this >43 ka-lake period exhibits feldspar influx similarly high as during LGM but the preceding sandy to marly sediment sequence, reflecting the onset of lake formation in Pit N-18. We thus assume that in this case humidity was not particularly high, but comparatively strong influx of feldspar rather derived from pluvial-fluvial resuspension of feldspar-rich pan sediments which do exist in proximity of the First Wife and Child Hills (Figure 2.7).

On the one hand, the ancient Tsodilo people lived in a highly dynamic landscape. On the other hand, lake highstands, which lasted a couple of thousand years, occurred at least two times and reflect relatively long periods of environmental stability during which a freshwater Palaeolake Tsodilo had an outflow feeding the Okavango Panhandle. During periods of lower lake levels with higher salinity, such as Phase 4, riverine inflow was still considerable and thus potable water was abundant. In contrast to the Okavango Panhandle and Delta, the Tsodilo region was tectonically rather calm. This is not only inferred from the single small fault we detected but also suggested by a lack of big boulders in the lake beds near the Tsodilo Hills. Extended dune formation rather occurred before ancient people arrived at the Tsodilos. The age of relief inversion of river bed sections is unknown. However, as some of the fossil rivers with positive relief are within the former lake basins (Figure 2.7), we tentatively consider the relief inversions (Figure 2.13) younger than 100 ka. Likely, these sand accumulations formed during dry periods when the lake beds were deflated.

2.5.2 Hunting, fishing and gathering under changing hydrological settings

A changing hydroclimate, with Palaeolake Tsodilo and Tamacha River present or absent, certainly influenced food supply for ancient Tsodilo people. Robbins et al. (2000) compiled a list of fossil mammal and reptile bones excavated at White Paintings Rock Shelter (WPS in Figures 2.3 and B.8). These remains were generally related to human palaeo-food

(Robbins et al., 2000); leopard and hyena, however, probably were not on the menu shale but indicate serious dangers for humans. Brain (1981) entitled his book about cave deposits and early humans "The hunters or the hunted?", questioning the dogma that stone age people could skilfully cope with their dangerous environments. During lake periods, e.g., elephants and lions must have been abundant at Tsodilo and thus the hills did not only provide shelter from weather hazards but also from dangerous animals which are not able to ascend the steep rocks. On the other hand, the hills were ideal watch towers for spotting either such dangerous animals or game. There can be little doubt that WPS was occupied over a hundred thousand years or so (Ivester et al., 2010) but the temporal resolution of sedimentological data (Robbins et al., 2000; Ivester et al., 2010) is too low to demonstrate permanent occupation sensu stricto. Quite some other vertebrates also use rock shelters as homing structures during absence of humans (e.g. Mentzer, 2017). Moreover, an undisturbed character of the WPS deposits is highly questionable. Staurset and Coulson (2014) pointed out that reversed dates (see Robbins et al., 2000) can be best explained by sloping deposits and post-depositional processes. Robbins et al. (2016) admitted large chronological uncertainties but found it feasible to outline general patterns of environmental change. The hunted game included wetland species such as cf. lechwe and cf. reedbuck during periods when fishing was particular important (Robbins et al., 2000).

Along this line, we suggest that radiocarbon- and OSL-dates (Feathers, 1997; Robbins et al., 2000, 2016) with improved ages based on Ivester et al. (2010) of the "Lower Fish" and "Upper Fish" deposits are uncertain enough that the MIS 3b- and LGM-lake-highstands we reconstructed can tentatively be related to them. Fish remains were basically found throughout the WPS sediment sections, however, during two sub-sections in high abundance (Robbins et al., 2000). We link the strong increase of fish consumption with an outflowing Palaeolake Tsodilo, creating the Tamacha River. Living fish could have reached the palaeolake only by upstream migration via the Tamacha River, which interconnected the lake with the Okavango (Figure 2.9). The fish fauna of the Okavango River is diverse and abundant and traditionally represents important nutrition (e.g. Merron, 1993; Mosepele et al., 2009). Robbins et al. (2000) mentioned large bivalves, possibly *Mutela*, collected from the WPS sediments. Such unionid bivalves can slowly migrate upstream as adults but fast and more commonly as larval stage attached to fish (e.g. Fryer, 1961; Graf and Cummings, 2006; Ortiz-Sepulveda et al., 2020). A detailed study of the WPS shells could show whether the abundances of fish and unionid bivalves correlate. Although fish remains are low in number before and after the "Lower and Upper Fish" deposits, they indicate that people were adapted to fishing. This baseline fish most likely originated from the Ncamasere River which could be

reached in a couple of hours when it was flowing from west to east "long ago" (orally passed indigenous knowledge in Robbins et al., 1994). Nowadays, the Ncamasere is periodically flooded by the Okavango, but only its lower reaches are affected (e.g. Nash et al., 1997).

Campbell (2010) emphasized the "wealth of edible plants" of Tsodilo. Such knowledge, however, is mainly based on oral communication with recent inhabitants but can hardly be related to ancient times (e.g. Robbins et al., 2010). For the period focused in this study (ca. 43–19 ka), only single Mongongo nuts (from the Manketti tree *Schinziophyton rautanenii*) were noted from WPS (Robbins et al., 2010) and Rhino Cave deposits (Robbins et al., 1996). This is in line with observations from other regions where Mongongo nuts were the major vegetable food, e.g., in sub-recent San camps (Yellen, 1976). It thus can only be speculated to which extent ancient humans of the Tsodilos sustained on gathering fruits. We briefly discuss, however, whether the existence of a lake and related hydroclimate favoured gathering or not. Our preliminary results confirm that vegetation in the lake beds is azonal, differing from the typical sandveld vegetation (e.g. Passarge, 1904; Brook, 2010) by higher diversity and density of shrubs and particularly trees (Figure 2.4). This is likely due to lower amounts of sand and the carbonatic duricrusts preventing quick seepage of precipitation. It is noteworthy that the arable farming of the Hambukushu, who have settled at Tsodilo since the 19th century (e.g. Giraudo, 2018), has concentrated on the southern lake depression and is perfectly delimited by the MIS 3b and LGM highstands' shorelines (Figure 2.7). The chernozem-like soil we excavated in Pit S2-18 further indicates fertility of lake depression land. Given that ancient humans also sustained on gathering fruits, Palaeolake Tsodilo significantly reduced the area where corresponding plants could grow.

2.5.3 Vector-borne diseases under changing hydrological settings

Impact of climate change on vector-borne tropical diseases (e.g. Thomson et al., 2018; Fouque and Reeder, 2019) has particularly been discussed in respect of malaria (e.g. Peterson, 2009; Tonnang et al., 2010; Endo and Eltahir, 2018; Moukam Kakmeni et al., 2018) and schistosomiasis (e.g. Yang and Bergquist, 2018; Adekiya et al., 2020) but also regarding less deadly or less common maladies such as fascioliasis (caused by liver flukes; e.g. Lu et al., 2018; Mahulu et al., 2019) and trypanosomosis (sleeping sickness; Sharma, 2001). The vectors of malaria and trypanosomosis are *Anopheles* mosquitos and *Glossina* (Tsetse) flies, respectively (e.g. Bogitsh et al., 2012). While trypanosomosis has been endemic until the 1980s along the Okavango and particularly in its delta (e.g. Sharma, 2001), malaria still prevails in northern

Botswana (e.g. Sinka et al., 2010). Malaria probably evolved in Africa (e.g. Rich et al., 1998) and possibly reached Eurasia during the out-of-Africa expansions as early as 60,000 years ago (e.g. Gelabert et al., 2017) and later eventually contributed to the fall of the Roman Empire (e.g. Soren, 2003; Sallares et al., 2004), under a climate (e.g. McCormick et al., 2012) favouring *Anopheles* habitats. Tishkoff et al. (2009) concluded that "malaria has had a major impact on humans" only since the Early Holocene, under a warmer and more humid climate. Generally, malaria incidence is correlated with rainfall and temperature (e.g. Mabaso et al., 2006; Jones et al., 2007), which define the geographic extent of *Anopheles* (e.g. Sinka et al., 2010; Gething et al., 2014). An inter-annual study in semi-arid Niger showed that a 16 % increase in rainfall led to a 132 % increase in mosquito abundance (Bomblies et al., 2008). Warm sunlit lakes and ponds provide optimal breeding habitats for *Anopheles* (e.g. Sinka et al., 2010) and Tishkoff et al. (2009) suggested that Late Stone Age settlements at lake shores could have facilitated the spread of malaria. On the other hand, Webb Jr. (2005) considered a much earlier influence of malaria on the peopling of tropical Africa. Considering the Middle to Late Stone Age people of the Tsodilo Hills, we assume that malaria, and trypanosomosis likely too, became more severe during lake periods, which sustained under increased rainfall and higher humidity, while temperature was possibly not lower than today (Wiese et al., 2020). Our hydromorphological models suggest that even during highstands extended areas of Palaeolake Tsodilo were rather shallow, exhibiting wetland character. The water temperature thus paralleled the tropical air temperature, and abundant breeding sites for *Anopheles* were provided.

Shallow vegetated areas of Palaeolake Tsodilo did also represent habitats for pulmonate gastropods such as *Bulinus*, *Biomphalaria* and *Radix* (Wiese et al., 2020). *Bulinus* and *Biomphalaria* are intermediate hosts of *Schistosoma* while *Radix* is intermediate host of *Fasciola* (Brown, 1994). Schistosomiasis has its origin in Africa and "human capture" (Despres et al., 1992) occurred earlier than Middle Stone Age (e.g. Wright, 1970; Despres et al., 1992). Based on molecular data, Crellen et al. (2016) suggested that adoption of fishing by humans triggered transmission during ca. 150–110 ka ago. Kloos and David (2002) referred to the fossil record of *Bulinus* and *Biomphalaria*, as an indicator for schistosomiasis risk in ancient human populations. Early documented evidence of schistosomiasis in Africans comes, e.g., from ancient Egyptian medical papyri (e.g. Kloos and David, 2002; Di Bella et al., 2018). In respect of public health, schistosomiasis is nowadays the most important water-based disease (e.g. Steinmann et al., 2006; Walz et al., 2015). The optimal water temperature for disease transmission ranges from 22 °C to 27 °C (e.g. Kalinda et al., 2017). African-origin *Schistosoma*, recently re-emerged in southern Europe (e.g. Ramalli et al., 2018)

demonstrating temperature tolerance, however. Transmission risk is highest under still-water conditions while in flowing water, the larvae, which emerge from the host snail, have lower chances to penetrate human skin (e.g. Secor, 2014 and references therein). A Lake Victoria study exhibited that about 40 % of the school-age children were infected (Kabatereine et al., 2011), which is a comparatively low infection rate, though (e.g. Mtethiwa et al., 2015). This might be due to the fact that a huge lake such as Victoria is more exposed to wind than a small lake or pond, and waves and currents and water mixing are generally stronger. On the other hand, rivers also often comprise stagnant water habitats where transmission risk can be similarly high as in lakes or ponds (e.g. Schwartz et al., 2005). Appleton et al. (2008) reported schistosomiasis from the Okavango Delta and Panhandle including habitats where the Tamacha River terminated. Robbins et al. (2000) noted the potential exposure of Tsodilo people to schistosomiasis. Shells of the vector *Bulinus* were extracted from the sediments of Palaeolake Tsodilo abundantly (Wiese et al., 2020; this study) and we assume that people were at high risk to get infected by *Schistosoma*. Transmission risk was highest during periods of smaller lake (pond) sizes and likely lower during lake highstands with active outflow and size-related, higher water turbulences. It is possible that the majority of ancient Tsodilo people was coinfected by schistosomiasis and malaria (see e.g. Kabatereine et al., 2011) during lake periods while a drier climate with no lake formation reduced the malaria risk significantly and schistosomiasis was even absent.

2.6 Conclusions

The Tsodilo Hills were possibly initially reached by early modern humans along the Tamacha palaeo-river, which represented the outflow of Palaeolake Tsodilo during its highstands. Three such periods were identified by remote sensing and sedimentological analyses. The highest lake level could not be dated but is tentatively related with a more humid climate in the Kalahari around 100 ka. Radiocarbon dating revealed that two of the highstands occurred during MIS 3b and LGM. A lake with no outflow existed several thousand years before and after the highstands, indicating that extended periods of higher than modern humidity existed. Possibly the periods during which a lake existed were more extended than the periods when the lake beds were dry. This could be part of the explanation why people have occupied the Tsodilo Hills since a hundred thousand years ago or even earlier. On the other hand, permanent water supply and thus game, fish and edible plants were abundant along the Okavango Panhandle and Delta. Why did groups of ancient humans leave that area? Social conflicts between populations could be one reason but we suppose that ancient

humans took particular advantage of the Tsodilo Hills as shelter from weather hazards and as a natural fortress, allowing better protection against predators and elephants. Additionally, the hills provided sheltered springs and could be used as watch towers to spot game. The area was geologically and hydrologically much calmer than the Okavango Graben with its high seismicity and periodically extreme floods. We consider the Palaeolake Tsodilo highstand periods "Garden of Eden" settings with a stable climate and game and fish in abundance. During periods with a smaller or even no lake there was still enough potable water and game, and the risk of infectious diseases even decreased when there was no standing water. The Tsodilo Hills represented a safe haven where social complexity could increase and a long-term social-ecological resilience be built up. Thus, the ancient people from the Tsodilo Hills are certainly worth consideration in the discussion when and where modern human behaviour began.

2.7 Acknowledgements

Precipitation over southern Africa: Moisture sources and isotopic composition.

This Chapter is the preprint version[1] of a manuscript submitted to the Journal of Geophysical Research: Atmospheres

Abstract

Southern Africa, with its vast arid areas, is considered vulnerable to precipitation changes and amplifying weather extremes. However, during the last 100 ka, huge lakes existed in the nowadays dry central Kalahari. It has been suggested that these lakes could have existed due to altered atmospheric circulations, leading to an increase in precipitation or to changes in the precipitation distribution. These past climate changes are recorded in palaeo-archives, yet, for a proper interpretation of palaeo-records, e.g., from sedimentological archives or fossils, a modern framework is fundamental. This study's objective is therefore, to analyse spatially differing precipitation distributions at multiple locations in southern Africa with respect to their stable water isotope composition, moisture transport pathways and sources. Five different precipitation distributions are identified by end-member modelling and respective rainfall zones are inferred, which differ significantly in their isotopic compositions. By calculating backward trajectories, different moisture source regions are identified for the rainfall zones and linked to typical circulation patterns. Our results furthermore show the importance of the seasonality, the amount effect and the travelled distance of the moisture for the general isotopic composition over the entire southern Africa. The identified pattern and relationships can be useful in the evaluation of isotope-enabled climate models for the region and are potentially of major importance for the interpretation of stable water isotope composition in palaeo-records in future research.

---

[1]Originally written in American English, edited into British English for consistency in this thesis.

3.1 Introduction

Southern Africa, with the Namib, Kalahari and Karoo, comprises vast arid areas (Figure 3.1), which, under contemporary climate change, receive specific attention due to particular vulnerability patterns (Sietz et al., 2011). These drylands are considered more prone to precipitation changes (Schlaepfer et al., 2017; Franchi et al., 2020) and amplifying weather extremes such as droughts and floods, than African landscapes with a humid climate (IPCC, 2021). This is not unambiguous, as it has been discussed controversially whether changes in observed daily precipitation (frequency, intensity, total) over Africa are significant at all (Hulme et al., 2001; Nicholson et al., 2018; Otto et al., 2018; Contractor et al., 2021).

While the Namib is a true desert, Kalahari and Karoo are home to considerable human populations (Nel et al., 2011; Walker et al., 2018), predominantly in small towns and villages. Flowing through the Karoo and the southern Kalahari Figure 3.1, the Orange represents the major southern African exogenous river, creating a green strip across the drylands and playing an important role for bulk water supply (Department of Water Affairs, South Africa, 2013).
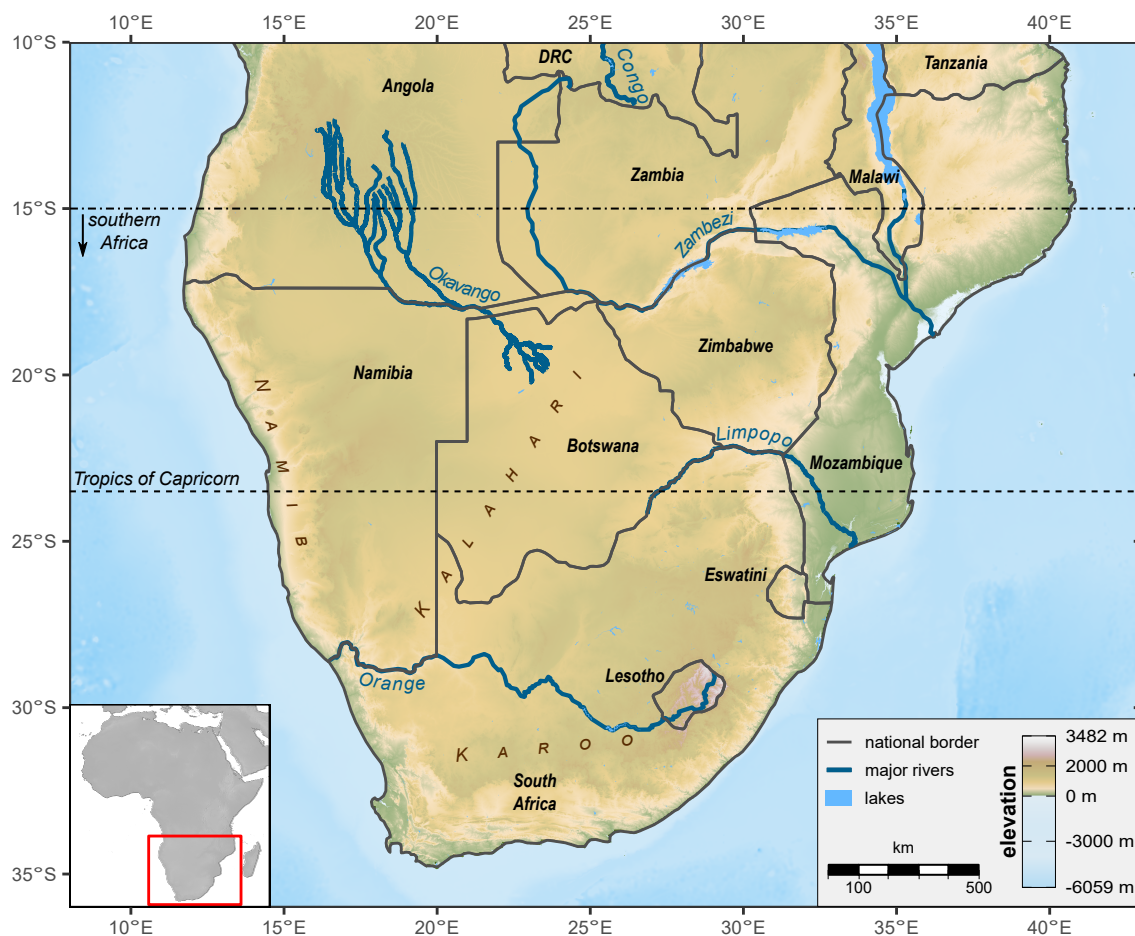
Figure 3.1: Digital elevation (GMTED; Danielson and Gesch, 2011) and bathymetry map (ETOPO1; Amante and Eakins, 2009; NOAA National Geophysical Data Center, 2009) of southern Africa (here south of 15°S) showing the drylands and major rivers.

Its active catchment lies in the highlands of Lesotho (Senqu river system) where two large water reservoirs were built (another one is currently under construction), acting as "water towers" for South Africa (World Bank Group, 2016). Supposedly water-rich Lesotho, however, was recently hit by severe droughts (Blamey et al., 2018) which led to an acute food crisis eventually triggering rural-urban migration (World Food Programme, 2021). Water (and food) security represents a notable and increasing problem in large parts of southern Africa and its growing human populations ((Muller et al., 2009; Department of Environmental Affairs, 2013).

In the drylands, access to potable water has been progressively secured by groundwater abstraction including supply for farmland and livestock (Cooke, 1985; Duraiappah and Perkins, 1999; Walker et al., 2018). Livestock is a major economic factor in the grassy drylands of the Kalahari and the Karoo, but also in the semi-humid highlands of Lesotho, and a good example of the limitations of adaptation strategies under climate change (Nhemachena and Hassan, 2007). Studies have shown that rainfall intensity and seasonality dominate over animal grazing intensity in determining the productivity of the grasslands (du Toit et al., 2018).

In historical times, livestock has been a traditional livelihood all over southern Africa (Sadr, 2015) and past climate change supposedly triggered large scale human migration (McLeman, 2014) although this view has recently been questioned (Hannaford, 2020). The pre-historic dispersal of ancient modern humans is commonly related to climate change too (Blome et al., 2012; Timmermann and Friedrich, 2016) and hunters and gatherers appeared in southern Africa not later than a hundred thousand years ago (Henshilwood et al., 2011; Robbins et al., 2016). It was suggested that out-of-Africa migration started in southern Africa and was triggered by a more humid climate opening gateways to East Africa (Rito et al., 2019).

On the other hand, ancient people occupied certain sites such as the Tsodilo Hills in the northern Kalahari over tens of thousands of years (Robbins et al., 2010) indicating that access to water and food was sustainable over long periods. Geppert et al. (2021) reconstructed the palaeo-hydrological setting of the Tsodilo site with multiple lake phases and concluded that periods with higher precipitation/lower evaporation were more extended than previously assumed (Thomas et al., 2003). In the nowadays dry central Kalahari, huge lakes existed repeatedly during the last 100 ka (Burrough et al., 2009a; Riedel et al., 2014; Schmidt et al., 2017). Geppert et al. (2021) emphasized that, beside climate, tectonic processes may have played a major role, particularly by the redirection of river systems (Riedel et al., 2014).

The past substantial climate changes are reflected in the landscape by palaeo-river beds, lake basins and their palaeo-shorelines (Burrough et al., 2009a; Riedel et al., 2014) and dunes (Chase, 2009), and are archived in sediments (Wiese et al., 2020; Geppert et al., 2021; Hahn et al., 2021) and speleothems (Holmgren et al., 2003; Chase et al., 2021). Regarding the last centuries, trees (Huffman and Woodborne, 2016; de Mil et al., 2021) archive climate signals in high resolution and narrative evidence interlinks with synoptical data (Nicholson et al., 2018; Nash et al., 2021).

Against this background, a considerable number of studies have focused on short- and long-term climate variability for a better understanding of past climate changes (Hart et al., 2013; Zhang et al., 2015; Chevalier and Chase, 2016; Dieppois et al., 2016) and on projections of future climate scenarios (Mayaud et al., 2017; Dunning et al., 2018; Maúre et al., 2018; Howard and Washington, 2020), eventually providing essential information on which political decisions can be based (Department of Environmental Affairs, 2017). The spatio-temporal behaviour of the ITCZ, the tropical rain belt, received particular attention for explaining major past and potential future precipitation changes over Africa (Collins et al., 2011; Schneider et al., 2014; Mamalakis et al., 2021).

Southward migration or extension of the ITCZ has been related with intensified austral summer precipitation over the Kalahari and subsequent development of vast lakes in the structural basins of the Kalahari (Burrough et al., 2009b). On the other hand, the behaviour of the southern Westerlies plays a major role in the regional climate system too (Perren et al., 2020; Figure 3.2). A northward shift of the Westerlies would enhance winter precipitation over large parts of southern Africa (Chase and Meadows, 2007) and development of ponds and lakes in the pans and basins of the Kalahari during the Last Glacial Maximum were associated with it (Riedel et al., 2014; Schüller et al., 2018).

Naturally, observational precipitation data from southern Africa are much more comprehensive than proxy data inferred from palaeo-archives and interlinking these research avenues remains an enormous challenge. Identifying moisture sources and trajectories and to assess their relevance for precipitation variability over southern Africa (Hewitson et al., 2004; Gimeno et al., 2020; Leketa and Abiye, 2020; Rapolaki et al., 2020) represents a possible bridge between the present and the past, in particular, via the analysis of stable water isotopes (Bowen et al., 2018; Wanke et al., 2018; Munksgaard et al., 2019).

Wiese et al. (2020) provided sclerochronological stable isotope patterns from Kalahari fossil lacustrine shells in a sub-monthly resolution, discussed past seasonality changes and speculated about the moisture sources. A modern framework of moisture sources, transport

pathways and sinks, and related isotope variations is considered fundamental to properly interpret the palaeo-records. Lagrangian diagnostics (Pfahl and Wernli, 2008; Nieto and Gimeno, 2019) is regarded as "a powerful tool" (Diekmann et al., 2021) to address such a framework.

The aim of our study is therefore to contribute to the identification of moisture sources, transport pathways and associated precipitation patterns at multiple locations in southern Africa for which δ^{18}O- and δ^2H-data are available or have been collected in the framework of this study. We want to test whether significant spatial differences in precipitation distributions are in phase with differences in the isotopic composition. Such relationships may subsequently be applied for the interpretation of palaeo-records. We attempt to go a step towards the integration of data sets with the possible evaluation of isotope-enabled climate models.

3.2 Contemporary climate setting

Southern Africa is influenced by both tropical and mid-latitude circulation systems (Figure 3.2; Tyson and Preston-Whyte, 2000) and thus the controls on climate variability are rather complex (Reason et al., 2006). The major climate features are the seasonally migrating Intertropical Convergence Zone (ITCZ) and the Congo Air Boundary (CAB), as well as the El Niño-Southern Oscillation (ENSO) (Gasse et al., 2008; Dieppois et al., 2016; Howard and Washington, 2019). The interplay of these systems triggers austral summer precipitation over most of southern Africa. The Botswana High interlinks with the South Indian Ocean Anticyclone (Figure 3.2; Miyasaka and Nakamura, 2010; Cherchi et al., 2018; Xulu et al., 2020), controlling the migration of so-called tropical-temperate troughs (TTT) over southern Africa. The TTTs originate from the South Indian Convergence Zone (Cook, 2000) and are visible as cloud bands in satellite images (Macron et al., 2014). During austral summer, the TTTs add significantly to the rainfall amount over southern Africa (Todd and Washington, 1999; Washington and Todd, 1999). The strength of the Botswana High is considered to be in phase with ENSO being stronger during low phases (El Niño) of the Southern Oscillation and weaker during high phases (La Niña) (Driver and Reason, 2017; Reason, 2019). During El Niño, the TTTs are shifted east of the continent which then generally leads to droughts over southern Africa (Tyson and Preston-Whyte, 2000). La Niña on the other hand leads to above-normal rainfall due to the shifting of the TTTs back above the continent (Tyson and Preston-Whyte, 2000). The drought pattern, however, is not fully understood yet. During a couple of El Niño events droughts over southern Africa did not materialize (Driver et al.,
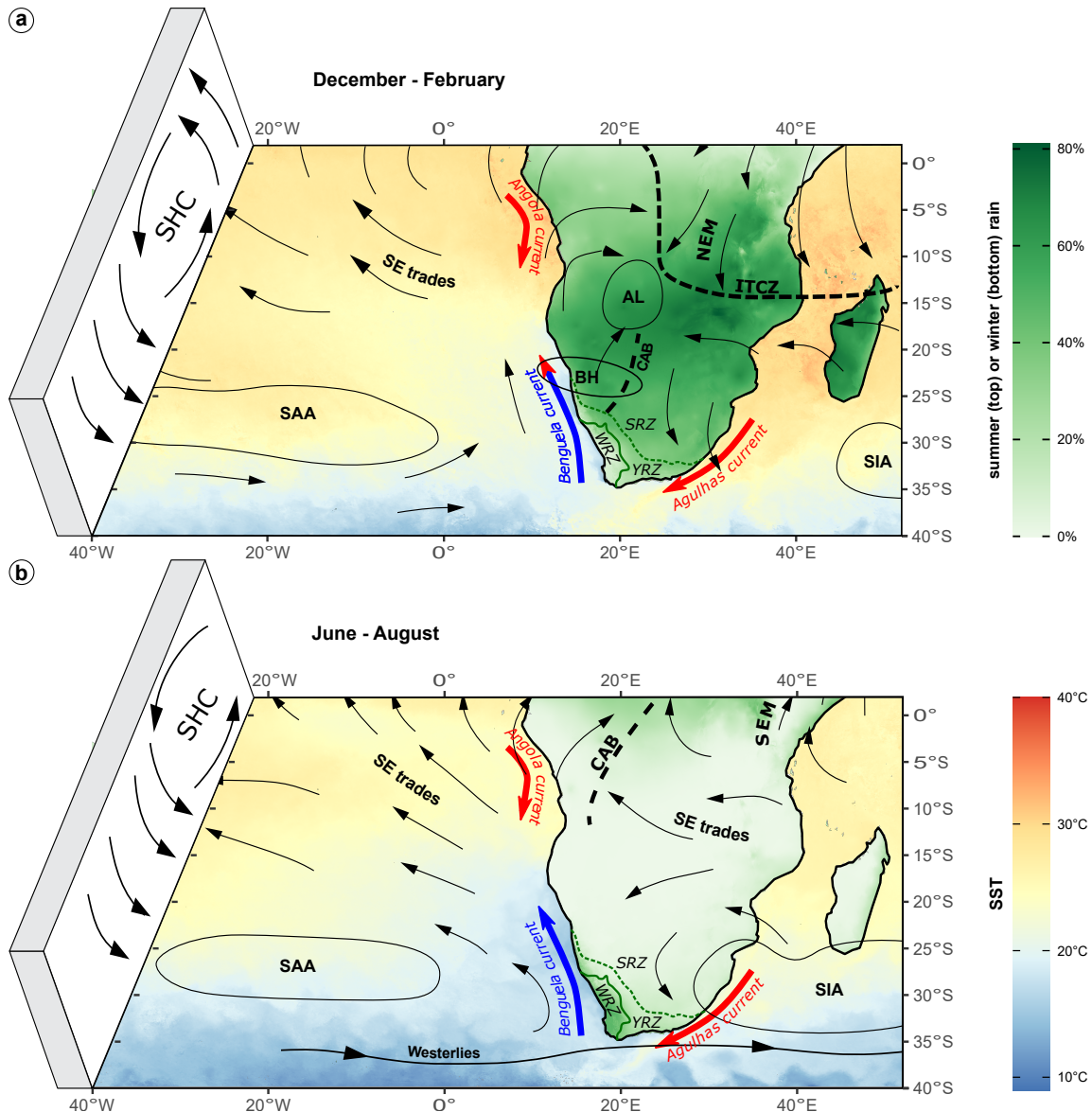
Figure 3.2: Some aspects of the present-day African climate during the **a)** austral summer and **b)** austral winter (after Nicholson, 1996; Gasse et al., 2008; Driver and Reason, 2017). The sea surface temperatures (SST) are shown for July and January 2020 (Data Source: NASA/JPL, 2020). Seasonality of continental precipitation is shown by percentage of annual precipitation of the summer (DJF) and winter (JJA) months (Data source: Fick and Hijmans, 2017) and the rainfall regimes over southern Africa (Chase and Meadows, 2007) are indicated by green (solid + dashed) lines: winter rainfall zone (WRZ); year-round rainfall zone (YRZ); summer rainfall zone (SRZ). Low-level wind and pressure patterns: Angola heat low (AL), Botswana High (BH), Congo Air Boundary (CAB), Intertropical Convergence Zone (ITCZ), northerly East African monsoon (NEM), South Atlantic Anticyclone (SAA), southerly East African monsoon (SEM), South Indian Anticyclone (SIA). In section: southern Hadley Cell (SHC). Oceanic surface currents are indicated by temperature: warm (red arrow) and cold (blue arrow).

2019; Pascale et al., 2019). It has been controversially discussed whether the Angola Low modulates the summer rainfall and eventually prevents drought conditions during certain El Niño events (Lyon and Mason, 2007; Pascale et al., 2019). Yet, the role of the Angola Low, e.g., for moisture transport from the Southern Atlantic is understudied, while the role of the Botswana High is better understood (Reason, 2019).

Total summer precipitation over southern Africa decreases from north to south into the southern Kalahari, and from east to west across the continent (Hewitson et al., 2004; Jury, 2012; Conway et al., 2015), from annually ca. 1.300 mm in central Mozambique (Silva and Matyas, 2014) to less than 50 mm in the Namib Desert (Figure 3.3a; Mendelsohn et al., 2002). The aridity of southern Africa is primarily caused by the descending dry air of the southern Hadley Circulation (Lu and Vecchi, 2015), but the Namib is also controlled by the cold Benguela Current and the upwelling along the coast of southwestern Africa (van Zinderen Bakker, 1975). On the other hand, the precipitation over the eastern coast of southern Africa (and beyond) is enhanced by moisture from the warm Agulhas Current (Reason, 2001; Nkwinkwa Njouodo et al., 2018). A fraction of the moisture of this summer precipitation, penetrating inland from the east, originates in the Southern Ocean and the Southern Atlantic, however (Leketa and Abiye, 2020; Rapolaki et al., 2020).

Austral winter precipitation is controlled by the southern Westerlies and falls predominantly in westernmost South Africa and to a smaller amount along the southern coast of South Africa (Chevalier and Chase, 2016). The influence of the Antarctic Oscillation on the austral winter precipitation is under discussion (Pohl et al., 2010).

Except for the transitional areas between summer and winter rainfall, and the southern coast of South Africa, seasonality is pronounced, with a stable dual pattern of wet and dry season (Tyson and Preston-Whyte, 2000; Chevalier and Chase, 2016). The Köppen-Geiger classification reflects this very well (Figure 3.3b; Peel et al., 2007; Engelbrecht and Engelbrecht, 2016).
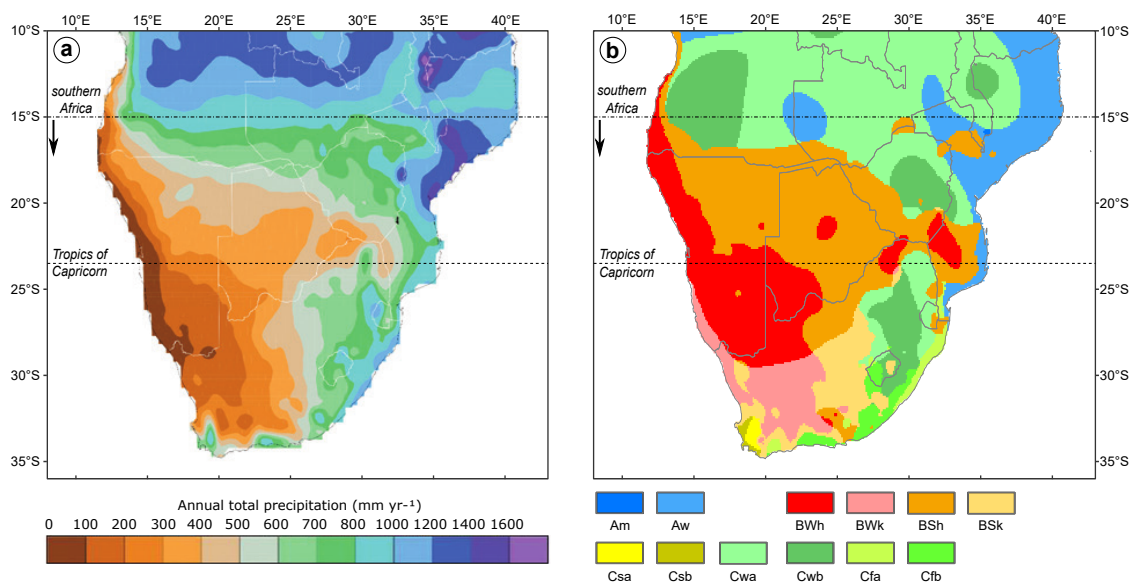
Figure 3.3: a) Average annual total precipitation (1961–1990) over southern Africa (modified from Conway et al., 2015) and **b)** Köppen-Geiger climate types in southern Africa (modified from Peel et al., 2007).

3.3 Material and methods

3.3.1 Precipitation distribution groups and seasonality

To determine different groups of annual precipitation distributions (PDs) in southern Africa, defined for purposes of this study as Africa south of 15°S, monthly precipitation data (in mm) from WorldClim 2.1 (Fick and Hijmans, 2017) was analysed using an end-member modelling algorithm. The identification of distinct annual precipitation patterns and their spatial distribution allows us to frame basic differences in precipitation regimes. The precipitation data was downloaded from http://worldclim.org, and represents average monthly climate data for the period 1970–2000. To reduce computing times, a spatial resolution of 10 minutes ($\sim$340 km^2 resulting in 25,881 points) was chosen for the classification.

The precipitation data set's underlying main PDs were unmixed and their contribution to the data set was determined using an end-member modelling approach by Dietze et al. (2012) with the R package EMMAgeo (Dietze and Dietze, 2019). On the one hand, a high goodness of fit (r^2) for variables and samples is wanted but on the other hand, the interpretation should be kept as simple as possible (Weltje, 1997). This suggests the choice of a model with high coefficients of determination (R^2) but a low number of end-members (EMs). After these considerations, a robust 3-EM model was identified as best choice.

For a differentiated consideration of the results according to the seasonality of precipitation, after prior examination of the different identified PD groups, at each location the months of the year were classified into three categories: precipitation season, off-season, and transition times (both, from season to off-season and from off-season to season). While months of the precipitation season are defined by >10 % of annual precipitation (P$_a$), off-season months have <5 % P$_a$ and months during the transition times have 5–10 % P$_a$.

3.3.2 Water samples and stable isotope analysis

Our compiled database includes 852 monthly samples (composites from the total precipitation during one calendar month) during the period 1958–2013 of the 8 GNIP (Global Network for Isotopes in Precipitation, IAEA/WMO, 2021) stations in southern Africa (Figure 3.4 and Table C.1) and 232 self-collected water samples (50 precipitation, 166 rivers, 9 lakes, 6 springs, 1 ocean) across southern Africa (Figure 3.4), collected during the period 2016–2021.

The self-collected samples were analysed for stable isotope ratios of oxygen (^{18}O/^{16}O) and hydrogen (^{2}H/^{1}H) using a PICARRO L1102-i isotope analyser, which is based on the

WS-CRDS (wavelength-scanned cavity ring down spectroscopy) technique (Gupta et al., 2009). Calibration of the measurements was done by linear regression with the standard calibration materials VSMOW (Vienna Standard Mean Ocean Water), SLAP (Standard Light Antarctic Precipitation) and GISP (Greenland Ice Sheet Precipitation) from the IAEA. The ratios are expressed in the conventional delta notation (δ^{18}O, δ^2H) in per mil (‰) relative to VSMOW as defined by Craig (1961b) and Gonfiantini (1978). A total of six replicate injections were performed for each sample and arithmetic average and standard deviations (1 sigma) were calculated, resulting in a reproducibility of the replicate measurements of generally better than 0.1‰ for oxygen and 0.5‰ for hydrogen. Values for the second-order isotope parameter deuterium excess (d-excess) for both datasets were calculated using the formula d $= \delta^2$H $- 8\,\delta^{18}$O (Dansgaard, 1964).

For further analysis, only samples with values for both δ^{18}O and δ^2H of a month/site were used. Samples from the same location and day were combined and their means used in the statistical analysis. As the respective precipitation amounts are unknown, normal means were used instead of the usually preferred amount weighted means.
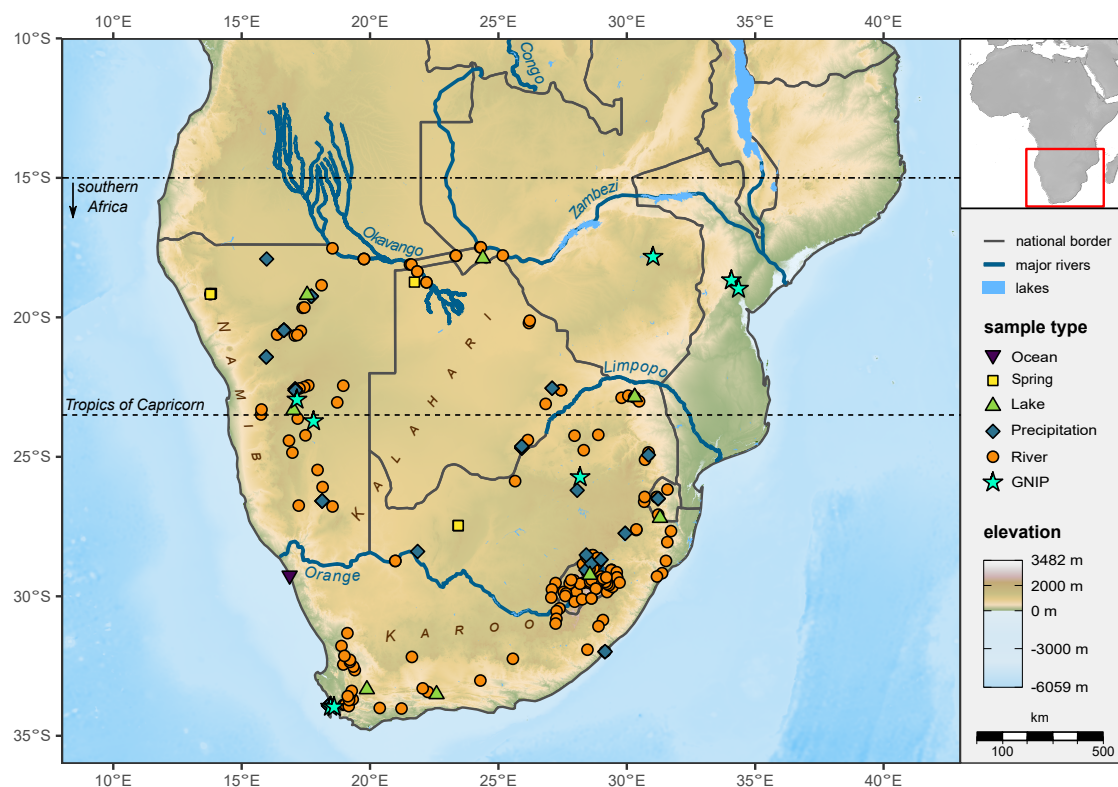
Figure 3.4: Digital elevation (GMTED; Danielson and Gesch, 2011) and bathymetry map (ETOPO1; Amante and Eakins, 2009; NOAA National Geophysical Data Center, 2009) of southern Africa showing the 8 GNIP stations used in this study and the sampling locations, colour-coded by type.

To test for significance of differences among the isotopic compositions of the different PD groups and among their precipitation seasonality, an ANOVA (Analysis of Variance) with Post Hoc Tukey HSD test (Tukey, 1949) was used in R (R Core Team, 2019).

3.3.3 Lagrangian moisture source diagnostic

To identify and compare the moisture sources of the collected water samples around southern Africa, backward trajectories were calculated with the LAGRANTO model (Wernli and Davies, 1997; Sprenger and Wernli, 2015), using the European Centre for Medium-Range Weather Forecasts (ECMWF's) latest three-dimensional reanalysis, ERA-5 (Hersbach et al., 2020) wind fields (u, v, w), available hourly with a horizontal grid spacing of 31 km on 137 vertical levels from the surface up to 0.01 hPa. Backward trajectories were calculated, starting at the specific sampling locations and at 18 different pressure levels (1013.25 hPa, and from 1000 hPa to 200 hPa in steps of 50 hPa). Depending on the type of water sample, multiple back-trajectories were calculated for different timespans: precipitation: 1 d, streamlet: 7 d, upper river: 14 d, middle river: 21 d, lower river or lake: 28 d (for sake of computation time) and started every 3 h for the 1 d and 7 d timespans, and every 6 h for 14 d and greater timespans (to reduce computation time). The springs and ocean samples were excluded for the trajectory analysis. Thus, a total, of 203 different target locations and times were used. Additionally, to analyse differences over time at one place, the station at Pretoria (South Africa) was chosen, as it has comparably few gaps in the dataset. For the period from 1996 to 2001, every 6 h, backward trajectories were calculated from the GNIP station location, based on pre-processed ERA-5 data with a grid spacing of 0.5°.

All trajectories were calculated 10 days (240 h) backward in time and specific humidity, among other variables, was recorded along the trajectories for each 1 h interval. The trajectory length of 10 days was chosen as maximum timescale on which integrity of the traced air parcel can be assumed (Pfahl and Wernli, 2008) and, according to analysis of Nieto and Gimeno (2019) also seems to be an appropriate integration time for the region of southern Africa. Trajectories for our collected samples were calculated inside the box of the coordinates 30.0°W, 70.0°E, 50.0°S, 10.0°N, as the fraction of moisture sources outside this box is minimal ($<2\%$ for GNIP-Pretoria).

To identify evaporative moisture sources along the trajectories, a method for moisture source attribution after Sodemann et al. (2008) was used. A moisture uptake is attributed to surface evaporation along the trajectory if it occurs within the atmospheric boundary layer. We also used the scaling factor of 1.5 for the boundary layer height (BLH), which was recommended

by Sodemann et al. (2008), because the BLH tends to be underestimated by models (Zeng et al., 2004). Furthermore, only those trajectories exceeding a relative humidity threshold of 80 % at the location of sample collection are selected for the analysis, as it is assumed that clouds are then existent, and precipitation is likely to occur.

For statistical analysis, the evaporation locations along each trajectory were weighted by their contribution to the precipitation of that specific trajectory at the target location. The trajectories for each target location were then weighted by their contribution to the cumulated precipitation at the specific target location. The contribution of each trajectory was measured by its negative change in specific humidity $-d$q in the last time step, with only trajectories with dq < 0 taken into account (Sodemann et al., 2008). Finally, for every traced variable, a weighted mean value over the identified source regions was calculated for further statistical analysis.

To analyse whether the land cover at the source locations shows an impact on the isotopic composition of the precipitation, land cover classes along the trajectories were extracted from the Global Land Cover 2000 database (GLC, 2003; resolution: 1 km at the equator). In order to analyse the continental isotope effect, the shortest path distance to the coast was calculated in ArcGIS Pro (ESRI, 2018). Additionally, we used the approach of Walter and Lieth (1960) to define humid and arid months, where arid months are defined as those with the monthly precipitation P in mm representing less than twice the average monthly temperature T_a in degrees Celsius (i.e., P $<$ 2T_a) and where months are classified as humid when the precipitation exceeds two times the average temperature (P $>$ 2T_a). This classification was also based on the WorldClim 2.1 Climate Data of monthly precipitation (mm) and additionally the average near-surface temperature (°C) with a spatial resolution of 30 seconds ($\sim$1 km^2).

For exploration of the relationships between the measured isotope values and diagnosed water vapour source conditions, Pearson correlation coefficients and linear regression models were determined, assuming Gaussian distributions for all variables. Here, only samples were used for which moisture uptakes below the BLH have been attributed for more than 60 % of the final precipitation (Ra $>$ 0.6), to get reliable statements about the relationship between isotope ratios and moisture source conditions, which is only possible if sources can be detected for the greater part of the precipitation (Pfahl and Wernli, 2008).

To assess the relative importance of meteorological variables for the stable isotope data, we applied the machine learning Random Forest (RF) regression algorithm, using the *cforest()* function of the R Package party (Hothorn et al., 2006; Strobl et al., 2007, 2008). This

function was chosen, because our predictor variables are of different types, and so the options to construct unbiased RF and to calculate the variable importance following the permutation principle could be used. As some of the predictor variables are furthermore highly correlated, the conditional importance was applied. Again, if the sample size allowed it, only samples with Ra > 0.6 were analysed. To ensure stable variable importance, after trial of different numbers, a large number of trees ($ntree = 10,000$) has been set (Behnamian et al., 2017). With this approach, at least the top five variables showed a stable ranking over multiple model-runs. Furthermore, the number of variables per level for the chosen number of trees was optimized by tuning in terms of out-of-back (OOB) -RMSE. The RF analysis represents an objective way to choose covariate setting for multiple regression in order to gain maximum multiple regression information and in contrast to the regression analysis, RF also allows including categorial variables for the importance analysis.

3.4 Results

3.4.1 Precipitation distribution groups

The unmixing of the PDs resulted in a model with 3 robust EM (spatial distribution in Figure C.1) explaining 64 % (mean $R^2 = 0.64$ between the original and modelled data) of the data variance (Figure C.2).

Based on this 3-EM model, five different PDs were identified for southern Africa which are clustering in space and match the spatial distribution of percent summer precipitation over southern Africa (in Figure 3.2). The corresponding inferred rainfall zones (RFZs) have been named according to their main precipitation season and location (Figure 3.5):

a summer rainfall zone in the western part (SRZw = EM1),

a summer rainfall zone in the eastern part (SRZe = EM3),

a mixed summer rainfall zone (SRZm) at the intersection of SRZw and SRZe,

a winter rainfall zone (WRZ = EM2),

and a year-round rainfall zone (YRZ) at the intersections of SRZw and/or SRZe with WRZ.

The assignment (cf. decision tree in Figure C.3) of the raster points to each RFZ is shown in Figure 3.5a. The average PD for each RFZ (Figure 3.5 b1-b5) was determined by the mean monthly precipitation amount relative to the annual precipitation. In the SRZw, YRZ and WRZ, during March there is a remarkably high variation in the precipitation fraction, which

is caused by outliers from the western and southern part of Namibia. The PDs of the RFZs differ in their general distribution as summarized in Table 3.1.

Table 3.1: Characteristics of the mean annual precipitation distributions from the five rainfall zones as shown in Figure 3.5 b1–b5. Note that for the YRZ there is no precipitation seasonality, and the precipitation fraction of the annual precipitation (P_a) is listed in transition time.

		SRZw	SRZm	SRZe	YRZ	WRZ
	mean P_a [mm] (95 % range)	564 (54–1287)	469 (209–902)	706 (360–1054)	305 (35.6–942)	234 (21–672)
prec. season	distribution	unimodal	unimodal	unimodal	multimodal	unimodal
	duration [months]	3–4	4–6	5–6	—	4–5
	during	Dec.–Mar.	Nov.–Mar.	Oct.– Mar.	—	Apr.–Aug.
off-season / transition	duration [months]	3–5	3–5	3–5	—	3–5
	during	May–Sep.	May–Sep.	May–Sep.	—	Sep.–Mar.
	prec. fraction of P_a per month [%]	< 1–2	< 2–3	< 5	5–14	< 5–10
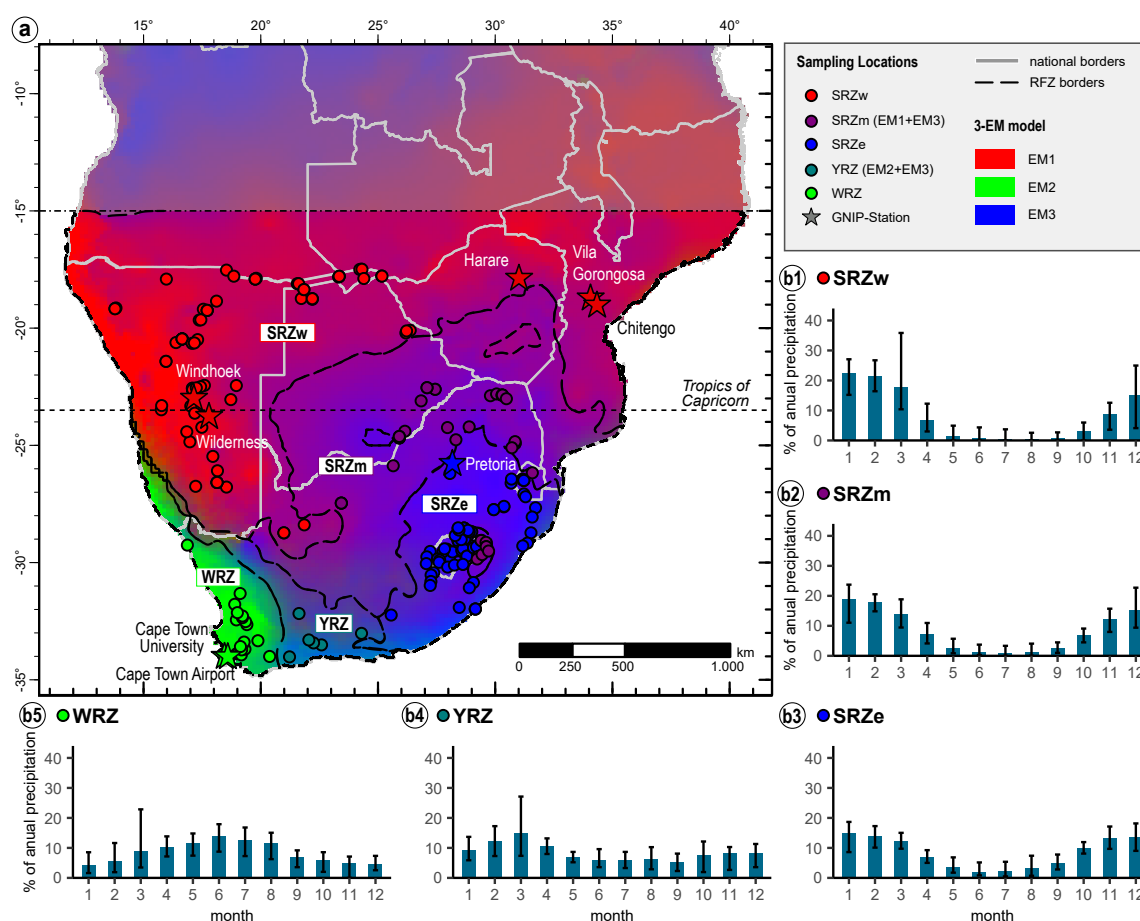
Figure 3.5: a) Map of southern Africa (south of 15°S) showing the spatial distribution of the five identified rainfall zones (RFZs). The RFZs resulted from the three end-member model, presented as base map where end-members (EM) 1–3 are shown in red, green, and blue. The sampling points are colour-coded by the affiliation to the respective RFZ. **b1-5)** Mean distribution of the precipitation over the year for the five identified RFZs. The 2.5th and 97.5th percentiles (error bars) show the ranges within the respective RFZ in southern Africa.

3.4.2 Stable water isotopes

The isotopic data of our water samples are shown in Figure 3.6 plotted against the global meteoric water line (GMWL: $\delta^2\mathrm{H} = (8.17 \pm 0.06)\,\delta^{18}\mathrm{O} + (10.35 \pm 0.65)$ with $\mathrm{r}^2 = 0.99$; Craig, 1961a, refined by Rozanski et al., 1993) and African meteoric water line (AMWL: $\delta^2\mathrm{H} = 7.4\,\delta^{18}\mathrm{O} + 10.1$; Durowoju et al., 2019) to illustrate the deviation from the lines. The $\delta^{18}\mathrm{O}$ and $\delta^2\mathrm{H}$ values vary from -15.56 to $7.09\,\permil$ and from -115.98 to $-40.18\,\permil$ respectively. D-excess ranges from 28.32 to $19.57\,\permil$.

The resulting regression lines are $\delta^2\mathrm{H} = (7.2 \pm 0.1)\,\delta^{18}\mathrm{O} + (5.8 \pm 0.6)$ for all collected samples and $\delta^2\mathrm{H} = (7.3 \pm 0.1)\,\delta^{18}\mathrm{O} + (7.5 \pm 1)$ for precipitation samples only, with a higher intercept, but a similar slope. This indicates a shift of precipitation samples in direction of higher $\delta^2\mathrm{H}$ and/or lower $\delta^{18}\mathrm{O}$ values in relation to all samples.

Most of our collected samples plot roughly along the GMWL and AMWL and are within the range of the samples of the 8 GNIP stations from southern Africa (long term statistics in Table C.2). Samples that plot below are mainly from lakes or the larger rivers (Figure 3.6). There are also quite a few precipitation samples from the GNIP dataset in the top right quadrant of the plot that deviate stronger from the GMWL. These are mostly precipitation samples from the WRZ during the off season of precipitation (Figure C.4).
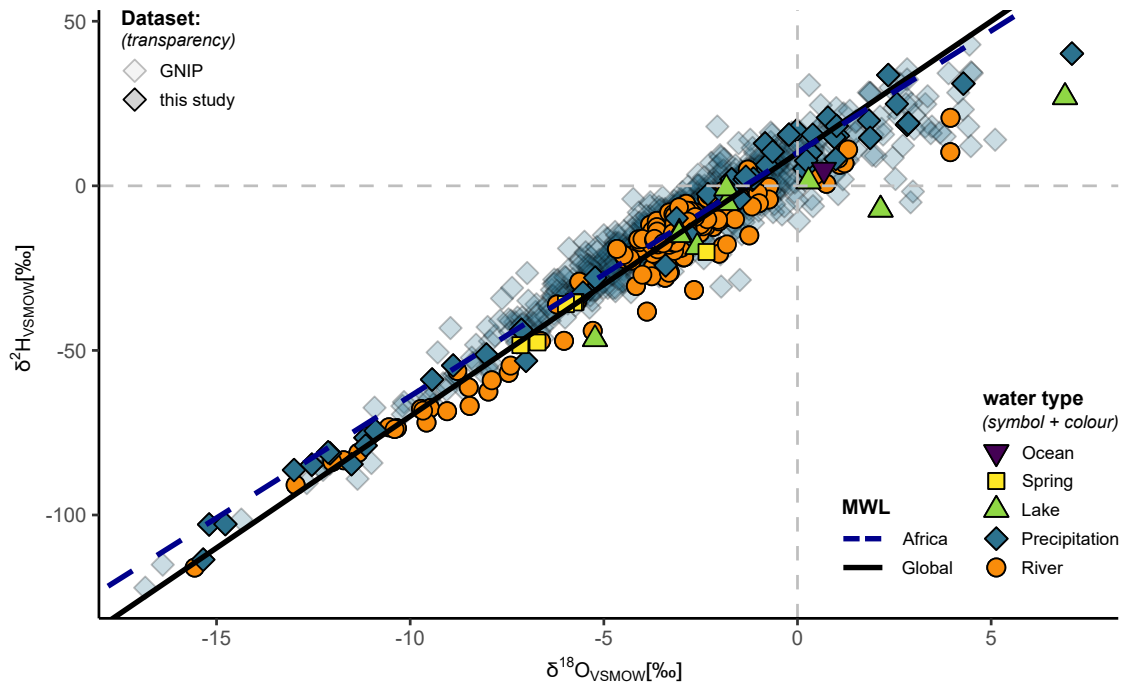
Figure 3.6: Correlation of $\delta^{18}\mathrm{O}$ and $\delta^2\mathrm{H}$ of the analysed water samples showing the deviation from the Global and African meteoric water lines (MWL). Samples are colour-coded by water type and different transparencies used for the two datasets. Please not that ocean and spring samples were excluded from the analysis and are just shown for completeness.

The following analysis regarding the isotopic compositions of the RFZs could only be done for the SRZw, SRZe and WRZ. The YRZ and SRZm, needed to be excluded from the statistical analysis, due to insufficient samples size. There are no GNIP stations in these regions and also none (YRZ) or only a few (SRZm; n = 6) of the collected precipitation samples belonged to these groups.

A comparison of the $\delta^{18}O$ frequency distributions of the precipitation samples from the RFZs shows that these obviously differ in median and variation (Figure 3.7a). SRZw differs from SRZe and WRZ and shows a comparably greater range and lower mean. Within the RFZ, there are also differences among the precipitation seasons (season, off-season, and transition times; Figure 3.7b). In the SRZ region, the isotopic ranges are slightly greater during the precipitation season compared to the off-season or transition times, while in the WRZ, the off-season samples show a greater range than the transition times or seasonal samples.

This general picture is supported by ANOVA and Post Hoc Tukey test concerning the $\delta^{18}O$ means (with 95 % family-wise confidence level). The $\delta^{18}O$ group mean of SRZw differs significantly from the means of the SRZe and WRZ (Table C.3) and in all three RFZs the $\delta^{18}O$ values of seasonal rainfall differ significantly compared to off-season rainfall (Table C.4). Additionally, in the SRZw the season and transition times differ significantly, while in the
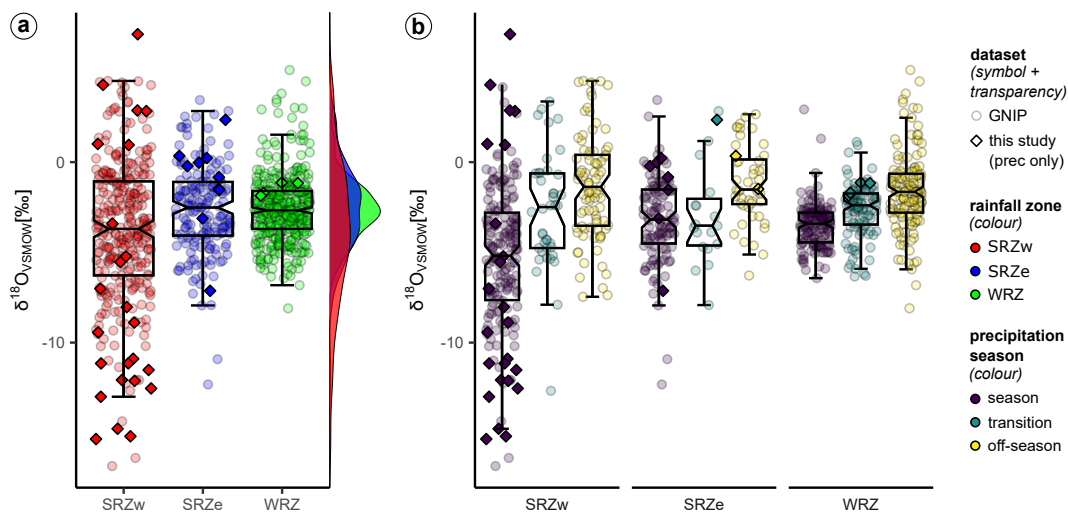
Figure 3.7: a) Boxplots and density plots displaying the stacked ranges of the $\delta^{18}O$ values of the precipitation samples from the RFZs. The SRZm and YRZ were excluded from the analysis, due to their small sample sizes ($n_{(SRZm)} = 6$ and $n_{(YRZ)} = 0$). **b)** Boxplots displaying the $\delta^{18}O$ values of the different precipitation seasons within these three RFZs showing the differences in ranges and medians. Samples are colour-coded by RFZ (left) or precipitation season (right) and different transparencies used for the two datasets. In the boxplots, the bottom and top edges of the box indicate the 25th and 75th percentiles of the (sub-)dataset, respectively and the central horizontal line represents the median. The whiskers extend to 1.5 times the interquartile range, while data beyond the end of the whiskers can be treated as outliers. The width of the notches indicates a 95 % confidence interval around the medians. Thus, if the notches do not overlap this indicates a group difference with 95 % confidence related to the median.
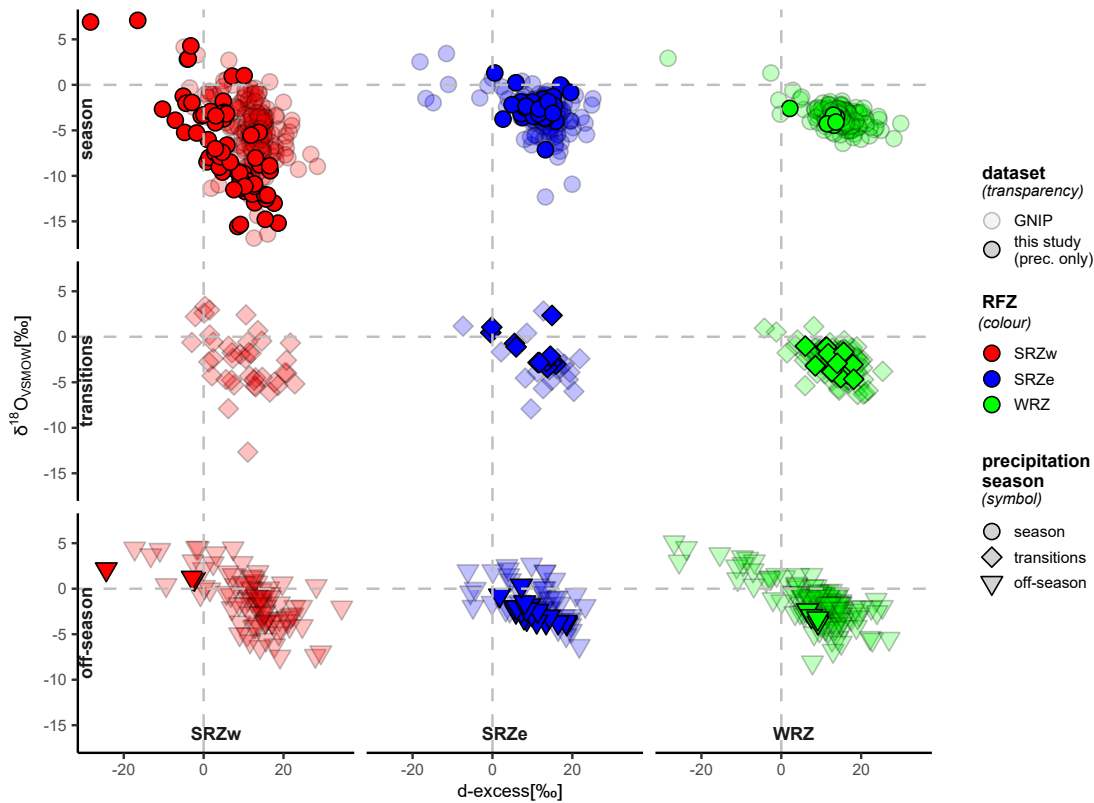
Figure 3.8: Facetted scatterplots of $\delta^{18}O$ plotted against d-excess for the GNIP and collected precipitation samples, facetted after RFZ and precipitation seasonality. Samples are colour-coded by RFZ, and different symbols were used for the precipitation seasons as well as different transparencies for the two datasets. The SRZm and YRZ needed to be excluded from the analysis, due to their small sample sizes ($n_{(SRZm)} = 6$ and $n_{(YRZ)} = 0$).

SRZe the off-season and the transition times are significantly different. In the WRZ, the $\delta^{18}O$ means are significantly different for all seasons (two-sided with $p < 5\%$).

Figure 3.8 shows the varying signature in d-excess among the precipitation samples from the three analysed RFZs for the different precipitation seasons in order to assess the potential impact of moisture source conditions. A dynamic d-excess in water samples might indicate moisture of different sources, for example from a warmer ocean versus a cooler ocean or colder high latitudes (Leketa et al., 2018). However, the ranges of the d-excess values among the RFZs and among the precipitation seasons do not differ significantly, except for samples from the WRZ during off-season, which are most scattered.

3.4.3 Moisture sources

The identified moisture sources for the different RFZs during the precipitation season are shown in Figure 3.9, and the proportions from the different areas are compiled in Table 3.2. Moisture source areas for off-season and the transition times as well as respective information

Table 3.2: Proportion of moisture uptake above main source regions for the SRZw, SRZe, SRZm and WRZ during precipitation season (months with $> 10\,\%\ P_a$). YRZ is not included, due to an insufficient number of samples. The African continent is furthermore subdivided into regions south of 15°S (southern Africa) and further north. Madagascar was merged with continental Africa because the contribution was very small ($< 0.4\,\%$).

source regions	SRZw	SRZe	SRZm	WRZ
South Atlantic Ocean	3.8 %	3.7 %	2.5 %	93.2 %
Indian Ocean	5.1 %	35.0 %	30.7 %	3.6 %
Mozambique Channel	3.2 %	4.4 %	14.7 %	0.2 %
Arabian Sea	0.1 %	0.001 %	0.3 %	-
continental Africa + Madagascar	87.8 %	56.9 %	51.9 %	3.0 %
north of 15°S	27.7 %	0.3 %	5.7 %	0.001 %
south of 15°S (southern Africa)	60.1 %	56.6 %	46.3 %	3.0 %
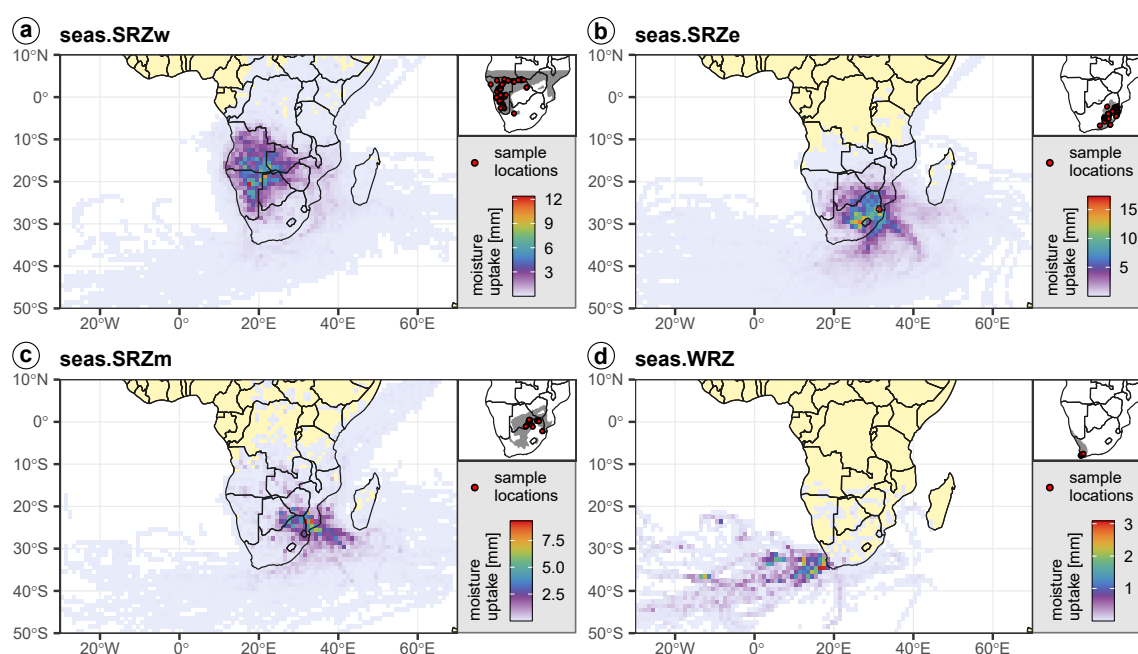
Figure 3.9: Moisture source regions for the samples from the different RFZ (a-d) during the precipitation season (months with $> 10\,\%\ P_a$). The figures show the amount of moisture uptake in mm that contributed to the final precipitation at the sampling locations. **a)** SRZw, **b)** SRZe, **c)** SRZm, **d)** WRZ. YRZ is not shown, due to insufficient number of samples (n=1) during months with $> 10\,\%\ P_a$.

about the proportions from the different sources are given in the Supplements (Figures C.5 and C.6 and Table C.5).

The SRZw (Figure 3.9a) is the region with the highest moisture uptake above the continent (87.5 %) during the precipitation season, mainly above northern Namibia (22 %), northern Botswana (11.4 %), southern Angola (25.6 %) and southern Zambia (11.6 %). The transport pattern shows three main directions: from the Atlantic Ocean with the low and mid-level westerlies mainly along the southern and western coast of Africa, with the low-level south-

easterly trade winds from the Indian Ocean south of Madagascar (Agulhas Current) and with the mid-level north-easterly trade winds from above the Congo basin.

The main moisture uptake during the precipitation season for the SRZe (Figure 3.9b) is located over the continent (56.6 %), mainly above eastern South Africa, and over the Indian Ocean (35.0 %). The majority of the trajectories come from the Atlantic Ocean with the low and mid-level westerlies along the southern and eastern coast of Africa, but there are also a few coming with the low-level south-easterly trade winds from the Indian Ocean south of Madagascar.

For the SRZm (Figure 3.9c), the main moisture uptake during the precipitation season is located over the south-eastern continent (> 50 %) above northern South Africa, eastern Botswana, and southern Zimbabwe & Mozambique as well as over the Indian Ocean (30.7 %) and the Mozambique Channel (14.7 %) near the eastern coast of Africa. The majority of the trajectories come from the Atlantic Ocean with the low and mid-level westerlies along the southern and western coast of Africa, but there are also quite a few coming from the Indian Ocean with the low-level south-easterly trade winds and the northerly east African monsoon along the eastern coast.

In the WRZ (Figure 3.9d) the main moisture uptake during the precipitation season origins from over the South Atlantic Ocean (> 90 %) west of South Africa. The main transport pattern is with the low-level westerlies from the Atlantic Ocean. For the YRZ, there is just one sample for this subgroup (here: precipitation season = months with > 10 % of P_a), thus this RFZ was not analysed as results would not have been representative.

In summary, during the precipitation season, the SRZw has the main moisture source region above the north-western region of southern Africa, while the SRZe and SRZm have their main moisture sources above the eastern region of southern Africa and additionally from the Indian Ocean near the western coast south of Madagascar. The WRZ has almost all the moisture sources from the Atlantic Ocean.

To additionally analyse differences between the precipitation seasons at one place, moisture source regions have been determined for the precipitation at Pretoria for a period of five years. The main moisture source regions (southeastern continental Africa and Indian Ocean) and transport ways (westerlies along the southern and eastern coast of Africa) are similar within the three precipitation seasons, however, during the main precipitation season, there are also trajectories coming from the northern Indian Ocean along the east African coast (Figure C.7). These results match with the source regions and transport pathways identified from the "spatial dataset" for SRZe (Figure 3.9; Figures C.5 and C.6). The main uptake

Table 3.3: Proportions of moisture uptake during the three precipitation seasons above main moisture source areas for the GNIP station at Pretoria. The African continent is subdivided into regions south of 15°S (southern Africa) and further north. Madagascar was merged with continental Africa because the contribution was very small ($< 1.9\,\%$). Other regions here are the Arabian Sea, the Southern Ocean, the South Pacific Ocean, Antarctica, and South America.

source regions	seas	trans	off
South Atlantic Ocean	2.1 %	3.3 %	3.9 %
Indian Ocean	26.0 %	36.5 %	22.7 %
Mozambique Channel	9.0 %	7.9 %	11.1 %
continental Africa + Madagascar	62.7 %	61.5 %	53.1 %
north of 15°S	7.6 %	7.6 %	0.9 %
south of 15°S (southern Africa)	55.1 %	53.9 %	52.2 %
other regions	0.2 %	0.1 %	0.05 %

above the African continent is concentrated on the southern part of southern Africa (south of 15°S) for all three precipitation seasons and is lowest during the transition times, while the uptake above the Indian Ocean is highest during these times (Table 3.3). The proportion of oceanic and continental uptake is similar for the precipitation season and the off-season. However, during the precipitation season, the uptake above southern Africa is a bit higher compared to the off-season, as is the uptake above the Indian Ocean.

3.4.4 Conditions at moisture source and during transport

Various variables were recorded along the backward trajectories to assess whether these have an impact on the final isotopic composition. Correlation and simple linear regression analysis were used to explore the statistical relationships between the measured isotope values and these variables of the diagnosed moisture source and sink conditions. Here, we laid special focus on the variables representing the isotope effects described by Dansgaard (1964): latitude effect, altitude effect, continental effect, amount effect, and seasonal effect. The results of the analysis are shown in Table 3.4 and Table 3.5.

For our collected samples, analyses show the importance of the amount effect and the travelled distance of the moisture. A multivariate regression with precipitation amount and travelled distance as independent variables showed a multiple R^2 of 0.63 (adjusted $R^2 = 0.58$; p-value = 0.00063) for $\delta^{18}O$, and for δ^2H a multiple R^2 of 0.54 (adjusted $R^2 = 0.48$; p-value = 0.0028). For the GNIP dataset, analyses also showed traces of the amount and the travelled distance of the moisture. A multivariate regression with precipitation amount and travelled distance as independent variables showed a multiple R^2 of 0.33 (adjusted $R^2 = 0.27$; p-value = 0.012) for $\delta^{18}O$, and for δ^2H a multiple R^2 of 0.32 (adjusted $R^2 = 0.25$; p-value = 0.015).

Table 3.4: Summary of regression parameters of selected variables, representing the isotope effects, on the collected precipitation samples (with Ra > 0.6). Variables are values at the target location (sink = Snk), weighted mean values of the trajectories at the target location (wmSnk) or the difference between the weighted mean source value and the value at the target location (wmSrc to Snk).

Isotope effect	Variable	R^2 (δ^{18}O)		R^2 (δ^2H)	
latitude effect	latitude (Snk)	(+) 0.03		(+) 0.001	
temperature effect	temperature (wmSnk)	(−) 0.03		(−) 0.03	
elevation effect	elevation (Snk)	(+) 0.00		(−) 0.01	
amount effect	total precipitation (Snk)	(−) 0.29	*	(−) 0.25	*
continental effect	distance to coast (Snk)	(+) 0.08		(+) 0.04	
	travelled time (wmSrc to Snk)	(+) 0.28	*	(+) 0.36	**
	travelled distance (wmSrc to Snk)	(−) 0.43	**	(−) 0.38	**

signif. codes: 0.001 '**'; 0.01 '*'; ≥0.1 ' '

Table 3.5: Summary of regression parameters of selected variables, representing the isotope effects, of the GNIP-Pretoria dataset (with Ra > 0.6). Variables are values at the target location (sink = Snk), weighted mean values of the trajectories at the target location (wmSnk) or the difference between the weighted mean source value and the value at the target location (wmSrc to Snk). Latitude and elevation effect were not considered, as there is only one sampling location.

Isotope effect	Variable	R^2 (δ^{18}O)		R^2 (δ^2H)	
temperature effect	temperature (wmSnk)	(−) 0.001		(−) 0.01	
amount effect	total precipitation (Snk)	(−) 0.29	**	(−) 0.31	**
continental effect	travelled time (wmSrc to Snk)	(+) 0.10		(+) 0.08	
	travelled distance (wmSrc to Snk)	(−) 0.22	*	(−) 0.15	*

signif. codes: 0.001 '**'; 0.01 '*'; ≥0.1 ' '

For our collected samples, including samples of all analysed water types (with Ra > 0.6; n = 117), the top 10 importance scores of the variables for the prediction of δ^{18}O, δ^2H, and d-excess are shown in Figure 3.10 (top plots: a-c). It was not possible to analyse a subset of only the precipitation samples due to the small sample size (n = 30 or $n_{(Ra>0.6)}$ = 18) of the subset. In all three models, the RFZ of sampling was among the most important variables. For the δ^{18}O and δ^2H models, also among the most important variables were the main water type (precipitation, river, lake) and the month of the sampling. Furthermore, for δ^{18}O and δ^2H, the top variable in the importance ranking had a score about 30–50 % higher than the second most important variable.

For the GNIP station at Pretoria (n = 50), the top 10 importance scores of the variables for the prediction of δ^{18}O, δ^2H, and d-excess are shown in Figure 3.10 (bottom plots: d-f). It was not possible to analyse a subset of only the samples with Ra > 0.6 due to the small sample size ($n_{(Ra>0.6)}$ = 25) of the subset.

spatial analysis (collected water samples, with Ra>0.6)
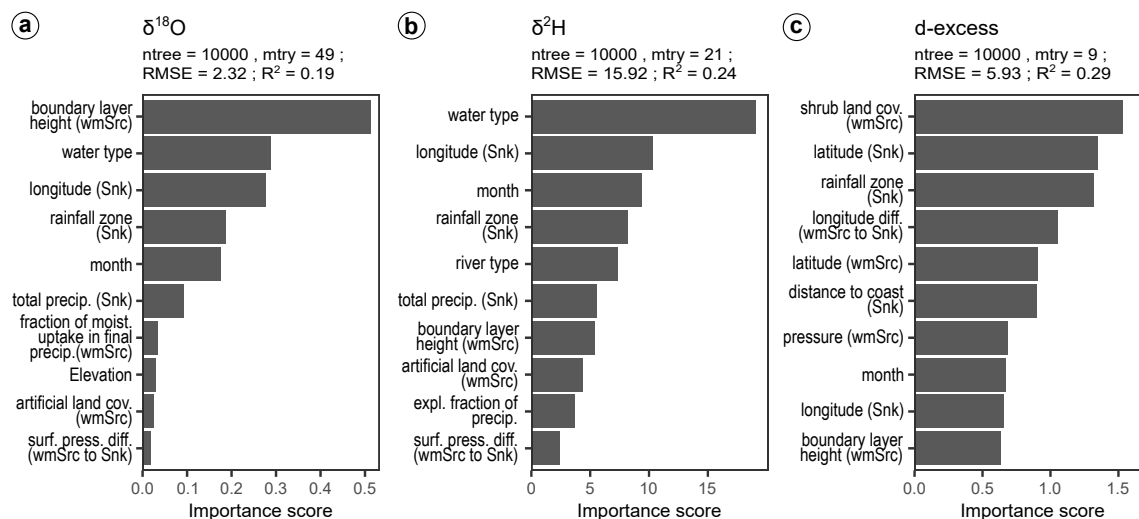
temporal analysis (GNIP Pretoria samples)
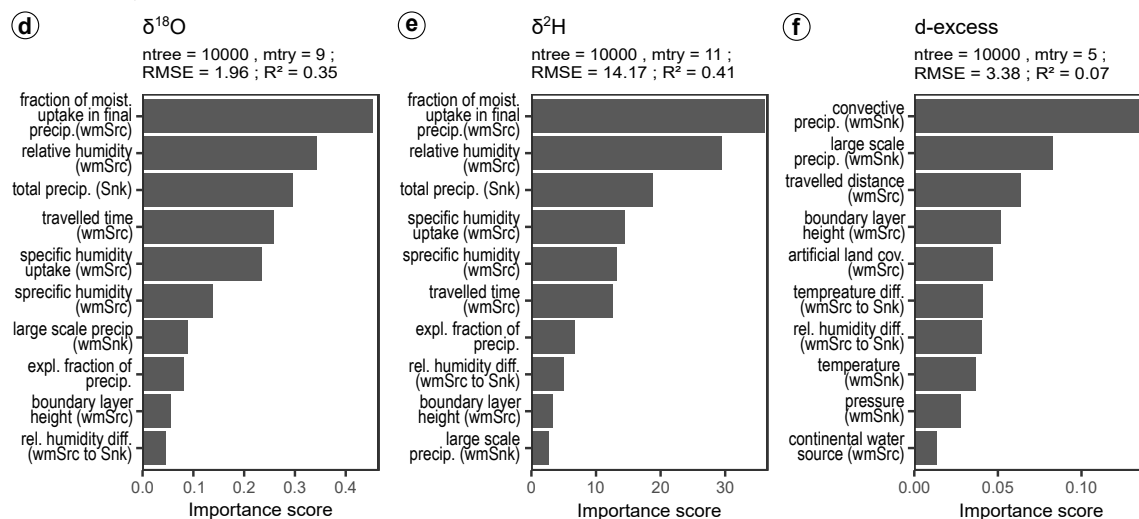
Figure 3.10: Top (a-c): Random Forest top 10 variable importance to predict δ^{18}O, δ^{2}H, and d-excess for the collected water samples (with Ra > 0.6; n = 117). **Bottom (d-f)**: Random Forest top 10 variable importance to predict δ^{18}O, δ^{2}H, and d-excess for the GNIP Pretoria dataset (n = 50). Note that the absolute values of the scores should not be interpreted (Strobl et al., 2009). Snk = sink (sample location); wmSnk = weighted mean values at sink; wmSrc = weighted mean values at source locations. Detailed meaning of the variables is given in Table C.6.

For δ^{18}O and δ^{2}H, the models show almost the same top 10 variables with only some variation in the order of importance, however, the top three have the same ranking. The most important variable in these two models is the weighted mean fraction of moisture uptake at the source locations that contributes to the precipitation at the sampling location. The second and third important variables are the weighted mean relative humidity at the source location and the total amount of precipitation at the sample location. For d-excess, the most important predictor variable is the convective precipitation at the sampling location, followed by the large-scale precipitation at the sampling location with a score a bit more than half as large.

3.5 Discussion

3.5.1 Classification of rainfall zones

Our results are generally in line with previous studies. Rainfall seasonality in southern Africa has commonly been classified into three zones: summer, winter, and year-round (e.g. Tyson and Preston-Whyte, 2000; Chase and Meadows, 2007; Dieppois et al., 2016). Our findings allow a further differentiation of the summer rainfall zone into western (SRZw), eastern (SRZe) and transitional (SRZm) zones. A similar sub-pattern of the SRZ was suggested by Liebmann et al. (2012), who studied the spatial and temporal distribution of rainfall by means of harmonic analysis. With focus on South Africa, in certain studies the SRZ was subdivided in early, mid, late and very late precipitation (EUMETSAT, 2011; Garnas et al., 2016; Botai et al., 2018). The early + mid-summer and late + very late summer rainfall zones roughly match with our SRZe and SRZm, respectively. Regarding Botswana, Maruatona and Moses (2021) considered the onset and length of the rainfall season to define three zones which roughly match our results. It has to be emphasized, however, that the cited zoning is based on meso-scale analyses, while our classification considers macro-scale rainfall variation. Moreover, our approach is independent from rather subjectively defining onset and termination of the precipitation season and no long time series are needed.

3.5.2 Spatial and temporal differences in the isotopic compositions

It is a novel finding that the δ^{18}O group mean of SRZw is significantly different to the means of SRZe and WRZ, while the latter two rainfall zones do not differ significantly from each other. There were not enough data for corresponding analyses of SRZm and YRZ. It is noteworthy that due to the high number of GNIP samples in our study these dominate the data analysis while own precipitation samples have relatively little influence. Our results indicate that within the different RFZs, the isotopic compositions differ significantly between seasons. Isotope values are on average lighter during rainfall seasons compared to off-season and transitional periods. This is consistent with a global analysis of isotopic seasonality in precipitation (Feng et al., 2009) as well as with regional studies from northern Namibia (Wanke et al., 2018) and South Africa (de Wet et al., 2020). Isotope values were highest during the end of the dry season until the onset of the rainy season. The values varied strongly during the early rainy season and were less variable and lightest during the rainfall peak.

3.5.3 Moisture source regions

The identified rainfall zones have different predominant moisture source regions. The moisture for SRZw comes mainly from the north-western subcontinent, while SRZe and SRZm receive moisture mainly from the eastern continent and to about one third from the Indian Ocean. The Mozambique Channel contributes 3-4 times more moisture to SRZm than to SRZw and SRZe. The WRZ receives moisture almost exclusively from the southern Atlantic Ocean. A global scale analysis by Gimeno et al. (2010) identified the southern Atlantic Ocean, the Indian Ocean, especially above the Agulhas Current and tropical southern Africa (only during JJA) as main source regions, thus partly matching our results. However, Gimeno et al. (2010) identified only those regions as main moisture sources, where the vertically integrated moisture flux divergence $(E - P)$ reached a certain threshold. For Namibia, Kaseke et al. (2016), based on gradients in isotope values, identified either both the Atlantic and Indian Oceans as source regions or the Indian Ocean alone, depending on the isoscape method used. Miralles et al. (2016) suggested that the Kalahari moisture largely originates from the continent and that recycling of the precipitation is highly relevant. This is in line with our results. They calculated that three quarters of the evaporation during the main growing season ($\sim$ our main precipitation season) originates from transpiration.

3.5.4 Impact of moisture source and transport on stable isotope ratios

The differences in the moisture sources of the three analysed RFZs are also evident in the d-excess vs δ^{18}O plot. The points from the WRZ are most clustered (except during off-season because of evapoconcentration). This is both because the Atlantic Ocean is the only source of moisture here, and oceanic values generally do not vary much (ocean source regions of our study are rather uniform in δ^{18}O, ranging from -1 to $+1‰$ (LeGrande and Schmidt, 2006). Furthermore, the source conditions apparently are quite stable, in terms of relative humidity and SST. Points from SRZe and SRZw are a bit more scattered, possibly due to the multiple and different moisture sources (Leketa et al., 2018) from above the African continent and the Indian Ocean (for SRZe). Especially the recycling of moisture originating from the evaporation of surface waters as well as ocean evaporation into dry air increase the d-excess because of kinetic isotope fractionation (Pfahl and Sodemann, 2014). However, local sub-cloud evaporation of the precipitation can also decrease the d-excess values due to evapoconcentration (Stewart, 1975; Froehlich et al., 2008), which is visible in the off-season plot in the WRZ (Figure C.4).

Several processes during transport and precipitation have been shown to influence the isotopic composition. In addition to the source conditions, the travelled distances between sources and sinks, as well as the seasonality and the amount of rainfall are principally controlling the values in our rainfall zones. The temperature effect is neglectable for the tropics and sub-tropics which was also demonstrated for Pretoria (Gat et al., 2001) and Johannesburg (Leketa and Abiye, 2020). The relevant role of the amount effect in our rainfall zones is indicated by the high correlation of isotope values with the total precipitation during the rainy season. Our data also support the general assumption that different travelled distances between sources and sinks lead to discriminable isotope values, predominantly due to preferred rainout of ^{18}O along a trajectory. That is, the depletion of the moisture from heavy isotopes depends significantly on travel/rain-out time. This is particularly supported by the dataset of our collected samples. Although this is likely the first study comparing isotopes in precipitation across southern Africa, it has to be noted that our precipitation samples are relatively few and somehow geographically clustered.

The Random Forest analysis showed that the distinction between the water types (precipitation, river, lake, spring) is crucial for considering the influence of moisture source and moisture transport on the stable isotope ratios. Isotope values of small rivers are very similar to those of precipitation though. When analysing d-excess, however, the type of water does not seem to play a role. In general, spatial and temporal distribution of the water samples have to be considered in more detail for a comprehensive analysis. This applies to both isotopic ratios as well as to d-excess. Consequently, the data set needs to be largely increased to obtain a more complete picture.

Our special focus on the GNIP dataset of Pretoria with corresponding Random Forest analysis exhibited that the most important factors are the evaporation rate and the humidity at the sources as well as the total amount of precipitation at the sink. On the other hand, the humidity gradient above the ocean determines the importance of nonequilibrium effects during evaporation (Pfahl and Wernli, 2008) and should thus mainly affect d-excess and less the individual ratios. For d-excess, however, we found the most important variables to be the amount of convective precipitation and large-scale precipitation. This importance could potentially be explained by corresponding differences in sub-cloud evaporation between the precipitation types (Aggarwal et al., 2016).

3.6 Summary and conclusions

In this study, we have analysed stable isotope data of water samples across whole southern Africa and their moisture sources. We identified five different annual precipitation distributions in southern Africa that cluster in space and inferred respective rainfall zones (RFZs): a winter rainfall zone (WRZ), a summer rainfall zone split in west (SRZw), east (SRZe), and mixed summer rainfall zone (SRZm) and a year-round rainfall zone (YRZ).

However, due to sampling numbers, only the isotopic compositions of the SRZw, SRZe, and WRZ could be further analysed. The isotopic composition of rainfall from the SRZw had the largest range and differed significantly from the WRZ and to SRZe. We also identified significant seasonal differences within the three analysed RFZ, as the mean isotope composition during the main precipitation season was significantly lower than during the off-season.

Our Lagrangian analysis suggested that these spatial differences are associated with notably different moisture source regions. While the moisture for SRZw originates mainly from the continent, the SRZe moisture sources are both the continent and the Indian Ocean, and the origin of the moisture that precipitates in the WRZ is the South Atlantic Ocean alone. These findings about the moisture source regions are quite important, as regions with only one or two main source regions might become more strongly affected by a changing water cycle due to climate change compared to regions where the moisture origins from multiple sources (Gimeno et al., 2010).

For the general isotopic composition over entire southern Africa, the amount effect and the travelled distance of the moisture were found to be important. For the precipitation over Pretoria, analyses also showed traces of the amount effect and the importance of the travelled distance of the moisture. The variable importance analysis by RF furthermore pointed to the spatial and temporal distribution of the samples as well as the water type as important variables. However, the conclusiveness of this statistical RF analysis is limited because of the limited sample size. Future analyses should therefore be based on even more isotopic measurements of precipitation from all RFZs and from all precipitation seasons. Yet, our findings enhance the understanding of the stable isotopes in the atmospheric water cycle over southern Africa and can be useful in the evaluation of isotope-enabled climate models for the region.

Our results provide important insights for the interpretation of palaeo-data in southern Africa, as knowledge of the different precipitation regimes, their source areas and resulting variations in the isotopic composition are important factors for palaeo-data interpretation.

3.7 Acknowledgements

Conclusion and outlook

4.1 Synthesis

The main objectives of this dissertation were to gain more reliable information about hydrological fluctuations of the catchment and basin dynamics of the palaeolake system at the Tsodilo Hills, and to investigate the influence of the recent climate on the isotope signal in precipitation, in order to provide a better basis for the interpretation of climate proxies based on stable water isotopes at the Tsodilo Hills and other systems in the Kalahari region.

For the reconstruction of Palaeolake Tsodilo a multidisciplinary approach was chosen, including various remote sensing and geophysical methods, comprehensive application of differential GPS, and sedimentological analyses. The catchment of ca. $1750\,km^2$ extends to about $120\,km$ west of the Tsodilo Hills and has a maximum N-S extension of $19\,km$. Five major, partly interconnected palaeo-channels have been identified, oriented from west to east, some of which run between the characteristic linear dunes, toward the lake basin. The interconnecting channels, trending in SW-NE direction, are less distinct and some even appear as positive relief. The central channel terminates in a large alluvial fan, separating the northern and southern lake basins. A channel located at the southern tip of the lake basin, about $2\,km$ south of Male Hill, can be traced to the Okavango Panhandle, where it ends in an about $10\,km$ wide asymmetric delta. Passing the village of Tamacha, it was named Tamacha River. Four palaeo-shorelines and thus four pronounced lake phases have been identified. Three of these indicate highstands during which the Tamacha palaeo-river drained Palaeolake Tsodilo out towards the Okavango Panhandle. The palaeolake most likely had its greatest extent about $100\,ka$ ago or earlier, when it encompassed about $70\,km^2$ and, based on present-day surface morphology, was about $16\,m$ deep. However, large areas of the western shore are very shallow, so the lacustrine environment was probably interlinked with wetlands. The two other highstands, are assigned to the mid MIS 3 and LGM, and thus are associated with periods documented by archaeologists when human fish consumption increased considerably. The mid MIS 3-lake-highstand was a stable and continuous freshwater lake that extended from the Child Hill to south of the Male Hill. Therefore, comparatively higher moisture is assumed for this period. At the shoreline, shallow water conditions prevailed and the pH value fluctuated around 8.5 throughout the lake. A remarkable difference between the LGM

highstand and the mid MIS 3 lake is that the LGM water level was 1–2 m higher. Accordingly, even higher moisture (than mid MIS 3) is assumed. Prior to the LGM highstand, moreover, a less extensive lake existed. During the phase of smallest lake extent, the Palaeolake Tsodilo was divided into two subsystems with the lake parts separated by an advancing alluvial fan delta, which formed in the central basin. The time period of this phase, however, could not be determined yet, as the sediment deposited during this phase is not archived, but possibly eroded during a subsequent dry phase when the lake bed was aerially exposed. Most likely, the outflow was not active during this phase, resulting in a higher salinity. There is no information on the age of the relief inversion of the riverbed sections. However, because some of the fossil rivers with positive relief are located within the former lake basin, it is assumed that the relief inversions are younger than 100 ka. Most likely, these sand accumulations developed during dry periods when the lake beds were deflated. In the very north of the lake basin, close to the Child Hill, a single (neo-)tectonic fault has been identified. Given its marginal location, it is considered to have had little or no influence on the mid MIS 3 and LGM lake periods, but possibly on the 100 ka BP highstand.

To investigate the influence of the recent climate on the isotopic signal in precipitation, the seasonal distribution of precipitation in southern Africa was investigated and the calculation of back trajectories was combined with stable isotopic measurements of precipitation from different locations in southern Africa. Five different annual precipitation distributions have been identified for southern Africa, which are spatially clustered. Based on these, corresponding rainfall zones (RFZ) were inferred: a winter rainfall zone (WRZ), a summer rainfall zone divided into a western (SRZw), an eastern (SRZe), and a mixed summer rainfall zone (SRZm), and a year-round rainfall zone (YRZ). The derived RFZs have distinctly different moisture sources. During the precipitation season, the main moisture source of the SRZw is over the northwestern region of southern Africa, while the SRZe and SRZm have their main moisture sources over the eastern region of southern Africa and additionally from the Indian Ocean near the western coast south of Madagascar. In the WRZ, almost all moisture sources are from the Atlantic Ocean. The isotopic composition also differs significantly among the RFZ. Precipitation from the SRZw has the widest range in isotopic composition and is significantly different from the SRZe and WRZ, with the WRZ having the most clustered isotope values. Moreover, significant seasonal differences are observed within these same three analysed RFZs; as such, the mean isotopic composition is significantly lower during the respective main precipitation season than during the off-season. This influence of the spatial and temporal distribution of the samples on the isotopic composition is confirmed in the variable importance analysis. For the general isotopic composition across southern Africa,

the amount effect and the travelled distance of moisture have been revealed as important influencing factors.

4.2 Additional analytical results

Some more knowledge has been gained within the encompassing DFG research project regarding the reconstruction of the Palaeolake Tsodilo and (palaeo-)climate variations. Within the project, three bachelor and two master theses were partially co-supervised by me. The results of these works, relevant to the topic of this dissertation, will be briefly presented in the following.

The results from Venise Gummersbach (Gummersbach, 2019: Reconstruction of transportation and depositional processes at the late Pleistocene lake basin at the Tsodilo Hills in NW Botswana on the basis of sediment analysis and multivariate statistic [master thesis]) were included in the first paper and will therefore not be repeated here.

The about 1 m thick soil-sequence of Pit S2-18 was analysed by Hannah Ackermann to determine the soil type (Ackermann, 2019: Processes of soil formation in the Kalahari: an example from the Tsodilo Hills, north-western Botswana [bachelor thesis]). Loss on ignition, pH-value and electric conductivity measurements as well as the carbon-nitrogen ratio revealed that the subsequent lacustrine sediments must have been eroded and substituted by a chernozem-like soil. This indicates fertility of the lake depression land but also shows that post-depositional alteration of the sedimentary deposits must be kept in mind when interpreting sedimentological features.

For a selected part of the study area in the Tsodilo Palaeolake basin, Jana Frenzel applied structure from motion photogrammetry to create high-resolution digital surface models, orthomosaics and DEMs from unmanned aerial system imagery (UAS) (Frenzel, 2020: Comparison of high-resolution digital elevation models based on an Unmanned Aerial System (UAS) and satellite remote sensing (TanDEM-X) [bachelor thesis]). Using this approach, an unprecedented level of detail of around 5 cm was achieved. Comparison of both the created UAS-based digital surface model and DEM with the TanDEM-X DEM, used in this doctoral thesis (resolution of 12 m), showed that the TanDEM-X DEM slightly overestimates the elevation for areas with relatively dense vegetation. This confirms the finding presented in Chapter 2 (Manuscript 1), where dense vegetation cover was identified to considerably influence the elevation values of the TanDEM-X data. However, as only slight differences exist, consequently, the major advantage of topographical mapping using UAS in similar

areas, vegetated by mainly shrubs and single trees, is the much higher resolution. Yet, while the use of a UAS can provide very high spatial resolution at relatively low cost and effort, TanDEM-X provides spatial coverage that cannot realistically be achieved through the elaborate UAS workflow. From the results, it is clear that the TanDEM-X DEM is a reliable data source for the identification of spatial patterns and geomorphological structures. For structures that are difficult to reach, for example due to dense vegetation, UAS imagery however offers a great alternative that allows a closer examination of these structures.

As part of his thesis, Florian Cordt determined the most relevant moisture source regions for precipitation over Pretoria for the period from 1996 to 2001 and analysed inter-annual and seasonal differences (Cordt, 2021: Bestimmung und Analyse des Feuchtigkeitsursprungs für Niederschläge in Pretoria, im Zeitraum 1996 bis 2001 [bachelor thesis]). Increased variability of moisture source areas was found in the summer months compared to the winter. Especially the months of the summers of 1995/96 and 1999/2000 show considerably more moisture source areas than the other four years considered. A possible connection to the La Niña phenomena, also prevalent during this period, was suspected here. In general, the highest numbers of trajectories relevant to precipitation have been identified during the summer and first autumn months (precipitation season). Particularly few trajectories, however, were determined within the summer of 1997/98. Since this was also a prolonged period of negative and particularly low Southern Oscillation Index values (Jan 1998: -2.7), a strong influence of the El Niño phenomenon is assumed. These findings support the influence of the ENSO in southern Africa, which has already been described in other studies.

The master thesis of Christoph Gey introduces the bivalve *Corbicula* sp. as an archive providing sclerochronological δ^{18}O and δ^{13}C records that reflect high-resolution present day annual cycles (Gey, 2021: Sclerochronological stable isotope patterns of modern bivalves as analogues to unravel climate and weather during the Late Glacial in the Kalahari, southern Africa [master thesis]). The isotopic values of the analysed modern representatives from the Limpopo River exhibited precise weather signals assignable to precipitation events and evaporation dominated periods up to a weekly resolution. In addition, two fossil *Corbicula fluminalis* from the adjacent Molopo riverbed (southern Kalahari), dated to the Late Glacial period, were analysed. The shell dated to 14.6 cal kyr BP indicates a bimodal annual cycle comparable to today, comprising a summer rainfall season and a drier winter period, along with slightly lower annual temperatures than today. The somewhat younger shell dated to 14.3 cal kyr BP, however, indicates an even stronger cooling and/or a decrease in evaporation. Hence, this would coincide with the onset of the Antarctic cold reversal assumed for this period. The work thus shows that the genus *Corbicula* is suitable as an archive for

palaeoclimate and -weather reconstructions and furthermore provides a first reliable reference for further analyses, for example to investigate the hypotheses concerning the LGM-climate features presented in the introduction.

4.3 Remaining challenges and future perspectives

The results of the first part of this dissertation contribute to our understanding of the catchment and basin of Palaeolake Tsodilo. This is a prerequisite for further interpretation of climate proxies from this study site. However, to fully reconstruct the lake-system some further studies are needed. The different lithologies of the pits on the one hand reflect contrasts in erosion and soil formation and on the other hand the specific positions regarding fluvial inputs. More sediment sections need to be analysed to resolve the detrital flux in all parts over the lake phases. This can be done for example with surface samples spatially distributed over the entire lake basin. Collection of such data has already been initiated during the field trips, but is limited in terms of area and this effort needs to be continued. Moreover, promising sediment pits from the deepest parts of the basin and additional locations close to the palaeo-shorelines of the different lake phases are useful. It is not known yet, which palaeo-channels were active at which time period and how much water inflow was necessary to fill the Tsodilo Basin. To resolve this, sedimentological analysis of at least the main channels would be worthwhile as well as hydrological modelling concerning the water balance and rainfall-runoff models. Sedimentological analysis of the outflow channel might provide a significant advance in a greater detail when reconstructing the lake phases; especially concerning, for example, the intensity of the outflow and when it was active, and consequently, whether the identified lake phases were open or closed basins.

The results of the second part of this dissertation provide a baseline on the influence of recent climate on the isotope signal in precipitation, which is essential for a reliable interpretation of isotope-based climate proxies. However, further investigations with more precipitation samples, especially from the rainfall zones YRZ and SRZm which are currently still under-represented in the dataset, would be valuable. Also, time series analyses at selected locations in the different rainfall zones could provide useful additional insights about inter-annual and seasonal variations.

Eventually, sclerochronological investigations of LGM-dated deposits would expand our understanding of hydroclimatic change during the LGM around Palaeolake Tsodilo and in entire southern Africa. Fossil shells have already been collected from the dry riverbeds of the

Okwa River and the Molopo River (both before and after confluence with the Nossob River). Based on the data along this north-south transect, the hypothesis that the winter rainfall zone extended further north during the LGM may eventually be confirmed or rejected.

References

Acharya, A., Das, S., Pan, I., Das, S. (2014). Extending the concept of analog Butterworth filter for fractional order systems. *Signal Processing* 94:409–420. doi:10.1016/j.sigpro.2013.07.012.

Ackermann, H. (2019). Processes of soil formation in the Kalahari: an example from the Tsodilo Hills, north-western Botswana. B. Sc. Thesis. Freie Universität Berlin. Berlin.

Adekiya, T.A., Aruleba, R.T., Oyinloye, B.E., Okosun, K.O., Kappo, A.P. (2020). The Effect of Climate Change and the Snail-Schistosome Cycle in Transmission and Bio-Control of Schistosomiasis in Sub-Saharan Africa. *International journal of environmental research and public health* 17(1):181. doi:10.3390/ijerph17010181.

Aggarwal, P.K., Romatschke, U., Araguas-Araguas, L.J., Belachew, D., Longstaffe, F.J., Berg, P., Schumacher, C., Funk, A. (2016). Proportions of convective and stratiform precipitation revealed in water isotope ratios. *Nature Geoscience* 9(8):624–629. doi:10.1038/ngeo2739.

Aitchison, J. (1982). The Statistical Analysis of Compositional Data. *Journal of the Royal Statistical Society* 44(2):139–177. URL: http://links.jstor.org/sici?sici=0035-9246%281982%2944%3A2%3C139%3ATSAOCD%3E2.0.CO%3B2-9.

Aitchison, J. (1986). The statistical analysis of compositional data. Monographs on statistics and applied probability, Chapman and Hall, London and New York.

Amante, C., Eakins, B.W. (2009). ETOPO1 1 Arc-Minute Global Relief Model: Procedures, Data Sources and Analysis. NOAA Technical Memorandum NESDIS NGDC-24. doi:10.7289/V5C8276M.

Appleton, C.C., Ellery, W.N., Byskov, J., Mogkweetsinyana, S.S. (2008). Epidemic transmission of intestinal schistosomiasis in the seasonal part of the Okavango Delta, Botswana. *Annals of tropical medicine and parasitology* 102(7):611–623. doi:10.1179/136485908X311867.

Bailly, C., Fortin, J., Adelinet, M., Hamon, Y. (2019). Upscaling of Elastic Properties in Carbonates: A Modeling Approach Based on a Multiscale Geophysical Data Set. *Journal of Geophysical Research: Solid Earth* 124(12):13021–13038. doi:10.1029/2019JB018391.

Baker, A.J., Sodemann, H., Baldini, J.U.L., Breitenbach, S.F., Johnson, K.R., van Hunen, J., Zhang, P. (2015). Seasonality of westerly moisture transport in the East Asian summer

monsoon and its implications for interpreting precipitation δ^{18}O. *Journal of Geophysical Research: Atmospheres* 120(12):5850–5862. doi:10.1002/2014JD022919.

Baray, J., Baldy, S., Diab, R., Cammas, J. (2003). Dynamical study of a tropical cut-off low over South Africa, and its impact on tropospheric ozone. *Atmospheric Environment* 37(11):1475–1488. doi:10.1016/S1352-2310(02)00999-8.

Bard, E., Hamelin, B., Fairbanks, R.G., Zindler, A. (1990). Calibration of the ^{14}C timescale over the past 30,000 years using mass spectrometric U–Th ages from Barbados corals. *Nature* 345(6274):405–410. doi:10.1038/345405a0.

Barton, N. (2006). Rock Quality, Seismic Velocity, Attenuation and Anisotropy. Balkema-proceedings and monographs in engineering, water and earth sciences, CRC Press, London. doi:10.1201/9780203964453.

Batini, C., Jobling, M.A. (2011). The jigsaw puzzle of our African ancestry: unsolved, or unsolvable? *Genome biology* 12(6):118. doi:10.1186/gb-2011-12-6-118.

Behnamian, A., Millard, K., Banks, S.N., White, L., Richardson, M., Pasher, J. (2017). A Systematic Approach for Variable Selection With Random Forests: Achieving Stable Variable Importance Values. *IEEE Geoscience and Remote Sensing Letters* 14(11):1988–1992. doi:10.1109/LGRS.2017.2745049.

Bekker, R.P., de Wit, P.V. (1991). Vegetation map of the Republic of Botswana: Soil Mapping and Advisory Services Project. (DP/BOT/85/011). FAO. Gaborone, Botswana.

Birsoy, R. (2002). Formation of sepiolite-palygorskite and related minerals from solution. *Clays and Clay Minerals* 50(6):736–745. doi:10.1346/000986002762090263.

Blamey, R.C., Kolusu, S.R., Mahlalela, P., Todd, M.C., Reason, C.J. (2018). The role of regional circulation features in regulating El Niño climate impacts over southern Africa: A comparison of the 2015/2016 drought with previous events. *International Journal of Climatology* 38(11):4276–4295. doi:10.1002/joc.5668.

Blome, M.W., Cohen, A.S., Tryon, C.A., Brooks, A.S., Russell, J. (2012). The environmental context for the origins of modern human diversity: a synthesis of regional variability in African climate 150,000-30,000 years ago. *Journal of Human Evolution* 62(5):563–592. doi:10.1016/j.jhevol.2012.01.011.

Bogitsh, B.J., Carter, C.E., Oeltmann, T.N. (2012). Human parasitology. 4 ed., Academic Press, Elsevier.

Bomblies, A., Duchemin, J.B., Eltahir, E.A.B. (2008). Hydrology of malaria: Model development and application to a Sahelian village. *Water Resources Research* 44(12). doi:10.1029/2008WR006917.

Botai, C., Botai, J.O., Adeola, A. (2018). Spatial distribution of temporal precipitation contrasts in South Africa. *South African Journal of Science* 114(7/8). doi:10.17159/sajs.2018/20170391.

Bowen, G.J., Putman, A., Brooks, J.R., Bowling, D.R., Oerter, E.J., Good, S.P. (2018). Inferring the source of evaporated waters using stable H and O isotopes. *Oecologia* 187(4):1025–1039. doi:10.1007/s00442-018-4192-5.

Brain, C.K. (1981). The hunters or the hunted? An introduction to African cave taphonomy. University of Chicago Press, Chicago, Illinois.

Breeze, P.S., Drake, N.A., Groucutt, H.S., Parton, A., Jennings, R.P., White, T.S., Clark-Balzan, L., Shipton, C., Scerri, E.M., Stimpson, C.M., Crassard, R., Hilbert, Y., Alsharekh, A., Al-Omari, A., Petraglia, M.D. (2015). Remote sensing and GIS techniques for reconstructing Arabian palaeohydrology and identifying archaeological sites. *Quaternary International* 382:98–119. doi:10.1016/j.quaint.2015.01.022.

Broccoli, A.J., Dahl, K.A., Stouffer, R.J. (2006). Response of the ITCZ to Northern Hemisphere cooling. *Geophysical Research Letters* 33(1). doi:10.1029/2005GL024546.

Brook, G.A. (2010). The Paleoenvironment of Tsodilo, in: Campbell, A.C., Robbins, L.H., Taylor, M. (Eds.), Tsodilo Hills. Michigan State University Press, East Lansing, pp. 30–49.

Brook, G.A., Cowart, J.B., Marais, E. (1996). Wet and dry periods in the southern African summer rainfall zone during the last 300 kyr from speleothem, tufa and sand dune age data, in: Heine, K., van Zinderen Bakker, E.M. (Eds.), Palaeoecology of Africa & of the surrounding islands & Antarctica (Vol.24). CRC Press, Rotterdam, pp. 147–158.

Brook, G.A., Haberyan, K.A., de Filippis, S. (1992). Evidence of a shallow lake at Tsodilo Hills, Botswana, 17'500 to 15'000 yr BP: Further confirmation of a widespread Late Pleistocene humid period in the Kalahari Desert, in: Heine, K. (Ed.), Palaeoecology of Africa & of the surrounding islands & Antarctica (Vol.23). A. A. Balkema, Rotterdam, pp. 165–175.

Brook, G.A., Marais, E., Srivastava, P., Jordan, T. (2007). Timing of lake-level changes in Etosha Pan, Namibia, since the middle Holocene from OSL ages of

relict shorelines in the Okondeka region. *Quaternary International* 175(1):29–40. doi:10.1016/j.quaint.2007.05.020.

Brook, G.A., Scott, L., Railsback, L.B., Goddard, E.A. (2010). A 35ka pollen and isotope record of environmental change along the southern margin of the Kalahari from a stalagmite and animal dung deposits in Wonderwerk Cave, South Africa. *Journal of Arid Environments* 74(7):870–884. doi:10.1016/j.jaridenv.2009.11.006.

Brown, D.S. (1994). Freshwater snails of Africa and their medical importance. CRC Press, London. doi:10.1201/9781482295184.

Burgman, J., Eriksson, E., Kostov, L., Moller, A. (1979). Application of oxygen-18 and deuterium for investigating the origin of groundwater in connection with a dam project in Zambia, in: International Atomic Energy Agency (Ed.), Isotope Hydrology 1978, International Atomic Energy Agency (IAEA), Vienna. pp. 27–40.

Burrough, S.L. (2016). Late Quaternary Environmental Change and Human Occupation of the Southern African Interior, in: Jones, S.C., Stewart, B.A. (Eds.), Africa from MIS 6-2. Springer, Dordrecht. Vertebrate Paleobiology and Paleoanthropology, pp. 161–174.

Burrough, S.L., Thomas, D.S., Bailey, R.M. (2009a). Mega-Lake in the Kalahari: A Late Pleistocene record of the Palaeolake Makgadikgadi system. *Quaternary Science Reviews* 28(15-16):1392–1411. doi:10.1016/j.quascirev.2009.02.007.

Burrough, S.L., Thomas, D.S., Singarayer, J.S. (2009b). Late Quaternary hydrological dynamics in the Middle Kalahari: Forcing and feedbacks. *Earth-Science Reviews* 96(4):313–326. doi:10.1016/j.earscirev.2009.07.001.

Butterworth, S. (1930). On the theory of filter amplifiers. *Wireless Engineer* 7(6):536–541.

Campbell, A.C. (2010). Visiting Tsodilo: Preparing the Imagination, in: Campbell, A.C., Robbins, L.H., Taylor, M. (Eds.), Tsodilo Hills. Michigan State University Press, East Lansing, pp. 16–29.

Campbell, A.C., Robbins, L.H. (2010). Tsodilo Hill, Botswana. *Adoranten 2009* pp. 34–48.

Cassidy, N.J. (2009). Electrical and Magnetic Properties of Rocks, Soils and Fluids, in: Jol, H.M. (Ed.), Ground penetrating radar. Elsevier Science and Elsevier, Amsterdam, Netherlands and Boston, pp. 41–72. doi:10.1016/B978-0-444-53348-7.00002-8.

Chan, E.K.F., Timmermann, A., Baldi, B.F., Moore, A.E., Lyons, R.J., Lee, S.S., Kalsbeek, A.M.F., Petersen, D.C., Rautenbach, H., Förtsch, H.E.A., Bornman, M.S.R., Hayes, V.M.

(2019). Human origins in a southern African palaeo-wetland and first migrations. *Nature* 575(7781):185–189. doi:10.1038/s41586-019-1714-1.

Chase, B.M. (2009). Evaluating the use of dune sediments as a proxy for palaeo-aridity: A southern African case study. *Earth-Science Reviews* 93(1-2):31–45. doi:10.1016/j.earscirev.2008.12.004.

Chase, B.M., Harris, C., de Wit, M.J., Kramers, J., Doel, S., Stankiewicz, J. (2021). South African speleothems reveal influence of high- and low-latitude forcing over the past 113.5 k.y. *Geology* 49(11):1353–1357. doi:10.1130/G49323.1.

Chase, B.M., Meadows, M.E. (2007). Late Quaternary dynamics of southern Africa's winter rainfall zone. *Earth-Science Reviews* 84(3-4):103–138. doi:10.1016/j.earscirev.2007.06.002.

Cherchi, A., Ambrizzi, T., Behera, S., Freitas, A.C.V., Morioka, Y., Zhou, T. (2018). The Response of Subtropical Highs to Climate Change. *Current Climate Change Reports* 4(4):371–382. doi:10.1007/s40641-018-0114-1.

Chevalier, M., Chase, B.M. (2016). Determining the drivers of long-term aridity variability: a southern African case study. *Journal of Quaternary Science* 31(2):143–151. doi:10.1002/jqs.2850.

Chiang, J.C.H., Biasutti, M., Battisti, D.S. (2003). Sensitivity of the Atlantic Intertropical Convergence Zone to Last Glacial Maximum boundary conditions. *Paleoceanography* 18(4). doi:10.1029/2003PA000916.

Cohen, A.S. (2003). Paleolimnology: The history and evolution of lake systems. New York and Oxford University Press, Oxford.

Cole, M.M., Brown, R.C. (1976). The Vegetation of the Ghanzi Area of Western Botswana. *Journal of Biogeography* 3(3):169. doi:10.2307/3038009.

Collins, J.A., Schefuß, E., Heslop, D., Mulitza, S., Prange, M., Zabel, M., Tjallingii, R., Dokken, T.M., Huang, E., Mackensen, A., Schulz, M., Tian, J., Zarriess, M., Wefer, G. (2011). Interhemispheric symmetry of the tropical African rainbelt over the past 23,000 years. *Nature Geoscience* 4(1):42–45. doi:10.1038/ngeo1039.

Contractor, S., Donat, M.G., Alexander, L.V. (2021). Changes in Observed Daily Precipitation over Global Land Areas since 1950. *Journal of Climate* 34(1):3–19. doi:10.1175/JCLI-D-19-0965.1.

Conway, D., van Garderen, E.A., Deryng, D., Dorling, S., Krueger, T., Landman, W., Lankford, B., Lebek, K., Osborn, T., Ringler, C., Thurlow, J., Zhu, T., Dalin, C. (2015).

Climate and southern Africa's water–energy–food nexus. *Nature Climate Change* 5(9):837–846. doi:10.1038/nclimate2735.

Cook, K.H. (2000). The South Indian Convergence Zone and Interannual Rainfall Variability over Southern Africa. *Journal of Climate* 13(21):3789–3804.

Cooke, H.J. (1980). Landform Evolution in the Context of Climatic Change and Neo-Tectonism in the Middle Kalahari of North-Central Botswana. *Transactions of the Institute of British Geographers* 5(1):80. doi:10.2307/622100.

Cooke, H.J. (1985). The Kalahari Today: A Case of Conflict over Resource Use. *The Geographical Journal* 151(1):75–85. URL: https://www.jstor.org/stable/633282?seq=1#metadata_info_tab_contents.

Copernicus Climate Change Service (2019). ERA5 explorer (Version 4.2.4 - build ed0a423) [Computer software]. European Centre for Medium-Range Weather Forecasts (ECMWF). URL: https://cds.climate.copernicus.eu/cdsapp#!/software/app-era5-explorer?tab=app.

Cordt, F. (2021). Bestimmung und Analyse des Feuchtigkeitsursprungs für Niederschläge in Pretoria, im Zeitraum 1996 bis 2001. B.Sc. Thesis. Freie Universität Berlin. Berlin, Germany.

de Cort, G., Chevalier, M., Burrough, S.L., Chen, C.Y., Harrison, S.P. (2021). An uncertainty-focused database approach to extract spatiotemporal trends from qualitative and discontinuous lake-status histories. *Quaternary Science Reviews* 258:106870. doi:10.1016/j.quascirev.2021.106870.

Coulthard, T.J., Ramirez, J.A., Barton, N., Rogerson, M., Brücher, T. (2013). Were rivers flowing across the Sahara during the last interglacial? Implications for human migration through Africa. *PloS one* 8(9):e74834. doi:10.1371/journal.pone.0074834.

Craig, H. (1961a). Isotopic Variations in Meteoric Waters. *Science* 133(3465):1702–1703. doi:10.1126/science.133.3465.1702.

Craig, H. (1961b). Standard for Reporting Concentrations of Deuterium and Oxygen-18 in Natural Waters. *Science* 133(3467):1833–1834. doi:10.1126/science.133.3467.1833.

Crellen, T., Allan, F., David, S., Durrant, C., Huckvale, T., Holroyd, N., Emery, A.M., Rollinson, D., Aanensen, D.M., Berriman, M., Webster, J.P., Cotton, J.A. (2016). Whole genome resequencing of the human parasite Schistosoma mansoni reveals population history and effects of selection. *Scientific reports* 6(1):20954. doi:10.1038/srep20954.

References

Croudace, I.W., Rindby, A., Rothwell, R.G. (2006). ITRAX: description and evaluation of a new multi-function X-ray core scanner. *Geological Society, London, Special Publications* 267(1):51–63. doi:10.1144/GSL.SP.2006.267.01.04.

Danielson, J.J., Gesch, D.B. (2011). Global multi-resolution terrain elevation data 2010 (GMTED2010). U.S. Geological Survey. Open-File Report. doi:10.3133/ofr20111073.

Dansgaard, W. (1964). Stable isotopes in precipitation. *Tellus* 16(4):436–468.

Dansgaard, W., Johnsen, S.J., Clausen, H.B., Dahl-Jensen, D., Gundestrup, N.S., Hammer, C.U., Hvidberg, C.S., Steffensen, J.P., Sveinbjörnsdottir, A.E., Jouzel, J., Bond, G. (1993). Evidence for general instability of past climate from a 250-kyr ice-core record. *Nature* 364(6434):218–220. doi:10.1038/364218a0.

Day, M., Edgett, K.S., Stumbaugh, D. (2019). Ancient Stratigraphy Preserving a Wet–to–Dry, Fluvio–Lacustrine to Aeolian Transition Near Barth Crater, Arabia Terra, Mars. *Journal of Geophysical Research: Planets* 124(12):3402–3421. doi:10.1029/2019JE006226.

de Mil, T., Meko, M., Belmecheri, S., February, E., Therrell, M., van den Bulcke, J., Trouet, V. (2021). A lonely dot on the map: Exploring the climate signal in tree-ring density and stable isotopes of clanwilliam cedar, South Africa. *Dendrochronologia* 69:125879. doi:10.1016/j.dendro.2021.125879.

de Wet, R.F., West, A.G., Harris, C. (2020). Seasonal variation in tap water δ^2H and δ^{18}O isotopes reveals two tap *water* worlds. *Scientific reports* 10(1):13544. doi:10.1038/s41598-020-70317-2.

de Wit, P.V., Bekker, R.P. (1990). Explanatory note on the land systems map of Botswana: Soil Mapping and Advisory Services Botswana. Gaborone, Botswana.

Department of Environmental Affairs (2013). Long-Term Adaptation Scenarios Flagship Research Programme (LTAS) for South Africa. Climate Change Implications for the Water Sector in South Africa (LTAS Phase 1, Technical Report No. 2). Pretoria, South Africa.

Department of Environmental Affairs (2017). South Africa's 2nd Annual Climate Change Report. Pretoria, South Africa.

Department of Water Affairs, South Africa (2013). Development of reconciliation strategies for large bulk water supply systems: Orange River (DWA Report Number: P RSA D000/00/18312/7).

Despres, L., Imbert-Establet, D., Combes, C., Bonhomme, F. (1992). Molecular evidence linking hominid evolution to recent radiation of schistosomes (Platyhelminthes:

Trematoda). *Molecular phylogenetics and evolution* 1(4):295–304. doi:10.1016/1055-7903(92)90005-2.

Di Bella, S., Riccardi, N., Giacobbe, D.R., Luzzati, R. (2018). History of schistosomiasis (bilharziasis) in humans: from Egyptian medical papyri to molecular biology on mummies. *Pathogens and Global Health* 112(5):268–273. doi:10.1080/20477724.2018.1495357.

Diekmann, C.J., Schneider, M., Knippertz, P., Vries, A.J., Pfahl, S., Aemisegger, F., Dahinden, F., Ertl, B., Khosrawi, F., Wernli, H., Braesicke, P. (2021). A Lagrangian perspective on stable water isotopes during the West African Monsoon. *Journal of Geophysical Research: Atmospheres* doi:10.1029/2021JD034895.

Dieppois, B., Pohl, B., Rouault, M., New, M., Lawler, D., Keenlyside, N. (2016). Interannual to interdecadal variability of winter and summer southern African rainfall, and their teleconnections. *Journal of Geophysical Research: Atmospheres* 121(11):6215–6239. doi:10.1002/2015JD024576.

Dietze, E., Dietze, M. (2019). Grain-size distribution unmixing using the R package EMMAgeo. *E&G Quaternary Science Journal* 68(1):29–46. doi:10.5194/egqsj-68-29-2019.

Dietze, E., Hartmann, K., Diekmann, B., Ijmker, J., Lehmkuhl, F., Opitz, S., Stauch, G., Wünnemann, B., Borchers, A. (2012). An end-member algorithm for deciphering modern detrital processes from lake sediments of Lake Donggi Cona, NE Tibetan Plateau, China. *Sedimentary Geology* 243-244:169–180. doi:10.1016/j.sedgeo.2011.09.014.

Dincer, T., Hutton, L.G., Kupee, B. (1979). Study, using stable isotopes, of flow distribution, surface-groundwater relations and evapotranspiration in the Okavango Swamp, Botswana, in: International Atomic Energy Agency (Ed.), Isotope Hydrology 1978, International Atomic Energy Agency (IAEA), Vienna. pp. 3–25. URL: https://inis.iaea.org/search/search.aspx?orig_q=RN:10460883.

DLR (2009). TerraSAR-X: Das deutsche Radar-Auge im All / The German Radar Eye in Space: Mission brochure. Bonn. URL: https://www.dlr.de/de/forschung-und-transfer/projekte-und-missionen/terrasar-x/terrasar-x-das-deutsche-radar-auge-im-all_622.pdf/@@download/file.

Doglioni, A., Simeone, V. (2014). Geomorphometric analysis based on discrete wavelet transform. *Environmental Earth Sciences* 71(7):3095–3108. doi:10.1007/s12665-013-2686-3.

Drake, N.A., El-Hawat, A.S., Turner, P., Armitage, S.J., Salem, M.J., White, K.H., McLaren, S. (2008). Palaeohydrology of the Fazzan Basin and surrounding regions: The

last 7 million years. *Palaeogeography, Palaeoclimatology, Palaeoecology* 263(3-4):131–145. doi:10.1016/j.palaeo.2008.02.005.

Driver, P., Abiodun, B.J., Reason, C.J. (2019). Modelling the precipitation response over southern Africa to the 2009–2010 El Niño using a stretched grid global atmospheric model. *Climate Dynamics* 52(7-8):3929–3949. doi:10.1007/s00382-018-4362-5.

Driver, P., Reason, C.J. (2017). Variability in the Botswana High and its relationships with rainfall and temperature characteristics over southern Africa. *International Journal of Climatology* 37(7/8):570–581. doi:10.1002/joc.5022.

du Toit, J.C.O., Ramaswiela, T., Pauw, M.J., O'Connor, T.G. (2018). Interactions of grazing and rainfall on vegetation at Grootfontein in the eastern Karoo. *African Journal of Range & Forage Science* 35(3-4):267–276. doi:10.2989/10220119.2018.1508072.

Dunning, C.M., Black, E., Allan, R.P. (2018). Later Wet Seasons with More Intense Rainfall over Africa under Future Climate Change. *Journal of Climate* 31(23):9719–9738. doi:10.1175/JCLI-D-18-0102.1.

Duraiappah, A.K., Perkins, J. (1999). Sustainable Livestock Management in the Kalahari: an Optimal Livestock Rangeland Model (OLR) (CREED Working Paper Series No. 23).

Durowoju, O.S., Odiyo, J.O., Ekosse, G.I.E. (2019). Determination of isotopic composition of rainwater to generate local meteoric water line in Thohoyandou, Limpopo Province, South Africa. *Water SA* 45(2 April). doi:10.4314/wsa.v45i2.04.

Endo, N., Eltahir, E.A.B. (2018). Environmental Determinants of Malaria Transmission Around the Koka Reservoir in Ethiopia. *GeoHealth* 2(3):104–115. doi:10.1002/2017GH000108.

Engelbrecht, C.J., Engelbrecht, F.A. (2016). Shifts in Köppen-Geiger climate zones over southern Africa in relation to key global temperature goals. *Theoretical and Applied Climatology* 123(1-2):247–261. doi:10.1007/s00704-014-1354-1.

ESRI (2018). ArcGIS Pro (Version 2.2.4) [Computer software]. Redlands, California, United States.

EUMETSAT (2011). Winter lightning with cut-off low over S Africa. URL: https://www.eumetsat.int/winter-lightning-cut-low-over-s-africa#ref.

FAO (2012). ETo Calculator (Version 3.2) [Computer software]. Rome, Italy. URL: http://www.fao.org/land-water/databases-and-software/eto-calculator/en/.

Feathers, J.K. (1997). Luminescence dating of sediment samples from White paintings Rockshelter, Botswana. *Quaternary Science Reviews* 16(3-5):321–331. doi:10.1016/S0277-3791(96)00083-2.

Feng, X., Faiia, A.M., Posmentier, E.S. (2009). Seasonality of isotopes in precipitation: A global perspective. *Journal of Geophysical Research* 114(D8):28721. doi:10.1029/2008JD011279.

Ferrio, J.P., Resco, V., Williams, D., Serrano, L., Voltas, J. (2005). Stable isotopes in arid and semi-arid forest systems. *Investigación agraria. Sistemas y recursos forestales* 14(3):371–382.

Fick, S.E., Hijmans, R.J. (2017). WorldClim 2: new 1–km spatial resolution climate surfaces for global land areas. *International Journal of Climatology* 37(12):4302–4315. doi:10.1002/joc.5086.

Fouque, F., Reeder, J.C. (2019). Impact of past and on-going changes on climate and weather on vector-borne diseases transmission: a look at the evidence. *Infectious diseases of poverty* 8(1):51. doi:10.1186/s40249-019-0565-1.

Franchi, F., Ahad, J.M.E., Geris, J., Jhowa, G., Petros, A.K., Comte, J.C. (2020). Modern sediment records of hydroclimatic extremes and associated potential contaminant mobilization in semi-arid environments: lessons learnt from recent flood-drought cycles in southern Botswana. *Journal of Soils and Sediments* 20(3):1632–1650. doi:10.1007/s11368-019-02454-9.

Frenzel, J. (2020). Comparison of high-resolution digital elevation models based on an Unmanned Aerial System (UAS) and satellite remote sensing (TanDEM-X): A case study at Late Quaternary Palaeolake Tsodilo, Kalahari, Botswana. B.Sc. Thesis. Freie Universität Berlin. Berlin.

Fritz, P., Poplawski, S. (1974). ^{18}O and ^{13}C in the shells of freshwater molluscs and their environments. *Earth and Planetary Science Letters* 24(1):91–98. doi:10.1016/0012-821X(74)90012-0.

Froehlich, K.F., Kralik, M., Papesch, W., Rank, D., Scheifinger, H., Stichler, W. (2008). Deuterium excess in precipitation of Alpine regions - moisture recycling. *Isotopes in environmental and health studies* 44(1):61–70. doi:10.1080/10256010801887208.

References

Fryer, G. (1961). The developmental history of *Mutela bourguignati* (Ancey) Bourguignat (Mollusca: Bivalvia). *Philosophical Transactions of the Royal Society of London. Series B, Biological Sciences* 244(711):259–298. doi:10.1098/rstb.1961.0009.

Galán, E., Pozo, M. (2011). Palygorskite and Sepiolite Deposits in Continental Environments. Description, Genetic Patterns and Sedimentary Settings, in: Singer, A., Galan, E. (Eds.), Developments in Palygorskite-Sepiolite Research. Elsevier professional, s.l.. Vol. 3 of *Developments in Clay Science*, pp. 125–173. doi:10.1016/B978-0-444-53607-5.00006-2.

Garnas, J., Hurley, B., Slippers, B., Wingfield, M.J., Roux, J. (2016). Insects and Diseases of Mediterranean Forests: A South African Perspective, in: Paine, T.D., Lieutier, F. (Eds.), Insects and diseases of mediterranean forest systems. Springer, Cham and Heidelberg and New York, pp. 397–430. doi:10.1007/978-3-319-24744-1_14.

Gasse, F., Chalié, F., Vincens, A., Williams, M.A., Williamson, D. (2008). Climatic patterns in equatorial and southern Africa from 30,000 to 10,000 years ago reconstructed from terrestrial and near-shore proxy data. *Quaternary Science Reviews* 27(25-26):2316–2340. doi:10.1016/j.quascirev.2008.08.027.

Gat, J.R. (1996). Oxygen and hydrogen isotopes in the hydrologic cycle. *Annual Review of Earth and Planetary Sciences* 24(1):225–262. doi:10.1146/annurev.earth.24.1.225.

Gat, J.R., Mook, W.G., Meijer, H.A. (2001). Vol. 2: Atmospheric Water, in: Mook, W.G. (Ed.), Environmental isotopes in the hydrological cycle. UNESCO - IAEA. Vol. 2 of *Technical documents in hydrology*, pp. 171–235.

Gelabert, P., Olalde, I., de Dios, T., Civit, S., Lalueza-Fox, C. (2017). Malaria was a weak selective force in ancient Europeans. *Scientific reports* 7(1):1377. doi:10.1038/s41598-017-01534-5.

Geppert, M., Riedel, F., Gummersbach, V.S., Gutjahr, S., Hoelzmann, P., Reyes Garzón, M.D., Shemang, E.M., Hartmann, K. (2021). Late Pleistocene hydrological settings at world heritage Tsodilo Hills (NW Kalahari, Botswana), a site of ancient human occupation. *Quaternary Science Advances* 3:100022. doi:10.1016/j.qsa.2021.100022.

Gething, P.W., Battle, K.E., Bhatt, S., Smith, D.L., Eisele, T.P., Cibulskis, R.E., Hay, S.I. (2014). Declining malaria in Africa: improving the measurement of progress. *Malaria journal* 13:39. doi:10.1186/1475-2875-13-39.

Gey, C. (2021). Sclerochronological stable isotope patterns of modern bivalves as analogues to unravel climate and weather during the Late Glacial in the Kalahari, southern Africa. M.Sc. Thesis. Freie Universität Berlin. Berlin, Germany.

Gibbons, A. (2019). Experts question study claiming to pinpoint birthplace of all humans. *Science* doi:10.1126/science.aba0155.

Gimeno, L., Drumond, A., Nieto, R., Trigo, R.M., Stohl, A. (2010). On the origin of continental precipitation. *Geophysical Research Letters* 37(13). doi:10.1029/2010GL043712.

Gimeno, L., Nieto, R., Sorí, R. (2020). The growing importance of oceanic moisture sources for continental precipitation. *npj Climate and Atmospheric Science* 3(1). doi:10.1038/s41612-020-00133-y.

Giraudo, R.F. (2018). Heteroglossic heritage and the first-place of the Kalahari. *International Journal of Heritage Studies* 24(2):128–141. doi:10.1080/13527258.2017.1317651.

GLC (2003). Global Land Cover 2000 database: European Commission, Joint Research Centre. URL: https://forobs.jrc.ec.europa.eu/products/glc2000/glc2000.php.

Goetz, A.F., Vane, G., Solomon, J.E., Rock, B.N. (1985). Imaging spectrometry for Earth remote sensing. *Science* 228(4704):1147–1153. doi:10.1126/science.228.4704.1147.

Gonfiantini, R. (1978). Standards for stable isotope measurements in natural compounds. *Nature* 271(5645):534–536. doi:10.1038/271534a0.

Graf, D.L., Cummings, K.S. (2006). Freshwater mussels (Mollusca: Bivalvia: Unionoida) of Angola, with description of a new species, Mutela wistarmorrisi. *Proceedings of the Academy of Natural Sciences of Philadelphia* 155(1):163–194. doi:10.1635/i0097-3157-155-1-163.1.

Grove, A.T. (1969). Landforms and climatic change in the Kalahari and Ngamiland. *The Geographical Journal* 135(2):191–212.

Guan, H., Zhang, X., Skrzypek, G., Sun, Z., Xu, X. (2013). Deuterium excess variations of rainfall events in a coastal area of South Australia and its relationship with synoptic weather systems and atmospheric moisture sources. *Journal of Geophysical Research: Atmospheres* 118(2):1123–1138. doi:10.1002/jgrd.50137.

Gummersbach, V.S. (2019). Reconstruction of transportation and depositional processes at the late Pleistocene lake basin at the Tsodilo Hills in NW Botswana on the basis of sediment analysis and multivariate statistic. M.Sc. Thesis. Freie Universität Berlin. Berlin, Germany.

References

Gunz, P., Bookstein, F.L., Mitteroecker, P., Stadlmayr, A., Seidler, H., Weber, G.W. (2009). Early modern human diversity suggests subdivided population structure and a complex out-of-Africa scenario. *Proceedings of the National Academy of Sciences* 106(15):6094–6098. doi:10.1073/pnas.0808160106.

Gupta, P., Noone, D., Galewsky, J., Sweeney, C., Vaughn, B.H. (2009). Demonstration of high-precision continuous measurements of water vapor isotopologues in laboratory and remote field deployments using wavelength-scanned cavity ring-down spectroscopy (WS-CRDS) technology. *Rapid communications in mass spectrometry: RCM* 23(16):2534–2542. doi:10.1002/rcm.4100.

Hahn, A., Schefuß, E., Groeneveld, J., Miller, C., Zabel, M. (2021). Glacial to interglacial climate variability in the southeastern African subtropics (25–20° S). *Climate of the Past* 17(1):345–360. doi:10.5194/cp-17-345-2021.

Hannaford, M. (2020). Climate Change and Society in Southern African History. Oxford Research Encyclopedia of African History. doi:10.1093/acrefore/9780190277734.013.294.

Harding, A.E., Forrest, M.D. (1989). Analysis of multiple geological datasets from the English Lake District. *IEEE Transactions on Geoscience and Remote Sensing* 27(6):732–739. doi:10.1109/36.35961.

Harris, C., Burgers, C., Miller, J., Rawoot, F., Burgers, C., Miller, J., Rawoot, F. (2010). O- and H-isotope record of Cape Town rainfall from 1996 to 2008, and its application to recharge studies of Table Mountain groundwater, South Africa. *South African Journal of Geology* 113(1):33–56. doi:10.2113/gssajg.113.1.33.

Hart, N.C.G., Reason, C.J., Fauchereau, N. (2013). Cloud bands over southern Africa: seasonality, contribution to rainfall variability and modulation by the MJO. *Climate Dynamics* 41(5-6):1199–1212. doi:10.1007/s00382-012-1589-4.

Hartmann, K., Wünnemann, B. (2009). Hydrological changes and Holocene climate variations in NW China, inferred from lake sediments of Juyanze palaeolake by factor analyses. *Quaternary International* 194(1-2):28–44. doi:10.1016/j.quaint.2007.06.037.

Hartmann, K., Wünnemann, B., Hölz, S., Kraetschell, A., Zhang, H. (2011). Neotectonic constraints on the Gaxun Nur inland basin in north-central China, derived from remote sensing, geomorphology and geophysical analyses. *Geological Society, London, Special Publications* 353(1):221–233. doi:10.1144/SP353.11.

Heine, K. (1981). Aride und pluviale Bedingungen während der letzten Kaltzeit in der Südwest-Kalahari (südliches Afrika): Ein Beitrag zur klimagenetischen Geomorphologie der Dünen, Pfannen und Täler. *Zeitschrift für Geomorphologie/Supplement* 38:1–37.

Heine, K. (1982). The main stages of the late Quaternary evolution of the Kalahari region, southern Africa. *Palaeoecology of Africa* 15:53–76.

Heine, K. (2019). Das Quartär in den Tropen: Eine Rekonstruktion des Paläoklimas. Springer Berlin and Springer Berlin Heidelberg, Berlin. doi:10.1007/978-3-662-57384-6.

Heiri, O., Lotter, A.F., Lemcke, G. (2001). Loss on ignition as a method for estimating organic and carbonate content in sediments: reproducibility and comparability of results. *Journal of Paleolimnology* 25::101–110.

Henn, B.M., Gignoux, C.R., Jobin, M., Granka, J.M., Macpherson, J.M., Kidd, J.M., Rodríguez-Botigué, L., Ramachandran, S., Hon, L., Brisbin, A., Lin, A.A., Underhill, P.A., Comas, D., Kidd, K.K., Norman, P.J., Parham, P., Bustamante, C.D., Mountain, J.L., Feldman, M.W. (2011). Hunter-gatherer genomic diversity suggests a southern African origin for modern humans. *Proceedings of the National Academy of Sciences* 108(13):5154–5162. doi:10.1073/pnas.1017511108.

Henshilwood, C.S., d'Errico, F., van Niekerk, K.L., Coquinot, Y., Jacobs, Z., Lauritzen, S.E., Menu, M., García-Moreno, R. (2011). A 100,000-Year-Old Ochre-Processing Workshop at Blombos Cave, South Africa. *Science* 334(6053):219. doi:10.1126/science.1211535.

Hersbach, H., Bell, B., Berrisford, P., Hirahara, S., Horányi, A., Muñoz-Sabater, J., Nicolas, J., Peubey, C., Radu, R., Schepers, D., Simmons, A., Soci, C., Abdalla, S., Abellan, X., Balsamo, G., Bechtold, P., Biavati, G., Bidlot, J., Bonavita, M., Chiara, G., Dahlgren, P., Dee, D., Diamantakis, M., Dragani, R., Flemming, J., Forbes, R., Fuentes, M., Geer, A., Haimberger, L., Healy, S., Hogan, R.J., Hólm, E., Janisková, M., Keeley, S., Laloyaux, P., Lopez, P., Lupu, C., Radnoti, G., Rosnay, P., Rozum, I., Vamborg, F., Villaume, S., Thépaut, J.N. (2020). The ERA5 global reanalysis. *Quarterly Journal of the Royal Meteorological Society* 146(730):1999–2049. doi:10.1002/qj.3803.

Hewitson, B.C., Tennant, W., Walawege, R. (2004). Atmospheric moisture transport and sources for southern Africa (WRC Report 1012/1/04).

Hoefs, J. (2004). Stable isotope geochemistry. 5. rev. and updated ed., Springer, Berlin and Heidelberg.

References

Hogg, A.G., Heaton, T.J., Hua, Q., Palmer, J.G., Turney, C.S.M., Southon, J., Bayliss, A., Blackwell, P.G., Boswijk, G., Bronk Ramsey, C., Pearson, C., Petchey, F., Reimer, P., Reimer, R.W., Wacker, L. (2020). SHCal20 Southern Hemisphere Calibration, 0–55,000 Years cal BP. *Radiocarbon* 62(4):759–778. doi:10.1017/RDC.2020.59.

Hollister, J.W. (2018). lakemorpho: Lake Morphometry Metrics (Version 1.1.1) [R package]. URL: https://CRAN.R-project.org/package=lakemorpho.

Hollister, J.W., Stachelek, J. (2017). lakemorpho: Calculating lake morphometry metrics in R. *F1000Research* 6:1718. doi:10.12688/f1000research.12512.1.

Holmgren, K., Karlén, W., Lauritzen, S.E., Lee-Thorp, J.A., Partridge, T.C., Piketh, S., Repinski, P., Stevenson, C., Svanered, O., Tyson, P.D. (1999). A 3000-year high-resolution stalagmite-based record of palaeoclimate for northeastern South Africa // A 3000-year high-resolution stalagmitebased record of palaeoclimate for northeastern South Africa. *The Holocene* 9(3):295–309. doi:10.1191/095968399672625464.

Holmgren, K., Lee-Thorp, J.A., Cooper, G.R., Lundblad, K., Partridge, T.C., Scott, L., Sithaldeen, R., Siep Talma, A., Tyson, P.D. (2003). Persistent millennial-scale climatic variability over the past 25,000 years in Southern Africa. *Quaternary Science Reviews* 22(21-22):2311–2326. doi:10.1016/S0277-3791(03)00204-X.

Hothorn, T., Buehlmann, P., Dudoit, S., Molinaro, A., van der Laan, M. (2006). Survival Ensembles. *Biostatistics* 7(3):355–373.

Howard, E., Washington, R. (2019). Drylines in Southern Africa: Rediscovering the Congo Air Boundary. *Journal of Climate* 32(23):8223–8242. doi:10.1175/JCLI-D-19-0437.1.

Howard, E., Washington, R. (2020). Tracing Future Spring and Summer Drying in Southern Africa to Tropical Lows and the Congo Air Boundary. *Journal of Climate* 33(14):6205–6228. doi:10.1175/JCLI-D-19-0755.1.

Huffman, T.N., Woodborne, S. (2016). Archaeology, baobabs and drought: Cultural proxies and environmental data from the Mapungubwe landscape, southern Africa. *The Holocene* 26(3):464–470. doi:10.1177/0959683615609753.

Hulme, M., Doherty, R., Ngara, T., New, M., Lister, D. (2001). African climate change: 1900-2100. *Climate Research* 17:145–168. doi:10.3354/cr017145.

Hunt, G.R. (1980). Electromagnetic radiation: The communication link in remote sensing, in: Siegal, B.S., Gillespie, A.R. (Eds.), Remote sensing in geology. Wiley, New York, pp. 5–45.

Hürkamp, K., Völkel, J., Heine, K., Bens, O., Leopold, M., Winkelbauer, J. (2011). Late quaternary environmental changes from aeolian and fluvial geoarchives in the southwestern Kalahari, South Africa: Implications for past african climate dynamics. *South African Journal of Geology* 114(3-4):459–474. doi:10.2113/gssajg.114.3-4.459.

Hutchins, D.G., Hutton, L.G., Hutton, S.M., Jones, C.R., Loenhert, E.P. (1976). A summary of the geology, seismicity, geomorphology and hydrogeology of the Okavango Delta. Gaborone, Botswana.

IAEA/WMO (2021). Global Network of Isotopes in Precipitation: The GNIP Database. URL: https://nucleus.iaea.org/wiser.

Imbroane, M.A., Melenti, C., Gorgan, D. (2007). Mineral Explorations by Landsat Image Ratios, in: IEEE Computer Society (Ed.), Proceedings of the 9th International Symposium on Symbolic and Numeric Algorithms for Scientific Computing, SYNASC 2007, IEEE, Piscataway, NJ. pp. 335–340. doi:10.1109/SYNASC.2007.52.

IPCC (2021). Climate Change 2021: The Physical Science Basis: Contribution of Working Group I to the Sixth Assessment Report of the Intergovernmental Panel on Climate Change [Masson-Delmotte, V., P. Zhai, A. Pirani, S. L. Connors, C. Péan, S. Berger, N. Caud, Y. Chen, L. Goldfarb, M. I. Gomis, M. Huang, K. Leitzell, E. Lonnoy, J. B. R. Matthews, T. K. Maycock, T. Waterfield, O. Yelekçi, R. Yu and B. Zhou (eds.)]. *Cambridge University Press* .

Ivester, A.H., Brook, G.A., Robbins, L.H., Campbell, A.C., Murphy, M.L., Marais, E. (2010). A sedimentary record of environmental change at Tsodilo Hills White Paintings Rock Shelter, Northwest Kalahari Desert, Botswana. *African Palaeoenvironments and Geomorphic Landscape Evolution: Palaeoecology of Africa Vol. 30, An International Yearbook of Landscape Evolution and Palaeoenvironments* 30:53.

Izzawati, Wallington, E.D., Woodhouse, I.H. (2006). Forest height retrieval from commercial X-band SAR products. *IEEE Transactions on Geoscience and Remote Sensing* 44(4):863–870. doi:10.1109/TGRS.2006.870828.

Jahn, B., Donner, B., Müller, P.J., Röhl, U., Schneider, R.R., Wefer, G. (2003). Pleistocene variations in dust input and marine productivity in the northern Benguela Current: Evidence of evolution of global glacial–interglacial cycles. *Palaeogeography, Palaeoclimatology, Palaeoecology* 193(3-4):515–533. doi:10.1016/S0031-0182(03)00264-5.

References

Jones, A.E., Wort, U.U., Morse, A.P., Hastings, I.M., Gagnon, A.S. (2007). Climate prediction of El Niño malaria epidemics in north-west Tanzania. *Malaria journal* 6(1):162. doi:10.1186/1475-2875-6-162.

Jury, M.R. (2012). An inter-comparison of model-simulated east–west climate gradients over South Africa. *Water SA* 38(4). doi:10.4314/wsa.v38i4.1.

Kabatereine, N.B., Standley, C.J., Sousa-Figueiredo, J.C., Fleming, F.M., Stothard, J.R., Talisuna, A., Fenwick, A. (2011). Integrated prevalence mapping of schistosomiasis, soil-transmitted helminthiasis and malaria in lakeside and island communities in Lake Victoria, Uganda. *Parasites & Vectors* 4(1):232. doi:10.1186/1756-3305-4-232.

Kahraman, S., Yeken, T. (2008). Determination of physical properties of carbonate rocks from P-wave velocity. *Bulletin of Engineering Geology and the Environment* 67(2):277–281. doi:10.1007/s10064-008-0139-0.

Kalbermatten, M., van de Ville, D., Turberg, P., Tuia, D., Joost, S. (2012). Multiscale analysis of geomorphological and geological features in high resolution digital elevation models using the wavelet transform. *Geomorphology* 138(1):352–363. doi:10.1016/j.geomorph.2011.09.023.

Kalinda, C., Chimbari, M.J., Mukaratirwa, S. (2017). Effect of temperature on the Bulinus globosus - Schistosoma haematobium system. *Infectious diseases of poverty* 6(1):57. doi:10.1186/s40249-017-0260-z.

Kaseke, K.F., Wang, L., Wanke, H., Turewicz, V., Koeniger, P. (2016). An Analysis of Precipitation Isotope Distributions across Namibia Using Historical Data. *PloS one* 11(5):e0154598. doi:10.1371/journal.pone.0154598.

Kearey, P., Brooks, M., Hill, I. (2002). An Introduction to Geophysical Exploration. 3 ed., Blackwell Science, Oxford.

Key, R.M., Ayres, N. (2000). The 1998 edition of the National Geological Map of Botswana. *Journal of African Earth Sciences* 30(3):427–451. doi:10.1016/s0899-5362(00)00030-0.

Kim, S.J., Crowley, T.J., Erickson, D.J., Govindasamy, B., Duffy, P.B., Lee, B.Y. (2008). High-resolution climate simulation of the last glacial maximum. *Climate Dynamics* 31(1):1–16. doi:10.1007/s00382-007-0332-z.

Kinabo, B.D., Atekwana, E.A., Hogan, J.P., Modisi, M.P., Wheaton, D.D., Kampunzu, A.B. (2007). Early structural development of the Okavango rift zone, NW Botswana. *Journal of African Earth Sciences* 48(2-3):125–136. doi:10.1016/j.jafrearsci.2007.02.005.

Kitagawa, H., van der Plicht, J. (1998). Atmospheric radiocarbon calibration to 45,000 yr B.P.: late glacial fluctuations and cosmogenic isotope production. *Science* 279(5354):1187–1190. doi:10.1126/science.279.5354.1187.

Kloos, H., David, R. (2002). The Paleoepidemiology of Schistosomiasis in Ancient Egypt. *Human Ecology Review* 9(1):14–25.

Lancaster, N. (1981). Paleoenvironmental implications of fixed dune systems in Southern Africa. *Palaeogeography, Palaeoclimatology, Palaeoecology* 33(4):327–346. doi:10.1016/0031-0182(81)90025-0.

LeGrande, A.N., Schmidt, G.A. (2006). Global gridded data set of the oxygen isotopic composition in seawater. *Geophysical Research Letters* 33(12):15833. doi:10.1029/2006GL026011.

Leketa, K., Abiye, T. (2020). Investigating stable isotope effects and moisture trajectories for rainfall events in Johannesburg, South Africa. *Water SA* 46(3 July). doi:10.17159/wsa/2020.v46.i3.8653.

Leketa, K., Abiye, T., Butler, M. (2018). Characterisation of groundwater recharge conditions and flow mechanisms in bedrock aquifers of the Johannesburg area, South Africa. *Environmental Earth Sciences* 77(21). doi:10.1007/s12665-018-7911-7.

Leng, M.J., Lamb, A.L., Lamb, H.F., Telford, R.J. (1999). Palaeoclimatic implications of isotopic data from modern and early Holocene shells of the freshwater snail Melanoides tuberculata,from lakes in the Ethiopian Rift Valley. *Journal of Paleolimnology* 21(1):97–106. doi:10.1023/A:1008079219280.

Leng, M.J., Marshall, J.D. (2004). Palaeoclimate interpretation of stable isotope data from lake sediment archives. *Quaternary Science Reviews* 23(7-8):811–831. doi:10.1016/j.quascirev.2003.06.012.

Liebmann, B., Bladé, I., Kiladis, G.N., Carvalho, L.M.V., B. Senay, G., Allured, D., Leroux, S., Funk, C. (2012). Seasonality of African Precipitation from 1996 to 2009. *Journal of Climate* 25(12):4304–4322. doi:10.1175/JCLI-D-11-00157.1.

Linol, B., de Wit, M.J., Guillocheau, F., de Wit, M.C.J., Anka, Z., Colin, J.P. (2015). Formation and Collapse of the Kalahari Duricrust ['African Surface'] Across the Congo Basin, with Implications for Changes in Rates of Cenozoic Off-Shore Sedimentation, in: de Wit, M.J., Guillocheau, F., de Wit, M.C.J. (Eds.), Geology and Resource Potential

of the Congo Basin. Springer, Berlin. Vol. 60 of *Regional Geology Reviews*, pp. 193–210. doi:10.1007/978-3-642-29482-2_10.

Loelkes, G.L. (1983). Land use/land cover and environmental photointerpretation keys. US Dept. of the Interior, Geological Survey.

Lu, J., Vecchi, G.A. (2015). Tropical Meteorology & Climate | Hadley Circulation, in: North, G.R. (Ed.), Encyclopedia of atmospheric sciences. Elsevier Science, Burlington, pp. 113–120. doi:10.1016/B978-0-12-382225-3.00161-4.

Lu, X.T., Gu, Q.Y., Limpanont, Y., Song, L.G., Wu, Z.D., Okanurak, K., Lv, Z.Y. (2018). Snail-borne parasitic diseases: an update on global epidemiological distribution, transmission interruption and control methods. *Infectious diseases of poverty* 7(1):28. doi:10.1186/s40249-018-0414-7.

Lyon, B., Mason, S.J. (2007). The 1997–98 Summer Rainfall Season in Southern Africa. Part I: Observations. *Journal of Climate* 20(20):5134–5148. doi:10.1175/JCLI4225.1.

Mabaso, M.L.H., Vounatsou, P., Midzi, S., Da Silva, J., Smith, T. (2006). Spatio-temporal analysis of the role of climate in inter-annual variation of malaria incidence in Zimbabwe. *International Journal of Health Geographics* 5(1):20. doi:10.1186/1476-072X-5-20.

Macron, C., Pohl, B., Richard, Y., Bessafi, M. (2014). How do Tropical Temperate Troughs Form and Develop over Southern Africa? *Journal of Climate* 27(4):1633–1647. doi:10.1175/JCLI-D-13-00175.1.

Mahulu, A., Clewing, C., Stelbrink, B., Chibwana, F.D., Tumwebaze, I., Russell Stothard, J., Albrecht, C. (2019). Cryptic intermediate snail host of the liver fluke Fasciola hepatica in Africa. *Parasites & Vectors* 12(1):573. doi:10.1186/s13071-019-3825-9.

Mamalakis, A., Randerson, J.T., Yu, J.Y., Pritchard, M.S., Magnusdottir, G., Smyth, P., Levine, P.A., Yu, S., Foufoula-Georgiou, E. (2021). Zonally contrasting shifts of the tropical rainbelt in response to climate change. *Nature Climate Change* 11:143–151. doi:10.1038/s41558-020-00963-x.

Martín-Fernández, J.A., Barceló-Vidal, C., Pawlowsky-Glahn, V. (2000). Zero Replacement in Compositional Data Sets, in: Kiers, H.A.l., Rasson, J.P., Groenen, P.J.f., Schader, M. (Eds.), Data Analysis, Classification, and Related Methods. Springer Berlin Heidelberg, Berlin, Heidelberg. Springer eBook Collection Mathematics and Statistics, pp. 155–160. doi:10.1007/978-3-642-59789-3_25.

Maruatona, P.B., Moses, O. (2021). Assessment of the onset, cessation, and duration of rainfall season over Botswana. *Modeling Earth Systems and Environment* doi:10.1007/s40808-021-01178-5.

Mason, S.J., Jury, M.R. (1997). Climatic variability and change over southern Africa: a reflection on underlying processes. *Progress in Physical Geography: Earth and Environment* 21(1):23–50. doi:10.1177/030913339702100103.

Maúre, G., Pinto, I., Ndebele-Murisa, M., Muthige, M., Lennard, C., Nikulin, G., Dosio, A., Meque, A. (2018). The southern African climate under 1.5 °C and 2 °C of global warming as simulated by CORDEX regional climate models. *Environmental Research Letters* 13(6):065002. doi:10.1088/1748-9326/aab190.

Mayaud, J.R., Bailey, R.M., Wiggs, G.F.S. (2017). Modelled responses of the Kalahari Desert to 21st century climate and land use change. *Scientific reports* 7(1):3887. doi:10.1038/s41598-017-04341-0.

McCall, G.S., Thomas, J.T. (2009). Re-examining the South African Middle-to-Later Stone Age transition: Multivariate analysis of the Umhlatuzana and Rose Cottage Cave stone tool assemblages. *Azania: Archaeological Research in Africa* 44(3):311–330. doi:10.1080/00672700903337519.

McCormick, M., Büntgen, U., Cane, M.A., Cook, E.R., Harper, K., Huybers, P., Litt, T., Manning, S.W., Mayewski, P.A., More, A.F.M., Nicolussi, K., Tegel, W. (2012). Climate Change during and after the Roman Empire: Reconstructing the Past from Scientific and Historical Evidence. *The Journal of Interdisciplinary History* 43(2):169–220. doi:10.1162/JINH_a_00379.

McDougall, I., Brown, F.H., Fleagle, J.G. (2005). Stratigraphic placement and age of modern humans from Kibish, Ethiopia. *Nature* 433(7027):733–736. doi:10.1038/nature03258.

McFarlane, M.J., Eckardt, F.D. (2007). Palaeodune morphology associated with the Gumare fault of the Okavango graben in the Botswana/Namibia borderland: a new model of tectonic influence. *South African Journal of Geology* 110(4):535–542. doi:10.2113/gssajg.110.4.535.

McGee, D., Donohoe, A., Marshall, J., Ferreira, D. (2014). Changes in ITCZ location and cross-equatorial heat transport at the Last Glacial Maximum, Heinrich Stadial 1, and the mid-Holocene. *Earth and Planetary Science Letters* 390:69–79. doi:10.1016/j.epsl.2013.12.043.

McLeman, R.A. (2014). Climate and human migration: Past experiences, future challenges. Cambridge University Press, New York. doi:10.1017/CBO9781139136938.

Mekiso, F.A., Ochieng, G.M. (2014). Stable Water Isotopes as Tracers at the Middle Mohlapitsi Catchment/ Wetland, South Africa. *International Journal of Engineering and Technology* 6(4).

Mendelsohn, J., Jarvis, A., Roberts, C., Robertson, T. (2002). Atlas of Namibia: A portrait of the land and its people. Ministry of Environment and Tourism, Windhoek, Namibia.

Mentzer, S.M. (2017). Rockshelter Settings, in: Gilbert, A.S., Goldberg, P., Holliday, V.T., Mandel, R.D., Sternberg, R.S. (Eds.), Encyclopedia of geoarchaeology. Springer, Dordrecht. Encyclopedia of earth sciences series, pp. 725–743. doi:10.1007/978-1-4020-4409-0_159.

Merlivat, L., Jouzel, J. (1979). Global climatic interpretation of the deuterium-oxygen 18 relationship for precipitation. *Journal of Geophysical Research* 84(C8):5029. doi:10.1029/JC084iC08p05029.

Merron, G.S. (1993). A Synopsis of Presentations and Discussions on the Fish and Fishery in the Okavango Delta, Botswana. *Botswana Notes and Records* 25:133–140. URL: http://www.jstor.org/stable/40979988.

Michczyński, A. (2007). Is it Possible to Find a Good Point Estimate of a Calibrated Radiocarbon Date? *Radiocarbon* 49(2):393–401. doi:10.1017/S0033822200042326.

Miller, C., Finch, J., Hill, T., Peterse, F., Humphries, M., Zabel, M., Schefuß, E. (2019). Late Quaternary climate variability at Mfabeni peatland, eastern South Africa. *Climate of the Past* 15(3):1153–1170. doi:10.5194/cp-15-1153-2019.

Miralles, D.G., Nieto, R., McDowell, N.G., Dorigo, W.A., Verhoest, N.E.C., Liu, Y.Y., Teuling, A.J., Dolman, A.J., Good, S.P., Gimeno, L. (2016). Contribution of water-limited ecoregions to their own supply of rainfall. *Environmental Research Letters* 11(12):124007. doi:10.1088/1748-9326/11/12/124007.

Mix, A. (2001). Environmental processes of the ice age: land, oceans, glaciers (EPILOG). *Quaternary Science Reviews* 20(4):627–657. doi:10.1016/S0277-3791(00)00145-1.

Miyasaka, T., Nakamura, H. (2010). Structure and Mechanisms of the Southern Hemisphere Summertime Subtropical Anticyclones. *Journal of Climate* 23(8):2115–2130. doi:10.1175/2009JCLI3008.1.

Mmualefe, L.C., Torto, N. (2011). Water quality in the Okavango Delta. *Water SA* 37(3). doi:10.4314/wsa.v37i3.68492.

Modisi, M.P., Atekwana, E.A., Kampunzu, A.B., Ngwisanyi, T.H. (2000). Rift kinematics during the incipient stages of continental extension: Evidence from the nascent Okavango rift basin, northwest Botswana. *Geology* 28(10):939. doi:10.1130/0091-7613(2000)28<939:RKDTIS>2.0.CO;2.

Moore, A.E., Cotterill, F.P.D., Eckardt, F.D. (2012). The Evolution and Ages of Makgadikdadi Paleo-Lakes: Consilient Evidence from Kalahari Drainage Evolution South-Central Africa. *South African Journal of Geology* 115(3):385–413. doi:10.2113/gssajg.115.3.385.

Mosepele, K., Moyle, P.B., Merron, G.S., Purkey, D.R., Mosepele, B. (2009). Fish, Floods, and Ecosystem Engineers: Aquatic Conservation in the Okavango Delta, Botswana. *BioScience* 59(1):53–64. doi:10.1525/bio.2009.59.1.9.

Moukam Kakmeni, F.M., Guimapi, R.Y.A., Ndjomatchoua, F.T., Pedro, S.A., Mutunga, J., Tonnang, H.E.Z. (2018). Spatial panorama of malaria prevalence in Africa under climate change and interventions scenarios. *International Journal of Health Geographics* 17(1):2. doi:10.1186/s12942-018-0122-3.

Mtethiwa, A.H.N., Nkwengulila, G., Bakuza, J., Sikawa, D., Kazembe, A. (2015). Extent of morbidity associated with schistosomiasis infection in Malawi: a review paper. *Infectious diseases of poverty* 4(1):25. doi:10.1186/s40249-015-0053-1.

Muller, M., Schreiner, B., Smith, L., van Koppen, B., Sally, H., Aliber, M., Cousins, B., Tapela, B., van der Merwe-Botha, M., Karar, E., Pietersen, K. (2009). Water security in South Africa. Number 12 in DBSA Development Planning Division Working Paper Series.

Munksgaard, N.C., Kurita, N., Sánchez-Murillo, R., Ahmed, N., Araguas, L., Balachew, D.L., Bird, M.I., Chakraborty, S., Kien Chinh, N., Cobb, K.M., Ellis, S.A., Esquivel-Hernández, G., Ganyaglo, S.Y., Gao, J., Gastmans, D., Kaseke, K.F., Kebede, S., Morales, M.R., Mueller, M., Poh, S.C., Santos, V.D., Shaoneng, H., Wang, L., Yacobaccio, H., Zwart, C. (2019). Data Descriptor: Daily observations of stable isotope ratios of rainfall in the tropics. *Scientific reports* 9(1):14419. doi:10.1038/s41598-019-50973-9.

Nash, D.J., Adamson, G.C.D., Ashcroft, L., Bauch, M., Camenisch, C., Degroot, D., Gergis, J., Jusopović, A., Labbé, T., Lin, K.H.E., Nicholson, S.D., Pei, Q., del Rosario Prieto, M., Rack, U., Rojas, F., White, S. (2021). Climate indices in historical climate reconstructions: a global state of the art. *Climate of the Past* 17(3):1273–1314. doi:10.5194/cp-17-1273-2021.

References

Nash, D.J., Meadows, M.E., Gulliver, V.L. (2006). Holocene environmental change in the Okavango Panhandle, northwest Botswana. *Quaternary Science Reviews* 25(11-12):1302–1322. doi:10.1016/j.quascirev.2005.11.004.

Nash, D.J., Meadows, M.E., Shaw, P.A., Baxter, A.J., Gieske, A. (1997). Late Holocene sedimentation rates and geomorphological significance of the Ncamasere valley, Okavango Delta, Botswana. *South African Geographical Journal* 79(2):93–100. doi:10.1080/03736245.1997.9713629.

Nel, E., Taylor, B., Hill, T., Atkinson, D. (2011). Demographic and Economic Changes in Small Towns in South Africa's Karoo: Looking from the Inside Out. *Urban Forum* 22(4):395–410. doi:10.1007/s12132-011-9131-z.

Nhemachena, C., Hassan, R. (2007). Micro-level analysis of farmers adaptation to climate change in Southern Africa (IFPRI Discussion Paper No. 714). Washington, D.C. (USA). IFPRI (International Food Policy Research Institute).

Nicholson, S.E. (1996). A Review of Climate Dynamics and Climate Variability in Eastern Africa, in: Whittaker, K.T., Johnson, T.C., Odada, E.O. (Eds.), The Limnology, Climatology and Paleoclimatology of the East African Lakes. Routledge, Amsterdam, pp. 25–56.

Nicholson, S.E., Flohn, H. (1980). African environmental and climatic changes and the general atmospheric circulation in late pleistocene and holocene. *Climatic Change* 2(4):313–348. doi:10.1007/BF00137203.

Nicholson, S.E., Funk, C., Fink, A.H. (2018). Rainfall over the African continent from the 19th through the 21st century. *Global and Planetary Change* 165:114–127. doi:10.1016/j.gloplacha.2017.12.014.

Nieto, R., Gimeno, L. (2019). A database of optimal integration times for Lagrangian studies of atmospheric moisture sources and sinks. *Scientific data* 6(1):59. doi:10.1038/s41597-019-0068-8.

Nkwinkwa Njouodo, A.S., Koseki, S., Keenlyside, N., Rouault, M. (2018). Atmospheric Signature of the Agulhas Current. *Geophysical Research Letters* 45(10):5185–5193. doi:10.1029/2018GL077042.

NOAA National Geophysical Data Center (2009). ETOPO1 1 Arc-Minute Global Relief Model.

Nthaba, B., Simon, R.E., Ogubazghi, G.M. (2018). Seismicity Study of Botswana from 1966 to 2012. *International Journal of Geosciences* 09(12):707–718. doi:10.4236/ijg.2018.912043.

Ntibinyane, O., Kwadiba, M.T., Maritinkole, J., Kelepile, P. (2019). Seismicity of the Okavango Delta Region: Contribution of IMS and Local stations. Science and Technology 2019. Vienna, Austria. doi:10.13140/RG.2.2.32138.21448.

Okada, K., Segawa, K., Hayashi, I. (1993). Removal of the vegetation effect from LANDSAT TM and GER imaging spectroradiometer data. *ISPRS Journal of Photogrammetry and Remote Sensing* 48(6):16–27. doi:10.1016/0924-2716(93)90052-O.

Oleś, A., Pau, G., Smith, M., Sklyar, O., Huber, Barry, J., Marais, P.A. (2018). EBImage: Image processing and analysis toolbox for R (Version 4.29.2) [R package].

Ortiz-Sepulveda, C.M., Stelbrink, B., Vekemans, X., Albrecht, C., Riedel, F., Todd, J.A., van Bocxlaer, B. (2020). Diversification dynamics of freshwater bivalves (Unionidae: Parreysiinae: Coelaturini) indicate historic hydrographic connections throughout the East African Rift System. *Molecular phylogenetics and evolution* 148:106816. doi:10.1016/j.ympev.2020.106816.

Otto, F.E.L., Wolski, P., Lehner, F., Tebaldi, C., van Oldenborgh, G.J., Hogesteeger, S., Singh, R., Holden, P., Fučkar, N.S., Odoulami, R.C., New, M. (2018). Anthropogenic influence on the drivers of the Western Cape drought 2015–2017. *Environmental Research Letters* 13(12):124010. doi:10.1088/1748-9326/aae9f9.

Parlov, J., Kovač, Z., Nakić, Z., Barešić, J. (2019). Using Water Stable Isotopes for Identifying Groundwater Recharge Sources of the Unconfined Alluvial Zagreb Aquifer (Croatia). *Water* 11(10):2177. doi:10.3390/w11102177.

Partridge, T.C., Scott, L., Hamilton, J.E. (1999). Synthetic reconstructions of southern African environments during the Last Glacial Maximum (21–18kyr) and the Holocene Altithermal (8–6kyr). *Quaternary International* 57-58:207–214. doi:10.1016/S1040-6182(98)00061-5.

Pascale, S., Pohl, B., Kapnick, S.B., Zhang, H. (2019). On the Angola Low Interannual Variability and Its Role in Modulating ENSO Effects in Southern Africa. *Journal of Climate* 32(15):4783–4803. doi:10.1175/JCLI-D-18-0745.1.

Passarge, S. (1904). Die Kalahari: Versuch einer physisch-geographischen Darstellung der Sandfelder des südafrikanischen Beckens. Dietrich Reimer (Ernst Vohsen), Berlin.

Pau, G., Fuchs, F., Sklyar, O., Boutros, M., Huber, W. (2010). EBImage – an R package for image processing with applications to cellular phenotypes. *Bioinformatics* 26(7):979–981. doi:10.1093/bioinformatics/btq046.

Peel, M.C., Finlayson, B.L., McMahon, T.A. (2007). Updated world map of the Köppen-Geiger climate classification. *Hydrology and Earth System Sciences* 11(5):1633–1644. doi:10.5194/hess-11-1633-2007.

Percival, J.B., White, H.P., Goodwin, T.A., Parsons, M.B., Smith, P.K. (2014). Mineralogy and spectral reflectance of soils and tailings from historical gold mines, Nova Scotia. *Geochemistry: Exploration, Environment, Analysis* 14(1):3–16. doi:10.1144/geochem2011-071.

Perko, R., Raggam, H., Deutscher, J., Gutjahr, K., Schardt, M. (2011). Forest Assessment Using High Resolution SAR Data in X-Band. *Remote Sensing* 3(4):792–815. doi:10.3390/rs3040792.

Perren, B.B., Hodgson, D.A., Roberts, S.J., Sime, L., van Nieuwenhuyze, W., Verleyen, E., Vyverman, W. (2020). Southward migration of the Southern Hemisphere westerly winds corresponds with warming climate over centennial timescales. *Communications Earth & Environment* 1(1). doi:10.1038/s43247-020-00059-6.

Peterson, A.T. (2009). Shifting suitability for malaria vectors across Africa with warming climates. *BMC infectious diseases* 9:59. doi:10.1186/1471-2334-9-59.

Pfahl, S., Sodemann, H. (2014). What controls deuterium excess in global precipitation? *Climate of the Past* 10(2):771–781. doi:10.5194/cp-10-771-2014.

Pfahl, S., Wernli, H. (2008). Air parcel trajectory analysis of stable isotopes in water vapor in the eastern Mediterranean. *Journal of Geophysical Research: Atmospheres* 113(D20):D03306. doi:10.1029/2008JD009839.

Pipaud, I., Loibl, D., Lehmkuhl, F. (2015). Evaluation of TanDEM-X elevation data for geomorphological mapping and interpretation in high mountain environments — A case study from SE Tibet, China. *Geomorphology* 246:232–254. doi:10.1016/j.geomorph.2015.06.025.

Pohl, B., Fauchereau, N., Reason, C.J., Rouault, M. (2010). Relationships between the Antarctic Oscillation, the Madden–Julian Oscillation, and ENSO, and Consequences for Rainfall Analysis. *Journal of Climate* 23(2):238–254. doi:10.1175/2009JCLI2443.1.

Pozo, M., Calvo, J. (2018). An Overview of Authigenic Magnesian Clays. *Minerals* 8(11):520. doi:10.3390/min8110520.

R Core Team (2019). R: A Language and Environment for Statistical Computing (Version 3.5.3) [Computer software]. Vienna, Austria. URL: http://www.R-project.org/.

Ramalli, L., Noël, H., Chiappini, J.D., Vincent, J., Barré-Cardi, H., Malfait, P., Normand, G., Busato, F., Gendrin, V., Mulero, S., Allienne, J.F., Fillaux, J., Boissier, J., Berry, A. (2018). A persistent risk of urogenital schistosomiasis transmission linked to the Cavu River in Southern Corsica since 2013. *Revue d'Épidémiologie et de Santé Publique* 66:S258–S259. doi:10.1016/j.respe.2018.05.064.

Ramisch, A., Bens, O., Buylaert, J.P., Eden, M., Heine, K., Hürkamp, K., Schwindt, D., Völkel, J. (2017). Fluvial landscape development in the southwestern Kalahari during the Holocene – Chronology and provenance of fluvial deposits in the Molopo Canyon. *Geomorphology* 281:94–107. doi:10.1016/j.geomorph.2016.12.021.

Rapolaki, R.S., Blamey, R.C., Hermes, J.C., Reason, C.J. (2020). Moisture sources associated with heavy rainfall over the Limpopo River Basin, southern Africa. *Climate Dynamics* 55:1473–1487. doi:10.1007/s00382-020-05336-w.

Reason, C.J. (2001). Evidence for the Influence of the Agulhas Current on Regional Atmospheric Circulation Patterns. *Journal of Climate* 14(12):2769–2778. doi:10.1175/1520-0442(2001)014<2769:EFTIOT>2.0.CO;2.

Reason, C.J. (2019). Low-frequency variability in the Botswana High and southern African regional climate. *Theoretical and Applied Climatology* 137:1321–1334. doi:10.1007/s00704-018-2661-8.

Reason, C.J., Landmann, W., Tennant, W. (2006). Seasonal to Decadal Prediction of Southern African Climate and Its Links with Variability of the Atlantic Ocean. *Bulletin of the American Meteorological Society* 87(7):941–956. doi:10.1175/BAMS-87-7-941.

Rich, S.M., Licht, M.C., Hudson, R.R., Ayala, F.J. (1998). Malaria's Eve: evidence of a recent population bottleneck throughout the world populations of Plasmodium falciparum. *Proceedings of the National Academy of Sciences* 95(8):4425–4430. doi:10.1073/pnas.95.8.4425.

Richter, T.O., van der Gaast, S., Koster, B., Vaars, A., Gieles, R., de Stigter, H.C., de Haas, H., van Weering, T.C.E. (2006). The Avaatech XRF Core Scanner: technical description

and applications to NE Atlantic sediments. *Geological Society, London, Special Publications* 267(1):39–50. doi:10.1144/GSL.SP.2006.267.01.03.

Riedel, F., Henderson, A.C.G., Heußner, K.U., Kaufmann, G., Kossler, A., Leipe, C., Shemang, E., Taft, L. (2014). Dynamics of a Kalahari long-lived mega-lake system: hydromorphological and limnological changes in the Makgadikgadi Basin (Botswana) during the terminal 50 ka. *Hydrobiologia* 739(1):25–53. doi:10.1007/s10750-013-1647-x.

Ringrose, S., Huntsman-Mapila, P., Downey, W., Coetzee, S., Fey, M., Vanderpost, C., Vink, B., Kemosidile, T., Kolokose, D. (2008). Diagenesis in Okavango fan and adjacent dune deposits with implications for the record of palaeo-environmental change in Makgadikgadi–Okavango–Zambezi basin, northern Botswana. *Geomorphology* 101(4):544–557. doi:10.1016/j.geomorph.2008.02.008.

Rito, T., Vieira, D., Silva, M., Conde-Sousa, E., Pereira, L., Mellars, P., Richards, M.B., Soares, P. (2019). A dispersal of Homo sapiens from southern to eastern Africa immediately preceded the out-of-Africa migration. *Scientific reports* 9(1):4728. doi:10.1038/s41598-019-41176-3.

Rizzoli, P., Martone, M., Gonzalez, C., Wecklich, C., Borla Tridon, D., Bräutigam, B., Bachmann, M., Schulze, D., Fritz, T., Huber, M., Wessel, B., Krieger, G., Zink, M., Moreira, A. (2017). Generation and performance assessment of the global TanDEM-X digital elevation model. *ISPRS Journal of Photogrammetry and Remote Sensing* 132:119–139. doi:10.1016/j.isprsjprs.2017.08.008.

Robbins, L.H., Brook, G.A., Murphy, M.L., Ivester, A.H., Campbell, A.C. (2016). The Kalahari During MIS 6-2 (190–12 ka): Archaeology, Paleoenvironment, and Population Dynamics, in: Jones, S.C., Stewart, B.A. (Eds.), Africa from MIS 6-2. Springer, Dordrecht. Vol. 35 of *Vertebrate Paleobiology and Paleoanthropology*, pp. 175–193. doi:10.1007/978-94-017-7520-5_10.

Robbins, L.H., Murphy, M., Campbell, A.C. (2010). Windows into the Past: Excavating Stone Age Shelters, in: Campbell, A.C., Robbins, L.H., Taylor, M. (Eds.), Tsodilo Hills. Michigan State University Press, East Lansing, pp. 50–63.

Robbins, L.H., Murphy, M.L. (2011). An overview of the Later and Middle Stone Age at Tsodilo Hills. *Botswana Notes and Records* 43:130–139.

Robbins, L.H., Murphy, M.L., Brook, G.A., Ivester, A.H., Campbell, A.C., Klein, R.G., Milo, R.G., Stewart, K.M., Downey, W.S., Stevens, N.J. (2000). Archaeology, Palaeoenvironment, and Chronology of the Tsodilo Hills White Paintings Rock Shelter,

Northwest Kalahari Desert, Botswana. *Journal of Archaeological Science* 27(11):1085–1113. doi:10.1006/jasc.2000.0597.

Robbins, L.H., Murphy, M.L., Campbell, A.C., Brook, G.A. (1996). Excavations at the Tsodilo Hills Rhino Cave. *Botswana Notes and Records* 28(1):23–53. URL: https://journals.co.za/doi/pdf/10.10520/aja052550590_398.

Robbins, L.H., Murphy, M.L., Stewart, K.M., Campbell, A.C., Brook, G.A. (1994). News and Short Contributions: Barbed Bone Points, Paleoenvironment, and the Antiquity of Fish Exploitation in the Kalahari Desert, Botswana. *Journal of Field Archaeology* 21(2):257–264. doi:10.2307/529874.

Rodriguez, F., Maire, E., Courjault-Radé, P., Darrozes, J. (2002). The Black Top Hat function applied to a DEM: A tool to estimate recent incision in a mountainous watershed (Estibère Watershed, Central Pyrenees). *Geophysical Research Letters* 29(6):9–1–9–4. doi:10.1029/2001GL014412.

Rozanski, K., Araguas-Araguas, L.J., Gonfiantini, R. (1993). Isotopic Patterns in Modern Global Precipitation, in: Swart, P.K., Lohmann, K.C., Mckenzie, J., Savin, S. (Eds.), Climate Change in Continental Isotopic Records. American Geophysical Union, Washington, DC. Vol. 27 of *Geophysical Monograph Series*, pp. 1–36. doi:10.1029/GM078p0001.

Sabins, F.F. (1999). Remote sensing for mineral exploration. *Ore Geology Reviews* 14(3-4):157–183. doi:10.1016/S0169-1368(99)00007-4.

Sadr, K. (2015). Livestock First Reached Southern Africa in Two Separate Events. *PloS one* 10(8):e0134215. doi:10.1371/journal.pone.0134215.

Sahra (2005). Isotopes & Hydrology. URL: http://web.sahra.arizona.edu/programs/isotopes/oxygen.html.

Sallares, R., Bouwman, A., Anderung, C. (2004). The spread of malaria to Southern Europe in antiquity: new approaches to old problems. *Medical History* 48(3):311–328. doi:10.1017/S0025727300007651.

Salzburger, W., Meyer, A. (2004). The species flocks of East African cichlid fishes: recent advances in molecular phylogenetics and population genetics. *Die Naturwissenschaften* 91(6):277–290. doi:10.1007/s00114-004-0528-6.

Sandmeier, K.J. (2017). REFLEXW - program for the processing of seismic, acoustic or electromagnetic reflection, refraction and transmission data (Version 8.4) [Computer software].

Scerri, E.M.L., Thomas, M.G., Manica, A., Gunz, P., Stock, J.T., Stringer, C., Grove, M., Groucutt, H.S., Timmermann, A., Rightmire, G.P., d'Errico, F., Tryon, C.A., Drake, N.A., Brooks, A.S., Dennell, R.W., Durbin, R., Henn, B.M., Lee-Thorp, J., deMenocal, P., Petraglia, M.D., Thompson, J.C., Scally, A., Chikhi, L. (2018). Did Our Species Evolve in Subdivided Populations across Africa, and Why Does It Matter? *Trends in ecology & evolution* 33(8):582–594. doi:10.1016/j.tree.2018.05.005.

Schlaepfer, D.R., Bradford, J.B., Lauenroth, W.K., Munson, S.M., Tietjen, B., Hall, S.A., Wilson, S.D., Duniway, M.C., Jia, G., Pyke, D.A., Lkhagva, A., Jamiyansharav, K. (2017). Climate change reduces extent of temperate drylands and intensifies drought in deep soils. *Nature communications* 8:14196. doi:10.1038/ncomms14196.

Schmidt, M., Fuchs, M., Henderson, A.C.G., Kossler, A., Leng, M.J., Mackay, A.W., Shemang, E., Riedel, F. (2017). Paleolimnological features of a mega-lake phase in the Makgadikgadi Basin (Kalahari, Botswana) during Marine Isotope Stage 5 inferred from diatoms. *Journal of Paleolimnology* 58(3):373–390. doi:10.1007/s10933-017-9984-9.

Schneider, T., Bischoff, T., Haug, G.H. (2014). Migrations and dynamics of the intertropical convergence zone. *Nature* 513:45–53. doi:10.1038/nature13636.

Schneider, W.A. (1978). Integral formulation for migration in two and three dimensions. *Geophysics* 43(1):49–76. doi:10.1190/1.1440828.

Scholz, C.H., Koczynski, T.A., Hutchins, D.G. (1976). Evidence for Incipient Rifting in Southern Africa. *Geophysical Journal International* 44(1):135–144. doi:10.1111/j.1365-246X.1976.tb00278.x.

Schüller, I., Belz, L., Wilkes, H., Wehrmann, A. (2018). Late Quaternary shift in southern African rainfall zones: sedimentary and geochemical data from Kalahari pans. *Zeitschrift für Geomorphologie* 61(4):339–362. doi:10.1127/zfg/2018/0556.

Schulze, D., Zink, M., Krieger, G., Fiedler, H., Böer, J., Moreira, A. (2008). TanDEM-X: TerraSAR-X add-on for Digital Elevation Measurements. Jahreskongress Nutzung des Weltraums. Berlin, Germany. URL: https://elib.dlr.de/56717/.

Schumann, G.J.P., Moller, D.K. (2015). Microwave remote sensing of flood inundation. *Physics and Chemistry of the Earth, Parts A/B/C* 83-84:84–95. doi:10.1016/j.pce.2015.05.002.

Schuster, M., Roquin, C., Duringer, P., Brunet, M., Caugy, M., Fontugne, M., Taïsso Mackaye, H., Vignaud, P., Ghienne, J.F. (2005). Holocene Lake Mega-Chad palaeoshorelines from space. *Quaternary Science Reviews* 24(16-17):1821–1827. doi:10.1016/j.quascirev.2005.02.001.

Schuster, S.C., Miller, W., Ratan, A., Tomsho, L.P., Giardine, B., Kasson, L.R., Harris, R.S., Petersen, D.C., Zhao, F., Qi, J., Alkan, C., Kidd, J.M., Sun, Y., Drautz, D.I., Bouffard, P., Muzny, D.M., Reid, J.G., Nazareth, L.V., Wang, Q., Burhans, R., Riemer, C., Wittekindt, N.E., Moorjani, P., Tindall, E.A., Danko, C.G., Teo, W.S., Buboltz, A.M., Zhang, Z., Ma, Q., Oosthuysen, A., Steenkamp, A.W., Oostuisen, H., Venter, P., Gajewski, J., Zhang, Y., Pugh, B.F., Makova, K.D., Nekrutenko, A., Mardis, E.R., Patterson, N., Pringle, T.H., Chiaromonte, F., Mullikin, J.C., Eichler, E.E., Hardison, R.C., Gibbs, R.A., Harkins, T.T., Hayes, V.M. (2010). Complete Khoisan and Bantu genomes from southern Africa. *Nature* 463(7283):943–947. doi:10.1038/nature08795.

Schwartz, E., Kozarsky, P., Wilson, M., Cetron, M. (2005). Schistosome infection among river rafters on Omo River, Ethiopia. *Journal of Travel Medicine* 12(1):3–8. doi:10.2310/7060.2005.00002.

Secor, W.E. (2014). Water-based interventions for schistosomiasis control. *Pathogens and Global Health* 108(5):246–254. doi:10.1179/2047773214Y.0000000149.

Segadika, P. (2006). Managing Intangible Heritage at Tsodilo. *Museum International* 58(1-2):31–40. doi:10.1111/j.1468-0033.2006.00548.x.

Sharma (2001). The resurgence of trypanosomosis in Botswana. *J. S. Afr. Vet. Assoc.* 72:232.

Shemang, E.M., Molwalefhe, L.N. (2011). Geomorphic Landforms and Tectonism Along the Eastern Margin of the Okavango Rift Zone, North Western Botswana as Deduced from Geophysical Data in the Area, in: Sharkov, E.V. (Ed.), New frontiers in tectonic research. InTech, Rijeka, Croatia, pp. 169–182. doi:10.5772/18863.

Sianga, K., Fynn, R. (2017). The vegetation and wildlife habitats of the Savuti-Mababe-Linyanti ecosystem, northern Botswana. *Koedoe* 59(2). doi:10.4102/koedoe.v59i2.1406.

References

Sietz, D., Lüdeke, M.K., Walther, C. (2011). Categorisation of typical vulnerability patterns in global drylands. *Global Environmental Change* 21(2):431–440. doi:10.1016/j.gloenvcha.2010.11.005.

Silva, J.A., Matyas, C.J. (2014). Relating Rainfall Patterns to Agricultural Income: Implications for Rural Development in Mozambique. *Weather, Climate, and Society* 6(2):218–237. doi:10.1175/WCAS-D-13-00012.1.

Singer, A. (1979). Palygorskite in sediments: Detrital, diagenetic or neoformed — A critical review. *Geologische Rundschau* 68(3):996–1008. doi:10.1007/BF02274683.

Singletary, S.J., Hanson, R.E., Martin, M.W., Crowley, J.L., Bowring, S.A., Key, R.M., Ramokate, L.V., Direng, B.B., Krol, M.A. (2003). Geochronology of basement rocks in the Kalahari Desert, Botswana, and implications for regional Proterozoic tectonics. *Precambrian Research* 121(1-2):47–71. doi:10.1016/S0301-9268(02)00201-2.

Sinka, M.E., Bangs, M.J., Manguin, S., Coetzee, M., Mbogo, C.M., Hemingway, J., Patil, A.P., Temperley, W.H., Gething, P.W., Kabaria, C.W., Okara, R.M., van Boeckel, T., Godfray, H.C.J., Harbach, R.E., Hay, S.I. (2010). The dominant Anopheles vectors of human malaria in Africa, Europe and the Middle East: occurrence data, distribution maps and bionomic précis. *Parasites & Vectors* 3(1):117. doi:10.1186/1756-3305-3-117.

Soares, P., Rito, T., Pereira, L., Richards, M.B. (2016). A Genetic Perspective on African Prehistory, in: Jones, S.C., Stewart, B.A. (Eds.), Africa from MIS 6-2. Springer, Dordrecht. Vertebrate Paleobiology and Paleoanthropology, pp. 383–405. doi:10.1007/978-94-017-7520-5_18.

Sodemann, H., Schwierz, C., Wernli, H. (2008). Interannual variability of Greenland winter precipitation sources: Lagrangian moisture diagnostic and North Atlantic Oscillation influence. *Journal of Geophysical Research* 113(D3):1939. doi:10.1029/2007JD008503.

Soren, D. (2003). Can archaeologists excavate evidence of malaria? *World Archaeology* 35(2):193–209. doi:10.1080/0043824032000111371.

Sparks, J., Smith, W. (2005). Freshwater Fishes, Dispersal Ability, and Nonevidence: "Gondwana Life Rafts" to the Rescue. *Systematic biology* 54(1):158–165. doi:10.1080/10635150590906019.

Spinage, C.A. (Ed.) (2012). African Ecology: Benchmarks and Historical Perspectives. Springer Geography, Springer Berlin Heidelberg, Berlin, Heidelberg. doi:10.1007/978-3-642-22872-8.

Sprenger, M., Wernli, H. (2015). The LAGRANTO Lagrangian analysis tool – version 2.0. *Geoscientific Model Development* 8(8):2569–2586. doi:10.5194/gmd-8-2569-2015.

Staurset, S., Coulson, S. (2014). Sub-surface movement of stone artefacts at White Paintings Shelter, Tsodilo Hills, Botswana: implications for the Middle Stone Age chronology of central southern Africa. *Journal of Human Evolution* 75:153–165. doi:10.1016/j.jhevol.2014.04.006.

Steinmann, P., Keiser, J., Bos, R., Tanner, M., Utzinger, J. (2006). Schistosomiasis and water resources development: systematic review, meta-analysis, and estimates of people at risk. *The Lancet Infectious Diseases* 6(7):411–425. doi:10.1016/S1473-3099(06)70521-7.

Stewart, M.K. (1975). Stable isotope fractionation due to evaporation and isotopic exchange of falling waterdrops: Applications to atmospheric processes and evaporation of lakes. *Journal of Geophysical Research* 80(9):1133–1146. doi:10.1029/JC080i009p01133.

Stone, A.E. (2014). Last Glacial Maximum conditions in southern Africa. *Progress in Physical Geography: Earth and Environment* 38(5):519–542. doi:10.1177/0309133314528943.

Stringer, C., Galway-Witham, J. (2017). Palaeoanthropology: On the origin of our species. *Nature* 546(7657):212–214. doi:10.1038/546212a.

Strobl, C., Boulesteix, A.L., Kneib, T., Augustin, T., Zeileis, A. (2008). Conditional variable importance for random forests. *BMC bioinformatics* 9:307. doi:10.1186/1471-2105-9-307.

Strobl, C., Boulesteix, A.L., Zeileis, A., Hothorn, T. (2007). Bias in random forest variable importance measures: illustrations, sources and a solution. *BMC bioinformatics* 8:25. doi:10.1186/1471-2105-8-25.

Strobl, C., Hothorn, T., Zeileis, A. (2009). Party on! *The R Journal* 1(2):14–17. URL: https://journal.r-project.org/archive/2009/RJ-2009-013/index.html.

Stuiver, M., Pearson, G.W. (1993). High-precision bidecadal calibration of the radiocarbon time scale. *Radiocarbon* 35(1):1–23.

Stuiver, M., Reimer, P.J. (1993). Extended ^{14}C data base and revised CALIB 3.0 ^{14}C age calibration program. *Radiocarbon* 35(1):215–230.

Stuiver, M., Reimer, P.J. (2020). CALIB Rev 8.1.0 [Computer software]: Radiocarbon Calibration Program. URL: http://calib.org.

Stuiver, M., Reimer, P.J., Reimer, R.W. (1999). CALIB 4.0 [www program]: Radiocarbon Calibration Program.

Taft, L., Mischke, S., Wiechert, U., Leipe, C., Rajabov, I., Riedel, F. (2014). Sclerochronological oxygen and carbon isotope ratios in *Radix* (Gastropoda) shells indicate changes of glacial meltwater flux and temperature since 4,200 cal yr BP at Lake Karakul, eastern Pamirs (Tajikistan). *Journal of Paleolimnology* 52(1-2):27–41. doi:10.1007/s10933-014-9776-4.

Taft, L., Wiechert, U., Riedel, F., Weynell, M., Zhang, H. (2012). Sub-seasonal oxygen and carbon isotope variations in shells of modern *Radix* sp. (Gastropoda) from the Tibetan Plateau: potential of a new archive for palaeoclimatic studies. *Quaternary Science Reviews* 34:44–56. doi:10.1016/j.quascirev.2011.12.006.

Taft, L., Wiechert, U., Zhang, H., Lei, G., Mischke, S., Plessen, B., Weynell, M., Winkler, A., Riedel, F. (2013). Oxygen and carbon isotope patterns archived in shells of the aquatic gastropod *Radix*: Hydrologic and climatic signals across the Tibetan Plateau in sub-monthly resolution. *Quaternary International* 290-291:282–298. doi:10.1016/j.quaint.2012.10.031.

Tanase, M.A., Ismail, I., Lowell, K., Karyanto, O., Santoro, M. (2015). Detecting and Quantifying Forest Change: The Potential of Existing C- and X-Band Radar Datasets. *PloS one* 10(6):e0131079. doi:10.1371/journal.pone.0131079.

The MathWorks, I. (2015a). MATLAB R2015a [Computer software]. Natick, Massachusetts, United States.

The MathWorks, I. (2015b). Wavelet Toolbox (Version 4.14.1) [Matlab Toolbox]. Natick, Massachusetts, United States.

Thomas, D.S., Brook, G.A., Shaw, P.A., Bateman, M.D., Haberyan, K.A., Appleton, C., Nash, D.J., McLaren, S., Davies, F. (2003). Late Pleistocene wetting and drying in the NW Kalahari: an integrated study from the Tsodilo Hills, Botswana. *Quaternary International* 104(1):53–67. doi:10.1016/S1040-6182(02)00135-0.

Thomas, D.S., Burrough, S.L. (2016). Luminescence-based dune chronologies in southern Africa: Analysis and interpretation of dune database records across the subcontinent. *Quaternary International* 410:30–45. doi:10.1016/j.quaint.2013.09.008.

Thomas, D.S., O'Connor, P.W., Bateman, M.D., Shaw, P.A., Stokes, S., Nash, D.J. (2000). Dune activity as a record of late Quaternary aridity in the Northern Kalahari: new evidence from northern Namibia interpreted in the context of regional arid and humid chronologies. *Palaeogeography, Palaeoclimatology, Palaeoecology* 156(3-4):243–259. doi:10.1016/S0031-0182(99)00143-1.

Thomas, D.S., Shaw, P.A. (2002). Late Quaternary environmental change in central southern Africa: new data, synthesis, issues and prospects. *Quaternary Science Reviews* 21(7):783–797. doi:10.1016/S0277-3791(01)00127-5.

Thomson, M.C., Muñoz, Á.G., Cousin, R., Shumake-Guillemot, J. (2018). Climate drivers of vector-borne diseases in Africa and their relevance to control programmes. *Infectious diseases of poverty* 7(1):81. doi:10.1186/s40249-018-0460-1.

Timmermann, A., Friedrich, T. (2016). Late Pleistocene climate drivers of early human migration. *Nature* 538:92–95. doi:10.1038/nature19365.

Tishkoff, S.A., Reed, F.A., Friedlaender, F.R., Ehret, C., Ranciaro, A., Froment, A., Hirbo, J.B., Awomoyi, A.A., Bodo, J.M., Doumbo, O., Ibrahim, M., Juma, A.T., Kotze, M.J., Lema, G., Moore, J.H., Mortensen, H., Nyambo, T.B., Omar, S.A., Powell, K., Pretorius, G.S., Smith, M.W., Thera, M.A., Wambebe, C., Weber, J.L., Williams, S.M. (2009). The genetic structure and history of Africans and African Americans. *Science* 324(5930):1035–1044. doi:10.1126/science.1172257.

Tiwari, M., Singh, A.K., Sinha, D.K. (2015). Stable Isotopes: Tools for Understanding Past Climatic Conditions and Their Applications in Chemostratigraphy, in: Ramkumar, M. (Ed.), Chemostratigraphy. Elsevier, Amsterdam, Netherlands. Vol. 19, pp. 65–92. doi:10.1016/B978-0-12-419968-2.00003-0.

Todd, M.C., Washington, R. (1999). Circulation anomalies associated with tropical-temperate troughs in southern Africa and the south west Indian Ocean. *Climate Dynamics* 15(12):937–951. doi:10.1007/s003820050323.

Tonnang, H.E.Z., Kangalawe, R.Y.M., Yanda, P.Z. (2010). Predicting and mapping malaria under climate change scenarios: the potential redistribution of malaria vectors in Africa. *Malaria journal* 9(1):111. doi:10.1186/1475-2875-9-111.

Tukey, J.W. (1949). Comparing Individual Means in the Analysis of Variance. *Biometrics* 5(2):99. doi:10.2307/3001913.

Tyson, P.D., Preston-Whyte, R.A. (2000). The weather and climate of Southern Africa. 2nd ed. ed., Oxford University Press, Cape Town.

UNESCO (2001). WHC Nomination Documentation Dossier: Tsodilo.

van den Boogaart, K.G., Tolosana-Delgado, R., Bren, M. (2020). compositions: Compositional Data Analysis (version 1.40-5) [R package]. URL: https://CRAN.R-project.org/package=compositions.

van Wyk, B., van Wyk, P. (1997). Field guide to trees of Southern Africa: Featuring more than 1000 species. 1 ed., Struik Publishers (Pty) Ltd, Cape Town.

van Zinderen Bakker, E.M. (1975). The Origin and Palaeoenvironment of the Namib Desert Biome. *Journal of Biogeography* 2(2):65–73. URL: https://www.jstor.org/stable/3038074.

van Zinderen Bakker, E.M. (1976). The evolution of Late Quaternary palaeoclimates of southern Africa. *Palaeoecology of Africa* 9:160–202.

Villa, P., Soriano, S., Tsanova, T., Degano, I., Higham, T.F.G., d'Errico, F., Backwell, L., Lucejko, J.J., Colombini, M.P., Beaumont, P.B. (2012). Border Cave and the beginning of the Later Stone Age in South Africa. *Proceedings of the National Academy of Sciences* 109(33):13208–13213. doi:10.1073/pnas.1202629109.

Vlag, P.A., Kruiver, P.P., Dekkers, M.J. (2004). Evaluating climate change by multivariate statistical techniques on magnetic and chemical properties of marine sediments (Azores region). *Palaeogeography, Palaeoclimatology, Palaeoecology* 212(1-2):23–44. doi:10.1016/j.palaeo.2004.05.015.

Walker, C., Milton, S.J., O'Connor, T.G., Maguire, J.M., Dean, W.R.J. (2018). Drivers and trajectories of social and ecological change in the Karoo, South Africa. *African Journal of Range & Forage Science* 35(3-4):157–177. doi:10.2989/10220119.2018.1518263.

Walter, H., Lieth, H. (1960). Klimadiagramm-Weltatlas. G. Fischer, Jena, Germany.

Walz, Y., Wegmann, M., Dech, S., Raso, G., Utzinger, J. (2015). Risk profiling of schistosomiasis using remote sensing: approaches, challenges and outlook. *Parasites & Vectors* 8(1):163. doi:10.1186/s13071-015-0732-6.

Wanke, H., Gaj, M., Beyer, M., Koeniger, P., Hamutoko, J.T. (2018). Stable isotope signatures of meteoric water in the Cuvelai-Etosha Basin, Namibia: Seasonal characteristics, trends and relations to southern African patterns. *Isotopes in environmental and health studies* 54(6):588–607. doi:10.1080/10256016.2018.1505724.

Washington, R., Todd, M.C. (1999). Tropical-temperate links in southern African and Southwest Indian Ocean satellite-derived daily rainfall. *International Journal of Climatology* 19(14):1601–1616. doi:10.1002/(SICI)1097-0088(19991130)19:14<1601::AID-JOC407>3.3.CO;2-S.

Weaver, T.D. (2012). Did a discrete event 200,000-100,000 years ago produce modern humans? *Journal of Human Evolution* 63(1):121–126. doi:10.1016/j.jhevol.2012.04.003.

Webb Jr., J.L.A. (2005). Malaria and the peopling of early tropical Africa. *Journal of World History* 16(3):269–291. URL: https://www.jstor.org/stable/20079330.

Weltje, G.J. (1997). End-member modeling of compositional data: Numerical-statistical algorithms for solving the explicit mixing problem. *Mathematical Geology* 29(4):503–549. doi:10.1007/BF02775085.

Weltje, G.J., Tjallingii, R. (2008). Calibration of XRF core scanners for quantitative geochemical logging of sediment cores: Theory and application. *Earth and Planetary Science Letters* 274(3-4):423–438. doi:10.1016/j.epsl.2008.07.054.

Wendorff, M. (2005). Outline of lithostratigraphy, sedimentation and tectonics of the Tsodilo Hills Group, a Neoproterozoic-Lower Palaeozoic siliciclastic succession in NW Botswana. *Annales Societatis Geologorum Poloniae* 75:17–25.

Wernli, H., Davies, H.C. (1997). A lagrangian-based analysis of extratropical cyclones. I: The method and some applications. *Quarterly Journal of the Royal Meteorological Society* 123(538):467–489. doi:10.1002/qj.49712353811.

Wessel, B., Huber, M., Wohlfart, C., Marschalk, U., Kosmann, D., Roth, A. (2018). Accuracy assessment of the global TanDEM-X Digital Elevation Model with GPS data. *ISPRS Journal of Photogrammetry and Remote Sensing* 139:171–182. doi:10.1016/j.isprsjprs.2018.02.017.

West, A.G., February, E.C., Bowen, G.J. (2014). Spatial analysis of hydrogen and oxygen stable isotopes ("isoscapes") in ground water and tap water across South Africa. *Journal of Geochemical Exploration* 145:213–222. doi:10.1016/j.gexplo.2014.06.009.

Weydahl, D.J., Sagstuen, J., Dick, Ø.B., Rønning, H. (2007). SRTM DEM accuracy assessment over vegetated areas in Norway. *International Journal of Remote Sensing* 28(16):3513–3527. doi:10.1080/01431160600993447.

Wiese, R., Hartmann, K., Gummersbach, V.S., Shemang, E.M., Struck, U., Riedel, F. (2020). Lake highstands in the northern Kalahari, Botswana, during MIS 3b and LGM. *Quaternary International* 558:10–18. doi:10.1016/j.quaint.2020.08.016.

World Bank Group (2016). Lesotho Water Security and Climate Change Assessment. Washington D. C. URL: https://openknowledge.worldbank.org/handle/10986/24905.

World Food Programme (2021). Climate change in southern Africa. Johannesburg, South Africa.

References

Wright, C.A. (1970). The ecology of African schistosomiasis." Symposia of the Society for the Study of Human Biology, Vol. 9. "Human ecology in the tropics. Oxford, England: Pergamon Press.

Wünnemann, B., Demske, D., Tarasov, P.E., Kotlia, B.S., Reinhardt, C., Bloemendal, J., Diekmann, B., Hartmann, K., Krois, J., Riedel, F. (2010). Hydrological evolution during the last 15kyr in the Tso Kar lake basin (Ladakh, India), derived from geomorphological, sedimentological and palynological records. *Quaternary Science Reviews* 29(9-10):1138–1155. doi:10.1016/j.quascirev.2010.02.017.

Xulu, N.G., Chikoore, H., Bopape, M.J.M., Nethengwe, N.S. (2020). Climatology of the Mascarene High and Its Influence on Weather and Climate over Southern Africa. *Climate* 8(7):86. doi:10.3390/cli8070086.

Yang, G.J., Bergquist, R. (2018). Potential Impact of Climate Change on Schistosomiasis: A Global Assessment Attempt. *Tropical Medicine and Infectious Disease* 3(4):117. doi:10.3390/tropicalmed3040117.

Yang, K., Han, G., Zeng, J., Liang, B., Qu, R., Liu, J., Liu, M. (2019). Spatial Variation and Controlling Factors of H and O Isotopes in Lancang River Water, Southwest China. *International journal of environmental research and public health* 16(24). doi:10.3390/ijerph16244932.

Yazdi, M., Taheri, M., Navi, P., Sadati, N. (2013). Landsat ETM+ imaging for mineral potential mapping: application to Avaj area, Qazvin, Iran. *International Journal of Remote Sensing* 34(16):5778–5795. doi:10.1080/01431161.2013.797127.

Yellen, J.E. (1976). Settlement Patterns of the !Kung: An Archaeological Perspective, in: Lee, R.B., DeVore, I. (Eds.), Kalahari Hunter-Gatherers. Harvard University Press, pp. 47–72. doi:10.4159/harvard.9780674430600.c5.

ZDF (2019). Terra X: Die Vermessung der Erde - Von Kolumbus bis ins All: Film documentary, Mainz. URL: https://www.zdf.de/dokumentation/terra-x/die-vermessung-der-erde-mit-harald-lesch-von-kolumbus-bis-ins-all-100.html.

Zeng, X., Brunke, M.A., Zhou, M., Fairall, C., Bond, N.A., Lenschow, D.H. (2004). Marine Atmospheric Boundary Layer Height over the Eastern Pacific: Data Analysis and Model Evaluation. *Journal of Climate* 17(21):4159–4170. doi:10.1175/JCLI3190.1.

Zhang, Q., Holmgren, K., Sundqvist, H. (2015). Decadal Rainfall Dipole Oscillation over Southern Africa Modulated by Variation of Austral Summer Land–Sea Contrast

along the East Coast of Africa. *Journal of the Atmospheric Sciences* 72(5):1827–1836. doi:10.1175/JAS-D-14-0079.1.

Supplementary material
for Introduction (chapter 1)

Table A.1: Summary of late-Quaternary lake sites shown in Figure 1.1 from the ESA lake-status database from de Cort et al., 2021

ID	Site Name	Latitude	Longitude	Current hydroloogy	
1	Lake Chilwa	-15.5	35.5	filled	closed
2	Lake Lungué	-24.762	33.6358	filled	closed
3	Ishiba Ngandu	-11.235	31.741	filled	open
4	Lake Nhauhache	-21.9807	35.2947	filled	closed
5	Lake Mapimbi	-22.4025	31.28	filled	closed, significant groundwater influence
6	Lake Sibaya	-27.3442	32.6122	filled	closed
7	Princess Vlei	-34.047	18.483	filled	open, significant groundwater influence
8	Lake Chilau	-23.9644	34.9486	filled	open
9	Lake Nhaucati	-22.0378	35.3121	filled	closed
10	Verlorenvlei	-32.35	18.433	filled	open
11	Lake Malawi	-12	34.5	filled	open
12	Urwi Pan	-23.3419	20.3659	dry	closed
13	Tsodilo Hills	-18.7847	21.735	dry	closed
14	#Gi	-19.6242	21.008	dry	closed
15	Alexandersfontein	-28.837	24.7854	dry	closed
16	Ngami	-20.4983	22.7315	seasonal	closed
17	Makgadikgadi	-20.7431	25.4884	dry	closed
18	Mababe	-18.8483	24.1586	dry	closed
19	Etosha	-18.8057	16.3017	dry	closed
20	Tsondab	-23.8851	15.1607	dry	closed
21	Branddam-East Pan	-26.3594	18.842	dry	closed
22	Omongwa Pan	-23.7065	19.3705	dry	closed
23	Kathu Pan	-27.6619	23.0083	dry	closed
24	Lebatse Pan	-23.883	23.8386	dry	closed
25	Witpan	-26.6667	20.15	dry	closed

Supplementary material
for 1st manuscript (Chapter 2)

This supplementary section includes eight supplementary figures concerning the landscape of the basin, the backscatter mechanisms of X-band, the TanDEM-X DEM and how it is impacted by vegetation cover, the remote sensing approaches, the results of the principal component analysis, the interpretation of the sediment properties of the pits and an animation of one of the Palaeolake highstands.

The six supplementary tables contain information about: precipitation and temperature for selected locations, the coordinates of the sampling sites, the used landsat images, the DGPS data, cross-correlation among DGPS Transects data and different investigated TanDEM-X filters and the original geochemical and mineralogical data.

Figure B.1: Heavy rains in March 2016 created a pond in a quarry (**top**, with Male Hill in right background) and filled shallow depressions (**bottom**) at the Tsodilo Hills demonstrating that the duricrusts of the palaeolake beds prevent quick seeping of water.

Short wavelength (X-band) scattering
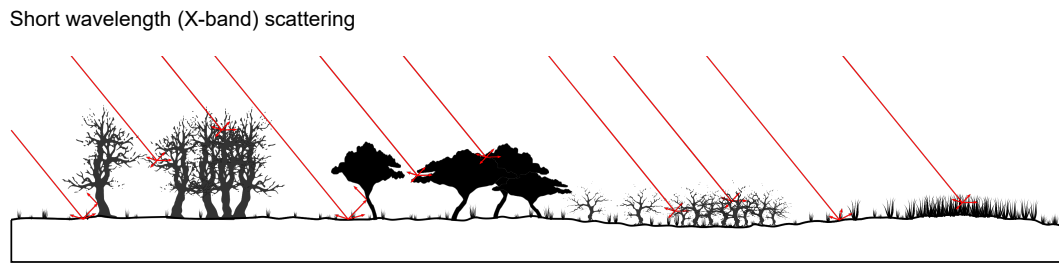
Figure B.2: Backscatter mechanisms typical for short synthetic aperture radar (SAR) wavelengths (e.g. X-band from TanDEM-X). Grass/shrubs/soil: Surface reflection due to relative roughness in addition to volume-backscatter from grass/shrubs with negligible penetration into the soil. Woodland: Scatter of short wavelength dominated by volume-scattering within the canopy and thus not reaching the surface below dense vegetation, however, double-bounce surface/trunk-backscatter is possible when vegetation is sparse.
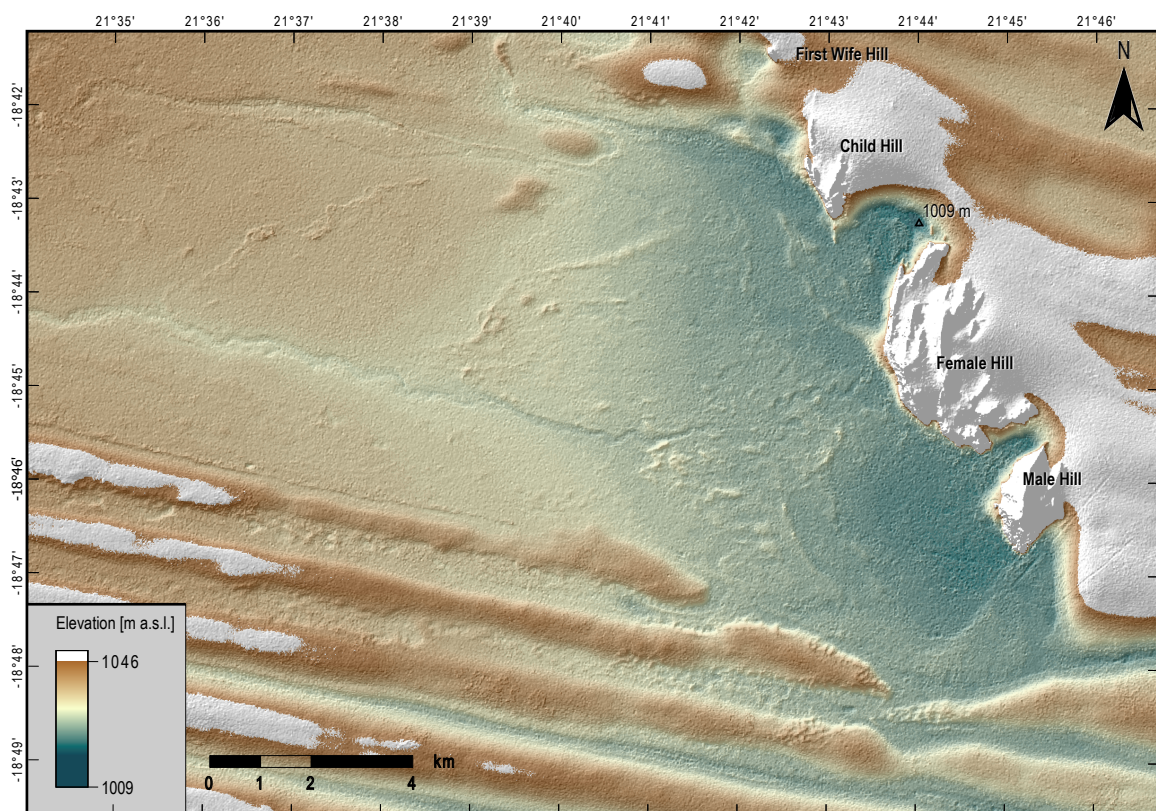
Figure B.3: TanDEM-X DEM without added information.
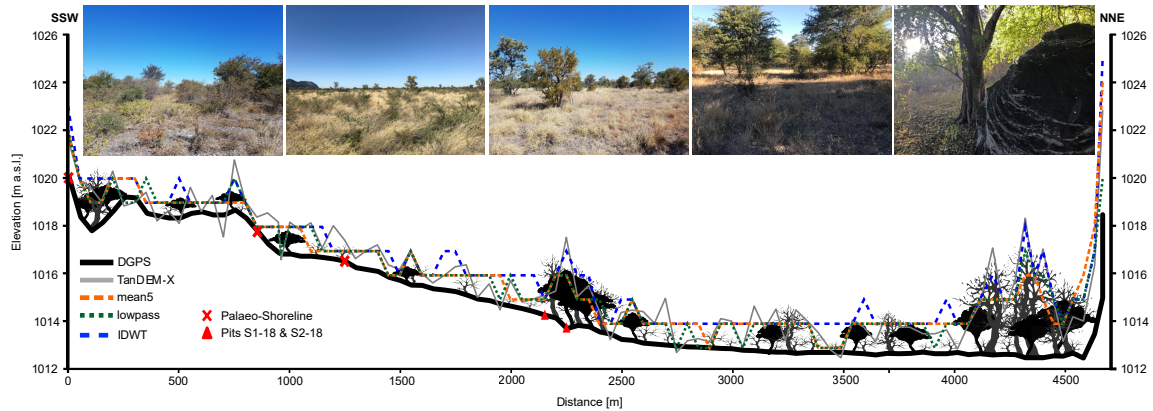
Figure B.4: Impact of vegetation cover on TanDEM-X elevations and comparison of different TanDEM-X noise filtering results along DGPS transect T1 (see Fig. 6). Inverse discrete wavelet transformation (IDWT; Haar wavelet at level 3), lowpass and mean (5-pixel-rectangle) filters showed best overall improvement.
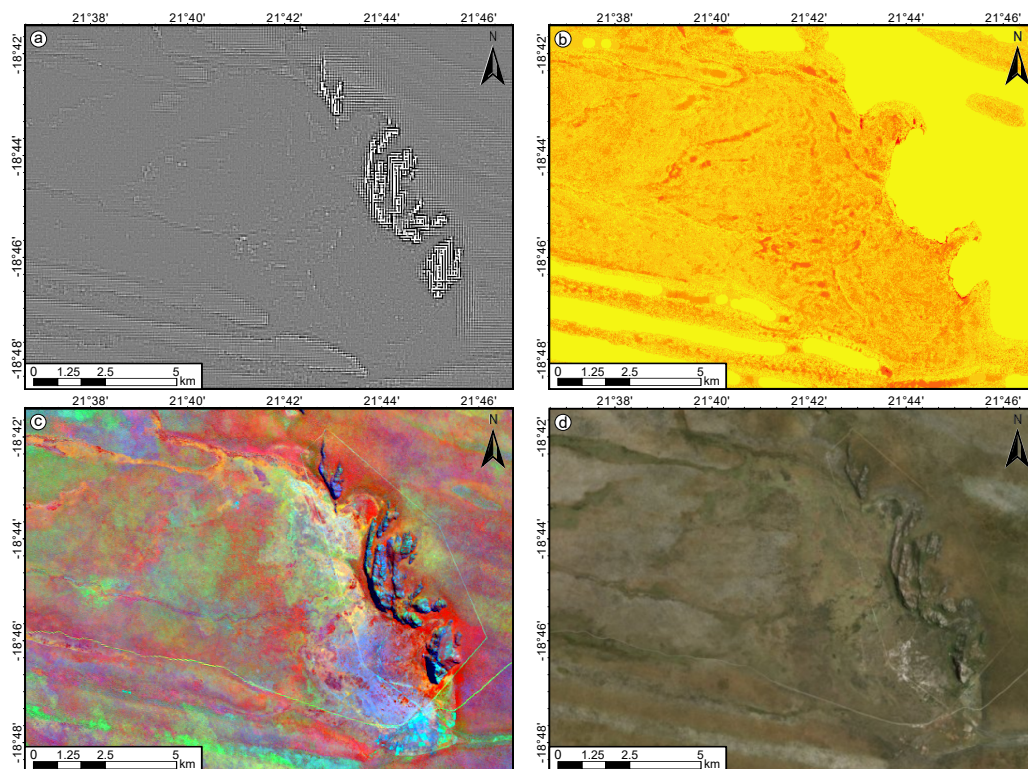
Figure B.5: Analytical approaches used for the detection of surface structures with examples. **a)** Discrete Wavelet Transformation filtering on TanDEM-X data: Details on level 3 using the Haar wavelet. **b)** Top Hat Transform function on TanDEM-X data: White TopHat with disc radius 27. **c)** Colour combinations, PCA and band ratios of Landsat images: Mineral composite of Landsat 8 image. **d)** Aerial images from World Imagery layer of ArcGIS: DigitalGlobe image.
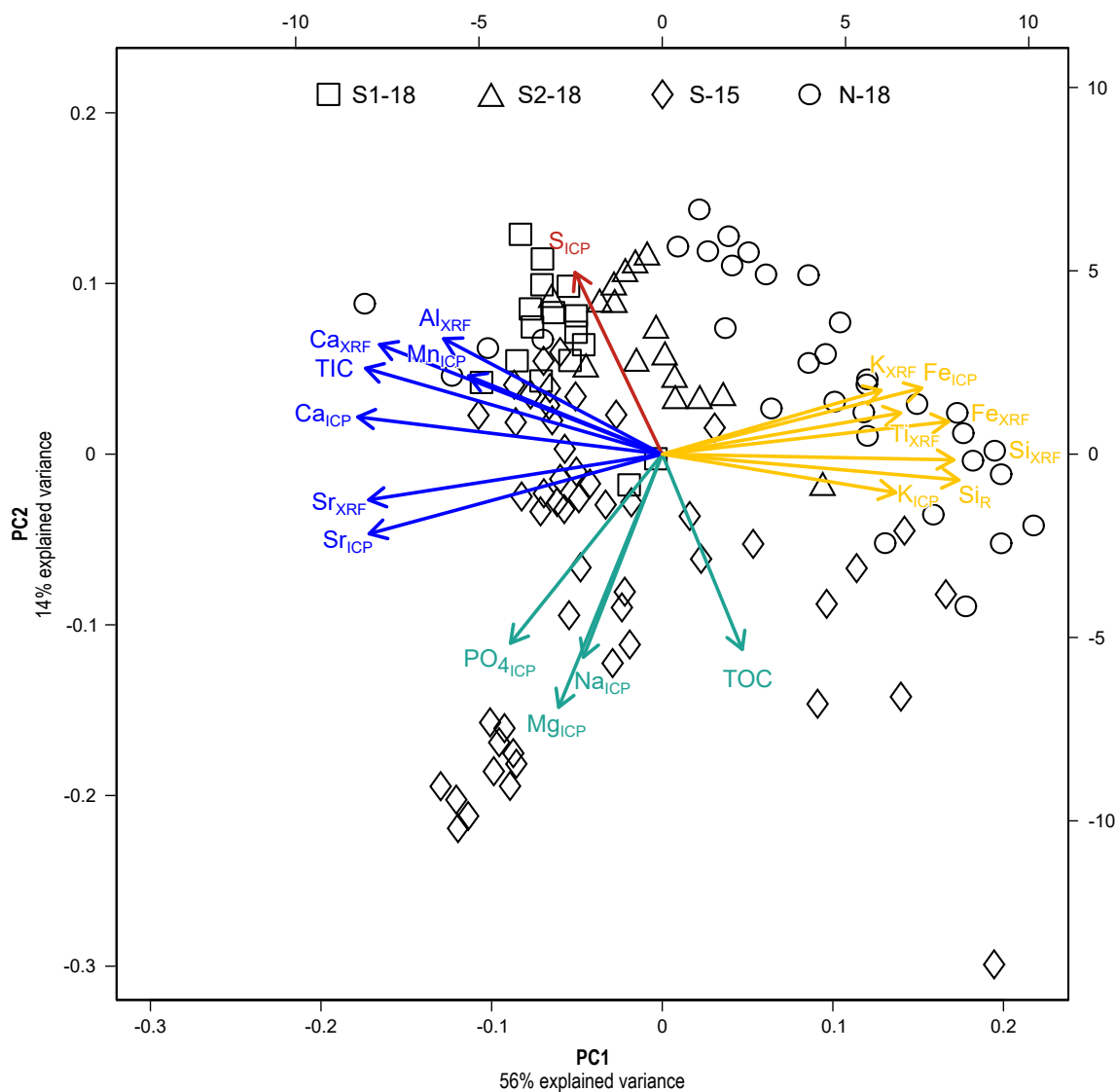
Figure B.6: Principal component analysis (PCA) biplot of geochemical data of the four studied pits along the first two components showing the loading of each variable (arrows) and scores of each sample (pit symbols). Length of arrows approximates the variance of the respective variable, while angles between arrows approximate their correlations. Colours of arrows indicate groups of strongly correlating variables.
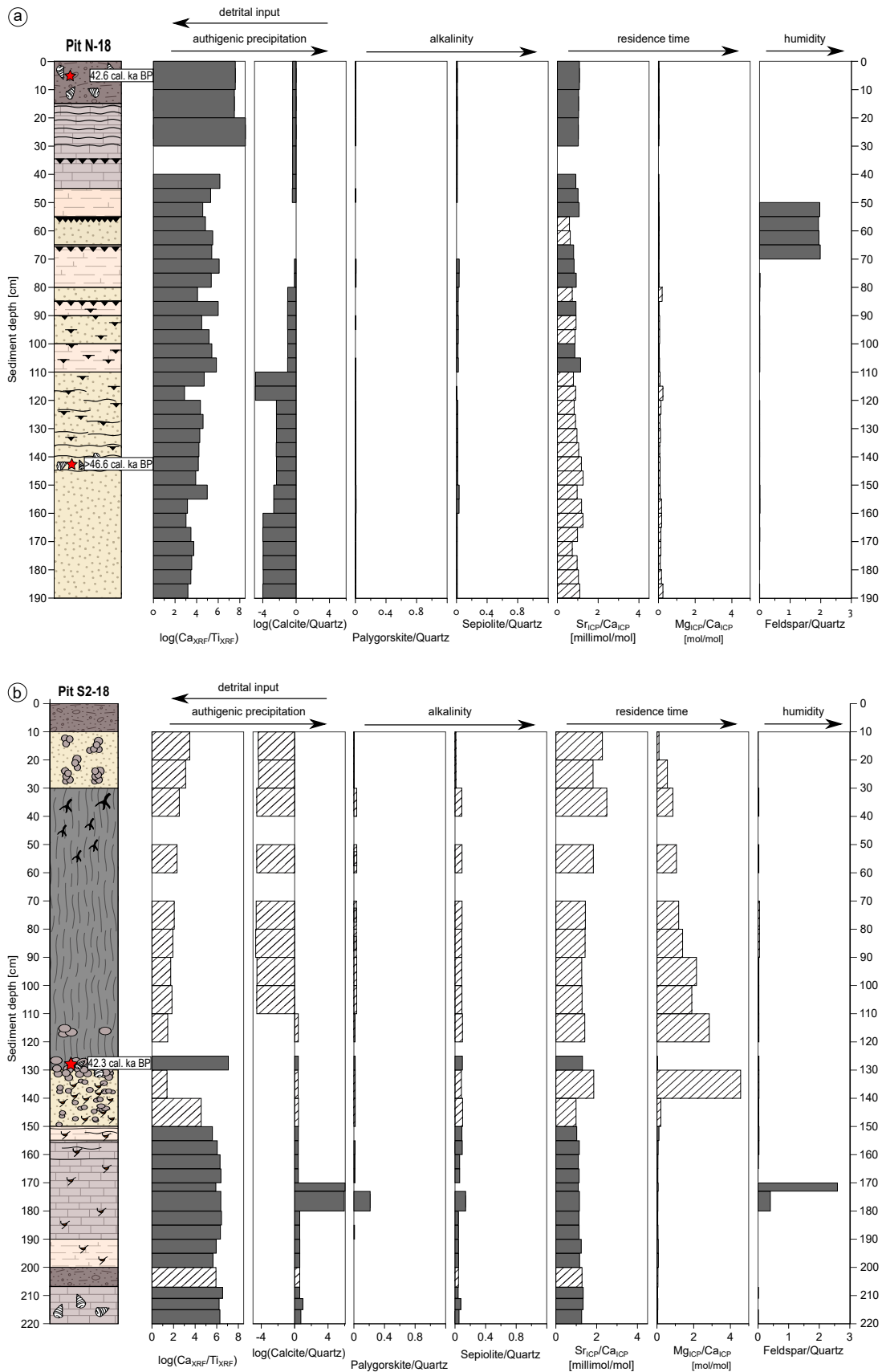
Figure B.7: a) Interpretation of geochemical and mineralogical properties of Pit N-18-sediments. Cross-striped bars indicate values not considered for interpretation due to allogenic deposition. **b)** Pit S2-18. **c)** Pit S1-18.
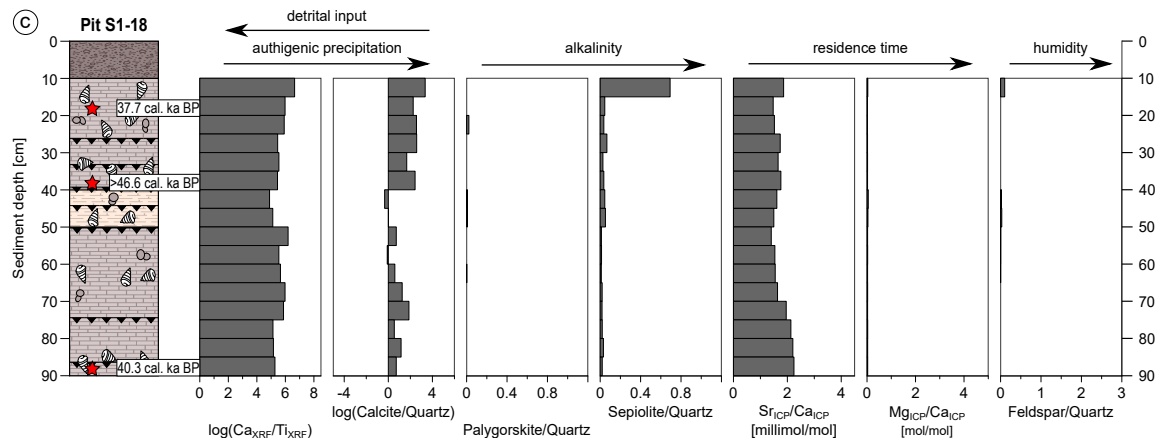
Figure B.7: *(continued).*

Figure B.8: Animation of a Palaeolake Tsodilo highstand with active outflow (modified from the TV documentary "Die Vermessung der Erde" (ZDF 2019)[a]). Red arrow indicates the position of White Paintings Shelter at the base of Male Hill.

Table B.1: Mean annual precipitation and temperature for selected locations (Fig. 2) from north to south into the Kalahari as tentative information on potential past precipitation changes over the Palaeolake Tsodilo drainage basin triggered by migrating moisture sources. Values are derived from the ERA5 reanalysis dataset and generated using the ERA5 explorer (Version: 4.2.4 - build ed0a423) of Copernicus Climate Change Service (2019)[1].

Location in Fig.1	Average annual total precipitation	Average annual temperature
Solwezi (Zambia)	1290 mm	20.7 °C
Cuito (Angola)	1488 mm	21.1 °C
Menongue (Angola)	1052 mm	20.6 °C
Mongu (Zambia)	1081 mm	22.1 °C
Katima Mulilo (Namibia)	639 mm	23.3 °C
Livingstone (Zambia)	595 mm	24.0 °C
Rundu (Namibia)	705 mm	22.6 °C
Tsodilo (Botswana)	705 mm	22.6 °C
Grootfontein (Namibia)	472 mm	21.1 °C
Maun (Botswana)	452 mm	22.9 °C
Francistown (Botswana)	449 mm	21.5 °C
Ghanzi (Botswana)	427 mm	22.7 °C
Palapye (Botswana)	415 mm	22.0 °C
Windhoek (Namibia)	229 mm	21.9 °C
Gaborone (Botswana)	415 mm	22.0 °C

Table B.2: Geographical coordinates of sampling sites at Palaeolake Tsodilo.

Site	Coordinates		m a.s.l.
Sample TD18-50	18.714 83°S;	21.711 63°E	1015
Pit N-18	18.716 09°S;	21.709 31°E	1015
Pit S2-18	18.780 69°S;	21.734 29°E	1014
Pit S1-18	18.781 51°S;	21.733 96°E	1014
Pit S-15	18.794 22°S;	21.737 68°E	1016

---

[1]Copernicus Climate Change Service, 2019: ERA5 explorer. European Centre for Medium-Range Weather Forecasts (ECMWF).

Table B.3: Landsat Images used for morphometric analyses, sorted in ascending order by date of acquisition (acqu.). Images were downloaded from USGS online earth explorer.

File-Name	Acqu. year	Acqu. month	Landsat mission	Tile
LT05_L1TP_175073_20080510_20161031_01_T1	2008	5	5	175073
LT05_L1TP_176073_20080821_20161030_01_T1	2008	8	5	176073
LT05_L1TP_175073_20080915_20161029_01_T1	2008	9	5	175073
LE07_L1TP_176073_20080930_20161224_01_T1	2008	9	7	176073
LT05_L1TP_176073_20081008_20161029_01_T1	2008	10	5	176073
LE07_L1TP_176073_20081016_20161224_01_T1	2008	10	7	176073
LE07_L1TP_175073_20081025_20161224_01_T1	2008	10	7	175073
LE07_L1TP_175073_20081009_20161224_01_T1	2008	10	7	175073
LE07_L1TP_176073_20081101_20161224_01_T1	2008	11	7	176073
LE07_L1TP_175073_20081126_20161223_01_T1	2008	11	7	175073
LT05_L1TP_175073_20090326_20161027_01_T1	2009	3	5	175073
LT05_L1TP_176073_20090520_20161026_01_T1	2009	5	5	176073
LE07_L1TP_175073_20110527_20161208_01_T1	2011	5	7	175073
LE07_L1TP_176073_20120808_20161129_01_T1	2012	8	7	176073
LE07_L1TP_176073_20120909_20161129_01_T1	2012	9	7	176073
LC08_L1TP_175073_20130524_20170504_01_T1	2013	5	8	175073
LC08_L1TP_176073_20130819_20170502_01_T1	2013	8	8	176073
LC08_L1TP_175073_20130812_20170503_01_T1	2013	8	8	175073
LC08_L1TP_175073_20140527_20170422_01_T1	2014	5	8	175073
LC08_L1TP_176073_20140806_20170420_01_T1	2014	8	8	176073
LC08_L1TP_176073_20150521_20170409_01_T1	2015	5	8	176073
LC08_L1TP_176073_20150809_20170406_01_T1	2015	8	8	176073
LC08_L1TP_176073_20160523_20170324_01_T1	2016	5	8	176073
LC08_L1TP_175073_20160804_20170322_01_T1	2016	8	8	175073
LC08_L1TP_175073_20170519_20170525_01_T1	2017	5	8	175073
LC08_L1TP_175073_20170807_20180526_01_T1	2017	8	8	175073
LC08_L1TP_175073_20180522_20180605_01_T1	2018	5	8	175073
LC08_L1TP_175073_20180810_20180815_01_T1	2018	8	8	175073

Table B.4: Data for differential GPS transects T0-T5: Lengths and mean (± SD) distance between measurement points; different dilution of precision (DOP) values for the quality of positioning: Horizontal DOP (2D), Vertical DOP (1D), Positional DOP (3D); numbers of used Real-Time Kinematic (RTK) positions and GPS and GLONASS satellites. *= data for northernmost 40 measurements available only.

Parameter/Transect	T0	T1	T2	T3	T4	T5
Measured km	11.94	4.74	2.11	0.58	1.13	0.81
Aligned km	11.86	4.65	2.08	0.58	1.08	0.78
m between points	134.49 ± 95.17	49.01 ± 5.17	47.36 ± 8.83	25.07 ± 1.31	43.55 ± 14.14	25.33 ± 2.02
m Height-correction	-1.22–1.68	1.41	-1.2	-1.9	2.4	0.44
HDOP	0.6 ± 0.02*	0.74 ± 0.19	0.69 ± 0.1	0.6 ± 0	0.61 ± 0.02	0.59 ± 0.02
VDOP	1.18 ± 0.08*	1.61 ± 0.45	1.4 ± 0.14	1.39 ± 0.05	1.38 ± 0.07	1.29 ± 0.1
PDOP	1.32 ± 0.07*	1.42 ± 0.42	1.22 ± 0.12	1.25 ± 0.06	1.23 ± 0.07	1.14 ± 0.11
numRTK	120.73 ± 1.02*	76 ± 23	50 ± 15	58 ± 13	86 ± 18	89 ± 23
GLONASS satellites	7 ± 1*	6 ± 2	7 ± 1	6 ± 0	7 ± 1	7 ± 1
GPS satellites	9 ± 1*	8 ± 1	7 ± 1	8 ± 0	8 ± 1	9 ± 1

Table B.5: Cross-correlation between the corrected DGPS transect elevation profiles and the respective profiles of the TanDEM-X data and selected filtered TanDEM-X.

Transect	TanDEM-X	IDWT(Haar3)	min3	max3	mean3
T0	0.92	0.95	0.87	0.88	0.88
T1	0.85	0.84	0.94	0.92	0.92
T2	0.95	0.9	0.97	0.88	0.88
T3	0.96	0.93	0.97	0.99	0.99
T4	0.91	0.95	0.94	0.95	0.95
T5	0.96	0.98	0.99	0.99	0.99

Table B.6: Tables for original geochemical (ICP-OES: inductively coupled plasma optical emission spectrometry; XRF: X-ray fluorescence; LOI: loss on ignition) and mineralogical data. Pit S1-18 ICP-OES

Lab. ID	Sample ID	mean depth	Ca ICP-OES	PO4 ICP-OES	Mn ICP-OES	Fe ICP-OES	Sr ICP-OES	Na ICP-OES	K ICP-OES	S ICP-OES	Mg ICP-OES
		[cm]	[mg/g]	[mg/g]	[mg/g]	[mg/g]	[mg/g]	[mg/g]	[mg/g]	[mg/g]	[mg/g]
T-16	TDP-S1-16	12.5	211.118	0.172	0.045	0.494	0.859	0.293	0.138	14.886	4.150
T-15	TDP-S1-15	17.5	196.061	0.424	0.049	0.602	0.632	0.485	0.138	15.752	2.276
T-14	TDP-S1-14	22.5	205.422	0.142	0.067	0.616	0.683	0.236	0.126	15.161	2.301
T-13	TDP-S1-13	27.5	175.569	0.121	0.059	0.577	0.666	0.204	0.110	15.016	2.259
T-12	TDP-S1-12	32.5	181.323	0.097	0.059	0.659	0.657	0.523	0.127	14.409	2.469
T-11	TDP-S1-11	37.5	166.551	0.085	0.053	0.518	0.641	0.445	0.108	14.310	2.214
T-10	TDP-S1-10	42.5	100.080	0.135	0.026	0.815	0.352	0.419	0.147	9.006	3.120
T-09	TDP-S1-09	47.5	104.061	0.176	0.031	0.536	0.341	0.461	0.119	8.461	2.393
T-08	TDP-S1-08	52.5	179.661	0.126	0.067	0.532	0.551	0.637	0.163	12.666	2.663
T-07	TDP-S1-07	57.5	143.959	0.110	0.052	0.606	0.484	0.479	0.135	11.790	2.371
T-06	TDP-S1-06	62.5	161.463	0.099	0.070	0.639	0.547	0.517	0.155	12.944	2.322
T-05	TDP-S1-05	67.5	182.697	0.152	0.076	0.701	0.653	0.822	0.218	13.570	2.868
T-04	TDP-S1-04	72.5	182.164	0.124	0.082	0.581	0.780	0.428	0.133	14.019	2.689
T-03	TDP-S1-03	77.5	146.589	0.132	0.061	0.654	0.683	0.385	0.120	13.707	2.568
T-02	TDP-S1-02	82.5	154.922	0.138	0.072	0.621	0.747	0.356	0.151	14.438	2.519
T-01	TDP-S1-01	87.5	153.922	0.164	0.073	0.635	0.756	0.315	0.237	14.456	2.612

Table B.6: *(continued).* Pit S1-18 XRF + LOI

Lab. ID	Sample ID	mean depth	Sr XRF	Fe XRF	Ti XRF	Ca XRF	K XRF	Si XRF	Al XRF	TOC LOI	TIC LOI	Si remain LOI
		[cm]	[ppm]	[ppm]	[ppm]	[ppm]	[ppm]	[ppm]	[ppm]	[%]	[%]	[%]
T-16	TDP-S1-16	12.5	1198.471	2063.673	476.928	307607.085	279.140	141677.560	35522.371	1.90	8.11	29.16
T-15	TDP-S1-15	17.5	962.256	2392.838	871.873	288008.388	388.909	180737.006	37146.654	1.63	7.50	34.69
T-14	TDP-S1-14	22.5	1080.020	2844.933	1053.863	328095.660	514.796	187906.292	42758.415	1.70	7.72	32.70
T-13	TDP-S1-13	27.5	1164.140	2811.608	1337.573	262940.899	300.138	209426.926	30715.290	1.69	6.65	41.68
T-12	TDP-S1-12	32.5	1047.053	2514.678	1226.134	263010.749	384.375	204179.933	30232.837	1.92	6.61	41.60
T-11	TDP-S1-11	37.5	1079.342	2349.856	1322.966	257370.604	293.784	241867.069	33422.104	1.66	6.26	45.01
T-10	TDP-S1-10	42.5	806.658	4899.501	1518.141	169005.436	456.602	303775.728	21823.806	2.37	3.57	66.19
T-09	TDP-S1-09	47.5	699.705	3661.160	1079.366	150704.258	347.659	282742.498	16161.612	2.08	3.72	65.39
T-08	TDP-S1-08	52.5	787.804	2313.450	653.649	266972.065	371.718	202008.986	32516.582	1.24	6.77	41.49
T-07	TDP-S1-07	57.5	850.694	2922.766	983.234	210138.476	400.486	232127.391	25731.176	1.69	5.30	52.89
T-06	TDP-S1-06	62.5	911.589	2896.010	1048.293	250501.461	639.079	220999.551	30323.294	1.65	6.04	46.82
T-05	TDP-S1-05	67.5	1052.587	2424.956	830.263	273785.504	457.682	180070.830	32128.056	2.04	6.72	40.51
T-04	TDP-S1-04	72.5	1216.104	2770.937	922.860	273443.987	497.112	204345.008	36555.833	2.23	6.82	39.32
T-03	TDP-S1-03	77.5	1334.813	3141.195	1621.936	229391.333	350.394	201125.557	23690.927	2.16	5.46	50.81
T-02	TDP-S1-02	82.5	1423.417	3605.607	1657.138	242261.549	548.951	207596.416	25656.291	2.14	5.80	48.01
T-01	TDP-S1-01	87.5	1370.928	3922.855	1492.793	242726.707	512.719	221056.009	31757.055	2.02	5.73	48.79

Table B.6: *(continued).* Pit S2-18 ICP-OES

Lab. ID	Sample ID	mean depth	Ca ICP-OES	PO4 ICP-OES	Mn ICP-OES	Fe ICP-OES	Sr ICP-OES	Na ICP-OES	K ICP-OES	S ICP-OES	Mg ICP-OES
		[cm]	[mg/g]	[mg/g]	[mg/g]	[mg/g]	[mg/g]	[mg/g]	[mg/g]	[mg/g]	[mg/g]
T-42	TDP-S2-26	15.0	37.907	0.204	0.042	0.723	0.189	0.197	0.343	2.998	2.531
T-41	TDP-S2-25	25.0	5.522	0.071	0.019	0.450	0.022	0.122	0.123	0.625	1.902
T-40	TDP-S2-24	35.0	6.410	0.497	0.275	1.493	0.035	0.109	0.308	0.755	3.366
T-39	TDP-S2-23	55.0	5.477	0.277	0.296	1.928	0.022	0.130	0.280	0.746	3.526
T-38	TDP-S2-22	75.0	4.111	0.230	0.219	1.676	0.013	0.097	0.266	0.471	2.949
T-37	TDP-S2-21	85.0	3.514	0.194	0.205	1.602	0.011	0.078	0.264	0.943	2.975
T-36	TDP-S2-20	95.0	2.884	0.169	0.204	1.904	0.008	0.071	0.276	0.362	3.765
T-35	TDP-S2-19	105.0	2.850	0.182	0.171	1.661	0.008	0.062	0.266	0.294	3.279
T-34	TDP-S2-18	115.0	2.258	0.217	0.221	1.864	0.007	0.107	0.313	0.417	3.900
T-33	TDP-S2-17	127.5	178.652	0.157	0.120	0.974	0.509	0.203	0.203	11.415	3.185
T-32	TDP-S2-16	135.0	1.477	0.180	0.176	2.359	0.006	0.089	0.392	0.377	4.083
T-31	TDP-S2-15	145.0	36.975	0.191	0.296	2.612	0.080	0.150	0.549	2.535	4.748
T-30	TDP-S2-14	152.5	73.725	0.156	0.232	1.989	0.165	0.140	0.404	4.651	4.881
T-29	TDP-S2-13	157.5	124.365	0.162	0.268	1.903	0.312	0.172	0.418	7.205	4.950
T-28	TDP-S2-12	162.5	133.582	0.152	0.212	1.591	0.322	0.175	0.331	8.360	4.307
T-27	TDP-S2-11	167.5	143.691	0.189	0.221	1.547	0.358	0.190	0.333	8.403	4.331
T-26	TDP-S2-10	171.5	116.206	0.216	0.220	1.802	0.279	0.170	0.381	6.945	4.765
T-25	TDP-S2-09	176.5	149.391	0.221	0.207	1.552	0.377	0.177	0.479	9.567	4.590
T-24	TDP-S2-08	182.5	151.267	0.164	0.179	1.149	0.374	0.191	0.372	9.375	4.026
T-23	TDP-S2-07	187.5	135.444	0.178	0.155	1.365	0.337	0.189	0.455	8.687	4.638
T-22	TDP-S2-06	192.5	114.265	0.191	0.143	1.551	0.311	0.149	0.439	7.526	5.087
T-21	TDP-S2-05	197.5	83.000	0.217	0.133	1.454	0.211	0.151	0.385	5.913	3.886
T-20	TDP-S2-04	203.5	102.751	0.214	0.120	1.297	0.288	0.166	0.332	7.038	3.351
T-19	TDP-S2-03	209.0	153.014	0.173	0.159	1.515	0.448	0.181	0.388	11.035	3.376
T-18	TDP-S2-02	213.0	137.439	0.131	0.126	1.711	0.401	0.214	0.474	10.254	4.004
T-17	TDP-S2-01	217.5	147.574	0.121	0.127	1.629	0.408	0.166	0.501	9.681	3.692

Lab. ID	Sample ID	mean depth	Sr XRF	Fe XRF	Ti XRF	Ca XRF	K XRF	Si XRF	Al XRF	TOC LOI	TIC LOI	Si remain LOI
		[cm]	[ppm]	[ppm]	[ppm]	[ppm]	[ppm]	[ppm]	[ppm]	[%]	[%]	[%]
T-42	TDP-S2-26	15.0	354.872	12859.884	2244.862	62368.707	3620.838	368376.062	41123.123	3.05	1.24	84.41
T-41	TDP-S2-25	25.0	50.954	3610.866	963.564	18249.110	1444.002	362698.060	13226.759	0.84	0.27	96.26
T-40	TDP-S2-24	35.0	78.342	18350.678	1166.522	12291.763	1860.304	398542.278	16633.496	6.01	0.55	85.06
T-39	TDP-S2-23	55.0	48.592	16161.669	1011.454	8657.917	1430.402	352070.567	13285.242	6.03	0.42	86.14
T-38	TDP-S2-22	75.0	33.150	20266.117	1265.783	8336.539	2066.265	398173.244	19021.661	5.08	0.32	88.54
T-37	TDP-S2-21	85.0	25.112	17924.550	1095.249	6350.793	1775.498	358938.554	15730.224	4.71	0.42	88.38
T-36	TDP-S2-20	95.0	22.423	20114.989	1223.598	5822.064	1958.389	424048.326	19238.458	4.14	0.39	89.60
T-35	TDP-S2-19	105.0	20.973	18452.371	1051.708	5629.400	1856.922	387359.459	15710.113	3.57	0.39	90.57
T-34	TDP-S2-18	115.0	16.969	19421.025	1008.870	3638.457	1728.464	408358.842	16044.485	3.35	0.40	90.86
T-33	TDP-S2-17	127.5	745.065	4075.950	265.562	262595.151	949.325	204409.886	35028.866	2.07	6.68	40.78
T-32	TDP-S2-16	135.0	20.416	22047.327	800.734	2701.176	1719.057	517010.914	12772.986	2.53	0.32	92.95
T-31	TDP-S2-15	145.0	155.820	22286.029	835.800	66615.385	1928.587	399726.610	18796.901	2.89	1.57	81.96
T-30	TDP-S2-14	152.5	288.640	13228.857	539.326	122020.098	1340.903	334853.154	19373.409	2.33	2.85	72.26
T-29	TDP-S2-13	157.5	497.027	13439.819	601.609	212373.931	1626.363	253377.891	29335.657	2.63	4.78	55.63
T-28	TDP-S2-12	162.5	478.820	8916.285	447.652	205974.810	1184.765	237903.018	29925.622	1.60	5.36	52.55
T-27	TDP-S2-11	167.5	527.987	8911.027	451.153	224557.660	1063.143	237127.023	31232.642	1.88	5.56	50.40
T-26	TDP-S2-10	171.5	433.474	11144.755	583.919	182171.996	1461.318	255171.962	26085.568	2.32	4.57	57.93
T-25	TDP-S2-09	176.5	580.651	9744.109	472.362	232714.117	90.000	227077.490	36627.829	2.25	5.75	48.24
T-24	TDP-S2-08	182.5	561.156	7562.539	454.381	238303.786	1241.018	203578.011	32229.781	2.07	5.92	47.11
T-23	TDP-S2-07	187.5	496.748	7455.147	419.002	199011.572	1259.009	239846.677	29172.631	2.34	4.93	54.90
T-22	TDP-S2-06	192.5	460.910	9473.904	584.417	187598.398	1745.103	261358.764	27532.940	2.61	4.17	60.72
T-21	TDP-S2-05	197.5	339.594	11489.542	586.601	140067.074	1620.286	316087.716	24356.952	2.48	3.12	69.73
T-20	TDP-S2-04	203.5	442.462	8674.622	507.419	159616.551	1315.689	278687.220	23107.322	2.60	3.76	64.15
T-19	TDP-S2-03	209.0	664.418	8286.864	412.829	240046.872	1335.544	222274.865	33866.978	2.36	5.68	48.64
T-18	TDP-S2-02	213.0	602.133	10480.206	505.352	212771.352	1526.697	244384.535	35753.494	1.75	5.63	50.10
T-17	TDP-S2-01	217.5	608.394	10167.652	491.066	223050.210	1949.502	239989.842	31738.980	1.95	5.54	50.51

Table B.6: *(continued).* Pit N-18 ICP-OES

Lab. ID	Sample ID	mean depth	Ca ICP-OES	PO4 ICP-OES	Mn ICP-OES	Fe ICP-OES	Sr ICP-OES	Na ICP-OES	K ICP-OES	S ICP-OES	Mg ICP-OES
		[cm]	[mg/g]	[mg/g]	[mg/g]	[mg/g]	[mg/g]	[mg/g]	[mg/g]	[mg/g]	[mg/g]
T -76	TDP-N-34	5.0	202.227	0.152	0.121	1.375	0.478	0.351	0.072	16.383	4.109
T -75	TDP-N-33	15.0	238.113	0.213	0.116	1.444	0.541	0.351	0.053	17.471	5.054
T -74	TDP-N-32	25.0	269.121	0.179	0.315	0.934	0.605	0.336	0.047	21.745	4.510
T -72	TDP-N-30	42.5	174.135	0.174	0.077	0.591	0.345	0.191	0.088	15.565	2.771
T -71	TDP-N-29	47.5	108.000	0.065	0.049	0.737	0.240	0.181	0.114	11.904	1.785
T -70	TDP-N-28	52.5	79.824	0.056	0.039	1.166	0.186	0.185	0.160	10.644	1.799
T -69	TDP-N-27	57.5	45.049	0.051	0.029	0.877	0.058	0.105	0.138	4.578	1.216
T -68	TDP-N-26	62.5	70.139	0.058	0.042	1.035	0.097	0.105	0.141	1.556	1.663
T -67	TDP-N-25	67.5	98.440	0.070	0.069	2.166	0.172	0.210	0.211	9.740	2.290
T -66	TDP-N-24	72.5	107.383	0.065	0.101	2.067	0.192	0.164	0.195	9.175	2.093
T -65	TDP-N-23	77.5	93.619	0.064	0.054	1.478	0.189	0.160	0.178	9.357	2.118
T -64	TDP-N-22	82.5	22.616	0.054	0.039	5.830	0.036	0.182	0.319	0.711	2.745
T -63	TDP-N-21	87.5	93.425	0.060	0.079	1.387	0.186	0.126	0.173	8.253	2.037
T -62	TDP-N-20	92.5	43.301	0.042	0.037	1.739	0.087	0.122	0.211	6.007	1.635
T -61	TDP-N-19	97.5	42.916	0.055	0.036	1.563	0.081	0.136	0.211	4.539	1.662
T -60	TDP-N-18	102.5	62.611	0.054	0.044	1.264	0.117	0.184	0.204	6.417	1.644
T -59	TDP-N-17	107.5	77.948	0.076	0.051	1.836	0.194	0.159	0.188	7.079	2.796
T -58	TDP-N-16	112.5	27.524	0.037	0.023	1.472	0.047	0.291	0.196	3.012	1.422
T -57	TDP-N-15	117.5	4.220	0.039	0.007	0.882	0.008	0.118	0.091	1.154	0.621
T -56	TDP-N-14	122.5	13.003	0.077	0.013	1.395	0.023	0.107	0.139	1.553	1.082
T -55	TDP-N-13	127.5	21.241	0.046	0.021	1.010	0.041	0.118	0.116	2.419	1.146
T -54	TDP-N-12	132.5	19.101	0.042	0.019	0.950	0.040	0.126	0.107	2.715	1.238
T -53	TDP-N-11	137.5	43.757	0.051	0.033	1.110	0.100	0.139	0.132	6.275	1.855
T -52	TDP-N-10	142.5	27.135	0.074	0.029	1.074	0.070	0.194	0.143	4.655	1.477
T -51	TDP-N-09	147.5	26.607	0.044	0.023	1.076	0.073	0.125	0.153	4.774	1.373
T -50	TDP-N-08	152.5	34.552	0.044	0.031	2.063	0.073	0.113	0.249	3.398	1.964
T -49	TDP-N-07	157.5	12.906	0.036	0.015	2.163	0.033	0.111	0.369	3.438	1.320
T -48	TDP-N-06	162.5	9.817	0.033	0.013	1.710	0.027	0.127	0.290	2.731	1.051
T -47	TDP-N-05	167.5	15.480	0.037	0.016	1.772	0.033	0.138	0.287	3.247	1.238
T -46	TDP-N-04	172.5	13.258	0.039	0.012	1.268	0.021	0.137	0.181	2.007	1.045
T -45	TDP-N-03	177.5	19.009	0.067	0.015	1.126	0.040	0.177	0.212	3.515	1.131
T -44	TDP-N-02	182.5	10.443	0.036	0.012	1.096	0.024	0.128	0.179	2.004	1.042
T -43	TDP-N-01	187.5	8.477	0.046	0.013	1.411	0.020	0.173	0.218	1.417	1.250

Lab. ID	Sample ID	mean depth	Sr XRF	Fe XRF	Ti XRF	Ca XRF	K XRF	Si XRF	Al XRF	TOC LOI	TIC LOI	Si remain LOI
		[cm]	[ppm]	[ppm]	[ppm]	[ppm]	[ppm]	[ppm]	[ppm]	[%]	[%]	[%]
T -76	TDP-N-34	5.0	624.275	9517.377	188.720	310221.126	90.000	67462.355	25707.117	1.73	7.33	35.92
T -75	TDP-N-33	15.0	745.375	9811.215	247.042	371703.771	172.217	47760.634	39172.056	2.55	8.75	22.65
T -74	TDP-N-32	25.0	789.016	5723.577	95.598	400375.536	90.000	41540.731	39631.581	1.74	9.99	13.76
T -72	TDP-N-30	42.5	534.538	5587.473	603.167	237610.193	90.000	222526.497	21082.297	1.84	6.32	44.20
T -71	TDP-N-29	47.5	418.846	8677.529	944.728	157989.383	570.213	333732.320	12498.312	1.33	4.08	63.71
T -70	TDP-N-28	52.5	379.764	19575.895	1603.290	129043.346	649.584	395472.277	11895.735	1.52	3.06	71.89
T -69	TDP-N-27	57.5	135.253	16948.556	857.543	88363.066	876.600	369312.200	9455.095	1.19	1.73	83.49
T -68	TDP-N-26	62.5	177.951	13643.472	569.456	115421.333	974.985	321548.331	9367.465	2.17	2.24	77.60
T -67	TDP-N-25	67.5	290.431	23519.628	785.108	145674.465	512.884	310396.707	11168.236	1.50	3.66	66.89
T -66	TDP-N-24	72.5	311.713	23615.380	448.416	165172.218	618.524	317105.501	12025.589	1.29	4.21	62.66
T -65	TDP-N-23	77.5	322.737	20693.345	826.605	146412.663	494.570	335367.522	11657.105	1.27	3.59	67.92
T -64	TDP-N-22	82.5	66.798	41301.075	768.077	38104.153	738.472	480721.981	5167.618	2.50	0.66	90.23
T -63	TDP-N-21	87.5	316.064	18577.457	439.428	148236.149	576.184	316975.458	11453.714	1.56	3.46	68.50
T -62	TDP-N-20	92.5	180.614	27658.916	1093.666	79882.401	647.208	390918.058	9075.019	1.95	1.56	83.68
T -61	TDP-N-19	97.5	166.243	25651.599	541.897	78232.775	737.245	403147.790	7238.812	1.46	1.59	84.25
T -60	TDP-N-18	102.5	214.101	22407.958	608.940	113903.319	560.649	352452.130	10581.556	1.18	2.46	77.50
T -59	TDP-N-17	107.5	358.907	18525.183	480.597	136890.361	620.240	301224.471	12291.673	1.56	3.04	72.02
T -58	TDP-N-16	112.5	97.840	21548.432	540.131	49727.888	581.723	423724.459	5391.812	2.95	1.02	86.41
T -57	TDP-N-15	117.5	15.096	9652.334	481.316	7187.683	763.677	512458.730	4000.000	0.58	0.14	97.87
T -56	TDP-N-14	122.5	57.400	16751.216	445.098	28905.972	617.125	445921.835	3597.468	0.92	0.46	94.61
T -55	TDP-N-13	127.5	88.991	11513.091	529.910	43919.446	362.738	432672.097	4801.548	1.04	0.68	92.53
T -54	TDP-N-12	132.5	92.214	9694.692	671.432	41228.884	445.167	446217.073	3848.799	0.63	0.74	92.78
T -53	TDP-N-11	137.5	216.816	11758.113	1444.727	81744.770	581.139	406063.022	7242.395	1.55	1.38	85.86
T -52	TDP-N-10	142.5	157.861	11711.426	1122.940	60038.550	631.404	384210.670	5941.517	1.05	0.97	90.10
T -51	TDP-N-09	147.5	168.502	17006.112	1382.451	58124.047	616.013	397082.591	4304.903	1.21	0.91	90.29
T -50	TDP-N-08	152.5	148.091	29115.066	491.330	60070.862	604.599	419914.574	5697.826	1.68	1.32	86.07
T -49	TDP-N-07	157.5	82.909	48004.809	1099.551	21530.166	729.004	458887.731	5031.946	1.67	0.53	92.67
T -48	TDP-N-06	162.5	68.777	38039.968	1008.668	17233.358	637.001	455934.366	4168.836	1.46	0.52	93.17
T -47	TDP-N-05	167.5	79.086	34447.090	1008.504	27214.439	711.466	476580.043	4320.903	1.58	0.56	92.60
T -46	TDP-N-04	172.5	43.226	19655.757	763.897	26869.223	983.860	484979.094	5411.008	0.87	0.52	94.18
T -45	TDP-N-03	177.5	96.555	17613.660	1285.528	37350.319	925.323	427786.070	6372.668	0.92	0.73	92.32
T -44	TDP-N-02	182.5	53.018	19318.095	895.219	23960.419	1032.314	407111.101	6006.135	0.94	0.42	94.89
T -43	TDP-N-01	187.5	42.211	21367.784	738.731	15057.124	997.420	475316.738	4329.564	0.98	0.32	95.65

Table B.6: *(continued).* Pit S-15 ICP-OES

Lab. ID	Sample ID	mean depth	Ca ICP-OES	PO4 ICP-OES	Mn ICP-OES	Fe ICP-OES	Sr ICP-OES	Na ICP-OES	K ICP-OES	S ICP-OES	Mg ICP-OES
		[cm]	[mg/g]	[mg/g]	[mg/g]	[mg/g]	[mg/g]	[mg/g]	[mg/g]	[mg/g]	[mg/g]
50.5	TD2-50-55	43.5	227.70	0.54	0.07	0.40	1.30	1.58	0.27	8.20	12.17
50	TD2-45-50	48.5	222.40	0.39	0.08	0.42	1.29	0.75	0.18	7.28	12.39
49	TD2-40-45	53.5	218.20	0.37	0.09	0.44	1.50	0.71	0.16	6.68	13.10
48	TD2-35-40	58.5	193.30	0.37	0.08	0.40	1.24	1.14	0.18	6.51	11.62
47	TD2-30-35	63.5	185.30	0.43	0.08	0.39	1.30	0.70	0.10	6.04	11.05
46	TD2-25-30	68.5	177.70	0.55	0.07	0.43	1.26	1.07	0.10	5.94	10.98
45	TD2-20-25	73.5	194.60	0.30	0.08	0.41	1.41	0.80	0.08	6.08	12.49
44	TD2-15-20	78.5	197.80	0.32	0.08	0.49	1.45	1.03	0.10	6.30	14.35
43	TD2-10-15	83.5	196.40	0.28	0.07	0.45	1.48	1.13	0.11	6.08	15.07
42	TD2-5-10	88.5	200.40	0.29	0.07	0.35	1.46	0.61	0.05	5.51	13.79
41	TD2-0-5	93.5	197.20	0.35	0.12	0.46	1.41	0.88	0.11	6.16	18.96
51	TD2-0-(-5)	98.5	187.70	0.15	0.10	0.58	0.97	0.98	0.20	6.27	4.67
52	TD2-(-5)-(-10)	103.5	195.60	0.15	0.11	0.67	1.09	0.74	0.22	6.18	5.98
53	TD2-(-10)-(-15)	108.5	193.90	0.18	0.11	0.62	1.04	0.94	0.18	6.54	4.58
4	TD-15-20	113.5	179.80	0.33	0.15	0.98	1.05	0.93	1.15	1.67	7.27
5	TD-20-25	118.5	58.19	0.22	0.05	1.39	0.32	0.36	1.14	0.74	5.32
6	TD-25-30	123.5	9.54	0.12	0.01	1.51	0.09	0.69	0.88	0.86	5.98
7	TD-30-35	128.5	183.20	0.25	0.16	1.78	1.30	0.45	0.51	2.18	10.40
8	TD-35-40	133.5	225.60	0.34	0.20	1.89	1.57	0.41	0.48	2.81	11.51
9	TD-40-45	138.5	224.30	0.40	0.19	1.39	1.46	0.74	0.42	2.76	12.53
10	TD-45-50	143.5	164.20	0.25	0.10	1.08	1.07	0.38	0.45	2.11	14.16
11	TD-50-55	148.5	78.99	0.10	0.05	0.88	0.35	0.06	0.63	1.00	6.24
12	TD-55-60	153.5	105.50	0.11	0.06	0.81	0.53	0.14	0.53	1.37	6.99
13	TD-60-65	158.5	151.10	0.24	0.08	0.80	0.83	0.57	0.58	2.13	8.14
14	TD-65-70	163.5	264.40	0.19	0.12	1.04	1.06	0.62	0.32	2.16	6.63
15	TD-70-75	168.5	233.40	0.22	0.17	1.27	0.69	0.62	0.27	2.03	4.45

Table B.6: *(continued).* Pit S-15 ICP-OES (Part 2)

Lab. ID	Sample ID	mean depth	Ca ICP-OES	PO4 ICP-OES	Mn ICP-OES	Fe ICP-OES	Sr ICP-OES	Na ICP-OES	K ICP-OES	S ICP-OES	Mg ICP-OES
		[cm]	[mg/g]	[mg/g]	[mg/g]	[mg/g]	[mg/g]	[mg/g]	[mg/g]	[mg/g]	[mg/g]
16	TD-75-80	173.5	209.30	0.16	0.09	0.90	0.64	0.68	0.25	2.27	3.89
17	TD-80-85	178.5	126.40	0.10	0.05	0.87	0.32	0.57	0.33	1.76	2.78
18	TD-85-90	183.5	152.00	0.16	0.11	0.66	0.55	0.56	0.40	2.20	3.02
19	TD-90-95	188.5	227.10	0.15	0.12	0.70	0.66	0.49	0.33	2.92	3.86
20	TD-95-100	193.5	176.60	0.17	0.09	0.76	0.60	0.56	0.32	2.71	3.89
21	TD-100-105	198.5	187.10	0.12	0.07	0.50	0.60	0.48	0.22	3.07	3.61
22	TD-105-110	203.5	232.20	0.15	0.14	0.50	0.79	0.40	0.21	3.62	3.88
23	TD-110-115	208.5	227.80	0.14	0.15	0.44	0.79	0.42	0.17	3.86	3.82
24	TD-115-120	213.5	207.60	0.21	0.13	0.45	0.65	1.38	0.21	4.04	3.38
25	TD-120-125	218.5	194.90	0.12	0.12	0.48	0.61	0.44	0.21	3.65	3.19
26	TD-125-130	223.5	187.20	0.09	0.13	0.42	0.60	0.48	0.22	3.57	2.82
27	TD-130-135	228.5	200.90	0.08	0.13	0.51	0.69	0.38	0.22	4.10	3.19
28	TD-135-140	233.5	147.70	0.18	0.08	0.36	0.46	0.90	0.27	3.24	2.28
29	TD-140-145	238.5	174.20	0.08	0.11	0.38	0.60	0.35	0.23	3.83	2.63
30	TD-145-150	243.5	210.80	0.10	0.15	0.40	0.76	0.44	0.20	4.34	3.00
31	TD-150-155	248.5	206.60	0.08	0.14	0.43	0.80	0.65	0.19	4.40	2.98
32	TD-155-160	253.5	156.60	0.08	0.13	0.43	0.61	0.48	0.19	3.70	2.80
33	TD-160-165	258.5	130.20	0.14	0.11	0.32	0.49	0.39	0.17	3.33	2.21
34	TD-165-170	263.5	89.49	0.13	0.08	0.29	0.33	0.40	0.17	3.19	1.76
35	TD-170-175	268.5	66.69	0.04	0.06	0.38	0.23	0.32	0.21	1.96	1.77
36	TD-175-180	273.5	26.25	0.09	0.02	0.58	0.10	0.51	0.26	1.22	1.68
37	TD-180-185	278.5	21.72	0.03	0.01	0.40	0.10	0.36	0.28	0.96	1.71
38	TD-185-190	283.5	13.44	0.02	0.01	0.47	0.06	0.14	0.23	0.58	1.46
39	TD-190-195	288.5	9.29	0.12	0.01	0.41	0.05	0.36	0.24	0.66	1.15
40	TD-195-200	293.5	7.50	0.02	0.01	0.50	0.05	0.35	0.29	0.64	1.72

Table B.6: *(continued).* Pit S-15 XRF + LOI

Lab. ID	Sample ID	mean depth	Sr XRF	Fe XRF	Ti XRF	Ca XRF	K XRF	Si XRF	Al XRF	TOC LOI	TIC LOI	Si remain LOI
		[cm]	[ppm]	[ppm]	[ppm]	[ppm]	[ppm]	[ppm]	[ppm]	[%]	[%]	[%]
50.5	TD2-50-55	43.5	1318.454	2793.493	311.993	239217.451	374.801	179331.977	22137.785	3.57	6.11	42.90
50	TD2-45-50	48.5	1331.918	2891.312	314.943	231145.510	318.796	184067.431	20834.310	3.65	6.06	43.16
49	TD2-40-45	53.5	1504.685	3265.535	356.226	220115.598	365.376	198860.589	19808.580	3.77	5.80	45.19
48	TD2-35-40	58.5	1355.878	3174.609	358.627	214717.573	283.076	197441.536	17601.140	3.59	5.45	48.36
47	TD2-30-35	63.5	1461.689	3146.454	349.673	207016.959	10.000	204583.255	20068.180	3.45	5.28	50.04
46	TD2-25-30	68.5	1455.919	3817.649	395.552	203320.971	257.830	215402.661	17513.040	3.58	5.28	49.82
45	TD2-20-25	73.5	1524.735	4037.467	442.063	215527.704	246.542	195066.754	19852.010	4.32	5.50	46.74
44	TD2-15-20	78.5	1540.207	3869.109	450.427	210412.619	10.000	193093.140	22125.920	4.14	5.47	47.25
43	TD2-10-15	83.5	1572.749	3846.957	409.196	210374.883	338.723	194109.748	18305.710	3.86	5.64	46.31
42	TD2-5-10	88.5	1543.123	3625.431	500.892	220887.522	10.000	174462.807	21607.320	3.74	5.87	44.64
41	TD2-0-5	93.5	1549.657	3633.046	492.310	219312.990	10.000	158853.611	20960.990	4.24	5.68	45.36
51	TD2-0-(-5)	98.5	1234.312	5418.100	543.014	232195.409	605.861	194596.411	23745.490	2.14	6.33	43.56
52	TD2-(-5)-(-10)	103.5	1158.043	6192.797	506.451	212719.804	634.883	203924.921	21091.960	2.29	5.15	53.15
53	TD2-(-10)-(-15)	108.5	1149.690	6088.267	592.537	224109.785	698.877	193796.023	19671.630	2.28	5.26	52.24
4	TD-15-20	113.5	803.863	5252.730	432.270	163261.594	2173.458	236369.070	13359.160	1.85	4.13	63.49
5	TD-20-25	118.5	326.122	12369.196	678.881	55140.688	2376.146	405666.997	6479.150	1.62	1.54	84.74
6	TD-25-30	123.5	152.236	11815.484	1035.252	7240.809	1957.248	438089.207	2156.790	1.74	0.51	92.85
7	TD-30-35	128.5	1004.667	10045.410	575.052	162497.193	1022.215	223246.351	14181.460	2.07	4.60	59.45
8	TD-35-40	133.5	1224.591	10017.728	529.225	214128.953	1034.853	160252.925	21409.100	2.26	5.41	52.76
9	TD-40-45	138.5	1078.470	8512.428	531.658	210052.714	1029.262	152352.151	20447.440	2.02	5.38	53.28
10	TD-45-50	143.5	833.437	8653.799	381.805	154817.528	834.359	199051.156	17005.920	2.30	3.97	64.25
11	TD-50-55	148.5	359.427	9202.842	593.147	108440.537	2081.665	216880.108	13290.690	2.05	1.51	84.31
12	TD-55-60	153.5	459.092	8365.749	539.680	134177.466	1854.943	188539.784	15033.210	2.14	2.26	78.14
13	TD-60-65	158.5	645.804	6861.254	409.465	178772.980	1847.867	154692.182	20827.200	2.05	3.34	69.63
14	TD-65-70	163.5	1046.314	5828.844	623.437	295640.234	871.990	101321.354	27905.370	2.11	7.48	36.30
15	TD-70-75	168.5	718.886	7226.528	636.966	274505.732	748.205	117819.101	25509.940	1.98	6.73	42.39

Table B.6: *(continued).* Pit S-15 XRF + LOI (Part 2)

Lab. ID	Sample ID	mean depth	Sr XRF	Fe XRF	Ti XRF	Ca XRF	K XRF	Si XRF	Al XRF	TOC LOI	TIC LOI	Si remain LOI
		[cm]	[ppm]	[ppm]	[ppm]	[ppm]	[ppm]	[ppm]	[ppm]	[%]	[%]	[%]
16	TD-75-80	173.5	696.055	7024.012	624.679	256236.617	782.915	141574.260	24429.260	2.34	6.08	47.38
17	TD-80-85	178.5	441.279	10787.895	852.449	150156.354	768.326	262569.768	14776.010	2.19	3.55	67.79
18	TD-85-90	183.5	613.691	12484.705	909.788	186267.702	694.276	179904.329	20390.450	2.44	4.33	61.24
19	TD-90-95	188.5	620.956	8715.555	404.041	263796.422	1218.672	118405.207	29330.560	2.38	6.12	46.97
20	TD-95-100	193.5	644.759	8460.955	693.808	237910.680	989.515	139346.543	26384.700	2.79	5.17	54.20
21	TD-100-105	198.5	721.896	6408.070	880.741	252342.598	826.642	135922.575	27682.270	2.83	5.71	49.86
22	TD-105-110	203.5	840.744	5794.797	407.881	297042.710	714.029	94090.315	30406.640	2.13	6.97	40.40
23	TD-110-115	208.5	918.592	3924.000	286.030	320674.969	486.395	84409.050	35044.760	1.94	7.60	35.43
24	TD-115-120	213.5	750.539	4481.534	418.802	285616.304	659.401	102422.625	27925.450	1.99	6.34	45.53
25	TD-120-125	218.5	726.015	4710.593	600.145	269142.024	751.224	110988.794	28305.460	2.30	5.90	48.78
26	TD-125-130	223.5	732.329	5019.016	464.516	281260.401	763.308	106704.218	28020.360	2.27	5.78	49.81
27	TD-130-135	228.5	756.885	5383.400	533.065	278844.297	725.628	98210.938	31019.830	2.12	6.23	46.34
28	TD-135-140	233.5	560.189	7581.282	563.510	212126.456	576.441	141625.432	22547.460	1.81	4.44	61.03
29	TD-140-145	238.5	722.712	6338.948	466.162	273080.381	866.108	100472.868	29065.910	1.97	5.64	51.22
30	TD-145-150	243.5	829.130	5312.861	331.630	288042.090	736.053	89774.164	27294.630	2.08	6.03	47.94
31	TD-150-155	248.5	872.115	4952.089	333.856	296069.643	522.794	78430.728	32200.760	1.98	6.15	47.05
32	TD-155-160	253.5	744.152	5096.184	358.731	262580.649	704.837	94578.175	25038.600	1.80	5.05	56.15
33	TD-160-165	258.5	610.785	5028.688	466.959	225398.972	858.304	131896.038	22338.500	1.49	4.29	62.61
34	TD-165-170	263.5	459.991	5487.917	415.956	183384.076	970.636	156365.359	20269.980	1.38	2.97	73.47
35	TD-170-175	268.5	303.720	7434.214	517.434	119933.970	1361.695	225075.254	12740.780	1.73	1.77	82.67
36	TD-175-180	273.5	191.197	10742.675	703.404	60128.945	1657.040	302843.691	11729.200	1.75	0.72	91.14
37	TD-180-185	278.5	166.495	11188.341	736.074	47901.312	1959.859	298954.877	10134.740	1.46	0.62	92.43
38	TD-185-190	283.5	120.405	9347.784	686.510	32056.817	1810.255	338508.005	9529.760	1.28	0.42	94.37
39	TD-190-195	288.5	98.107	10184.488	638.043	20823.817	1935.749	347381.335	9557.800	1.28	0.26	95.67
40	TD-195-200	293.5	90.330	10654.432	774.552	16023.020	2063.329	347605.304	8639.730	0.96	0.34	95.54

Table B.6: *(continued).* Pit S1-18 minerals

Lab. ID	Sample ID	mean depth	Quartz	Calcite	Sepiolite	Palygorkite	Illite	Albite low	Gypsum	Leucite + Feldspar Sr
		[cm]	[cps]	[cps]	[cps]	[cps]	[cps]	[cps]	[cps]	[cps]
T-16	TDP-S1-16	12.5	3428.68	97096.04	2372.16	0	505.93	347.57	1453.29	0
T-15	TDP-S1-15	17.5	10278.33	98220.59	466.56	0	0	0	1763.08	0
T-14	TDP-S1-14	22.5	8147.88	104891.52	294.43	181.53	172.74	0	2141.46	0
T-13	TDP-S1-13	27.5	7138.09	93514.69	472.54	0	238.97	0	2537.07	0
T-12	TDP-S1-12	32.5	15962.29	84796.45	430.65	0	186.85	0	2851.24	0
T-11	TDP-S1-11	37.5	7369.39	83463.45	265.02	0	0	0	2673.90	0
T-10	TDP-S1-10	42.5	75252.46	53885.86	3422.49	561.37	1199.73	1680.12	12487.08	0
T-09	TDP-S1-09	47.5	57395.07	57932.48	2973.34	466.66	1096.23	1687.20	10733.66	0
T-08	TDP-S1-08	52.5	43528.44	89557.42	528.73	0	226.24	0	5821.38	135.15
T-07	TDP-S1-07	57.5	80505.05	72981.05	1063.66	0	429.78	227.24	11563.03	0
T-06	TDP-S1-06	62.5	44872.25	81084.11	498.76	82.86	0	0	8064.79	46.89
T-05	TDP-S1-05	67.5	23744.01	83550.82	458.27	0	0	0	4509.16	0
T-04	TDP-S1-04	72.5	13602.21	88274.19	249.55	0	0	0	2985.55	0
T-03	TDP-S1-03	77.5	43066.13	74072.96	873.56	0	377.77	0	5938.23	0
T-02	TDP-S1-02	82.5	25163.14	80071.35	807.93	0	308.17	0	4457.44	0
T-01	TDP-S1-01	87.5	38132.03	78344.17	772.69	0	288.22	0	5822.16	0

Table B.6: *(continued).* Pit S2-18 minerals

Lab. ID	Sample ID	mean depth	Quartz	Calcite	Sepiolite	Palygorkite	Illite	Albite low	Gypsum	Leucite + Feldspar Sr
		[cm]	[cps]	[cps]	[cps]	[cps]	[cps]	[cps]	[cps]	[cps]
T-42	TDP-S2-26	15.0	490138.09	6201.84	5684.80	924.15	1205.98	1679.85	89510.95	0
T-41	TDP-S2-25	25.0	477129.88	6305.30	5830.15	835.19	1074.37	1617.15	89048.25	0
T-40	TDP-S2-24	35.0	192737.81	2059.12	17178.60	6983.58	6099.03	5017.07	32348.10	0
T-39	TDP-S2-23	55.0	190962.36	2036.14	17471.88	7131.21	6500.39	4923.27	32272.76	0
T-38	TDP-S2-22	75.0	192429.69	1914.13	17724.52	6329.81	5925.89	4949.32	31797.06	4266.30
T-37	TDP-S2-21	85.0	194204.67	1821.04	17404.84	6279.39	6275.95	4859.12	32141.25	4232.60
T-36	TDP-S2-20	95.0	193915.77	2115.27	17215.97	7075.59	5943.58	5032.57	32148.57	0
T-35	TDP-S2-19	105.0	193532.09	2070.96	17573.96	6971.76	6221.32	5158.81	31832.74	0
T-34	TDP-S2-18	115.0	51151.91	79152.52	4977.50	745.43	1719.86	1436.94	13521.09	0
T-33	TDP-S2-17	127.5	51029.71	79387.20	4922.15	845.10	1816.48	1450.31	13951.21	0
T-32	TDP-S2-16	135.0	51813.17	78865.83	4324.65	889.05	1678.86	1566.02	14110.71	0
T-31	TDP-S2-15	145.0	49625.91	78276.42	4916.54	852.50	1432.79	1044.06	13320.64	0
T-30	TDP-S2-14	152.5	50769.07	79096.52	4582.39	0	1523.95	1616.28	13856.37	0
T-29	TDP-S2-13	157.5	51156.44	79113.75	4847.38	777.37	1488.77	1530.08	13730.64	0
T-28	TDP-S2-12	162.5	56043.38	86390.06	3387.15	639.81	1305.98	584.37	9862.68	0
T-27	TDP-S2-11	167.5	56099.85	87106.57	3426.97	607.85	1296.20	638.32	9938.71	0
T-26	TDP-S2-10	171.5	330.64	138591.16	0	0	0	721.60	0	138.66
T-25	TDP-S2-09	176.5	361.94	139253.30	49.67	77.28	0	0	0	146
T-24	TDP-S2-08	182.5	51468.88	94828.87	2258.33	0	904.33	0	10994.60	0
T-23	TDP-S2-07	187.5	51461.32	94652.58	2297.71	410.34	808.76	0	11004.44	0
T-22	TDP-S2-06	192.5	51122.97	94779.52	2302.22	0	867.37	0	11054.57	0
T-21	TDP-S2-05	197.5	51201.30	94894.90	2369.79	0	795.55	0	11399.10	0
T-20	TDP-S2-04	203.5	51305.34	94479.79	2302.82	0	909.59	0	10998.60	0
T-19	TDP-S2-03	209.0	51734.99	95285.22	2141.39	0	861.16	679.13	11326.02	0
T-18	TDP-S2-02	213.0	29187.30	78064.76	2196.28	0	992.24	0	8580.19	0
T-17	TDP-S2-01	217.5	38401.64	80964.42	2024.93	0	871.81	395.71	6721.11	0

Table B.6: *(continued).* Pit N-18 minerals

Lab. ID	Sample ID	mean depth	Quartz	Calcite	Sepiolite	Palygorkite	Illite	Albite low	Gypsum	Leucite + Feldspar Sr
		[cm]	[cps]	[cps]	[cps]	[cps]	[cps]	[cps]	[cps]	[cps]
T -76	TDP-N-34	5.0	100958.28	66068.11	1144.58	386.12	363.13	0	16163.00	0
T -75	TDP-N-33	15.0	100804.96	65897.32	1101.58	355.36	418.26	0	16486.00	0
T -74	TDP-N-32	25.0	100244.09	65316.12	1153.53	362.70	467.16	0	16313.00	0
T- 73	TDP-N-31	35.0	101070.84	66165.30	1105.44	0	532.54	0	16328.00	0
T -72	TDP-N-30	42.5	101064.04	66048.89	1067.48	0	407.20	0	16187.00	0
T -71	TDP-N-29	47.5	102805.32	65059.14	1088.03	347.37	454.49	0	16208.00	0
T -70	TDP-N-28	52.5	11545.80	0	0	0	5580.06	1505	2169.00	21233
T -69	TDP-N-27	57.5	11684.07	0	0	0	5520.45	1512	2111.00	20978
T -68	TDP-N-26	62.5	11623.47	0	0	0	5543.44	1496	2171.00	21073
T -67	TDP-N-25	67.5	11584.60	0	0	0	5554.81	1355	2144.00	21626
T -66	TDP-N-24	72.5	73701.80	60048.88	2631.29	710.37	1244.65	0	21400.00	0
T -65	TDP-N-23	77.5	73527.87	59395.45	2542.10	627.44	1004.67	1338	20778.00	0
T -64	TDP-N-22	82.5	154019.08	55832.86	3574.37	0.00	1121.98	1348	28304.00	0
T -63	TDP-N-21	87.5	153390.13	55079.71	3202.34	0.00	960.10	673	274.77	0
T -62	TDP-N-20	92.5	154877.39	55399.86	3725.55	806.13	881.86	1318	28046.00	0
T -61	TDP-N-19	97.5	153388.80	55569.52	3593.38	0	928.75	1339	27773.00	0
T -60	TDP-N-18	102.5	154091.05	56086.20	3044.28	0	1137.71	1351	28467.00	0
T -59	TDP-N-17	107.5	154687.69	55672.50	3767.35	751.02	938.10	1379	28451.00	0
T -58	TDP-N-16	112.5	451898.78	3503.85	0	634.32	359.25	0	70781.00	0
T -57	TDP-N-15	117.5	453581.31	3452.00	1453.13	625.44	0	0	70895.00	0
T -56	TDP-N-14	122.5	245347.81	23083.35	4197.42	993.68	1094.86	1552	52512.00	0
T -55	TDP-N-13	127.5	246837.03	23280.02	3979.85	1048.97	1092.89	1541	51846.00	0
T -54	TDP-N-12	132.5	245245.94	23156.20	4166.23	1004.88	1088.48	1592	49756.00	0
T -53	TDP-N-11	137.5	248950.94	22990.96	4235.79	986.66	1138.16	1757	52616.00	0
T -52	TDP-N-10	142.5	246279.31	23375.80	4137.87	1020.75	1130.84	1515	50015.00	0
T -51	TDP-N-09	147.5	244755.42	23145.81	3995.54	1013.31	1174.89	1598	52801.00	0
T -50	TDP-N-08	152.5	149889.67	10222.51	5221.50	1300.47	2041.98	2310	30629.00	0
T -49	TDP-N-07	157.5	146985.83	9997.98	4923.70	1392.92	2142.11	2444	305.01	0
T -48	TDP-N-06	162.5	359187.75	6765.32	3692.04	1148.78	1083.84	1567	66339.00	0
T -47	TDP-N-05	167.5	359054.09	6593.21	3855.62	1273.95	1149.19	1589	67084.00	2282
T -46	TDP-N-04	172.5	353029.78	6709.25	3655.67	1252.13	1088.40	1628	65259.00	0
T -45	TDP-N-03	177.5	358897.03	6771.65	3592.64	225.71	929.61	1571	66596.00	0
T -44	TDP-N-02	182.5	360158.91	6904.47	3789.31	1189.23	1105.53	0	66759.00	0
T -43	TDP-N-01	187.5	358947.75	6594.02	3780.84	1272.22	1155.81	1522	66410.00	0

Table B.6: *(continued).* Pit S-15 minerals

Lab. ID	Sample ID	mean depth	Quartz	Calcite	Sepiolite	Palygorkite	Illite	Albite low	Gypsum	Leucite + Feldspar Sr
		[cm]	[cps]	[cps]	[cps]	[cps]	[cps]	[cps]	[cps]	[cps]
50.5	TD2-50-55	43.5	11843	76376	3340	1200	1095	1215	5966	0
50	TD2-45-50	48.5	4055	68449	4449	4449	1390	1281	5402	1200
49	TD2-40-45	53.5	10586	63295	4727	4727	1488	1348	2525	1436
48	TD2-35-40	58.5	7776	61667	4909	4909	1575	1373	4959	1358
47	TD2-30-35	63.5	9155	61662	4614	4757	1690	1464	4478	1446
46	TD2-25-30	68.5	11970	54890	5617	518	1834	1477	3668	1459
45	TD2-20-25	73.5	13781	55386	6394	451	1925	1646	6725	1414
44	TD2-15-20	78.5	13856	57650	6088	0	1911	1669	3629	1424
43	TD2-10-15	83.5	7578	59656	6868	635	2283	1776	3326	1507
42	TD2-5-10	88.5	6104	65633	6829	0	2253	1734	4161	1342
41	TD2-0-5	93.5	15679	68066	7208	0	2379	1825	4486	0
51	TD2-0-(-5)	98.5	17125	77389	1834	873	514	0	5187	0
52	TD2-(-5)-(-10)	103.5	27223	70151	4141	0	1434	1272	3057	0
53	TD2-(-10)-(-15)	108.5	14701	78094	1833	1035	622	0	2487	0
4	TD-15-20	113.5	84021	57643	2496	1039	734	556	21239	879
5	TD-20-25	118.5	188610	19387	3649	1790	1415	858	29876	0
6	TD-25-30	123.5	129925	2185	4568	1657	1577	1205	24791	1588
7	TD-30-35	128.5	80440	53685	5033	1450	1666	1784	14643	0
8	TD-35-40	133.5	25642	71563	5880	1329	1878	1524	6029	0
9	TD-40-45	138.5	32174	72217	6759	1292	2154	1766	7510	0
10	TD-45-50	143.5	57942	61156	10655	2574	2964	2421	18499	0
11	TD-50-55	148.5	104797	46209	5271	2490	1736	1131	22060	1494
12	TD-55-60	153.5	96185	55128	4397	2028	1511	1643	37640	0
13	TD-60-65	158.5	119936	71360	3506	1429	1172	818	29254	0
14	TD-65-70	163.5	37730	84532	1290	929	517	818	29254	0
15	TD-70-75	168.5	46098	82799	939	966	474	0	5415	712
16	TD-75-80	173.5	22697	83411	840	1293	489	0	6031	678
17	TD-80-85	178.5	92638	59932	1403	2350	827	0	5614	0
18	TD-85-90	183.5	34803	78039	1733	2542	0	0	9711	0
19	TD-90-95	188.5	18841	99235	2282	1492	837	0	6947	0
20	TD-95-100	193.5	27353	92155	2009	1471	815	0	4806	0
21	TD-100-105	198.5	36214	86619	1588	924	671	0	47	0
22	TD-105-110	203.5	26453	102551	1659	828	545	0	2885	442
23	TD-110-115	208.5	54497	110562	0	0	400	0	6199	0
24	TD-115-120	213.5	28762	103242	1759	564	469	0	4159	0
25	TD-120-125	218.5	35345	102169	1866	395	438	626	6922	0
26	TD-125-130	223.5	16316	110724	1709	325	391	443	5223	0
27	TD-130-135	228.5	36146	105722	1405	373	455	0	4400	0
28	TD-135-140	233.5	53760	92142	2183	826	855	472	10284	866
29	TD-140-145	238.5	14430	108137	2027	0	647	0	6117	0
30	TD-145-150	243.5	7608	112193	1810	0	686	0	3931	0
31	TD-150-155	248.5	25581	108375	1779	0	563	0	4506	0
32	TD-155-160	253.5	26584	100718	1735	0	0	0	5916	0
33	TD-160-165	258.5	123451	95260	1761	0	0	0	8456	0
34	TD-165-170	263.5	169732	81165	2084	589	688	0	33218	0
35	TD-170-175	268.5	129130	57261	2932	1230	1051	1555	18734	0
36	TD-175-180	273.5	131792	28129	3921	2082	1468	1820	39125	0
37	TD-180-185	278.5	112390	22401	4966	2442	1875	2167	24150	0
38	TD-185-190	283.5	216814	13072	3229	1713	1187	1005	54135	0
39	TD-190-195	288.5	326902	8820	4380	2214	1322	1986	67879	0
40	TD-195-200	293.5	187808	7128	4558	1721	1871	1945	56216	0

Supplementary material
for 2nd manuscript (Chapter 3)

This supplementary section includes seven supplementary figures related to the end-member modelling analysis, the assignment of raster points to the rainfall zones, the isotopic composition of the precipitation from the winter rainfall zone and the determined moisture source regions of the rainfall zones.

The six supplementary tables contain information about the GNIP stations used in the study, the ANOVA (Analysis of Variance) Post Hoc Tukey's test results, the proportions of moisture uptake above the main source regions of the rainfall zones and the explanation of variables displayed in the linear regression and random forest analysis.
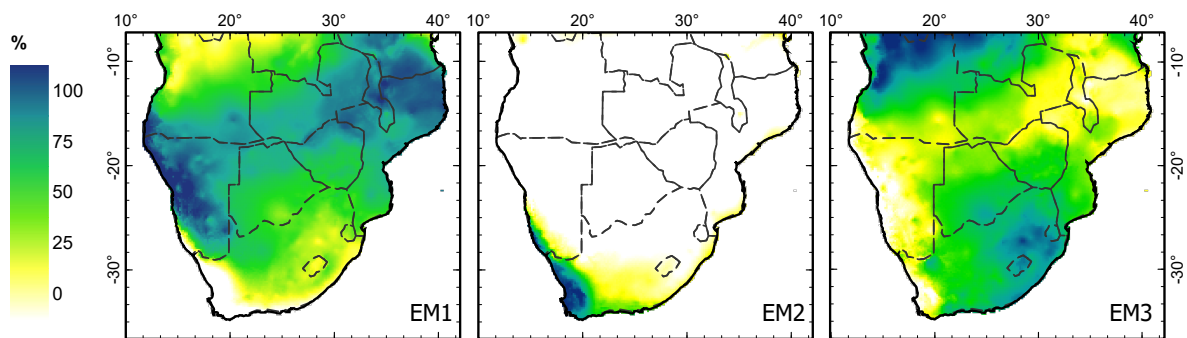

Figure C.1: Maps showing the spatial distribution of the three end-members (EM) representing the main groups of annual precipitation distributions (PD) in southern Africa. blue: location belongs to 100 % to the respective PD; green: location belongs to 50 % to the respective PD; yellow: location belongs to 25 % to the respective PD; white: location does not belong to the respective PD.
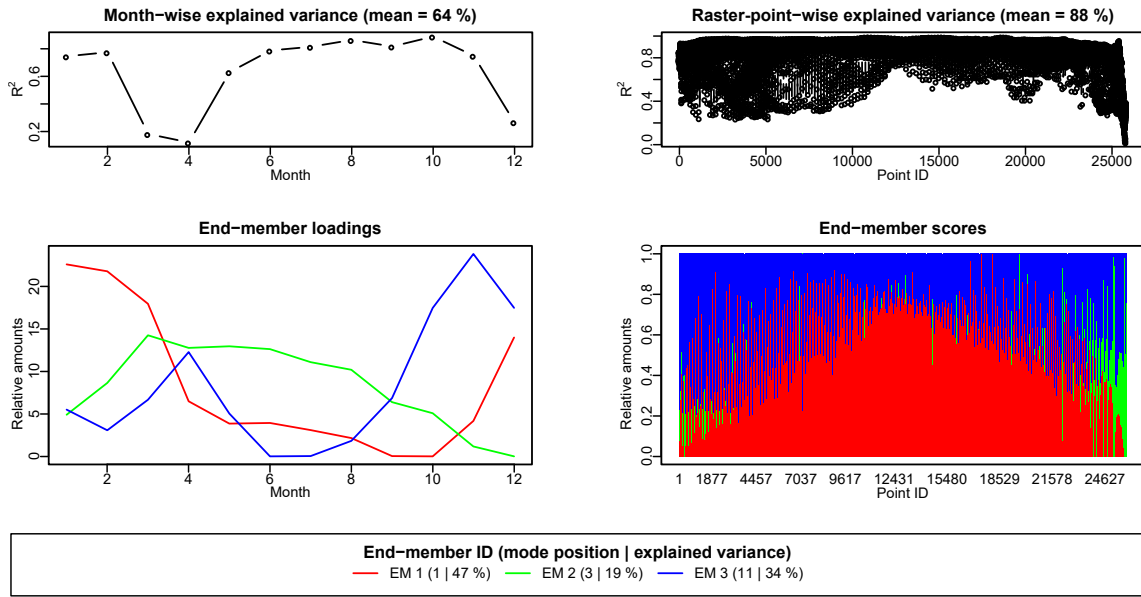
Figure C.2: Results of the 3 end-member model for the precipitation distributions of raster points within southern Africa.
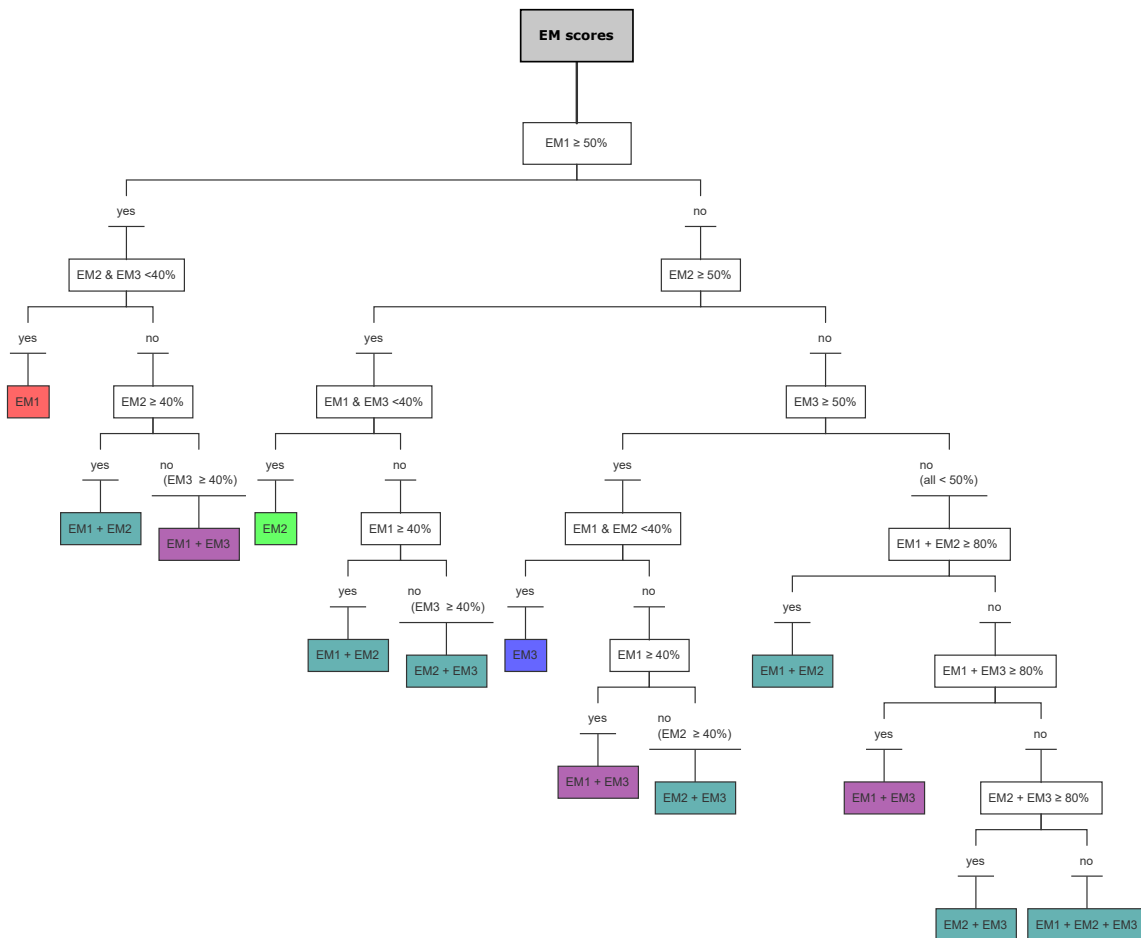

Figure C.3: Decision tree for the assignment of each raster point to one of the five rainfall zones based on the end-member (EM) scores of the 3 EM model. SRZw = EM1, SRZe = EM3, SRZm = EM1 + EM3, WRZ = EM2, YRZ= combination of EM2 and EM2 and/or EM3.
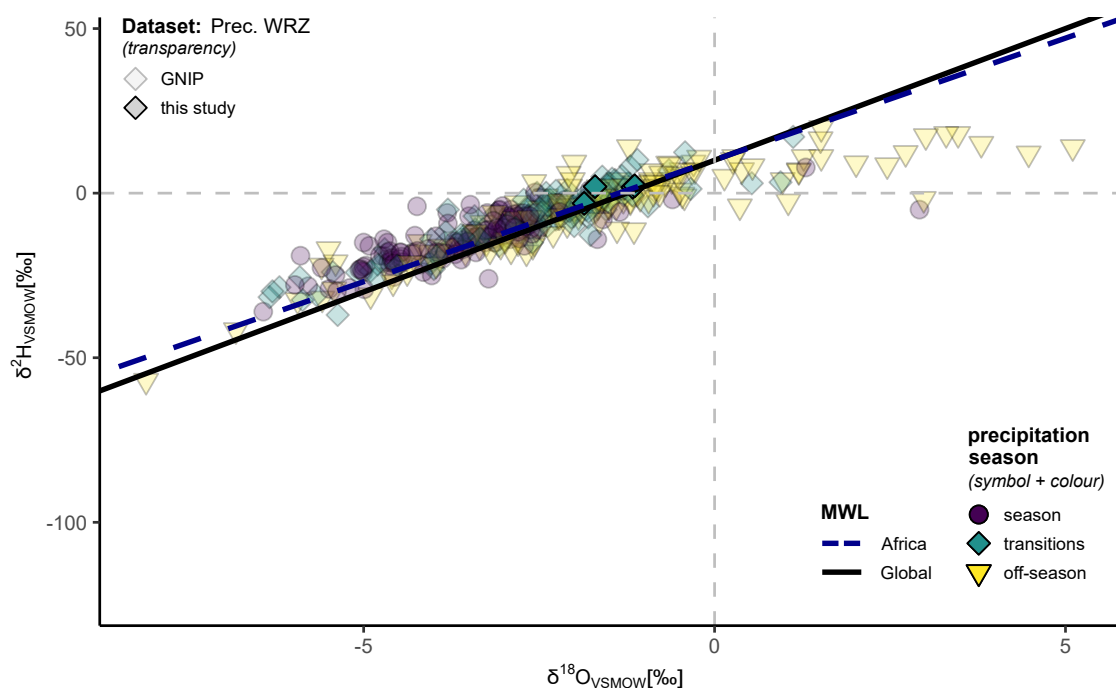
Figure C.4: Plot of δ^2H against δ^{18}O for the WRZ showing the deviation from the Global and African meteoric water lines (MWL) of precipitation samples mainly during the off-season of precipitation. Samples are colour coded by precipitation season and different transparencies used for the two datasets.

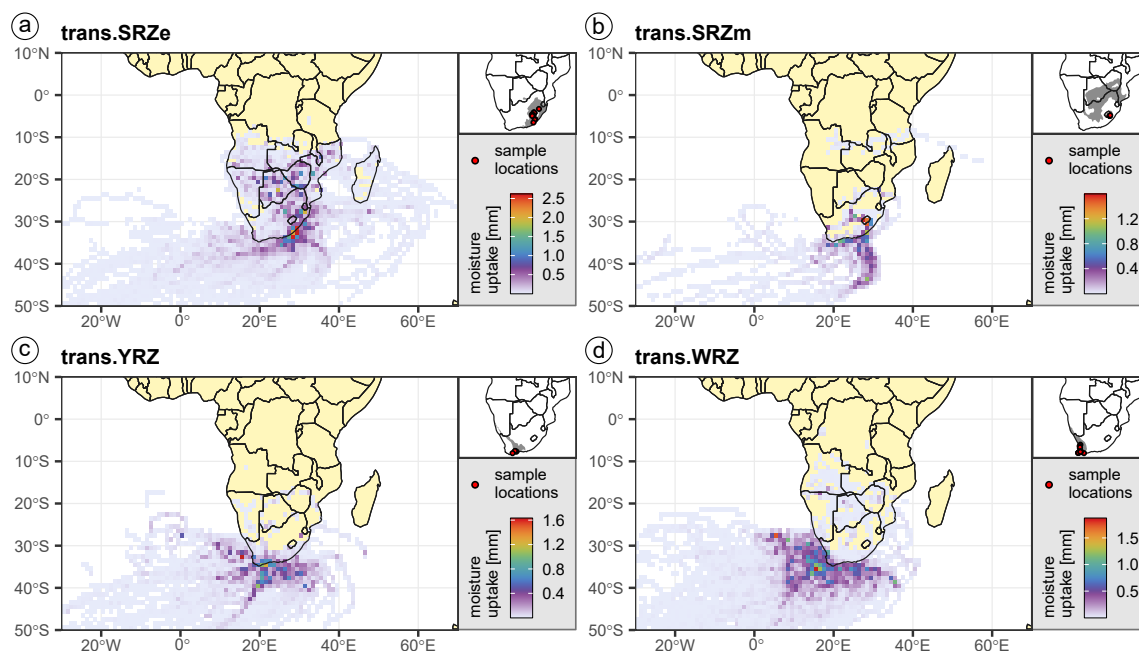**Figure C.5:** Moisture source regions for the samples from the different RFZ (a-d) during the transition precipitation seasons (5–10 % P_a). Shown is the amount of moisture uptake in mm that contributed to the final precipitation at the sampling locations. **a)** SRZe, **b)** SRZm, **c)** YRZ, **d)** WRZ. SRZw is not shown, due to insufficient number of samples (n = 0) during the transition times.
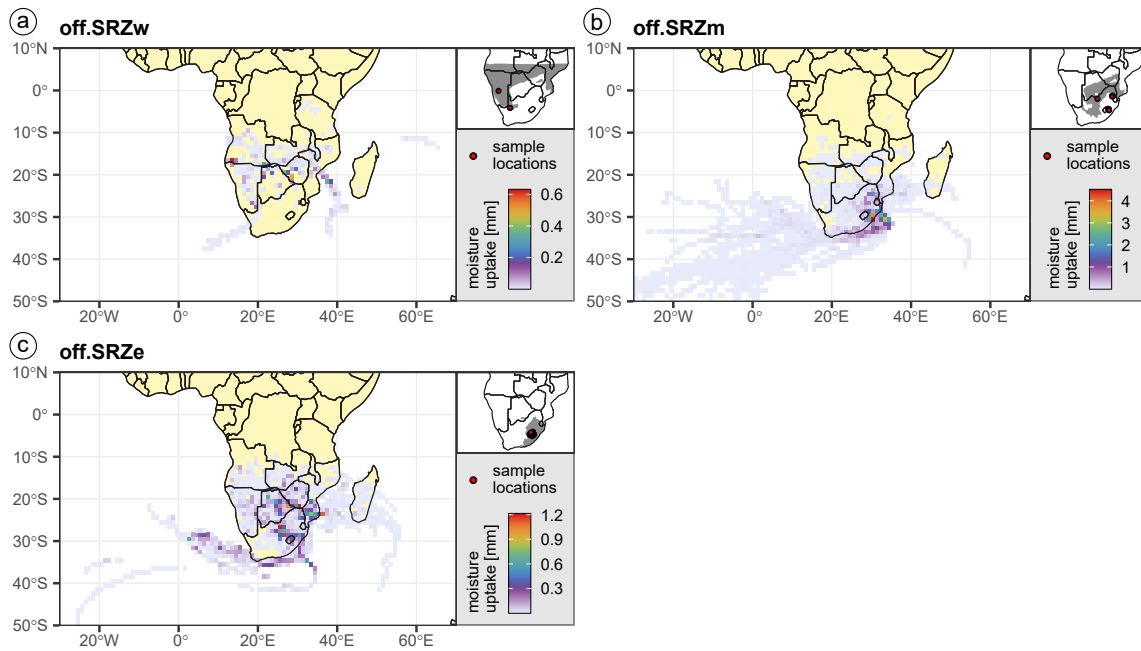
Figure C.6: Moisture source regions for the samples from the different RFZ (a-c) during the off-season of precipitation ($< 5\,\%$ P_a). Shown is the amount of moisture uptake in mm that contributed to the final precipitation at the sampling locations. **a)** SRZw, **b)** SRZm, **c)** SRZe. YRZ and WRZ are not shown, due to insufficient number of samples ($n_{(YRZ)} = 1$) and too low amount of precipitation (sum of $P_{(WRZ)} < 1\,\text{mm}$) during the off-season time of precipitation.

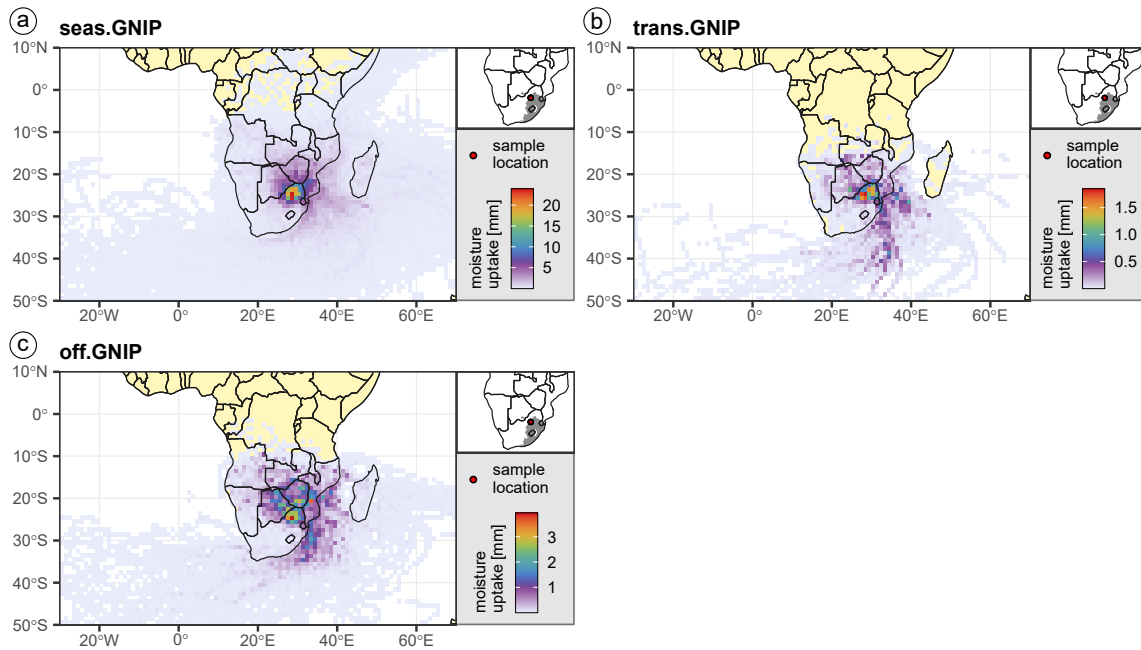**Figure C.7:** Moisture source regions for samples from the GNIP station at Pretoria during the precipitation seasons (a-c). The figures show the amount of moisture uptake in mm that contributed to the final precipitation at the sampling location. **a)** precipitation season ($n = 36$ months), **b)** transition times ($n = 6$ months), **c)** off-season ($n = 30$ months).

Table C.1: General information about the 8 included GNIP Stations. [1]Project and site reference: Harris et al. (2010)

GNIP Site	Latitude	Longitude	Elevation [m a.s.l.]	No. of records	Sampling period from	to
Windhoek	-22.948056	17.152500	1685	92	15.01.1961	15.12.2001
Pretoria	-25.730000	28.180000	1330	170	15.01.1958	15.12.2001
Cape Town University[1]	-33.958333	18.461111	105	151	15.01.1995	15.12.2008
Cape Town Airport	-33.970000	18.600000	44	236	15.01.1961	15.12.2013
Harare	-17.830000	31.020000	1471	188	15.01.1960	15.12.2003
Wilderness	-23.723056	17.798889	1260	3	15.01.2000	15.03.2000
Chitengo	-18.975156	34.348425	34	4	15.08.2010	15.03.2011
Gorongosa	-18.671787	34.072393	346	8	15.09.2010	15.10.2011

Table C.2: Long-term statistics of the included GNIP stations. For the stations Wilderness, Chitengo and Gorongosa, no long-term statistics are available, due to the low number of records (cf. Table C.1).

GNIP Site	Prec. Total	δ^{18}O Avg	δ^2H Avg	d-excess Avg	Air Temp. Avg	VP Avg	LSR Regression a	b
	[mm]	[‰]	[‰]	[‰]	[°C]	[hPa]		
Windhoek	366.0 ± 134.7	-4.99 ± 2.39	-2.59 ± 1.73	-24.3 ± 14.4	-11.3 ± 11.4	12.6 ± 3.7	10.1 ± 3.5	19.3 ± 0.7
Pretoria	690.8 ± 162.2	-3.85 ± 1.11	-2.68 ± 0.91	-16.8 ± 7.0	-8.8 ± 6.4	14.1 ± 4.3	12.1 ± 4.8	17.8 ± 0.7
Cape Town University	1,368.5 ± 245.4	-3.33 ± 0.36	-2.64 ± 0.40	-12.6 ± 2.4	-8.4 ± 2.7	14.0 ± 3.8	12.6 ± 2.8	17.2 ± 0.4
Cape Town Airport	522.4 ± 125.4	-3.51 ± 0.74	-2.57 ± 0.66	-12.9 ± 4.4	-8.2 ± 3.7	14.1 ± 2.8	11.8 ± 4.0	16.5 ± 0.6
Harare	852.8 ± 198.2	-6.18 ± 1.32	-3.78 ± 1.12	-34.3 ± 12.7	-15.8 ± 9.5	13.4 ± 3.1	11.8 ± 3.5	17.9 ± 0.4

Table C.3: ANOVA (Analysis of Variance) Post Hoc Tukey's test results showing the difference in means, confidence levels (upper and lower) and the adjusted p-values for all possible pairs of the rainfall zones (RFZs). The SRZm and YRZ were excluded from the analysis, due to their small sample sizes ($n_{(SRZm)} = 6$ and $n_{(YRZ)} = 0$). The confidence levels and p-values show significance between-all groups except for SRZe vs WRZ. Note that this pair contains zero in the confidence interval and thus, has no significant difference.

compared RFZ	diff	lwr	upr	p adj
WRZ vs. **SRZw**	1.32	0.75	1.89	**0.00**
SRZw vs. **SRZe**	1.28	0.57	1.99	**0.00**
SRZe vs. WRZ	0.04	-0.64	0.73	1.00

Table C.4: ANOVA (Analysis of Variance) Post Hoc Tukey's test showing the difference in means, 95 % family-wise confidence levels (upper and lower) and the adjusted p-values for all possible pairs of precipitation seasons within the rainfall zones (RFZs). The SRZm and YRZ were excluded from the analysis, due to their small sample sizes ($n_{(SRZm)} = 6$ and $n_{(YRZ)} = 0$). Note that pairs containing zero in the confidence intervals will have no significant difference.

RFZ	Compared seasons	diff	lwr	upr	p adj
	transition vs. off-season	1.35	-0.29	2.99	0.13
SRZw	**season vs. off-season**	3.96	2.85	5.07	**0.00**
	season vs. transition	2.61	1.11	4.10	**0.00**
	transition vs. off-season	1.04	0.53	1.55	**0.00**
WRZ	**season vs. off-season**	1.90	1.42	2.37	**0.00**
	season vs. transition	0.86	0.34	1.37	**0.00**
	transition vs. off-season	1.68	0.16	3.20	**0.03**
SRZe	**season vs. off-season**	1.96	0.99	2.92	**0.00**
	season vs. transition	0.28	-1.11	1.67	0.88

Table C.5: Proportion of moisture uptake above the main source regions for the five RFZ during the precipitation season (months with >10% Pa). The African continent is furthermore subset by regions below 15°S (southern Africa) and above.

RFZ	Prec. seas.	No. of sampl.	Oceans			Land					Other regions
			South Atlantic Ocean	Indian Ocean	Mozambique Channel	Madagascar	Continental Africa	*<15°S*	*>15°S (Southern Africa)*	Arabian Sea	
			[%]	[%]	[%]	[%]	[%]	[%]	[%]	[%]	
WRZ	seas	6	93.2	3.6	0.2	0.01	3.0	*<0.01*	*2.9*	-	
	trans	11	67.6	25.5	0.2	-	6.6	*0.2*	*6.4*	-	
	off	4	-	-	-	-	100.0	-	*100.0*	-	
	all	**21**	**81.5**	**13.5**	**0.2**	**<0.01**	**4.7**	*0.1*	*4.6*	-	
YRZ	seas	1	1.0	44.3	6.2	0.01	48.5	*0.1*	*48.4*	-	
	trans	4	43.2	43.2	0.1	-	13.4	*<0.01*	*13.4*	-	
	off	1	70.9	14.5	-	-	14.6	-	*14.6*	-	
	all	**6**	**33.9**	**42.6**	**1.6**	**<0.01**	**21.9**	*0.01*	*21.9*	-	
SRZw	seas	52	3.8	5.1	3.2	0.2	87.5	*27.7*	*59.8*	0.1	
	trans	0	-	-	-	-	-	-	-	-	
	off	3	1.7	3.1	15.4	0.03	79.8	*5.4*	*74.3*	-	
	all	**55**	**3.8**	**5.1**	**3.3**	**0.2**	**87.5**	*27.6*	*59.9*	**0.1**	
SRZe	seas	42	3.7	35.0	4.4	0.3	56.6	*0.3*	*56.3*	0.0	
	trans	12	14.1	32.5	2.1	0.4	51.0	*4.1*	*46.9*	-	
	off	20	13.8	13.6	5.6	0.6	66.4	*1.7*	*64.7*	-	
	all	**74**	**5.0**	**34.2**	**4.2**	**0.4**	**56.3**	*0.7*	*55.6*	**0.0**	
SRZm	seas	18	2.5	30.7	14.7	0.3	51.6	*5.7*	*45.9*	0.3	
	trans	5	14.8	54.0	0.2	0.01	31.0	*0.4*	*30.6*	-	
	off	12	13.9	36.2	2.1	0.1	47.7	*0.04*	*47.6*	-	
	all	**35**	**4.9**	**33.0**	**11.9**	**0.3**	**49.7**	*4.5*	*45.1*	**0.2**	

Table C.6: Explanation of the variables displayed in the linear regression and Random Forest results.

Variable short description	Detailed meaning of the variable
artificial land cov. (wmSrc)	weighted mean fraction of artificial land cover at the source location
boundary layer height (wmSrc)	weighted mean height of the boundary layer at the source location
continental water source (wmSrc)	weighted mean fraction of continent (versus ocean) as source for water
convective precip. (wmSnk)	weighted mean amount of convective precipitation at the target location
distance to coast (Snk)	distance to the coast of the target location
elevation (Snk)	elevation of the target location
expl. fraction of precip.	fraction of final total precipitation at the target location explained by moisture uptake below the BLH
fraction of moist. uptake in final precip. (wmSrc)	weighted mean fraction of moisture uptake at source locations that contributes to precipitation at the target location
large scale precip. (wmSnk)	weighted mean amount of large-scale precipitation at the target location
latitude (Snk)	latitude of the target location
latitude (wmSrc)	weighted mean latitude of the sources
longitude (Snk)	longitude of the target location
longitude diff (wmSrc to Snk)	weighted mean longitude difference from the sources to the target location
month	month of the sampling
pressure (wmSrc)	weighted mean pressure at the source locations
pressure (wmSnk)	weighted mean pressure at the target location
rel. humidity diff. (wmSrc to Snk)	weighted mean difference in relative humidity (from sources to target location)
relative humidity (wmSrc)	weighted mean relative humidity at the source locations
rainfall zone (Snk)	rainfall zone of the target location
river type	type of the sampled river (if river sample) e.g., creek, streamlet, major river, . . .
shrub land cov. (wmSrc)	weighted mean amount of shrub land cover at the source locations
specific humidity (wmSrc)	weighted mean amount of specific humidity at the source locations
specific humidity uptake (wmSrc)	weighted mean amount of specific humidity uptake at the source locations
surf. Press. Diff (wmSrc to Snk)	weighted mean difference in surface air pressure from sources to target location
temperature (wmSnk)	weighted mean temperature at the target location
temperature diff. (wmSrc to Snk)	weighted mean difference in temperature from sources to target location
total precip. (Snk)	amount of final total precipitation at the target location
travelled distance (wmSrc to Snk)	weighted mean travelled distance from sources to target location
travelled time (wmSrc to Snk)	weighted mean travelled time from sources to target location
water type	type of the water sample (e.g., precipitation, river, lake)

Curriculum Vitae

Due to data protection regulations, the curriculum vitae is not included in the online version of this doctoral thesis.

Due to data protection regulations, the curriculum vitae is not included in the online version of this doctoral thesis.

List of publications

JOURNAL ARTICLES

2021 **Geppert, M.**, Riedel, F., Gummersbach, V.S., Gutjahr, S., Hoelzmann, P., Reyes Garzón, M.D., Shemang, E.M. & Hartmann, K. (2021) Late Pleistocene hydrological settings at world heritage Tsodilo Hills (NW Kalahari, Botswana), a site of ancient human occupation. *Quaternary Science Advances*, *3*, 100022. https://doi.org/10.1016/j.qsa.2021.100022

2016 Kleeberg, A., **Neyen, M.**, Schkade, U. K., Kalettka, T., & Lischeid, G. (2016). Sediment cores from kettle holes in NE Germany reveal recent impacts of agriculture. *Environmental Science and Pollution Research*, *23*(8), 7409-7424. https://doi.org/10.1007/s11356-015-5989-y

2016 Kleeberg, A., **Neyen, M.**, & Kalettka, T. (2016). Element-specific downward fluxes impact the metabolism and vegetation of kettle holes. *Hydrobiologia*, *766*(1), 261-274. https://doi.org/10.1007/s10750-015-2460-5

CONFERENCE CONTRIBUTIONS

2021 **Geppert, M.**, Riedel, F., Gummersbach, V.S., Gutjahr, S., Hoelzmann, P., Reyes Garzón, M.D., Shemang, E.M. & Hartmann, K. Environmental conditions at a paleo lake system on the UNESCO World Heritage Site Tsodilo Hills, Kalahari Botswana, during the Last Glacial Maximum – *Arbeitskreis Wüstenrandforschung*, online, 08.02.2021. (Oral presentation)

2020 **Geppert, M.**, Pfahl, S., Struck, U, Ingo Kirchner, Shemang, E.M., Hartmann, K. & Riedel, F., Identification of source-sink relationships in southern Africa by stable water isotopes analysis and Lagrangian moisture source diagnostics – *EGU General Assembly*, online, 4.-8.5.2020 (Poster)

2019 **Neyen, M.**, Hartmann, K., Gummersbach, V.S., Reyes Garzón, Gutjahr, S., M.D., Shemang, E.M. & Riedel, F. Late Pleistocene lake-level fluctuations and relief inversion at Paleolake Tsodilo, Kalahari, NW Botswana – *EGU General Assembly*, Vienna, Austria, 7.-12.4.2019 (Poster)

2019 **Neyen, M.**, Hartmann, K., Gummersbach, V.S., Reyes Garzón, Gutjahr, S., M.D., Shemang, E.M. & Riedel, F. Late Pleistocene lake-level fluctuations and relief inversion at Paleolake Tsodilo, Kalahari, NW Botswana – *Arbeitskreis Wüstenrandforschung*, Rauischholzhausen, Germany, 08.-09.02.2019 (Poster)

2018 **Neyen, M.**, Hartmann, K., Bayer, V.S., Reyes Garzón, Gutjahr, S., Ramotoroko, C., M.D., Shemang, E.M. & Riedel, F. Geomorphological features derived by wavelet-based analysis of high-resolution TanDEM-X digital elevation models at Late Quaternary Paleo-lake Tsodilo, Kalahari, NW Botswana – *Central European Conference on Geomorphology and Quaternary Sciences*, Giessen, Germany, 23.-27.9.2018. (Oral Presentation)

2018 **Neyen, M.**, Bayer, V.S., Wiese, R., Reyes Garzón, M.D., Shemang, E.M., Hartmann, K. & Riedel, F. Reconstruction of the Palaeo-lake system Tsodilo, Kalahari, Botsuana – *Arbeitskreis Wüstenrandforschung*, Rauischholzhausen, Germany, 09.-10.02.2018 (Oral Presentation)

2014 **Neyen, M.**, Schkade, U. K., Kalettka, T., & Kleeberg, A. Besonderheiten der Sedimentation und Stoffakkumulation in glazial geprägten Ackerhohlformen (Söllen) der Uckermark (Nordost-Brandenburg). *Conference of the German Limnological Society*, Magdeburg, Germany, 29.09.-02.10.2014 (Oral Presentation).

Acknowledgements

This dissertation would not have been possible without the support and help of numerous people to whom I would like to express my gratitude.

First and foremost I am extremely grateful to my supervisors, Prof. Dr. Frank Riedel and Dr. Kai Hartmann for the opportunity to carry out this interesting research, for the trust they have placed in me and for all the time and expertise they have offered. Their enthusiastic manner, valuable ideas, encouragement and constructive feedback supported me to stay motivated and focused during my PhD study and to constantly grow and improve my research skills. I am also very appreciative for their empathy, especially in difficult times. It has been a pleasure to work and to travel with you! I would also like to express my deepest gratitude to Prof. Dr. Stephan Pfahl, for his supervision on the trajectory analyses and for welcoming me so warmly into his working group. Special thanks also to Dr. Ingo Kirchner and Thomas Bergman for their support and patience with all the technical and programming questions. For agreeing to review this thesis and for the always kind and helpful cooperation I also sincerely thank Prof. Dr. Ulrich Struck.

I would like to extend my sincere thanks to my co-authors for their contributions to the respective manuscripts and to all colleagues, especially the working group of Prof. Dr. Elisha Shemang, to the students and local people for their help and great times during the field trips. I would also like to acknowledge Frank Kutz, Manuela Abendroth and Maike Glos for their assistance with the laboratory work.

I thank Dr. Georg Schwamborn, Mona Storms and Venise Gummersbach, for the great working atmosphere, endless cups of tea and waffels in our office. It was a pleasure to share an office room with you! Thanks should also go to all the other friends and colleagues at the department, especially my next door-roommates Robert Arendt and Leona Faulstich, for their company, their help, the hallway chats, cake breaks and working group activities. Special thanks to Dr. Carolina Müller and Dr. Georg Schwamborn for reading carefully and improving the thesis and to Theresa, Sophia, Mona and Venise for proofreading parts of the thesis and your deep friendship and support already since our student life.

Finally and most important, I would like to thank with all my heart my family. My parents who allowed me to follow my interests and supported me at all points, my husband, Enrico, for his unlimited patience, great understanding, encouragement and overwhelming love. You had my back the whole time and I cannot even begin to tell you how grateful I am! And last but not least our soon to be born daughter, for literally kicking me towards the finish line.

Declaration of Academic Integrity

I, Marielle Geppert, hereby declare that as the author of this dissertation entitled *"Reconstruction of a palaeolake system at the UNESCO World Heritage Site Tsodilo Hills, Kalahari, Botswana: LGM climate, weather and environmental variation"*, I have prepared the work independently and without unauthorized assistance. The co-authors' contributions to the scientific publications are presented in Section 1.5. Furthermore, I assure that I have not used any sources and aids other than those indicated. All statements taken verbatim or in content from other writings are properly denoted as such.

This thesis has not been accepted or rejected in any other doctoral procedure.

_____

Berlin, 24.05.2022